Dissertation

submitted to the
Combined Faculties for the Natural Sciences and for Mathematics
of the Ruperto-Carola University of Heidelberg, Germany
for the degree of
Doctor of Natural Sciences

presented by
Alexej Weber
born in Dushanbe, Tajikistan
Oral examination: 23. June 2010

ii

Interplay Between Geometry and Temperature In The Casimir Effect

Referees: **Prof. Dr. Holger Gies**
           Prof. Dr. Michael G. Schmidt

Wechselwirkung zwischen Geometrie und Temperatur im Casimir Effekt

Zusammenfassung

In dieser Arbeit untersuchen wir die Wechselwirkung zwischen Geometrie und Temperatur im Casimir-Effekt. Dabei betrachten wir insbesondere die Konfigurationen der geneigten Platten und einer Kugel, bzw. eines Zylinders über einer Platte. Wir verwenden den Weltlinienzugang, welcher einen stringinspirierten quantenfeldtheoretischen Formalismus mit Monte Carlo-Techniken vereint. Der Weltlinienformalismus ermöglicht eine präzise Berechnung der Casimir-Energien in beliebigen Geometrien. Wir analysieren die Abhängigkeit der Casimir-Energie, der Kraft und des Drehmoments vom Abstandsparameter und von der Temperatur und finden Casimir Phänomene, welche von langreichweitigen Fluktuationen dominiert werden. Es zeigt sich, dass in so genannten offenen Geometrien thermische Energie-Dichten typischerweise über Bereiche von Größenordnungen thermischer Wellenlängen verteilt sind. Als Folge dessen werden Näherungsverfahren für die thermischen Korrekturen, die auf lokalen Abschätzungen der Energie-Dichte basieren, als unzuverlässig erkannt – sogar im Grenzwert kleiner Abstände. Wärend sich Casimir-Energie, Kraft und Drehmoment bei hohen Temperaturen immer proportional zur Temperatur verhalten, findet sich bei tiefen Temperaturen ein vielfältigeres Bild. Als Spezialfall zeigen wir thermische Kräfte auf, die ein nicht-monotones Verhalten entwickeln. Es werden viele neue numerische und analytische Ergebnisse präsentiert.

Interplay between geometry and temperature in the Casimir effect

Abstract

In this thesis, we investigate the interplay between geometry and temperature in the Casimir effect for the inclined-plates, sphere-plate and cylinder-plate configurations. We use the worldline approach, which combines the string-inspired quantum field theoretical formalism with Monte Carlo techniques. The approach allows the precise computation of Casimir energies in arbitrary geometries. We analyze the dependence of the Casimir energy, force and torque on the separation parameter and temperature T, and find Casimir phenomena which are dominated by long-range fluctuations. We demonstrate that for open geometries, thermal energy densities are typically distributed on scales of thermal wavelengths. As an important consequence, approximation methods for thermal corrections based on local energy-density estimates, such as the proximity-force approximation, are found to become unreliable even at small surface-separations. Whereas the high-temperature behavior is always found to be linear in T, richer power-law behaviors at small temperatures emerge. In particular, thermal forces can develop a non-monotonic behavior. Many novel numerical as well as analytical results are presented.

Contents

Contents

Contents

viii

1 Introduction

1.1 Casimir effect and its applications

The subject of this thesis is the physical phenomenon which is named after the Dutch physicist Hendrik B. G. Casimir. In his seminal paper from 1948 [1], Casimir predicted an attractive force between a pair of neutral parallel conducting plates placed in empty space. For such parallel plates made of an ideal metal, the attractive force per unit area, i.e. the pressure, is given by

$$P_c(a) = -\frac{\pi^2}{240} \frac{\hbar c}{a^4}.$$

(1.1)

Here, $\hbar$ is the Planck constant, c the velocity of light and a the distance between the plates. As an example, for $a = 1\mu m$, the Casimir pressure is $P_c \approx 1.3$ mPa. According to Casimir's prediction, the force results from the modification of the electromagnetic vacuum by the presence of the plates. The attraction between neutral metallic plates was first observed experimentally in [2]; for a discussion of this and other recent experimental developments, see for example [3–5]. Today, the Casimir effect, being a purely quantum effect, is commonly understood as a direct physical manifestation of the vacuum energy and vacuum fluctuations [4, 6].

In the last fifteen years, the Casimir effect has become a field witnessing rapid experimental as well as theoretical progress. Originally closely related to the phenomenon of van der Waals attraction, the Casimir effect has developed into a broad interdisciplinary subject being relevant on all physical scales. It plays an important role in virtually all fields of modern theoretical and applied physics such as nanotechnology, condensed matter physics, quantum field theory, chemistry and molecular physics, gravitation and cosmology, see [3, 4, 6–18]. It continues to stimulate mathematical physics and string theory, and has been applied in

unification theories beyond the Standard Model, see [3, 4, 6, 19, 20] for further details and references.

Measurements of the Casimir force lead to strong constraints on long-range interactions between neutral macrobodies in addition to Newtonian gravity which many extensions to the Standard Model predict, see [21–32]. These extensions are for example approaches which exploit the Kaluza-Klein unification, where in addition to four spacetime dimension, compactified extra dimensions are believed to exist. The Casimir effect also provides a possible mechanism for compactification of these extra dimensions and may give rise to the cosmological constant [6].

Exploring the Casimir and van der Waals forces is essential for the understanding of atom-atom and atom-wall interactions [33]. Both of these closely related forces play an important role in the absorption of atoms by various microstructures as for example carbon nanotubes [34]. A promising application of carbon nanotubes is the proposed possibility of storage of great amounts of hydrogen [35]. A profound knowledge of the interaction details between graphite and hydrogen is indispensable for the solution of this problem and requires extensive theoretical as well as experimental investigation.

In condensed matter physics, the Casimir effect gives rise to forces in layered systems, has implications on properties of thin films and plays a role in surface critical phenomena. Measurements of the Casimir force use test bodies composed of real materials and bounded by rough surfaces. To compare a real experiment with theory, a number of material properties have to be taken into account. In general, the resulting corrections to an idealized situation are far from trivial. New theoretical concepts have been developed in recent years – in many respects especially because of the experimental advances. Fortunately, theory and experiment go hand in hand here and are mutually influencing each other.

The Casimir force is strongly distance-dependent and is increasingly more relevant at smaller separations. Advances in modern technology steadily allow to shrink dimensions of mechanical and electromechanical devices. Thus, the Casimir effect is becoming more important also in nanoscience and nanotechnology.

1.2 Geometry-temperature interplay

The Casimir effect features a decisive geometry dependence: the fluctuation-induced interaction between test bodies or surfaces depends on their shape and orientation. This is because the Casimir effect arises from the fluctuation spectrum in presence of the surfaces relative to the vacuum fluctuations. The spectral properties in turn are a direct consequence of the geometry.

The geometry dependence becomes even more pronounced at finite temperature T: thermal fluctuations can be predominantly associated with a characteristic length scale, the thermal wavelength $\lambda_T \sim \hbar c/(k_{\mathrm{B}}T)$. Thermal fluctuations contribute to the Casimir force, whenever the scale set by the thermal wavelength is commensurate with a mode of the fluctuation spectrum as defined by the geometry. Therefore, thermal corrections to the zero-temperature Casimir effect generally cannot be described by universal additive terms or other simple recipes but require a careful analysis of the interplay between geometry and temperature (the so called *geothermal* interplay), as first anticipated in [36].

The purpose of the present thesis is to develop the general physics picture underlying the geothermal Casimir phenomena. The origin of a nontrivial interplay between geometry and temperature in the Casimir effect can be understood in simple terms. Consider the classic parallel plate case: as the wavelengths of the fluctuations orthogonal to the plates have to be commensurate with the distance a between the plates, this corresponding relevant part of the spectrum (we use natural units from now on, meaning $\hbar = c = k_{\mathrm{B}} = 1$)

$$\omega_p{}^2(a) = p_\parallel^2 + (\pi\, m/a)^2$$

has a gap of wave number $k_{\mathrm{gap}} = \pi/a$. As is obvious, for example, from the partition function (for one mode p)

$$Z_p = \sum_{n=1}^{\infty} \exp\left(-\frac{\omega_p(a)(n+1/2)}{T}\right),$$

the gapped modes are exponentially suppressed at small temperatures $T \ll k_{\mathrm{gap}}$. In $D = 4$ spacetime dimensions, the integration over the parallel modes $p_\parallel$ and summation over m converts this exponential dependence into the low-temperature power law T^4 for the parallel-plate Casimir force. The corresponding thermal contribution to the free interaction energy (apart from a distance-independent term) is

$$\Delta E_\parallel(T) = \frac{\pi^2}{90}\, A\, a\, T^4, \quad aT \ll 1, \tag{1.2}$$

3

where A denotes the plate's area. The argument for a suppression of thermal contributions given above applies to all geometries with a gap in the relevant part of the spectrum – for example concentric cylinders or spheres, Casimir pistons and so forth. These geometries are called *closed*.

By contrast, *open* geometries with a gapless relevant part of the spectrum have no such suppression of thermal contributions. Any small value of the temperature can always excite the low-lying modes in the spectrum. Therefore, we expect a generically stronger thermal contribution $\sim (aT)^\alpha$ with $0 < \alpha < 4$.

Another argument for the fundamental difference between open and closed geometries and thermal corrections is the following: Eq. (1.2) can also be written as

$$\Delta E_\parallel(T) = V \, \epsilon_{\mathrm{SB}},$$

where $V = aA$ is the volume between the parallel plates, and ϵ_{SB} is the Stefan-Boltzmann free energy density of the radiation field. Hence, we can understand the low-temperature correction in the parallel-plate case as an excluded volume effect: the thermal modes of the radiation field at low temperatures do not fit in between the plates, and therefore the corresponding volume does not contribute to the total thermal free energy. By contrast, open geometries by construction cannot be associated with any unambiguously defined excluded volume, such that significant deviations from a T^4 behavior can be expected.

These considerations immediately point to the possibility that the thermal part of the low-temperature Casimir effect can be dominated by long-range fluctuations. This is because a temperature much lower than the inverse distance, $aT \ll 1$, sets a new length scale which can be much larger than the plate distance as well as any other length scale of the geometry (such as a sphere radius).

In closed geometries, this length scale is effectively cut off by the gap in the spectrum, implying the parametric suppression of thermal effects. In open geometries, this length scale sets a relevant scale that can, for instance, reflect the spatial extent of the distribution of the thermal energy density. The total thermal energy thus can receive dominant contributions from long-range modes corresponding to significantly extended thermal energy distributions.

The considerations have so far concentrated on the low-temperature limit. In fact, the high-temperature limit exhibits a universal linear dependence on the temperature for the following reason: At high temperature in the imaginary-time formalism, only the zeroth Matsubara mode can contribute as all higher modes acquire thermal masses $\sim \pi T$ and hence are largely suppressed. The zeroth Matsubara mode has no temperature dependence at all, such that the only temperature dependence arises from the measure of the fluctuation trace, which

is linear in T. A less technical argument with the same result can be based on the underlying Bose-Einstein distribution governing the bosonic thermal fluctuations of the radiation field. This distribution increases as $\sim T$ in the high-temperature limit, inducing this linear temperature dependence directly in the free energy. The properties of the geometry only enter the prefactor in the high-temperature limit.

1.3 Field theoretical approach

The investigation of geothermal phenomena demands methods which can tackle arbitrary geometries. The calculation of Casimir energies for more involved geometries is a complicated task. It should be clear that for more complex configurations, the Casimir energy can only be evaluated numerically. However, the general expressions for the Casimir energy contain infinite sums and integrals, from which ultraviolet divergences have to be separated first before a numerical evaluation even becomes possible. Finding and separating these divergences is a delicate business, such that in almost all cases a direct numerical treatment is next to impossible.

A powerful numerical method which does not contain any divergences at intermediate steps is *worldline numerics* [37–40]. Worldline numerics originates in the string-inspired approach to quantum field theory [41–44] and is based on a mapping of field-theoretic fluctuation averages onto quantum-mechanical path integrals [45–50]. It is independent of the Casimir geometry and can easily deal with finite temperature. The problem of determining the fluctuation spectrum with the followed summation is elegantly circumvented and substituted by one single step. In this thesis, we choose worldline numerics for the investigation of geothermal phenomena. Surprisingly, it turns out that wordline numercis can also be used to find novel analytical results.

In addition to the worldline methods [37–40, 51–61] used in this work, a variety of approaches has been developed in recent years, such as a functional integral approach [62–64] and scattering theory [65–82]. An extension of these methods to finite temperature is usually straightforward and highly worthwhile in view of the geometry-temperature interplay.

As we pointed out in the previous section, geothermal phenomena can be dominated by long-range fluctuations in open geometries. An important consequence can already be anticipated at this point: approximation methods that are based on local considerations will generically fail to predict the correct low-temperature correction in open geometries. An example is given by the proximity force ap-

proximation (PFA) which is based on the assumption that the Casimir energy can be estimated by integrating over local parallel-plates energy densities [83, 84]. Whereas this approximation may or may not work at zero temperature depending on the geometric details of the configuration, it is even conceptually questionable at finite temperature, as open geometries should not be approximated by closed-geometry building blocks. Quantitatively, such a procedure is expected to fail, as local energy-density approximations will not be able to capture the contributions from larger length scales induced by long-range modes.

The temperature-geometry interplay is not an academic problem: experimentally important configurations such as the sphere-plate or the cylinder-plate geometry belong to this class of open geometries, but thermal corrections have so far been approximated by the PFA. Whether or not a potentially significant geothermal interplay may exist in the relevant parameter range $aT \sim 0.01 \ldots 0.1$ is a technically challenging problem, which will be addressed in this thesis.

1.4 Organization of the thesis

The present thesis is organized as follows: In chapter 2, we review the classic Casimir configuration of two ideal parallel plates and relate the Casimir effect to van der Waals forces.

Chapter 3 presents the worldline approach to the Casimir effect.

Chapter 4 is devoted to a study of the zero-temperature Casimir effect for the inclined plates configuration. We extend the analysis of inclined plates to finite temperatures in chapter 5.

The sphere-plate and cylinder-plate configurations at zero temperature are studied in chapter 6. We develop an approach to direct force computation, rather than calculating the interaction energy. This leads to enormous simplifications in the numerics and enables us to extend the parameter range studied so far.

We show the great advantage of the algorithm for the direct force calculation in chapter 7. Here, the sphere-plate and cylinder-plate configurations are studied at finite temperature.

In chapter 8, we deduce the PFA from the worldline path integral. This helps to understand the differences between the exact and approximate treatments. For comparison, we also work out the PFA estimates for the sphere-plate and cylinder-plate configurations in great detail.

For the sake of completeness, we present and prove the Poisson summation in appendix A.

The conclusions of the thesis are provided in chapter 9.

2 Essentials of the Casimir effect

2.1 Connection with the van der Waals-London forces

Let us consider the classical Casimir configuration consisting of two parallel, uncharged and perfectly conducting plates at a distance a. Nowadays, it is common to emphasize the spectacularity and the mystery of the fact that the two neutral plates do indeed exhibit a force in the vacuum. Intuitively, it should be no surprise that an attractive force between the plates arises. Long range forces, other than gravity but acting between neutral atoms, are well-known. These are the dispersion forces, also called van der Waals-London forces [85, 86]. Van der Waals forces play an important role in biology and are particularly significant for surface phenomena.

The origin of the dispersion force can be understood in simple terms. For a non polar atom, the expectation value of the dipole moment in the ground state is zero. Due to its quantum mechanical nature, however, the mean value of the dipole moment squared is different from zero, such that the interaction between fluctuating dipoles gives rise to a weak attractive force.

The quantum theory of the van der Waals interaction was presented by London in 1930 [86]. The London theory was entirely quantum mechanical (since it contained $\hbar$) but it was not relativistic (since c was absent). London considered only dipole moments induced instantaneously and the theory was therefore valid for relatively small separations. The force between two neutral atom at the distance a was found to be $\sim 1/a^7$.

The relativistic theory of the van der Waals attraction was considered for the first time by Casimir and Polder in 1948 [33]. They considered retarded interactions and were able to show that the van der Waals force between two atoms changed from $\sim 1/a^7$ to $\sim 1/a^8$ as the separation a increased.

Of course, the generators of the van der Waals attraction, the fluctuating dipoles, generate fluctuating electromagnetic fields, and they themselves induce fluctuating moments. In principle, the dispersion force can then be attributed to

the fluctuating electro-magnetic field alone, without a reference to the atoms as the generators of fields.

In 1948 Casimir calculated an attractive force between two idealized parallel plates by considering only the fluctuating fields in the vacuum. He used a novel technique and derived the attraction between the plates from the zero point energy of the fluctuating electromagnetic field. This, indeed, was an equivalent description of the same physical effect.

One should not forget that the force was derived for an ideal metal, thus leading to an universal result. Dealing with realistic materials, the Casimir force should transform to the van der Waals-London force at short separations, and above all, the force will disappear if the plates were made transparent for the fluctuating field.

2.2 The mystery of the Casimir effect

Note that the apparently trivial shift of emphasis from fluctuating dipoles to fluctuating fields not only facilitates the calculation of forces by allowing the use of quantum field theoretic techniques, it also leads to new theoretical predictions which by no means can be related to van der Waals forces. This is the mystery of the Casimir effect [20]. The prominent example is the Casimir effect for a single spherical shell. The interest in this boundary is enormous for a number of reasons.

One application was given by Casimir himself. In 1953, he proposed a model for the electron. The charge of the electron was assumed to be uniformly distributed over a conductive spherical shell. Since the Casimir force between two parallel plates was attractive, Casimir hoped that the resulting electrostatic self-repulsion of the charge could be balanced by the Casimir force arising from the conductive shell. Unfortunately, the Casimir force for a conducting shell turned out to be repulsive. This was shown first by Boyer 1968 [87]. The result has since been independently confirmed [88–91].

The Casimir effect for spherical shells also appears in Kaluza-Klein theories in $4 + N$ dimensions, where the extra dimensions are compactified into a sphere. For a fluctuating scalar field and a single sphere S^N, the Casimir energy is divergent for even N, negative for $N = 1$ and positive for odd N up to $N = 19$. For $N \geq 21$ the energy becomes increasingly negative [6, 92].

In particle physics, the Casimir effect for a sphere is used in the phenomenological bag model of hadrons [6, 93–99]. In this model, a hadron is modeled as quarks confined to the interior of a spherical cavity. The interior of the cavity is assumed

to be a chromomagnetic vacuum, while the exterior is a perfect chromomagnetic conductor. Given Boyer's repulsive result for the spherical shell, this model seems to be physically unsatisfactory, however, the repulsive result in this situation is less clear since there are no exterior modes.

Another reason for the interest in repulsive spherical geometries is the hope of finding a repulsive Casimir force between real bodies. If found, it would provide a mechanism to reduce stiction in nanomechanical systems [4].

In the course of time the Casimir effect also developed from being an alternative explanation for the retarded van der Waals force to being evidence of the reality of the quantum fluctuations and the quantum vacuum [4, 6, 100–104]. The question of whether zero point fluctuations are real, or of whether the Casimir effect can be used as evidence for their reality, is beyond the scope of this thesis, see for example [100, 105–107]. We will, however, make use of the modern definition of the Casimir effect as the dependence of the vacuum energy of a field on the boundary [6].

In our case, the boundaries are represented by rigid bodies. The boundaries restrict the modes of the fluctuating field and give rise to a measurable force between the bodies. This force then depends on the nature of the field, on the geometry of the boundary and on the dimension of spacetime.

2.3 Basic recipe for the Casimir calculations

The roots of the Casimir effect trace back to the most fundamental principles of quantum mechanics. According to quantum mechanics, a harmonic oscillator has discrete energy levels

$$E_n = \hbar\omega \left(n + \frac{1}{2} \right), \tag{2.1}$$

where $n = 0, 1, 2, \ldots$ and ω is the angular frequency of the oscillator. The ground (vacuum) state energy of the oscillator is

$$E_0 = \frac{1}{2}\hbar\omega, \tag{2.2}$$

which, escpecially, is not equal to zero.

In the quantum field theory, any quantized field is considered as a set of oscillators of all frequencies. Then, using Eq. (2.2), the vacuum energy of a field is given by

$$E = \frac{\hbar}{2} \sum_J \omega_J, \tag{2.3}$$

which is the sum over all ground state energies, or zero point oscillations. The index J in Eq. (2.3) labels the quantum numbers of the field modes. For instance, for the electromagnetic field in free space, the index J contains a continuous component **k** (the wave vector) and a two-valued discrete component which characterizes the polarization state.

Introducing rigid bodies into the free space, we impose boundary conditions on the field, thus restricting the possible field modes ω. For two parallel plates, for example, one component of the wave vector **k** becomes discrete. The basic procedure to calculating the Casimir energy E for two ideal parallel plates is similar for many different approaches. The recipe can be formulated in two steps:

1. find the mode spectrum of the fluctuating field;

2. sum up the mode spectrum to obtain the Casimir energy.

Obviously, the two steps can be performed for a few highly symmetric configurations only. The parallel plates configuration is one of them. In general, however, the mode spectrum cannot be found analytically, and if found, the summation itself would be far from obvious. One therefore has to retreat to approximate and numerical methods.

In the next section, we perform the calculation for Casimir's parallel plates. The final result turns out to be of key importance for worldline numerics, as will become clear in Sect. 4.4. At the end of this chapter, we then present the proximity force approximation (PFA), which, using the analytic result for two parallel plates, approximates a given geometry by infinitesimal parallel plates.

2.4 Casimir's parallel plates

Let us consider two idealized perfectly conducting parallel plates in $D = d + 1$ dimensions. The surface area of the plates is then $d - 1$ dimensional. The separation between the plates is a. For simplicity, let us take a massless scalar field to be the fluctuating field. We assume that the field satisfies Dirichlet boundary conditions on the plates, and therefore vanishes there. We set $\hbar = c = 1$ and label the modes of the field by the integer $n > 0$ and the transverse momentum k. The Casimir energy per unit transverse area is obtained by summing over the zero-point energies of all modes,

$$\frac{E(a)}{A} = \frac{1}{2} \sum\!\!\!\!\!\!\int \omega = \frac{1}{2} \sum_{n=1}^{\infty} \int \frac{\mathrm{d}^{D-2}k}{(2\pi)^{D-2}} \sqrt{k^2 + \frac{n^2\pi^2}{a^2}}. \qquad (2.4)$$

The integral is terribly divergent for large k. Introducing a cutoff Λ and using

$$\mathrm{d}^D k = \frac{2\pi^{D/2}}{\Gamma(D/2)}\, k^{D-1}\mathrm{d}k, \tag{2.5}$$

we can express the integral in terms of hypergeometric functions.

A finite Casimir energy can then be obtained by expanding the result around $\Lambda = \infty$ and taking the Λ independent contribution only. This contribution can then be summed up to produce the correct result.

In order to get rid of the Λ divergent terms, we subtract from Eq. (2.4) the free value $E(a \to \infty)$. Let us take an arbitrary $b > a$, and subtract $E(b)$ from $E(a)$. The value of b will be sent to infinity at the end. Using Eq. (2.4) and (2.5), this gives

$$\frac{E(a) - E(b)}{A} = \sum_{n=1}^{\infty} \int_0^{\infty} \frac{\mathrm{d}k\, k^{D-3}\, 2^{2-D}\, \pi^{1-D/2}}{\Gamma(-1 + D/2)} \left(\sqrt{k^2 + \frac{n^2\pi^2}{a^2}} - \sqrt{k^2 + \frac{n^2\pi^2}{b^2}} \right) \tag{2.6}$$

$$= \frac{\pi^{(D-1)/2}\Gamma\left(\frac{D-1}{2}\right)\zeta(1-D)}{2^D} \left(\frac{1}{b^{D-1}} - \frac{1}{a^{D-1}} \right). \tag{2.7}$$

Actually, the integral in Eq. (2.6) converges for $2 < D < 3$ only, but we use analytical continuation in D and treat Eq. (2.7) as a formal answer for all D.

For $D > 1$, we can safely perform the $b \to \infty$ limit. Using the reflection property of the ζ function,

$$\zeta(1 - D)\,\Gamma\left(\frac{1-D}{2}\right)\pi^{(D-1)/2} = \zeta(D)\,\Gamma\left(\frac{D}{2}\right)\pi^{-D/2}, \tag{2.8}$$

we finally get

$$\frac{E(a) - E(b \to \infty)}{A} = -\frac{\Gamma(D/2)\,\zeta(D)}{(4\pi)^{D/2}a^{D-1}}, \tag{2.9}$$

in agreement with [108, 109]. The force per unit area, F/A, is obtained by taking the negative derivative with respect to a. Especially for $D = 4$, the force per unit area becomes

$$\frac{F(a)}{A} = -\frac{\pi^2}{480\, a^4}. \tag{2.10}$$

This result represents the Casimir force for a fluctuating scalar field. The corresponding result due to an electromagnetic field is obtained by multiplying the

scalar case result by a factor of 2, which accounts for the two polarization states of the photon.

It is tempting to try to approximate an arbitrary Casimir configuration by small parallel plates. Then, using Eq. (2.8) and (wrongly) assuming additivity of the Casimir force, one would have a simple approximate method. This widely used technique, the proximity force approximation (PFA), is subject of the next section.

2.5 The proximity force approximation

The standard and the most simple approximation method for estimating Casimir energies between separated rigid bodies is the proximity force approximation (PFA) [83, 84]. The PFA is still widely used for comparison of experiment and theory, since the resulting estimates can easily be generalized to the case of bodies made of real materials. In this thesis, we will compare our most important results with the PFA estimates as well.

The PFA treats the Casimir configuration as a superposition of infinitesimal parallel plates and then integrates them up

$$E^{\mathrm{PFA}}(a) = \int_{\Sigma} \varepsilon^{\mathrm{PP}}(h) \, \mathrm{d}\sigma. \tag{2.11}$$

Here, one integrates over an auxiliary surface Σ, which should be chosen appropriately. We have introduced $\varepsilon^{\mathrm{PP}}(h)$ which denotes the energy per unit area of two parallel plates at a distance h apart, see Eq. (2.9). At zero temperature and for $D = 4$, this quantity reads

$$\varepsilon^{\mathrm{PP}}(h) = -\frac{c_{\mathrm{PP}}}{h^3}, \tag{2.12}$$

where $c_{\mathrm{PP}} = \pi^2/1440$ for the Dirichlet scalar case. Of course, by definition, $E^{\mathrm{PFA}}(a)$ is ambiguous since there is no prescription on how to choose the auxiliary surface Σ. There is also no reference to boundary conditions, therefore, all PFA formulae are analogously valid for the electromagnetic case as well, with the restriction that all force or energy formulae must be multiplied by a factor of two accounting for two polarization modes.

The distance is conventionally measured along the normal to Σ. The two extreme cases in which Σ coincides with one of the two bodies provide us with a region spanning the inherently ambiguous estimates of the PFA.

Strictly speaking, the PFA contradicts the Heisenberg's uncertainty principle [52]. The quantum fluctuations, acting via the parallel plates prescription,

are supposed to probe the configuration pointwise, thereby neglecting the whole neighborhood. However, the fluctuations should not be localizable.

As we will see in the next chapter, the worldline approach respects this quantum mechanism: the sum over modes of a field is represented by a sum over non local space-time trajectories (worldlines) of quantum fluctuations, which directly sample the geometric properties of the surfaces. The PFA then turns out to be the one-dimensional version of worldline numerics, where instead of complicated multi-dimensional worldlines one uses simple straight lines.

3 Casimir effect in the worldline formalism

This chapter provides an introduction into the worldline approach to the Casimir effect. For simplicity and clarity, we study the Casimir effect induced by a fluctuating real scalar field obeying Dirichlet boundary conditions ("Dirichlet scalar"). We start with the field theoretic framework and show how the problem of computing the Casimir energy can efficiently be treated numerically.

These concepts have been originally presented by Gies *et al.* (2003) in [37] and are based on the "string-inspired" worldline formalism, in which field-theoretic fluctuation averages are mapped onto quantum-mechanical path integrals [41–48]. For arbitrary backgrounds, this worldline integral representing the spacetime trajectories of the quantum fluctuations can straightforwardly be computed by Monte Carlo methods [39]. As the computational algorithm is generally independent of the background, i.e., the Casimir geometry, Casimir problems for arbitrary configurations can straightforwardly be tackled with this method.

In contrast to the worldline approach, standard strategies perform the Casimir calculations in two separate steps, namely by identifying the mode spectrum of the quantum fluctuations in a given geometry and then by summing it up. In the worldline approach, these two steps are combined and are performed not separately but simultaneously. This is particularly advantageous, since both steps, being highly non trivial and increasingly difficult for more involved Casimir configurations, combined become geometry independent and quite easy to perform in the worldline approach.

The worldline approach can also be straightforwardly extended to non zero temperature by the Matsubara formalism. As it will become clear in this chapter, the geometry-dependent part of the calculation remains the same for zero and finite temperature. Thus, the modifications to the technical realization of the numerical algorithms are rather minor compared with other methods.

In the worldline picture, quantum fluctuations are represented by closed trajectories of virtual particles allowing for an intuitive approach to the Casimir effect and quantum phenomena in general. Computing the Casimir force between two

rigid bodies for a Dirichlet scalar, we will see that only trajectories intersecting both bodies contribute to the Casimir force. With this in mind, many geometry specific features of the Casimir force, such as the dependence on the separation and the sign of the interaction, the role of curvature and of the edges, and especially the geometry-temperature interplay can be understood in the worldline picture.

The worldline approach has proven to be very successful yielding many surprising predictions for various Casimir geometries [37, 51–60].

3.1 Field theoretic framework

Let us consider a real scalar quantum field ϕ. The field ϕ is coupled to a background potential $V(x)$. The Casimir effect is then defined as the dependence of the vacuum energy of the field ϕ on the potential $V(x)$. In this work we focus on the Casimir forces between *disconnected* rigid bodies $\Sigma_1, \Sigma_2, \ldots$ which can be represented by the background potential V. The functional form of V in general allows modeling many physical properties of real materials and types of boundary conditions. For instance, the Dirichlet boundary conditions imply that all modes of the field ϕ are suppressed on V and thus can be modeled by idealized delta potentials in space as a special case, see Fig. 3.1 for an illustrative example. For now, let us take V as general as possible and postpone the discussion of its specific form.

Coupling the fluctuating field ϕ to the background potential according to $\sim V(x) \phi^2$, we can write the field theoretic Lagrangian as

$$\mathcal{L} = \frac{1}{2} \phi \left(-\partial^2 + m^2 + V(x) \right) \phi. \tag{3.1}$$

This implies that the potential $V(x)$ has mass dimension 2 and can therefore be considered to form a spacetime dependent contribution to mass squared. As we work in $D = d + 1$ dimensional Euclidean spacetime, we use

$$\partial^2 = \partial_{x_1}^2 + \cdots + \partial_{x_d}^2 + \partial_{x_D}^2. \tag{3.2}$$

Not considering further fields or couplings, the classical action becomes

$$S = \int \mathrm{d}^D x \, \mathcal{L}. \tag{3.3}$$

The complete unrenormalized quantum effective action Γ is then given by the relation

$$\exp(-\Gamma) = \int \mathcal{D}\phi \, \exp(-S). \tag{3.4}$$
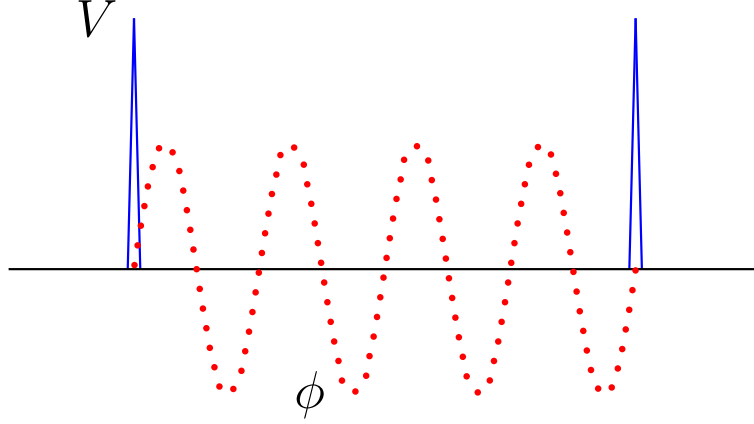
Figure 3.1: A schematic illustration of the Dirichlet boundary conditions in $d = 1$. The delta potentials V, shown as narrow peaks, live on the boundaries and cause the fluctuating quantum field ϕ (dotted line) to vanish there. In between the field propagates freely.

The path integral in Eq. (3.4) states that to obtain the effective action Γ, we have to sum over all field configurations, where the statistical weight of a given configuration is $\exp(-S)$. The (unimportant) normalization constant in front of the path integral has been omitted for clarity.[1]

For time-independent Casimir configurations, the Casimir energy $\mathcal{E}$ is related to the effective action via

$$\mathcal{E} = \frac{\Gamma}{\int \mathrm{d}x_D}, \tag{3.5}$$

so that our main aim in this section is to compute Γ.

Since the path integral in Eq. (3.4) is Gaußian, we obtain for Γ

$$\Gamma[V] = -\ln\left(\int \mathcal{D}\phi \, \exp(-S)\right) = -\ln\left(\det\left(\frac{-\partial^2 + m^2 + V(x)}{2\pi}\right)^{-\frac{1}{2}}\right), \tag{3.6}$$

where we used the familiar formula for Gaußian integrals. Using the relation

$$\ln\det = \mathrm{Tr}\ln \tag{3.7}$$

and normalizing Γ to satisfy

$$\Gamma[V = 0] = 0, \tag{3.8}$$

---

[1]Both Γ and S have of course the same dimension of an action, (energy $\times$ time), such that the exponents in (3.4) shall be divided by Planck's constant $\hbar$, which we, however, have set to 1. Also Eq. (3.2) is in agreement with the dimensional analysis as $c = 1$ has been used.

gives the complete unrenormalized quantum effective action:

$$\Gamma[V] = \frac{1}{2} \text{Tr} \ln \left[\frac{-\partial^2 + m^2 + V(x)}{-\partial^2 + m^2} \right]. \tag{3.9}$$

Next, we want to rewrite Eq. (3.9) using the propertime representation of the logarithm. To derive this representation, we observe that for a positive number A we have

$$\frac{\mathrm{d}}{\mathrm{d}A} \ln(A) = \frac{1}{A}, \tag{3.10}$$

and also

$$-\frac{\mathrm{d}}{\mathrm{d}A} \int_0^\infty \mathrm{d}\mathcal{T} \, \frac{\exp(-A\mathcal{T})}{\mathcal{T}} = \int_0^\infty \mathrm{d}\mathcal{T} \, \exp(-A\mathcal{T}) = \frac{1}{A}, \tag{3.11}$$

where we have interchanged differentiation and integration. Thus, formally, for positive A and B we can write

$$\ln \left(\frac{A}{B} \right) = -\int_0^\infty \frac{\mathrm{d}\mathcal{T}}{\mathcal{T}} \left(\exp(-A\mathcal{T}) - \exp(-B\mathcal{T}) \right). \tag{3.12}$$

Eq. (3.12) is a special case of a Frullani's integral, see [110].

We can generalize Eq. (3.12) to positive definite operators A, B. The parameter $\mathcal{T}$ is then usually called *Fock-Schwinger propertime*.

Let us return to Eq. (3.9). Performing the trace in x space,

$$\text{Tr}[\ldots] = \int \mathrm{d}^D x \, \langle x | \ldots | x \rangle, \tag{3.13}$$

and using Eq. (3.12), we get

$$\Gamma[V] = -\frac{1}{2} \int_{1/\Lambda^2}^\infty \frac{\mathrm{d}\mathcal{T}}{\mathcal{T}} \int \mathrm{d}^D x \left[\langle x | e^{-\mathcal{T}(-\partial^2 + m^2 + V(x))} | x \rangle - \langle x | e^{-\mathcal{T}(-\partial^2 + m^2)} | x \rangle \right]$$

$$= -\frac{1}{2} \int_{1/\Lambda^2}^\infty \frac{\mathrm{d}\mathcal{T}}{\mathcal{T}} \int \mathrm{d}^D x \left[\langle x | e^{-\mathcal{T}(-\partial^2 + m^2 + V(x))} | x \rangle - \frac{e^{-m^2 \mathcal{T}}}{(4\pi \mathcal{T})^{D/2}} \right]. \tag{3.14}$$

Here we have taken into account the UV cutoff Λ at the lower bound of the $\mathcal{T}$ integral for the sake of definiteness only. It will not be present in the end formula for the Casimir interaction energy.

Now, let us compare the matrix element $\langle x | \ldots | x \rangle$ with the quantum mechanical transition amplitude in propertime $\mathcal{T}$, which can be written in terms of path integrals.

For a particle of mass $\widetilde{m}$ in a time-independent potential $\widetilde{V}$, this transition amplitude reads [44, 111, 112]

$$\langle x'|\exp(-itH)|x\rangle = \mathcal{N} \int_{x(0)=x}^{x(t)=x'} \mathcal{D}x \exp\left(i\int_0^t \mathrm{d}\tilde{t}\, L\right),$$ (3.15)

where

$$H = \frac{p^2}{2\widetilde{m}} + \widetilde{V}(x)$$ (3.16)

and

$$L = \frac{\widetilde{m}\,\dot{x}^2}{2} - \widetilde{V}(x).$$ (3.17)

Using in (3.15)

$$\widetilde{V}(x) = m^2 + V(x), \quad \widetilde{m} = \frac{1}{2}, \quad it = \mathcal{T},$$ (3.18)

we conclude that the matrix element $\langle x|\dots|x\rangle$ in Eq. (3.14) can be written as

$$\langle x|e^{-\mathcal{T}(-\partial^2 + m^2 + V)}|x\rangle = \mathcal{N} \int_{x(0)=x}^{x(\mathcal{T}/i)=x} \mathcal{D}x \exp\left(i\int_0^{\mathcal{T}/i} \mathrm{d}\tilde{t}\left[\frac{1}{4}\dot{x}^2 - m^2 - V(x(\tilde{t}))\right]\right)$$

$$= \mathcal{N} \int_{x(0)=x}^{x(\mathcal{T})=x} \mathcal{D}x \exp\left(-\int_0^{\mathcal{T}} \mathrm{d}\tau\left[\frac{1}{4}\dot{x}^2 + m^2 + V(x(\tau))\right]\right).$$ (3.19)

This is a path integral over all *closed* paths, or *worldlines*, starting and ending at $x(0) = x(\mathcal{T}) = x$ fixed. In Eq. (3.14), the trace operation induces an integration over all possible x representing an integration over all starting (and end) points of worldlines. Thereby, everywhere in spacetime closed worldlines are generated.

For practical purposes, it is useful to shift x,

$$x \rightarrow x_{\mathrm{CM}} + x,$$ (3.20)

and not to integrate over the initial points x but over the centers of mass x_{CM}. This shift implies

$$\int_0^{\mathcal{T}} \mathrm{d}\tau\, x_\mu(\tau) = 0.$$ (3.21)

The normalization constant $\mathcal{N}$ in Eq. (3.19) can be found by taking the limit $V \to 0$ since for zero potential the matrix element can be evaluated analytically:

$$\langle x| e^{\mathcal{T}\partial^2} |x\rangle = \frac{1}{(4\pi\mathcal{T})^{D/2}} = \mathcal{N} \int_{x(0)=x(\mathcal{T})} \mathcal{D}x \ \exp\left(-\int_0^{\mathcal{T}} \mathrm{d}\tau \frac{1}{4}\dot{x}^2 \right). \qquad (3.22)$$

This form of $\mathcal{N}$ allows us to interpret the path integral in simple terms, namely as an expectation value of $\exp(-\int_0^{\mathcal{T}} \mathrm{d}\tau(m^2 + V))$ with respect to an ensemble of worldlines with Gaußian velocity distribution,

$$\mathcal{N} \int_{x(0)=x(\mathcal{T})} \mathcal{D}x \ \exp\left(-\int_0^{\mathcal{T}} \mathrm{d}\tau \left[\frac{1}{4}\dot{x}^2 + m^2 + V(x_{\mathrm{CM}} + x(\tau)) \right] \right)$$

$$= \frac{\exp\left(-m^2\mathcal{T}\right)}{(4\pi\mathcal{T})^{D/2}} \left\langle \exp\left(-\int_0^{\mathcal{T}} \mathrm{d}\tau \, V(x_{\mathrm{CM}} + x(\tau)) \right) \right\rangle_x. \qquad (3.23)$$

The quantum effective action (3.14) then eventually reads

$$\Gamma[V] = -\frac{1}{2(4\pi)^{D/2}} \int_{1/\Lambda^2}^{\infty} \frac{\mathrm{d}\mathcal{T}}{\mathcal{T}^{1+D/2}} \exp\left(-m^2\mathcal{T}\right)$$

$$\times \int \mathrm{d}^D x_{\mathrm{CM}} \left\langle \exp\left(-\int_0^{\mathcal{T}} \mathrm{d}\tau \, V(x_{\mathrm{CM}} + x(\tau)) \right) - 1 \right\rangle_x, \qquad (3.24)$$

where the expectation value is given by

$$\left\langle \exp\left(-\int_0^{\mathcal{T}} \mathrm{d}\tau \, V(x_{\mathrm{CM}} + x(\tau)) \right) \right\rangle_x$$

$$= \frac{\int_{x(0)=x(\mathcal{T})} \mathcal{D}x \ \exp\left(-\int_0^{\mathcal{T}} \mathrm{d}\tau \left[\frac{1}{4}\dot{x}^2 + V(x_{\mathrm{CM}} + x(\tau)) \right] \right)}{\int_{x(0)=x(\mathcal{T})} \mathcal{D}x \ \exp\left(-\int_0^{\mathcal{T}} \mathrm{d}\tau \frac{1}{4}\dot{x}^2 \right)}. \qquad (3.25)$$

3.2 The Casimir interaction energy

As we have stated above, in this work we are merely interested in calculating Casimir forces between disconnected rigid bodies $\Sigma_1, \Sigma_2, \ldots$ Furthermore, we want to consider only static configurations. A configuration Σ consisting of such static disconnected bodies may be written in the form

$$\Sigma = \Sigma_1 + \Sigma_2 + \ldots \qquad (3.26)$$

and can be represented by a time-independent background potential $V_\Sigma(\mathbf{x})$ as

$$V_\Sigma(\mathbf{x}) = V_{\Sigma_1}(\mathbf{x}) + V_{\Sigma_2}(\mathbf{x}) + \ldots \qquad (3.27)$$

The potentials $V_{\Sigma_i}(\mathbf{x})$ for the single bodies shall not overlap, meaning that at each point $\mathbf{x}$ we have

$$V_{\Sigma_i}(\mathbf{x})\, V_{\Sigma_j}(\mathbf{x}) = 0, \quad \text{for} \quad i \neq j. \tag{3.28}$$

The Casimir energy is then obtained from the effective action by dividing the latter by the time integration, see Eq. (3.5).[2] This Casimir energy may be infinite due to self energies of the single bodies. However, these self energies do not contribute to the Casimir *force* between the bodies, such that it suffices to study the *interaction* Casimir energy E_c, defined by subtracting the self energies $\mathcal{E}_{\Sigma_i}$ of the single bodies from the total Casimir energy $\mathcal{E}_\Sigma$:

$$E_\mathrm{c} = \frac{\Gamma[V_\Sigma] - \Gamma[V_{\Sigma_1}] - \Gamma[V_{\Sigma_1}] - \dots}{\int \mathrm{d}x_{\mathrm{CM},D}}$$

$$= \mathcal{E}_\Sigma - \mathcal{E}_{\Sigma_1} - \mathcal{E}_{\Sigma_2} - \dots \tag{3.29}$$

The Casimir interaction energy E_c then only depends on the relative positions of the objects. The Casimir forces F_c or torques D_c are obtained by differentiating the (negative) interaction energy with respect to parameters characterizing the separation or orientation of the bodies. These are, e.g., distances a or angles φ. As the subtractions drop out by taking the derivative, the Casimir force and torque can also be obtained from the total interaction energy

$$F_\mathrm{c} = -\frac{\mathrm{d}}{\mathrm{d}a} E_\mathrm{c} = -\frac{\mathrm{d}}{\mathrm{d}a} \mathcal{E}_\Sigma, \quad D_\mathrm{c} = -\frac{\mathrm{d}}{\mathrm{d}\varphi} E_\mathrm{c} = -\frac{\mathrm{d}}{\mathrm{d}\varphi} \mathcal{E}_\Sigma. \tag{3.30}$$

Subtracting the self energies also removes the field theoretic UV divergences in Eq. (3.24) since any divergence induced locally by the potentials is canceled. We can therefore take the limit $\Lambda \to \infty$. Also from the numerical point of view, the interaction energy E_c is favorable as it allows us to deal with comparably "small" numbers.

The definition of the interaction energy in Eq. (3.29) shall not be confused with renormalization. The interaction energy can be well defined even if the self energies might be ill-defined in the ideal boundary-condition limit, where the examples are the perfect conductivity or infinitely thin surfaces [114–118].

---

[2]This can be seen by remembering how the vacuum-persistence amplitude $\langle 0 | \exp(-iHT) | 0 \rangle = \exp(-iE_0 T)$ is related to the path integral $\int \mathcal{D}\phi\, e^{-S}$. In absence of external sources, one finds [113] the relation $\lim_{t\to\infty} \langle 0 | \exp(-iHt) | 0 \rangle_{|_{t\to -it}} = \lim_{t\to\infty} \exp(-E_0 t) = \int \mathcal{D}\phi\, e^{-S} = \exp(-\Gamma)$, and thereby $E_0 = \Gamma/(\int (\text{time}))$. Here, H denotes the quantum mechanical Hamiltonian and E_0 the ground-state energy.

Eq. (3.29) is a procedure to find the exact Casimir force between rigid bodies. The question as to whether the local Casimir energy densities are well defined is circumvented and remains unanswered. Therefore the computation of Casimir stresses of single bodies, as e.g. a sphere, can not be tackled by the concept of interaction energy and the renormalization procedure has to be carefully performed, see [13, 87, 119–125].

Let us return to the form of the background potential V_Σ in Eq. (3.27) and confine ourselves to an idealized situation where the boundary conditions are realized on infinitely thin surfaces. A simple way to model the Casimir configuration Σ would then be to choose the following background potential

$$V_\Sigma(\mathbf{x}) = \lambda \int_\Sigma \mathrm{d}\sigma \, \delta^{(d)}(\mathbf{x} - \mathbf{x}_\sigma). \qquad (3.31)$$

Here, the Casimir configuration Σ is taken to be a $d-1$ dimensional surface, $\mathrm{d}\sigma$ denotes the integration measure, and is assumed to be re-parametrization invariant, and $\mathbf{x}_\sigma$ shall point onto the surface. The positive coupling constant λ has mass dimension 1.

Eq. (3.31) merely says that if $\mathbf{x}$ is on Σ, the value of the potential is λ. For all other $\mathbf{x}$ the potential is zero. Sending λ to infinity, $\lambda \to \infty$, causes all modes of the field ϕ to vanish on Σ. In this limit the potential implies Dirichlet boundary conditions on Σ [126, 127]. The coupling constant can therefore be considered as a kind of plasma frequency of the boundary material: if λ is infinite, all fluctuation frequencies are perfectly reflected. For finite λ on the other hand, the Casimir boundaries become transparent for frequencies $w \gg \lambda$ [37].

At first sight, the realization of Neumann boundary conditions shall be similar. One would follow the approach for the Dirichlet case and to impose the Neumann boundary conditions, one would include terms which are proportional to the normal derivative of the δ function. However, due to these highly singular objects, the numerical realization becomes very expensive, and also non local terms have to be taken into account. No simple form for the Casimir energy (similar to the one which will be given in Eq. (3.34)), suitable for the fast numerical evaluation, has been found so far to our best knowledge. We will not pursue Neumann boundary conditions in this work, for further details, see [128, 129].

3.3 The worldline functional

Let us now insert the potential (3.31) into Eq. (3.24) and evaluate the τ integral. Using the familiar rule for the integral with a δ function, we find

$$I_\Sigma[\mathbf{x}(\tau)] \equiv \int_0^{\mathcal{T}} d\tau\, V(\mathbf{x}(\tau)) = \lambda \sum_{\{\tau_\sigma;\; \mathbf{x}(\tau_\sigma) \in \Sigma\}} \frac{1}{|\dot{\mathbf{x}}_\perp(\tau_\sigma)|}, \qquad (3.32)$$

where $\dot{\mathbf{x}}_\perp(\tau_\sigma)$ denotes the component of the τ derivative perpendicular to the surface at an intersection point and we sum over all intersection points $\mathbf{x}(\tau_\sigma)$ of the worldline with the surface. If a worldline does not pierce the surface, then $I_\Sigma[\mathbf{x}(\tau)]$ is zero. There are also worldlines which merely touch Σ. In this case, the inverse velocity $1/|\dot{\mathbf{x}}_\perp(\tau_\sigma)|$ diverges on the surface. The value of I_Σ then also diverges, but since it occurs in the argument of an exponential function, the latter becomes zero. These worldlines, however, form a null set and can be neglected anyway.

Let the Casimir configuration Σ now consist of two disconnected bodies, $\Sigma = \Sigma_1 + \Sigma_2$. Then the potential is $V_\Sigma = V_{\Sigma_1} + V_{\Sigma_2}$ and the argument of the expectation value $\langle \ldots \rangle_x$ in Eq. (3.24) for the interaction energy (3.29) becomes

$$\left(e^{-I_{\Sigma_1+\Sigma_2}[\mathbf{x}(\tau)]} - 1\right) - \left(e^{-I_{\Sigma_1}[\mathbf{x}(\tau)]} - 1\right) - \left(e^{-I_{\Sigma_2}[\mathbf{x}(\tau)]} - 1\right) \in [0,1]. \qquad (3.33)$$

Eq. (3.33) is only non zero if the worldline $\mathbf{x}(\tau)$ does intersect both bodies $\Sigma = \Sigma_1 + \Sigma_2$. Indeed, if $\mathbf{x}(\tau)$ does not intersect Σ, then we have

$$(1-1) - (1-1) - (1-1) = 0$$

since all I's are zero, $I_{\Sigma_1+\Sigma_2} = I_{\Sigma_1} = I_{\Sigma_2} = 0$. If only one body is intersected by $\mathbf{x}(\tau)$, say Σ_1, then

$$I_{\Sigma_1+\Sigma_2}[\mathbf{x}(\tau)] = I_{\Sigma_1}[\mathbf{x}(\tau)] \quad \text{and} \quad I_{\Sigma_2}[\mathbf{x}(\tau)] = 0,$$

and the sum in Eq. (3.33) again becomes zero. Thus, we learn that only those worldlines which intersect *both* surfaces contribute to the interaction energy, see Fig. 3.2.

In the Dirichlet limit $\lambda \to \infty$, Eq. (3.33) becomes exactly 1 if both Σ_1 and Σ_2 are intersected. Introducing the worldline functional $\Theta_\Sigma[\mathbf{x}(\tau)]$ allows us to write the interaction energy in a compact form [37, 51]

$$E_{\mathrm{c}} = -\frac{1}{2\,(4\pi)^{D/2}} \int_0^\infty \frac{d\mathcal{T}\, \exp\left(-m^2 \mathcal{T}\right)}{\mathcal{T}^{1+D/2}} \int d^d x_{\mathrm{CM}} \langle \Theta_\Sigma[\mathbf{x}(\tau)] \rangle_x. \qquad (3.34)$$
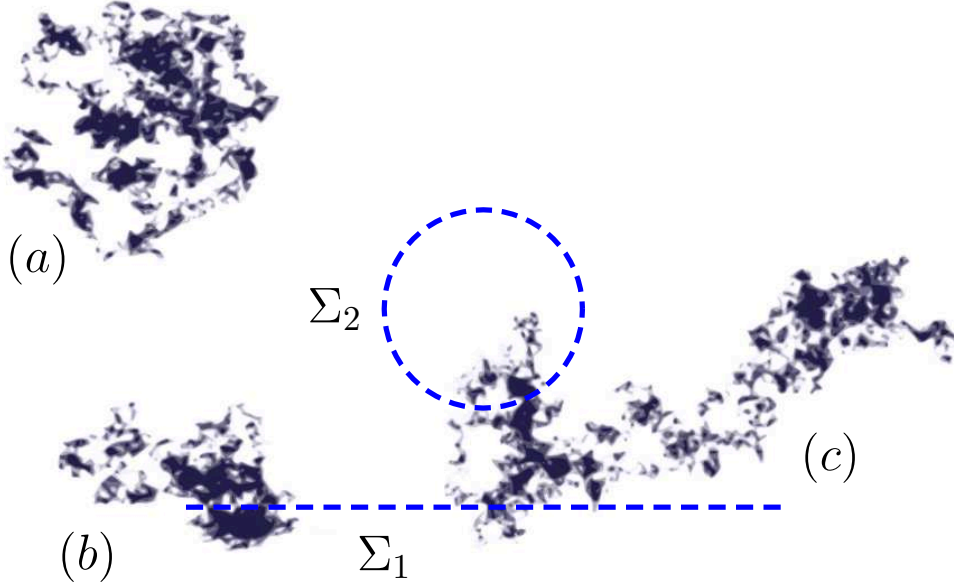
Figure 3.2: Worldline contribution to the Casimir interaction energy between a plate (dashed blue line), denoted by Σ_1, and a sphere (dashed blue circle), denoted by Σ_2. A worldline which does not intersect any surface, case (a), does not contribute to the Casimir energy at all, it is an ordinary vacuum fluctuation. If a worldline intersects only one surface, case (b), it contributes only to the local energy density, but not to the interaction energy. Only wordlines which see both surfaces, case (c), contribute to the interaction energy, and thereby to the Casimir force.

The worldline functional then has the following property

$$
\Theta_\Sigma[\mathbf{x}(\tau)] = \begin{cases} 1 & \text{if the worldline } \mathbf{x}(\tau) \text{ intersects both boundaries} \\ 0 & \text{otherwise} \end{cases} \tag{3.35}
$$

One realizes that the worldline functional Θ_Σ is analogous to the standard step function.

The expectation value in Eq. (3.34) is taken with respect to an ensemble of d-dimensional closed worldlines with a common center of mass $\mathbf{x}_{\mathrm{CM}}$ and a Gaußian velocity distribution, see Eq. (3.25),

$$
\langle \dots \rangle = \frac{\int_{\mathbf{x}_{\mathrm{CM}}} \mathcal{D}\mathbf{x} \dots e^{-\frac{1}{4}\int_0^{\mathcal{T}} \mathrm{d}\tau\, \dot{\mathbf{x}}^2(\tau)}}{\int_{\mathbf{x}_{\mathrm{CM}}} \mathcal{D}\mathbf{x}\, e^{-\frac{1}{4}\int_0^{\mathcal{T}} \mathrm{d}\tau\, \dot{\mathbf{x}}^2(\tau)}}. \tag{3.36}
$$

Eq. (3.34) has an intuitive interpretation: All worldlines intersecting both surfaces do not satisfy Dirichlet boundary conditions on both surfaces. They are

removed from the ensemble of allowed fluctuations by the Θ_Σ functional and thus contribute to the negative Casimir interaction energy.

The auxiliary parameter $\mathcal{T}$, the so-called propertime, effectively governs the size of a worldline: In the process of the $\mathcal{T}$ integration, the propertime parameter $\mathcal{T}$ scales the extent of a worldline by a factor of $\sqrt{\mathcal{T}}$. Large $\mathcal{T}$ correspond to long-wavelength or IR fluctuations, small $\mathcal{T}$ to short-wavelength or UV fluctuations.

Within the worldline picture, it becomes intuitively evident that for a Dirichlet scalar the Casimir interaction energy is negative. The interaction energy then monotonously increases with the (suitably defined) distance a between the surfaces, meaning that the resulting force is always attractive. This is in agreement with a theorem stated in [70].

3.4 Temperature in the worldline formalism

Finite temperature can be implemented with the aid of the Matsubara formalism [130], which is equivalent to compactifying Euclidean time on the interval $[0, \beta]$. For bosonic fields, as in the present case, we furthermore have to impose periodic boundary conditions. As a consequence, the closed worldlines now live on a cylindrical surface $S^1 \times \mathbb{R}^d$ and can carry a winding number. The worldlines $\mathbf{x}^{(n)}(\tau)$ winding n times around the cylinder can be decomposed into a worldline $\tilde{\mathbf{x}}(\tau)$ with no winding number and a winding motion at constant speed,

$$x_i^{(n)}(\tau) = \tilde{x}_i(\tau) + \frac{n\beta\tau}{\mathcal{T}}\delta_{iD}, \tag{3.37}$$

where the Dth component corresponds to Euclidean time. Let us confine ourselves to a massless scalar field. The Casimir interaction energy (3.34) now becomes

$$E_{\mathrm{c}} = -\frac{1}{2(4\pi)^{D/2}} \int_0^\infty \frac{\mathrm{d}\mathcal{T}}{\mathcal{T}^{1+D/2}} \sum_{n=-\infty}^\infty e^{-\frac{n^2\beta^2}{4\mathcal{T}}} \int \mathrm{d}^d x_{\mathrm{CM}} \left\langle \Theta_\Sigma[\mathbf{x}(\tau)] \right\rangle. \tag{3.38}$$

The finite-temperature worldline formalism for static configurations thus boils down to a winding-number prefactor in front of the worldline expectation value together with a sum over winding numbers:

$$\langle \dots \rangle \;\to\; \left(1 + 2\sum_{n=1}^\infty e^{-\frac{n^2\beta^2}{4\mathcal{T}}} \right) \langle \dots \rangle. \tag{3.39}$$

The winding-number sum is directly related to the standard Matsubara sum by a Poisson resummation,

$$\left(1 + 2\sum_{n=1}^\infty e^{-\frac{n^2\beta^2}{4\mathcal{T}}} \right) = \frac{\sqrt{4\pi\mathcal{T}}}{\beta} \sum_{m=-\infty}^\infty e^{-\left(\frac{2\pi m}{\beta}\right)^2 \mathcal{T}}. \tag{3.40}$$

The Poisson ressumation turns out to be a crucial tool for studies of high temperature effects, see Appendix A. The winding-number sum converges rapidly in the low- and intermediate temperature range, where this range depends on the configuration parameters. At high temperatures on the other hand, the Matsubara sum converges rapidly, such that fast convergence is provided for all temperatures.

This is already sufficient to understand the high-temperature limit of generic Casimir configurations: at high temperatures $\beta \to 0$, only the zeroth Matsubara frequency survives as higher modes receive thermal masses of order $\sim 2\pi/\beta = 2\pi T$ and decouple. All remaining temperature dependence arises from the dimensional prefactor $1/\beta = T$, and the dependence on the Casimir geometry only enters the prefactor. The calculation of the latter is a dimensionally reduced problem in $D-1$ dimensions. This is a general mechanism of *dimensional reduction* in high-temperature field theories. The linear high-temperature asymptotics is also clear from the fact that the Bose-Einstein distribution governing the distribution of bosonic thermal fluctuations increases as $\sim T$ in the high-temperature limit. Universal features of thermal Casimir energies with an emphasis on the high-temperature limit have been systematically studied in [131–134].

3.5 Worldline numerics

For numerical as well as analytical calculations, it is advantageous to rescale the worldlines such that the velocity distribution becomes independent of $\mathcal{T}$,

$$\boldsymbol{\gamma}(t) := \frac{1}{\sqrt{\mathcal{T}}}\mathbf{x}(\mathcal{T}t) \quad \to \quad \exp\left(-\frac{1}{4}\int_0^{\mathcal{T}} \dot{\mathbf{x}}^2 \mathrm{d}\tau\right) = \exp\left(-\frac{1}{4}\int_0^1 \dot{\boldsymbol{\gamma}}^2 \mathrm{d}t\right), \quad (3.41)$$

where the dot always denotes a derivative with respect to the argument, e.g., $\dot{\boldsymbol{\gamma}} = \mathrm{d}\boldsymbol{\gamma}(t)/\mathrm{d}t$. In terms of these normalized worldlines $\boldsymbol{\gamma}$ and the center-of-mass coordinate $\mathbf{x}_{\mathrm{CM}}$, the Θ_Σ functional reads more explicitly

$$\Theta_\Sigma[\mathbf{x}] \equiv \Theta_\Sigma[\mathbf{x}_{\mathrm{CM}} + \sqrt{\mathcal{T}}\boldsymbol{\gamma}(t)]. \quad (3.42)$$

The involved worldline integrals can be evaluated numerically by Monte Carlo methods in a straightforward manner. For this, the path integral over an operator $\mathcal{O}$ is approximated by a sum over a finite ensemble of n_{L} loops,

$$\langle \mathcal{O}[\boldsymbol{\gamma}] \rangle \to \frac{1}{n_{\mathrm{L}}} \sum_{\ell=1}^{n_{\mathrm{L}}} \mathcal{O}[\boldsymbol{\gamma}_\ell], \quad (3.43)$$

where ℓ counts the worldlines in the ensemble. Each worldline $\boldsymbol{\gamma}(t)$ is furthermore discretized by a finite set of N points per loop (ppl),

$$\boldsymbol{\gamma}(t) \to \boldsymbol{\gamma}_i = \boldsymbol{\gamma}(t_i), \quad t_i = \frac{i}{N}, \quad i = 0, \dots, N, \quad (3.44)$$

where $\boldsymbol{\gamma}_0 = \boldsymbol{\gamma}_N$ are identified as the worldlines are closed. Various efficient ab initio algorithms for generating discretized worldlines with Gaußian velocity distribution have been developed, see, e.g., [37, 135]. In this work, the worldlines were generated using the "v-loop" algorithm [37], which we present in Sec. 3.6.

We conclude that for the numerical evaluation of the Casimir energy (3.38), two discretizations have to be performed: The path integral is approximated by a finite sum over an ensemble of n_L worldlines, where each path is discretized, i.e. is represented by N points. The discretization error then depends on two parameters n_L and N. The number of worldlines in the ensemble determines the statistical error of the arithmetic mean. The statistical error is therefore $\sim 1/\sqrt{n_L}$ as the worldlines do not depend on each other. The systematic error is related to the number of points per worldline N. The generated worldlines are systematically too small, where the systematic error is $\sim 1/\sqrt{N}$, see next section.

The number of points N has to be chosen appropriately, such that the systematic error is less than the statistical one. Depending on the configuration, N can be much smaller, equal or much larger than n_L. For instance, in some cases, the systematic error can be partially canceled by an appropriate normalization of the Casimir force to a result which can also be calculated analytically. For example, the Casimir force for a sphere above a plate at small separations is related to the worldline extent λ as

$$F_c(a) \sim \frac{\langle \lambda^4 \rangle}{a^3}.$$

As we will see in chapter 4, $\langle \lambda^4 \rangle$ can be evaluated fully analytically, such that normalizing F_c to $\langle \lambda \rangle$ allows us to use large n_L along with comparable small N for high precision calculations. A counter-example to this case is a sphere above a plate, where the separation a is much larger than the radius. In order to resolve the sphere, "high" values for N have to be chosen, such that for the case where the systematic error is equal to the statistical one, we nevertheless have $N \gg n_L$.

In this work we have used ensembles with up to $n_L = 1.5 \cdot 10^6$ and $N = 60 \cdot 10^6$. The computational effort scales only linearly with N and n_L.

Notice that despite the described discretization, spacetime is still treated as a continuum. In this sense worldline numerics is superior to conventional lattice computations. Indeed, using a discrete spacetime lattice for resolving a smoothly curved or sharp edged boundary, necessarily a tiny lattice spacing is required, resulting in a huge numerical effort.

Although, intrinsically, worldline numerics is completely independent of the background geometry, the computational time can be considerably reduced by adapting the algorithms to a given configuration. We will present such algorithms

for various non-trivial Casimir configurations in the chapters to follow. In many cases, we even obtain novel analytical results using, actually, a numerical method.

In the remainder of this chapter we describe an efficient method for the generation of worldline ensembles, the "v-loop" algorithm [37].

3.6 The "v-loop" algorithm

In this section, we give a possible numerical realization of the worldline integrals in Eq. (3.25), the "v-loop" algorithm, as it was originally proposed in [37]. Our aim is to approximate the analytical integrals over infinitely many closed worldlines by an ensemble average over finitely many closed loops obeying a Gaußian velocity distribution $P[\boldsymbol{\gamma}(t)]$,

$$P[\boldsymbol{\gamma}(t)] = \delta\left(\int_0^1 \mathrm{d}t\,\boldsymbol{\gamma}(t)\right)\exp\left(-\frac{1}{4}\int_0^1 \mathrm{d}t\,\dot{\boldsymbol{\gamma}}^2\right), \quad \text{with } \boldsymbol{\gamma}(0) = \boldsymbol{\gamma}(1). \quad (3.45)$$

The condition $\boldsymbol{\gamma}(0) = \boldsymbol{\gamma}(1)$ ensures that the worldlines are closed. Due to the δ constraint, the worldlines are centered upon a common center of mass. Here, we work with rescaled worldlines $\boldsymbol{\gamma}(t)$, as introduced in Eq. (3.41), such that the velocity distribution becomes independent of $\mathcal{T}$. We also have dropped the normalization of the distribution since it becomes irrelevant when taking expectation values.

As stated in Eq. (3.44), we discretize the propertime parameter t and thereby the wordline $\boldsymbol{\gamma}(t)$ as,

$$\boldsymbol{\gamma}(t) \;\rightarrow\; \{\boldsymbol{\gamma}_i\} \in \mathbb{R}^D, \quad t \;\rightarrow\; \frac{i}{N}, \quad \mathrm{d}t \;\rightarrow\; \frac{1}{N}, \quad i = 0,\dots,N, \quad (3.46)$$

where $\boldsymbol{\gamma}_0 = \boldsymbol{\gamma}_N$ and N is the number of points per worldlines.

By discretizing $\dot{\boldsymbol{\gamma}}$ in the exponent of Eq. (3.45),

$$\dot{\boldsymbol{\gamma}} \;\rightarrow\; N(\boldsymbol{\gamma}_i - \boldsymbol{\gamma}_{i-1}),$$

the probability distribution $P[\boldsymbol{\gamma}(t)]$ becomes

$$P[\boldsymbol{\gamma}(t)] \;\rightarrow\; P[\{\boldsymbol{\gamma}_i\}] = \delta\left(\boldsymbol{\gamma}_1 + \dots + \boldsymbol{\gamma}_N\right)\exp\left(-\frac{N}{4}\sum_{i=1}^{N}(\boldsymbol{\gamma}_i - \boldsymbol{\gamma}_{i-1})^2\right). \quad (3.47)$$

Now, we want to perform a linear variable transformation

$$\{\boldsymbol{\gamma}_k\} \;\rightarrow\; \{\overline{v}_k\},$$

such that the discretized distribution (3.47) becomes purely Gaußian. This is at heart of the "v-loop" algorithm: The purely Gaußian numbers can be straight-forwardly generated by standard methods, as e.g. with the Box-Mueller method; the $\{\gamma_k\}$ can then be obtained by the inverse transformation.

Let us now perform this linear transformation. Because of the δ function, we may express for example γ_N as

$$\gamma_N = -\gamma_1 - \ldots - \gamma_{N-1}. \tag{3.48}$$

This gives

$$P[\{\gamma_i\}] = \exp\Big(-\frac{N}{4}\big((2\gamma_1 + \gamma_2 + \ldots + y_{N-1})^2 + (\gamma_1 + \gamma_2 + \ldots + 2\gamma_{N-1})^2\big)$$

$$-\frac{N}{4}\sum_{i=2}^{N-1}(\gamma_i - \gamma_{i-1})^2\Big) = \exp\Big(-\frac{N}{4}\Gamma\Big) \tag{3.49}$$

In order to diagonalize the quadratic form Γ in the exponent, let us define

$$\overline{v}_1 \equiv \frac{3}{2}\gamma_1 + \gamma_2 + \gamma_3 + \ldots + \gamma_{N-2} + \frac{3}{2}\gamma_{N-1},$$

$$v_i \equiv \gamma_i - \gamma_{i-1}, \quad i = 2, 3, \ldots, N-1. \tag{3.50}$$

It is also useful to introduce

$$v_{i,j} \equiv v_i + v_{i-1} + \ldots + v_{j+1} \equiv \gamma_i - \gamma_j, \quad \text{for } i \geq j = 1, 2, \ldots, N-1. \tag{3.51}$$

The quadratic form Γ now takes the form

$$\Big(\overline{v}_1 - \frac{1}{2}v_{N-1,1}\Big)^2 + \Big(\overline{v}_1 + \frac{1}{2}v_{N-1,1}\Big)^2 + \sum_{i=2}^{N-1} v_i^2 = 2\overline{v}_1^2 + \frac{1}{2}v_{N-1,1}^2 + \sum_{i=2}^{N-1} v_i^2. \tag{3.52}$$

We shall denote variables appearing purely quadratically, as it is the case here for $\overline{v}_1$, by an overline. From the last two terms of Eq. (3.52), we can construct another purely quadratic variable. Using the definition (3.51), we note

$$v_{N-1,1} = v_{N-1} + v_{N-2,1}.$$

From the last two terms of Eq. (3.52) we then obtain

$$\frac{1}{2}v_{N-1,1}^2 + \sum_{i=2}^{N-1} v_i^2 = \frac{1}{2}(v_{N-1} + v_{N-2,1})^2 + v_{N-1}^2 + \sum_{i=2}^{N-2} v_i^2 \tag{3.53}$$

$$= \frac{3}{2}\overline{v}_{N-1}^2 + \frac{1}{2}v_{N-2,1}^2 + \sum_{i=2}^{N-2} v_i^2, \tag{3.54}$$

where the purely quadratic $\overline{v}_{N-1}$ has been defined as

$$\overline{v}_{N-1} \equiv v_{N-1} + \frac{1}{3}v_{N-2,1}. \tag{3.55}$$

The same form can be achieved for the remaining $v_2 \dots v_{N-2}$ by the following prescription

$$\overline{v}_{N-i} \equiv v_{N-i} + \frac{1}{i+2}v_{N-i-1,1}, \quad i = 1, \dots, N-2. \tag{3.56}$$

The quadratic form Γ then becomes purely Gaußian, and one finds

$$\Gamma = 2\overline{v}_1^2 + \frac{3}{2}\overline{v}_{N-1}^2 + \frac{4}{3}\overline{v}_{N-2}^2 + \dots + \frac{i+2}{i+1}\overline{v}_{N-i}^2 + \dots + \frac{N}{N-1}\overline{v}_2^2. \tag{3.57}$$

Of course, the variable transformation will generate a Jacobian, however, this (non zero) Jacobian will only modify the normalization of the distribution, being irrelevant for the expectation values. Thus, we will not discuss this issue.

For the construction of a $\{\boldsymbol{\gamma}_i\}$, all steps have to be performed backwards. The "v-loop" algorithm consists of four steps:

1. generate $N-1$ numbers w_i, $i = 1, \dots, N-1$, distributed according to $\exp(-w_i^2)$;

2. compute the $\overline{v}_i$, $i = 1, \dots, N-1$, by normalizing the w_i:

$$\overline{v}_1 = \sqrt{\frac{2}{N}}\, w_1,$$

$$\overline{v}_i = \sqrt{\frac{4(N+1-i)}{N(N+2-i)}}\, w_i, \quad i = 2, \dots, N-1;$$

3. compute the v_i, $i = 2, \dots, N-1$ according to

$$v_i = \overline{v}_i - \frac{v_{i-1,1}}{N+2-i}, \quad \text{where } v_{i-1,1} = \sum_{j=2}^{i-1} v_j \; ;$$

4. construct the $\boldsymbol{\gamma}_i$, $i = 1, \dots, N$ via

$$\boldsymbol{\gamma}_1 = \frac{1}{N}\left(\overline{v}_1 - \sum_{i=2}^{N-1}\left(N-i+\frac{1}{2}\right)v_i\right),$$

$$\boldsymbol{\gamma}_i = \boldsymbol{\gamma}_{i-1} + v_i, \quad i = 2, \dots, N-1,$$

$$\boldsymbol{\gamma}_N = -\sum_{i=1}^{N-1} y_i \; .$$

A d-dimensional worldline can be build up using one-dimensional worldlines for each of the d components. Of course, repeating the algorithm d times, one has to use each time new random numbers. For the generation of an ensemble consisting of n_{L} (d-dimensional) worldlines, the algorithm has to be repeated $(d \times n_{\mathrm{L}})$ times.

The complexity of the "v-loop" algorithm is $\mathcal{O}(N)$, such that the numerical effort scales linearly with d, N and n_{L}. The systematic error for the maximal extent of a worldline is aboout the average spacing $\langle |\boldsymbol{\gamma}_i - \boldsymbol{\gamma}_{i-1}| \rangle$, which is roughly $\langle |v_2| \rangle = \langle |w_2| \rangle \sqrt{4/N} \approx \sqrt{1/N}$, and therefore $\mathcal{O}(1/\sqrt{N})$.

4 Inclined plates at zero temperature

In this chapter, we investigate the Casimir effect for inclined Casimir plates in D dimensions using the worldline formalism. We start with a detailed analysis at zero temperature, which will be extended to finite temperature in the next chapter.

We compute the Casimir energy, force and torque for the case of a fluctuating scalar field obeying Dirichlet boundary conditions on the plates and compare our results with two other established approximate schemes, the proximity force approximation and the optical approximation. These alternative schemes are found to be applicable for very small angles of inclination only. For larger inclinations, the PFA and optical estimates totally disagree with worldline numerical results. Only recently, results for the inclined plate configuration have been obtained at zero temperature using scattering theory [136]. This recent solution nicely agrees with our studies for all angles and therefore confirms worldline numerics.

In the sections to follow, we present many numerical as well as analytical worldline results, which were published in [57, 58]. We also provide more details of the calculations.

4.1 Introduction

The dependence of the Casimir force on the separation a between two infinitely extended parallel plates can be determined by dimensional analysis alone, as long as the plates are considered as ideal metals and no other dimensionful quantities are taken into account, as for example temperature or surface roughness. However, the prediction of the sign of the force (the exact prefactor let alone) is impossible without a detailed calculation. Since the dimension of $\hbar c$ is that of (energy $\times$

length) we conclude that the force per unit area in four spacetime dimensions takes the form

$$\frac{F_{\mathrm{c}}}{A} = -\frac{\mathrm{d}}{\mathrm{d}a}\frac{E_{\mathrm{c}}}{A} \sim \frac{\hbar c}{a^4},\tag{4.1}$$

where A is the plates' area and a the separation distance. The constant of proportionality is a dimensionless number, which does not depend on the microscopic details of the interaction since ideal metals are characterized by the vanishing absorption wave length. Therefore, the force law (4.1) is universal and should apparently be valid for arbitrary separation a.

However, at "small" separations, the Casimir force becomes a van der Waals-London force which depends differently on a, see Sec. 2.1. This seeming contradiction has a simple explanation. Since no microscopic details were considered by deriving Eq. (4.1), the transition to the non relativistic London-van der Waals forces at small separations cannot be obtained from the idealistic force law (4.1). A unified theory of both the van der Waals-London and Casimir forces for a configuration of two parallel plates was developed by Lifshitz (1956) [137], which, however, is not subject of the present thesis.

In this chapter we will determine the correct universal prefactors for the Casimir force F_{c} and the Casimir torque D_{c} for two ideal inclined plates. Unlike the case of two parallel plates, the force for inclined plates is proportional to the plate's *length* L_y. The dependence of F_{c} and D_{c} on the separation a can again be obtained from dimensional analysis:

$$\frac{F_{\mathrm{c}}}{L_y} \sim \frac{\hbar c}{a^3},\tag{4.2}$$

$$\frac{D_{\mathrm{c}}}{L_y} = \frac{\mathrm{d}}{\mathrm{d}\varphi}\frac{E_{\mathrm{c}}}{L_y} \sim \frac{\hbar c}{a^2},\tag{4.3}$$

where φ is the angle of inclination. For the idealized Casimir configuration, the prefactors then only depend on the configuration itself, i.e. the angle of inclination φ, the nature of the fluctuating field, and the boundary conditions imposed. For instance, the coefficient in (4.1) is twice as large for a fluctuating electromagnetic field, if compared with the corresponding coefficient for a fluctuating real scalar field. Of course, we keep in mind that the obtained results lose their validity at very small separations when dealing with real materials.

For simplicity, we restrict ourselves to the Casimir effect induced by a fluctuating scalar field obeying Dirichlet boundary conditions. Therefore, our results do not directly predict the Casimir force induced by the fluctuating electromagnetic field, the universal coefficients will differ quantitatively. However, the qualitative

behavior is expected to be similar. Examples are the edge effect and the transition from finite to vanishing angles of inclination, see following sections.

Very recently, results for inclined plates have been obtained for the electromagnetic case at zero temperature within scattering theory [136]. The coefficient for two perpendicular plates was found to be nearly the same as in the Dirichlet-scalar case, whereas in the limit of two parallel plates the result is, as expected, exactly twice as large to the leading order.

The two limiting cases of the inclined plates configuration, namely perpendicular plates and a semi-infinite plate parallel to an infinite one, were studied in [54, 56] at zero temperature using worldline numerics. We review and generalize those known results and exemplify how the Casimir effect can be understood in terms of simple geometric properties of the worldlines.

Before we start with worldline analysis, let us consider a much simpler approximate method, the proximity force approximation (PFA). This simple method is widely used for comparison. We have already made contact with the PFA in the introductory chapter.

4.2 PFA for inclined plates

Here we restrict ourselves to four-dimensional spacetime and give the PFA estimates for the configuration of inclined plates, which is studied in the following sections using worldline numerics. The configuration is shown in Fig. 4.1: the upper semi-infinite plate is above an infinite plate at an angle φ. The minimal distance between the plates is $a = h(r = 0)$. Both plates are assumed to be perfectly thin. The semi-infinite plate has an edge with a length L_y.

As we have seen in Sec. 2.5, the proximity force approximation is directly related to the parallel plates result. In the PFA scheme, the inclined plates geometry is approximated by infinitesimal parallel plates. However, the PFA is ambiguous. We can either take the lower plate as a "basis" and approximate the upper plate by parallel plates as illustrated in Fig. 4.1, or we approximate the lower plate as in Fig. 4.2.

Both cases are not identical and indeed, the Casimir force depends differently on φ. On the other hand, the dependence on the minimal distance a between the plates is universal and is determined by dimensional analysis alone.

The Casimir energy per unit area for two parallel plates, according to the

Eq. (4.1) is

$$\frac{E_c^{\parallel}}{A} = -\frac{c_{\parallel}}{a^3}, \quad c_{\parallel} = \frac{\pi^2}{1440} \tag{4.4}$$

for a fluctuating real scalar field.

In the first case, we use the lower plate as a basis and obtain for the height

$$h_{\mathrm{LP}}(r) = a + r \tan(\varphi). \tag{4.5}$$

Integrating with this height over the lower plate we find

$$\frac{E_c^{\mathrm{i.p.-PFA-LP}}}{L_y} = c_{\parallel} \int_0^{\infty} \frac{\mathrm{d}r}{h_{\mathrm{LP}}^3(r)} = \frac{c_{\parallel}}{2} \frac{\cos(\varphi)}{\sin(\varphi)\, a^2}. \tag{4.6}$$

On the other hand, using the upper plate for the determination of the height we get

$$\frac{E_c^{\mathrm{i.p.-PFA-UP}}}{L_y} = c_{\parallel} \int_0^{\infty} \frac{\mathrm{d}r}{h_{\mathrm{UP}}^3(r)} = \frac{c_{\parallel}}{2} \frac{\cos^3(\varphi)}{\sin(\varphi)\, a^2}. \tag{4.7}$$

Eq. (4.7) can be deduced from Eq. (4.6) by replacing in Eq. (4.6) a by $a/\cos(\varphi)$.

According to the PFA, the true behavior shall lie somewhere in between these two results. We will compare these two estimates with the worldline result in Fig. 4.8. There, we will see that the PFA and worldline results only agree to leading order in φ. However, the force per unit *length* diverges for vanishing φ. Replacing the divergent energy per unit *length* by finite energy per unit *area*, we will obtain a contribution arising from the the edge of the upper plate in the worldline approach. This so called edge effect is missing in the PFA results.

For two perpendicular plates, $\varphi = \pi/2$, the PFA predicts no force at all, whereas the worldline result remains finite. A systematic treatment of the PFA, specializing to sphere-cylinder configurations, is given in chapter 8, where we also compare the PFA with the worldline approach. Let us now return to worldline numerics.
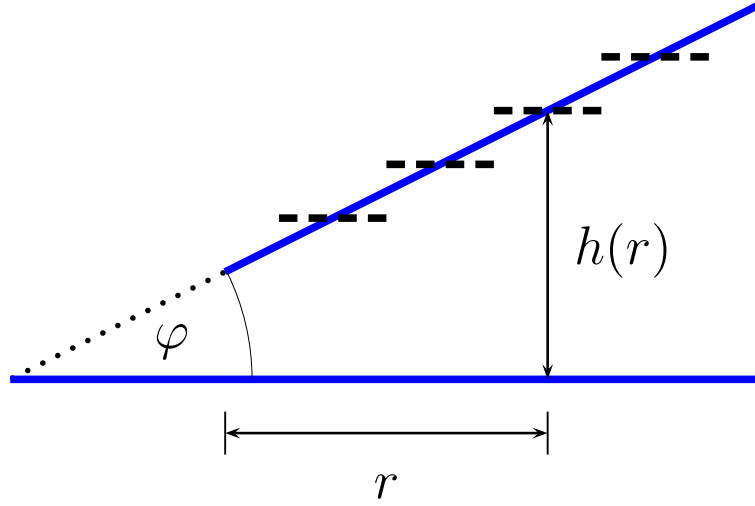
Figure 4.1: The inclined plates and the proximity force approximation. The lower plate is taken to be infinite and the upper plate semi-infinite. The upper plate is inclined at an angle φ. The plates' depth L_y (out of page) is assumed to be infinite. The minimal distance between the plates is $a = h(r = 0)$. In this figure, the PFA scheme replaces the upper plate by a superposition of infinitesimal parallel plates.

Figure 4.2: In this figure, the PFA sees the lower plate as a superposition of parallel plates

4.3 Worldline numerics

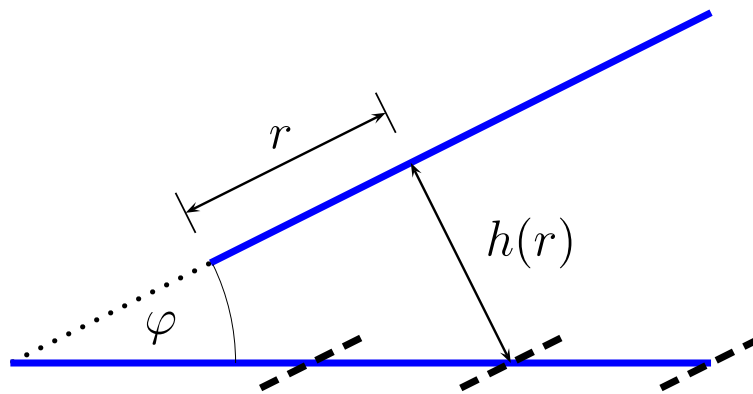In the following, we will thoroughly use the worldline representation of the Casimir interaction energy, which we derived in the previous chapter. For a configuration Σ consisting of two rigid bodies with surfaces Σ_1 and Σ_2, this representation in $D = d + 1$ dimensional spacetime reads

$$E_{\mathrm{c}} = -\frac{1}{2(4\pi)^{D/2}} \int_0^\infty \frac{\mathrm{d}\mathcal{T}}{\mathcal{T}^{1+D/2}} \int \mathrm{d}^d x_{\mathrm{CM}} \, \langle \Theta_\Sigma[\mathbf{x}(\tau)] \rangle \,. \tag{4.8}$$

Here, the generalized step functional obeys $\Theta_\Sigma[\mathbf{x}] = 1$ if a worldline

$$\mathbf{x}(\tau) = \mathbf{x}_{\mathrm{CM}} + \sqrt{\mathcal{T}} \, \boldsymbol{\gamma}(\tau)$$

intersects both surfaces $\Sigma = \Sigma_1 \cup \Sigma_2$, and is zero otherwise. The expectation value in Eq. (4.8) is taken with respect to an ensemble of d-dimensional closed worldlines with a common center of mass $\mathbf{x}_{\mathrm{CM}}$ and a Gaußian velocity distribution.

4.4 Parallel plates

We start with Casimir's classic configuration of two infinitely extended parallel plates. Let the lower and upper plate lie in the $z = -a$ and $z = 0$ planes, respectively, see Fig. 4.3. In d space dimensions the surface area A of the plates is then $d-1$ dimensional. The worldline functional Θ for this configuration reads

$$\Theta_\parallel \left[z_{\mathrm{CM}} + \sqrt{\mathcal{T}} \boldsymbol{\gamma}_{z,\ell} \right] = \theta \left(z_{\mathrm{CM}} + \sqrt{\mathcal{T}} \boldsymbol{\gamma}_{z_{\mathrm{max}},\ell} \right) \theta \left(-z_{\mathrm{CM}} - \sqrt{\mathcal{T}} \boldsymbol{\gamma}_{z_{\mathrm{min}},\ell} - a \right), \quad (4.9)$$

where $\boldsymbol{\gamma}_{z,\ell}$ is the z coordinate of the ℓ'th worldline (measured with respect to the center of mass). The quantities $\boldsymbol{\gamma}_{z_{\mathrm{max}},\ell}$, $\boldsymbol{\gamma}_{z_{\mathrm{min}},\ell}$ denote the worldline's maximal and minimal extent in the z direction, respectively, see Fig. 4.3. The total maximal extent λ_ℓ of the ℓ'th worldline then is

$$\lambda_\ell = \boldsymbol{\gamma}_{z_{\mathrm{max}},\ell} - \boldsymbol{\gamma}_{z_{\mathrm{min}},\ell}. \tag{4.10}$$

In order to obtain Eq. (4.9), we note that the worldline functional for two parallel plates $\Theta_\parallel$ is only non zero if both plates are intersected by the inserted worldline. This clearly is the case when $z_{\mathrm{CM}} + \sqrt{\mathcal{T}} \boldsymbol{\gamma}_{z_{\mathrm{max}},\ell}$ is above the upper plate,

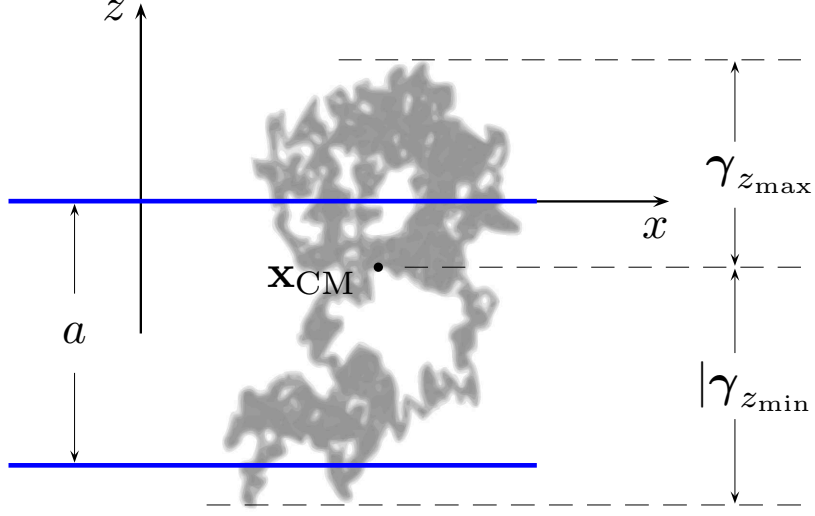$$z_{\mathrm{CM}} + \sqrt{\mathcal{T}} \boldsymbol{\gamma}_{z_{\mathrm{max}},\ell} \overset{!}{>} 0, \tag{4.11}$$

Figure 4.3: Sketch of the parallel-plates configuration. A worldline only contributes to the Casimir energy if it itersects both plates. All information needed for the evaluation of the Casimir energy is then contained in its extent $\lambda = \gamma_{z_{\max}} + |\gamma_{z_{\min}}|$ along the z direction, see Eq. (4.15).

and $z_{\mathrm{CM}} + \sqrt{\mathcal{T}}\gamma_{z_{\min},\ell}$ below the lower plate,

$$z_{\mathrm{CM}} + \sqrt{\mathcal{T}}\gamma_{z_{\min},\ell} \overset{!}{<} -a. \qquad (4.12)$$

The conditions (4.11) and (4.12) are formulated in terms of the two θ functions in (4.9).

Now, we can do the integral in Eq. (4.8),

$$E_{\mathrm{c}}^{\|} = -\frac{1}{2(4\pi)^{D/2}} \int_0^\infty \frac{\mathrm{d}\mathcal{T}}{\mathcal{T}^{1+D/2}} \int \mathrm{d}^d x_{\mathrm{CM}} \left\langle \Theta_{\|}[\mathbf{x}(\tau)] \right\rangle. \qquad (4.13)$$

All spatial integrals apart from the z_{CM} one are trivial and result in the plates' $d-1$ dimensional area A. For the z_{CM} integral one obtains

$$\int_{-\infty}^\infty \mathrm{d}z_{\mathrm{CM}}\, \theta\left(z_{\mathrm{CM}} + \sqrt{\mathcal{T}}\gamma_{z_{\max},\ell}\right) \theta\left(-z_{\mathrm{CM}} - \sqrt{\mathcal{T}}\gamma_{z_{\min},\ell} - a\right)$$

$$= \left(\sqrt{\mathcal{T}}\lambda_\ell - a\right) \theta\left(\sqrt{\mathcal{T}}\lambda_\ell - a\right). \quad (4.14)$$

With this result we can evaluate the remaining propertime integral analytically,

$$\frac{E_{\mathrm{c}}^{\|}}{A} = -\frac{1}{2(4\pi)^{D/2}} \left\langle \int_{a^2/\lambda_\ell^2}^\infty \frac{\mathrm{d}\mathcal{T}\left(\sqrt{\mathcal{T}}\lambda_\ell - a\right)}{\mathcal{T}^{1+D/2}} \right\rangle, \qquad (4.15)$$
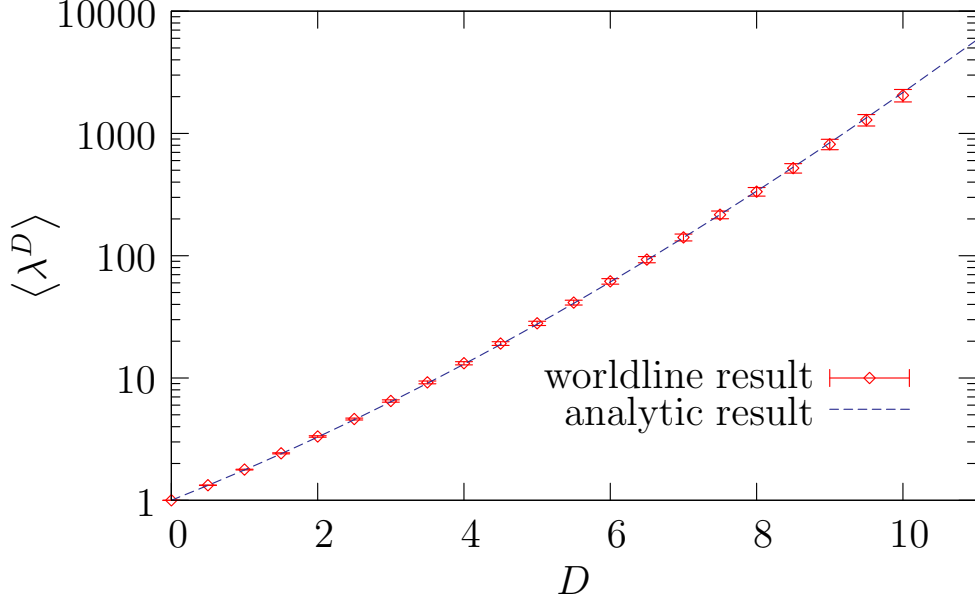
Figure 4.4: Dth moment of the maximum spatial extent λ of a worldline as a function of D. This geometric object (which is the same in any target dimension of the worldline) is related to the Casimir energy of the parallel-plates configuration in D spacetime dimensions by Eqs. (4.17) and 4.18. The plot compares the exact analytical result with the worldline numerical computation based on 1000 worldlines with 2×10^6 ppl (points per loop) each.

and obtain the Casimir energy density (suppressing the index ℓ from now on)

$$\frac{E_{\mathrm{c}}^{\parallel}}{A} = -\frac{\langle\lambda^D\rangle}{D(D-1)(4\pi)^{D/2}\, a^{D-1}}. \qquad (4.16)$$

We observe that the D-dimensional parallel-plate Casimir energy is related to the Dth cumulant of the extent of the worldlines [53]. This is a first example for a relation between Casimir energies and geometric properties of the worldlines. Instead of computing these cumulants directly, let us simply compare Eq. (4.16) with the well-known analytic result [108, 109], which was derived in Sec. 2.4,

$$\frac{E_{\mathrm{c}}^{\parallel}}{A} = -\frac{\Gamma(D/2)\zeta(D)}{(4\pi)^{D/2}\, a^{D-1}}, \qquad (4.17)$$

yielding

$$\langle\lambda^D\rangle = D(D-1)\Gamma(D/2)\zeta(D). \qquad (4.18)$$

A comparison of the analytical result to a numerical evaluation of the cumulants is displayed in Fig. 4.4. Also, the Casimir force density can straightforwardly be obtained as the derivative of Eq. (4.16) with respect to a. Incidentally, the connection between Casimir energies and worldline properties also induces a relation between Casimir energies and questions in polymer physics, as first observed in [53].
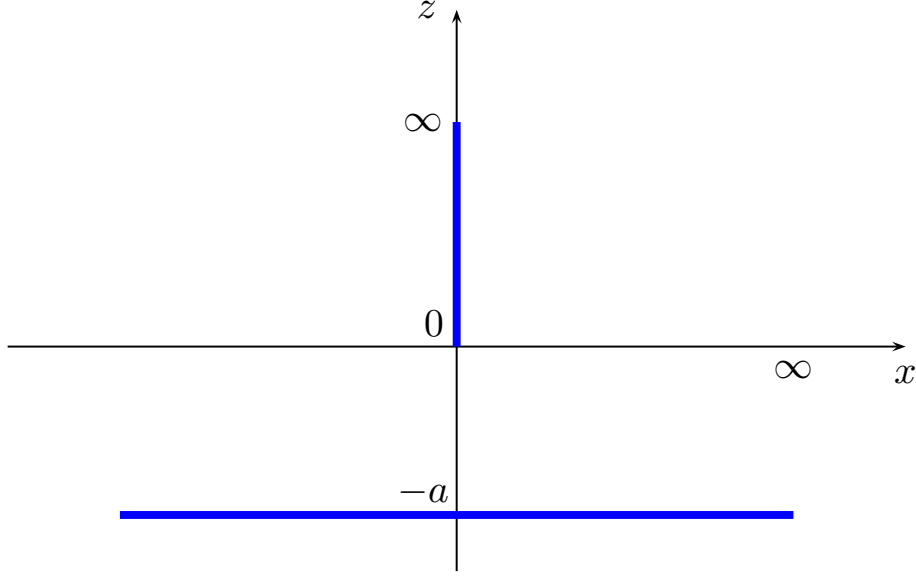
Figure 4.5: Sketch of the perpendicular-plates configuration. The upper semi-infinite plate, lying in the $x = 0$ plane, is perpendicular to an infinite plate (blue lines). The minimal distance between the plates is a.

4.5 Perpendicular plates

Let us now shortly review the perpendicular plates' configuration, as studied at zero temperature in [54, 56]. Both plates are again assumed to be perfectly thin.

The perpendicular-plates configuration consists of a semi-infinite plate perpendicular to an infinite plate, see Fig. 4.5. The semi-infinite plate has an edge with a ($d-2$ dimensional) length L_y. The infinite plate has a ($d-1$) dimensional area A.[1] Let a be the minimal distance between the plates. The lower plate shall lie in the $z = -a$ plane. The upper plate shall cover the $x = 0$ plane for positive z values. In the following, we omit the center-of-mass subscript CM and the index ℓ.

The full worldline functional for this configuration reads

$$\Theta_\perp = \theta\left(-z - \sqrt{\mathcal{T}}\gamma_{z_{\min}} - a\right)$$

$$\times\, \theta\left(z + \sqrt{\mathcal{T}}\gamma_{z_{\max}}\left(-\frac{x}{\sqrt{\mathcal{T}}}\right)\right)\theta\left(-x - \sqrt{\mathcal{T}}\gamma_{x_{\min}}\right)\theta\left(x + \sqrt{\mathcal{T}}\gamma_{x_{\max}}\right). \quad (4.19)$$

---

[1]Of course, the labels "semi-infinite" and "infinite" imply that both L_y and A are considered in the limit $L_y, A \to \infty$.

4 Inclined plates at zero temperature

The $\Theta_\perp$ functional is non zero if both plates are intersected by a worldline. This happens if, first, the the lower end of the worldline $z_{\mathrm{CM}} + \sqrt{\mathcal{T}}\gamma_{z_{\min}}$ is below the lower plate,

$$z_{\mathrm{CM}} + \sqrt{\mathcal{T}}\gamma_{z_{\min}} \overset{!}{<} -a. \tag{4.20}$$

The condition (4.20) agrees, of course, with the condition (4.12) for two parallel plates and corresponds to the first θ function in Eq. (4.19). The lower plate is then automatically intersected if the upper plate is also intersected, which is ensured by the last three θ functions.

These θ functions are non zero if the worldline crosses the $x = 0$ plane (last two θ functions), and if at $x = 0$ its z coordinate is positive.

Now, we can do the integral in Eq. (4.8) for the Casimir energy,

$$E_{\mathrm{c}}^\perp = -\frac{1}{2(4\pi)^{D/2}} \int_0^\infty \frac{\mathrm{d}\mathcal{T}}{\mathcal{T}^{1+D/2}} \int \mathrm{d}^d x \, \langle \Theta_\perp[\mathbf{x}(\tau)] \rangle . \tag{4.21}$$

All spatial integrals apart from the x and z integrals are trivial. They result in the upper plates' $d - 2$ dimensional edge, which we denote by L_y.

We can rescale x as $x \to -\sqrt{\mathcal{T}}x$, then the last two θ functions become the upper and lower bounds of the x integral and the z integral can be done analytically:

$$\int_{-\infty}^\infty \mathrm{d}z \, \theta\left(-z - \sqrt{\mathcal{T}}\gamma_{z_{\min}} - a\right) \theta\left(z + \sqrt{\mathcal{T}}\gamma_{z_{\max}}(x)\right)$$

$$= \int_{\sqrt{\mathcal{T}}\gamma_{z_{\min}}+a}^{\sqrt{\mathcal{T}}\gamma_{z_{\max}}(x)} \mathrm{d}z \, \theta\left(\sqrt{\mathcal{T}}\left(\gamma_{z_{\max}}(x) - \gamma_{z_{\min}}\right) - a\right)$$

$$= \left(\sqrt{\mathcal{T}}\left(\gamma_{z_{\max}}(x) - \gamma_{z_{\min}}\right) - a\right) \theta\left(\sqrt{\mathcal{T}}\left(\gamma_{z_{\max}}(x) - \gamma_{z_{\min}}\right) - a\right). \tag{4.22}$$

The θ function in Eq. (4.22) bounds the propertime integral from below.

Rescaling $\mathcal{T}$ as

$$\mathcal{T} \to \frac{a^2}{(\gamma_{z_{\max}}(x) - \gamma_{z_{\min}})^2} \mathcal{T},$$

we eventually obtain

$$\frac{E_{\mathrm{c}}^\perp}{L_y} = -\frac{1}{2(4\pi)^{D/2}a^{D-2}} \int_1^\infty \frac{\sqrt{\mathcal{T}} - 1}{\mathcal{T}^{(D+1)/2}} \mathrm{d}\mathcal{T} \left\langle \int_{\gamma_{x_{\min}}}^{\gamma_{x_{\max}}} \mathrm{d}x \, (\gamma_{z_{\max}}(x) - \gamma_{z_{\min}})^{D-1} \right\rangle$$

$$= -\frac{1}{(4\pi)^{D/2}(D-1)(D-2)a^{D-2}} \left\langle \int_{\gamma_{x_{\min}}}^{\gamma_{x_{\max}}} \mathrm{d}x \, (\gamma_{z_{\max}}(x) - \gamma_{z_{\min}})^{D-1} \right\rangle. \tag{4.23}$$

Note that all relevant information needed for the evaluation of the Casimir energy is contained in the function $\boldsymbol{\gamma}_{z_{\max}}(x) - \boldsymbol{\gamma}_{z_{\min}}$, see Fig. 4.7, where

$$\boldsymbol{\gamma}_{z_{\min}} = \boldsymbol{\gamma}_{z_{\min}}(\varphi = \pi/2).$$

For $D = 4$, the Eq. (4.23) reads

$$\frac{E_{\mathrm{c}}^{\perp}}{L_{\mathrm{y}}} = -\frac{c_{\perp}}{a^2}. \tag{4.24}$$

For the universal coefficient $c_{\perp}$, we obtain

$$c_{\perp} = 6.03(2) \cdot 10^{-3}, \tag{4.25}$$

in agreement with the value

$$c_{\perp} = 6.00(2) \cdot 10^{-3}$$

from previous worldline studies [54, 56] and a recent result obtained using scattering theory [136], where

$$c_{\perp} = 6.0484 \cdot 10^{-3}.$$

The statistical error in (4.25) is about 0.33%. We used $50\,000$ worldlines with $2.5 \cdot 10^6$ ppl each.

The computational time for determining the function $\boldsymbol{\gamma}_{z_{\max}}(x) - \boldsymbol{\gamma}_{z_{\min}}$ is relatively short. For example, a modern desktop PC needs roughly 0.6 seconds per loop with $2.5 \cdot 10^6$ ppl. The time for the numerical integration is then negligible. As a comparison, for the corresponding evaluation of the Casimir energy of two parallel plates, the determination of the maximal extent λ in z direction requires roughly 0.2 seconds for the same loop.

Since for a given worldline $(\boldsymbol{\gamma}_x(t), \boldsymbol{\gamma}_z(t))$ there exists a corresponding worldline in the ensemble with $(\boldsymbol{\gamma}_x(t), -\boldsymbol{\gamma}_z(t))$, it is advantageous to reflect a worldline on its z axis, i.e. to evaluate the $\boldsymbol{\gamma}_{z_{\min}}(x) - \boldsymbol{\gamma}_{z_{\max}}$ function as well. This results in an effective doubling of the worldline ensemble.

The Casimir force can easily be obtained from (4.23) upon differentiation with respect to a.

4.6 Inclined plates

The inclined-plates (i.p.) configuration consists of a perfectly thin semi-infinite plate above an infinite plate at an angle φ, see Fig. 4.6. As in the perpendicular plates configuration, the semi-infinite plate has an edge with a $(d-2$ dimensional) length L_y and the infinite plate's area A is $(d-1)$ dimensional. Again, the labels "semi-infinite" and "infinite" imply the limit $L_y, A \to \infty$. The minimal distance between the plates is a.

This configuration can be obtained from the setup of perpendicular plates by rotating the infinite plate in the x, z plane. We note that the conditions for the intersection with the semi-infinite plate are identical for both configurations. The corresponding condition for the intersection with the infinite plate can be obtained by a coordinate transformation. Therefore, to obtain the worldline functional $\Theta_{\text{i.p.},\varphi}$, we can use Eq. (4.19), where only the first θ function (belonging to the infinite plate) has to be modified. The $\Theta_{\text{i.p.},\varphi}$ functional for the inclined plates configuration then reads

$$\Theta_{\text{i.p.},\varphi} = \theta\left(-x\cos(\varphi) - z\sin(\varphi) - \sqrt{\mathcal{T}}\boldsymbol{\gamma}_{x_{\min}}(\varphi) - a\right)$$

$$\times \theta\left(z + \sqrt{\mathcal{T}}\boldsymbol{\gamma}_{z_{\max}}\left(-\frac{x}{\sqrt{\mathcal{T}}}\right)\right)\theta\left(-x - \sqrt{\mathcal{T}}\boldsymbol{\gamma}_{x_{\min}}\right)\theta\left(x + \sqrt{\mathcal{T}}\boldsymbol{\gamma}_{x_{\max}}\right),$$

(4.26)

where the first θ function ensures the intersection of the worldline with the infinite plate. The remaining three ones account for the intersection with the semi-infinite plate and are the same as in (4.19). In Eq. (4.26), we have used

$$\boldsymbol{\gamma}_{x_{\min}}(\varphi) \equiv \min_t \left(\boldsymbol{\gamma}_x(t)\cos(\varphi) + \boldsymbol{\gamma}_z(t)\sin(\varphi)\right), \tag{4.27}$$

where t parameterizes the worldline; i.e., in the discretized version, we have $t = 1\ldots N$ with N being the number of points per worldline loop (ppl). Trivially, it holds that

$$\boldsymbol{\gamma}_{x_{\min}}(0) = \boldsymbol{\gamma}_{x_{\min}} \quad \text{and} \quad \boldsymbol{\gamma}_{x_{\min}}(\pi/2) = \boldsymbol{\gamma}_{z_{\min}}. \tag{4.28}$$

In other words, $\boldsymbol{\gamma}_{x_{\min}}(\varphi)$ measures the minimal extent of the worldline in the x direction of a coordinate system rotated by the angle φ. In Eq. (4.26), we also encounter $\boldsymbol{\gamma}_{z_{\max}}(x)$, denoting the x-dependent envelope of the worldline in positive z direction. All these geometric properties of a worldline are displayed in Fig. 4.7.

The $\Theta_{\text{i.p.},\varphi}$ functional in Eq. (4.26) generalizes the case of perpendicular plates ($\perp$) for $\varphi = \pi/2$ and the case of one semi-infinite plate parallel to a infinite one (1si) for $\varphi \to 0$; both edge configurations were studied in detail in [54, 56].
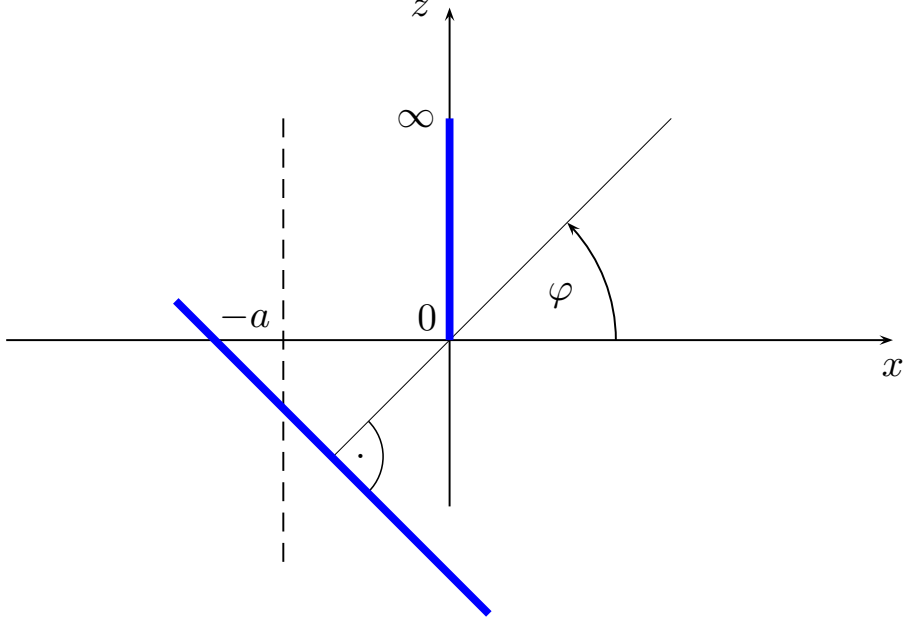
Figure 4.6: Sketch of the inclined-plates configuration. The infinite plate (dashed line) is rotated in the x, z plane by an angle φ. As special cases, $\varphi = 0$ corresponds to the configuration of one semi-infinite plate parallel to an infinite plate (1si configuration), whereas $\varphi = \pi/2$ yields the perpendicular-plates configuration.

Inserting $\Theta_{\text{i.p.},\varphi}$ for $\varphi \neq 0$ into Eq. (6.1) leads to the Casimir energy density of the inclined plates

$$
\frac{E_c^{\text{i.p.},\varphi}}{L_y} = -\frac{1}{2(4\pi)^{D/2}} \left\langle \int_0^\infty \mathrm{d}\mathcal{T} \frac{\sqrt{\mathcal{T}}}{\mathcal{T}^{1+D/2}} \int_{-\sqrt{\mathcal{T}}\gamma_{z_{\max}}(x)}^\infty \mathrm{d}z \right.
$$

$$
\left. \times \int_{\gamma_{x_{\min}}}^{\gamma_{x_{\max}}} \mathrm{d}x\, \theta\left(-a - \sqrt{\mathcal{T}}\gamma_{x_{\min}}(\varphi) + \sqrt{\mathcal{T}}x\cos(\varphi) - z\sin(\varphi)\right) \right\rangle, \quad (4.29)
$$

where x was rescaled as $x \to -x/\sqrt{\mathcal{T}}$.

For $\sin(\varphi) \neq 0$ the θ function translates to an upper bound on the z integral. Doing the z integral for $\sin(\varphi) \neq 0$ results in,
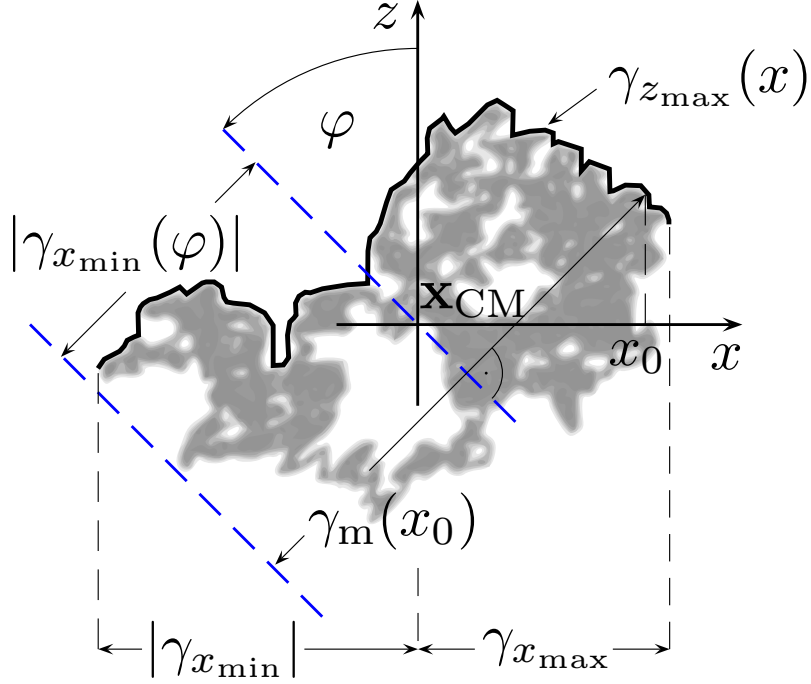
Figure 4.7: All relevant information for the evaluation of the Casimir energy of the inclined plates, (4.32), is encoded in the function $\boldsymbol{\gamma}_{\mathrm{m}}(x)$, which has to be integrated from $\boldsymbol{\gamma}_{x_{\min}}$ to $\boldsymbol{\gamma}_{x_{\max}}$.

$$
\frac{E_{\mathrm{c}}^{\mathrm{i.p.},\varphi}}{L_y} = -\frac{1}{2(4\pi)^{D/2}} \left\langle \int_0^\infty \frac{\mathrm{d}\mathcal{T}}{\mathcal{T}^{(1+D)/2}} \int_{\boldsymbol{\gamma}_{x_{\min}}}^{\boldsymbol{\gamma}_{x_{\max}}} \mathrm{d}x \right.
$$

$$
\times \left(\frac{\sqrt{\mathcal{T}}(x\cos(\varphi) - \boldsymbol{\gamma}_{x_{\min}}(\varphi)) - a}{\sin(\varphi)} + \sqrt{\mathcal{T}} \boldsymbol{\gamma}_{z_{\max}}(x) \right)
$$

$$
\times\, \theta \left. \left(\frac{\sqrt{\mathcal{T}}(x\cos(\varphi) - \boldsymbol{\gamma}_{x_{\min}}(\varphi)) - a}{\sin(\varphi)} + \sqrt{\mathcal{T}} \boldsymbol{\gamma}_{z_{\max}}(x) \right) \right\rangle. \quad (4.30)
$$

Let us define

$$
\boldsymbol{\gamma}_{\mathrm{m}}(x) \equiv x\cos(\varphi) + \sin(\varphi)\boldsymbol{\gamma}_{z_{\max}}(x) - \boldsymbol{\gamma}_{x_{\min}}(\varphi). \tag{4.31}
$$

The function $\boldsymbol{\gamma}_{\mathrm{m}}(x)$ is shown in Fig. 4.7.

The θ function in Eq. (4.30) imposes a lower bound $a^2/\boldsymbol{\gamma}_{\mathrm{m}}^2(x)$ on the $\mathcal{T}$ integral. With $\mathcal{T} \to \mathcal{T} a^2/\boldsymbol{\gamma}_{\mathrm{m}}^2(x)$ we eventually obtain

$$\frac{E_{\mathrm{c}}^{\mathrm{i.p.},\varphi}}{L_y} = -\frac{\csc(\varphi)}{(4\pi)^{D/2}(D-1)(D-2)\,a^{D-2}} \left\langle \int_{\boldsymbol{\gamma}_{x_{\min}}}^{\boldsymbol{\gamma}_{x_{\max}}} \mathrm{d}x\ \boldsymbol{\gamma}_{\mathrm{m}}^{D-1}(x) \right\rangle. \qquad (4.32)$$

Actually, the integrand in Eq. (4.32) should be multiplied by $\theta(\boldsymbol{\gamma}_{\mathrm{m}}(x))$. As $\boldsymbol{\gamma}_{\mathrm{m}}(x)$ is never negative, see Fig. 4.7, this θ function can be omitted.

We can write Eq. (4.32) as

$$\frac{E_{\mathrm{c}}^{\mathrm{i.p.},\varphi}}{L_y} = -\frac{c(D,\varphi)}{\sin(\varphi)\,a^{D-2}}, \qquad (4.33)$$

where the function $c(D,\varphi)$ depends only on D and φ.

For $\varphi = \pi/2$ and $D = 4$, we rediscover the perpendicular plates result [54, 56] as a special case. Incidentally, the integral in Eq. (4.32) can be done analytically for $\varphi = 0$ resulting in

$$\frac{\left\langle \lambda^D \right\rangle}{D} = (D-1)\Gamma(D/2)\zeta(D). \qquad (4.34)$$

We therefore find an analytical expression for $c(D, \varphi = 0)$

$$c(D, \varphi = 0) = \frac{\Gamma(D/2)\zeta(D)}{(4\pi)^{D/2}(D-2)} = \frac{c_\|(D)}{D-2}, \qquad (4.35)$$

where $c_\|(D)$ is the parallel plates coefficient, see Eq. (4.17).

The function $c(D,\varphi)$, normalized to its value at $\varphi = 0$, is shown as a function of φ in Fig. 4.8 for $D = 4$. In Fig. 4.8 we also plot the naive PFA estimate, a result from optical approximation [36, 138] (see appendix B) and a solution found recently for inclined plates at zero temperature by Graham et al. using scattering theory [136]. In all these cases the Casimir energy can be written as in Eq. (4.33), where only the coefficient $c(D, \varphi)$ is characteristic for a case chosen. Our data nicely agrees with the latter solution [136]. On the other hand, the PFA and the optical approximation fail to predict even the correct sign of the small φ correction. .

Note that together with the φ-dependent prefactor, Eq. (4.32) diverges as $\varphi \to 0$ as it should, see Eq. (4.35) This is because Eq. (4.32) corresponds to the energy per unit *edge length*, whereas for $\varphi \to 0$ the Casimir energy becomes proportional to the *area* of the semi-infinite plate. At first glance, at least the divergent $\varphi = 0$ behavior is described correctly by the PFA. We devote the whole next section to analyzing how the limit $\varphi \to 0$ yielding the 1si configuration can be obtained. In this 1si configuration configuration, a subleading contribution arising from the edge emerges, which is not seen by the PFA, even in the limit $\varphi \to 0$.
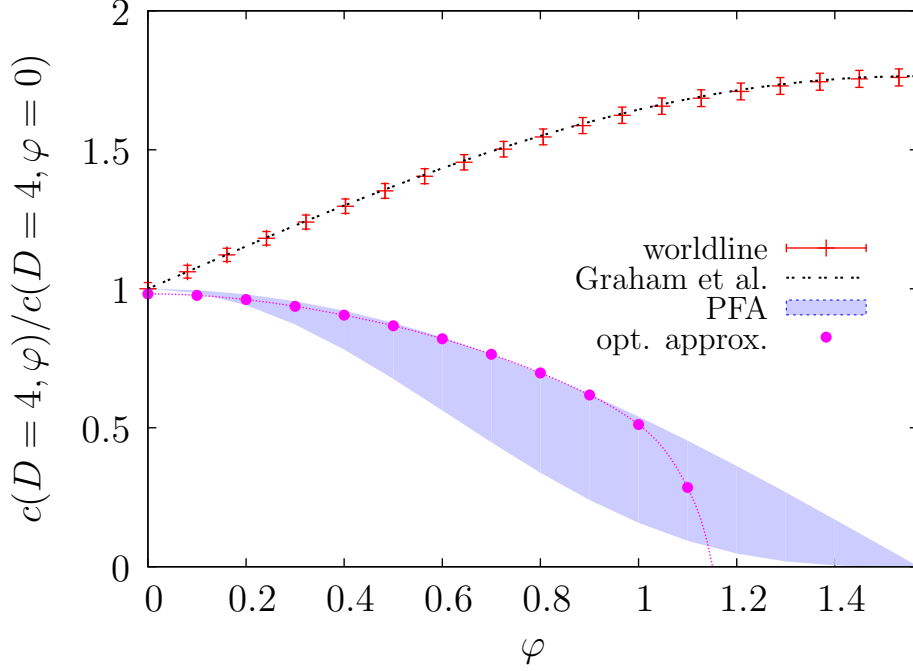
Figure 4.8: Normalized inclined plates coefficient $c(D, \varphi)$ for $D = 4$ versus the angle of inclination for different approximation schemes. Our worldline data nicely agrees with the Graham et al. solution [136] (double dashed black line). The blue area corresponds to the PFA prediction: for the upper bound, we have used the infinite plate as a basis, for the lower bound the semi infinite plate, yielding $\cos(\varphi)$ and $\cos^3(\varphi)$ as bounding curves, respectively (see Sec. 4.2). For the optical approximation (pink circles), we have plotted the first four terms of the full result, which can be found in appendix B. We expect the full result to be slightly greater, such that the normalized coefficient becomes 1 for all curves at $\varphi = 0$. Surprisingly, in the optical approximation, the coefficient $c(4, \varphi)$ diverges for $\varphi \to \pi/2$, resulting in a vanishing coefficient for $\varphi \approx 1.15$ and an attractive Casimir force for $\varphi \gtrsim 1.15$. Around $\varphi = 0$, the optical approximation is very well described by the upper PFA bound. For the worldline points, we have used 50000 worldlines with $2.5 \cdot 10^6$ ppl each and have plotted the errorbars five times larger.

4.7 Inclined plates, $\varphi \to 0$ limit

It is instructive to study the limit of a semi-infinite plate parallel to an infinite plate (1si), $\varphi \to 0$, as it involves a subtle limiting process. Recalling the general considerations of [54, 56] for the 1si case, the total Casimir interaction energy decomposes into

$$E_{\mathrm{c}}^{\mathrm{1si}} = E_{\mathrm{c}}^{\mathrm{1si},\|} + E_{\mathrm{c}}^{\mathrm{1si,edge}}, \tag{4.36}$$

where $E_{\mathrm{c}}^{\mathrm{1si},\|}/A$ is the usual Casimir energy per unit area of two parallel plates Eq. (4.17), with A now being the area of the semi infinite plate. The so called edge energy $E_{\mathrm{c}}^{\mathrm{1si,edge}}$ measures the contribution that arises solely due to the presence of the edge.

In the limit $\varphi \to 0$, this decomposition is naturally achieved by inserting $\Theta_{\text{i.p.},\varphi=0}$ of Eq. (4.26) into Eq. (6.1) and performing the z integral first. This leads to

$$\frac{E_{\text{c}}^{\text{1si,edge}}}{L_y} = -\frac{1}{(4\pi)^{D/2}(D-2)a^{D-2}} \left\langle \int_{\boldsymbol{\gamma}_{x_{\min}}}^{\boldsymbol{\gamma}_{x_{\max}}} \mathrm{d}x \ \boldsymbol{\gamma}_{z_{\max}}(x)(x - \boldsymbol{\gamma}_{x_{\min}})^{D-2} \right\rangle. \quad (4.37)$$

This representation can straightforwardly be computed numerically. For $D = 4$, we find with $50\,000$ worldlines and $2.5 \cdot 10^6$ ppl

$$\frac{E_{\text{c}}^{\text{1si,edge}}}{L_y} = -\frac{c_{\text{edge}}(D=4)}{a^2} \quad (4.38)$$

$$= -\frac{2.63(1) \cdot 10^{-3}}{a^2}, \quad (4.39)$$

in agreement with $0.00262(1)$ in [54]. Within the scattering approach [136], the authors obtain 0.0025. However, their data suggests that the result should be rather greater and agree with Eq. (4.39), see Fig. 4.9.

Of course, for truly infinite plates, the edge effect being proportional to the length of the edge is completely negligible in comparison with $E_{\text{c}}^{\text{1si},\|}$, the latter being proportional to the area of the plates. However, dealing with finite plates, the edge effect contributes to the Casimir force, effectively increasing the plate's area [54].

Of course, the same result has to arise from the general inclined-plates formula Eq. (4.32) in the limit $\varphi \to 0$. However, this representation naively exhibits a divergence in this limit. To find the origin of the divergence, we decompose Eq. (4.32) into the parts corresponding to the edge effect $E_{\text{c}}^{\text{edge},\varphi}$ and the semi-infinite-plates energy $E_{\text{c}}^{\|,\varphi}$, characterized by the integrals

$$\int_{-\boldsymbol{\gamma}_{z_{\max}}(x)}^{0} \dots \ \mathrm{d}z \quad \text{and} \quad \int_{0}^{L_z/2} \dots \ \mathrm{d}z,$$

respectively . Here $L_z/2$ denotes the (infinite) length of the semi-infinite plate in z direction. The result for $E_{\text{c}}^{\text{edge},\varphi}$ reads

$$E_{\text{c}}^{\text{edge},\varphi} = -\frac{L_y}{(4\pi)^{D/2}(D-2)a^{D-2}} \left\langle \int_{\boldsymbol{\gamma}_{x_{\min}}}^{\boldsymbol{\gamma}_{x_{\max}}} \boldsymbol{\gamma}_{z_{\max}}(x)\boldsymbol{\gamma}_{\text{m}}^{D-2}(x)\mathrm{d}x \right\rangle, \quad (4.40)$$

which becomes $E_{\text{c}}^{\text{edge}}$ in Eq. (4.37) as $\varphi \to 0$; Eq. (4.40) is therefore valid for $\varphi = 0$.

4 Inclined plates at zero temperature

On the other hand, if we naively expand the result for $E_c^{\parallel,\varphi}$ for small φ, we obtain

$$E_c^{\parallel} \overset{?}{=} - \frac{\langle \lambda^D \rangle L_y}{(4\pi)^{D/2}(D-2)(D-1)Da^{D-2}\varphi}$$

$$+ \frac{\langle \lambda_x^{D-1} \gamma'_{x_{\min}}(\varphi=0) \rangle L_y}{(4\pi)^{D/2}(D-2)(D-1)a^{D-2}} + \mathcal{O}(\varphi), \qquad (4.41)$$

which is only valid for $\varphi \neq 0$ and does not reproduce Eq. (4.16) in the limit $\varphi \to 0$. (We argue in the end of this subsection that the second term is zero.)

Instead of the energy per area, we have obtained the energy per length, which of course diverges in this limit. In order to rediscover the Casimir energy for the 1si configuration, the limits $\varphi \to 0$ and the implicit limit $L_z \to \infty$ have to be taken in the right order. In Eq. (4.41), the limit $L_z \to \infty$ has implicitly been performed first, which precisely leads to the divergence of the energy per edge length. Therefore, we need to first perform the limit $\varphi \to 0$ at finite L_z in order to obtain the desired energy per area. Starting from $E_c^{\parallel,\varphi}$ at small φ,

$$E_c^{\parallel,\varphi \to 0} = -\frac{L_y}{2(4\pi)^{D/2}} \left\langle \int_0^\infty \frac{\mathrm{d}\mathcal{T}}{\mathcal{T}^{(D+1)/2}} \int_0^{L_z/2} \mathrm{d}z \right.$$

$$\left. \times \int_{\gamma_{x_{\min}}}^{\gamma_{x_{\max}}} \mathrm{d}x\, \theta\left(-a + \sqrt{\mathcal{T}}x - z\varphi - \sqrt{\mathcal{T}}\gamma_{x_{\min}}\right) \right\rangle, \qquad (4.42)$$

we do the $\mathcal{T}$ integral *first* and obtain

$$E_c^{\parallel,\varphi \to 0} = -\frac{L_y \langle \lambda^D \rangle (a^{2-D} - (a + L_z\varphi/2)^{2-D})}{(4\pi)^{D/2}(D-2)(D-1)D\varphi}. \qquad (4.43)$$

For small $(L_z\varphi)$, i.e., finite L_z and $\varphi \to 0$, we can expand the last factor in φ,

$$E_c^{\parallel,\varphi \to 0} \cong -\frac{L_y \langle \lambda^D \rangle}{(4\pi)^{D/2}(D-1)D} \left(\frac{1}{2}a^{1-D}L_z - \frac{1}{8}a^{-D}(D-1)L_z^2\varphi \right), \qquad (4.44)$$

which for $\varphi \equiv 0$ corresponds exactly to the parallel-plates contribution $E_c^{1\mathrm{si},\parallel}$ in Eq. (4.16). From Eq. (4.43), we also observe that the other order of limits, taking first $L_z \to \infty$ while keeping φ finite, reproduces the divergent behavior of the energy per edge length in Eq. (4.41) (as long as $\mathrm{Re}[D] > 2$). The proper order of limits is similarly important at finite temperature with the additional complication that another dimensionful parameter occurs.
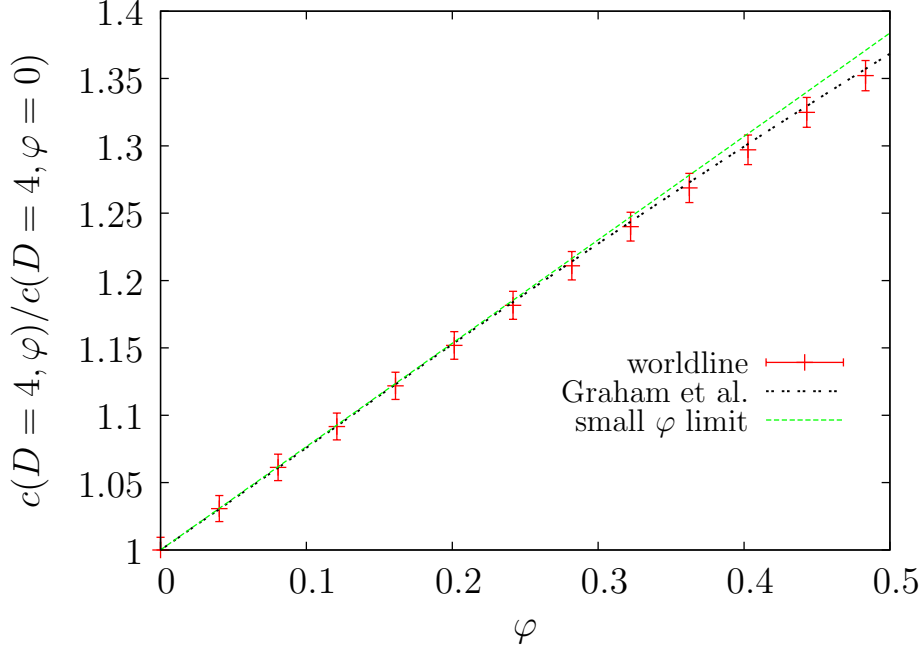
Figure 4.9: Normalized inclined plates coefficient $c(D, \varphi)$ for $D = 4$ versus the angle of inclination in the vicinity of $\varphi = 0$. The small φ limit (dashed green line) was calculated using the Eq. (4.48), resulting in $1 + 2 \left(c_{\text{edge}}(4)/c_{\parallel}(4) \right) \varphi \approx 1 + 0.767\,\varphi$. This limit agrees with the Graham et al. solution [136] (double dashed black line) and our worldline data, which verifies Eq. (4.48). We have used 50000 worldlines with $2.5 \cdot 10^6$ ppl each and have plotted the errorbars two times larger.

Let us return to Eq. (4.41). In the following, we argue that its second term vanishes. Note that

$$\gamma'_{x_{\min}}(\varphi = 0) = \gamma_{z_{\min}}(\gamma_{x_{\min}}). \tag{4.45}$$

As $\gamma_{z_{\min}}(\gamma_{x_{\min}})$ is the z coordinate of the worldline at the very left end, its average is zero by symmetry arguments,

$$\langle \gamma_{z_{\min}}(\gamma_{x_{\min}}) \rangle = 0. \tag{4.46}$$

Since the extent in x-direction λ_x of a worldline and its z coordinate at the left end, $\gamma_{z_{\min}}(\gamma_{x_{\min}})$, are uncorrelated, it follows that

$$\langle \lambda_x^{D-1} \gamma_{z_{\min}}(\gamma_{x_{\min}}) \rangle = \langle \lambda_x^{D-1} \rangle \langle \gamma_{z_{\min}}(\gamma_{x_{\min}}) \rangle = 0, \tag{4.47}$$

such that the $\mathcal{O}(\varphi)$ correction to Eq. (4.35) consists only of the edge effect. We conclude that for small φ, the coefficient $c(D, \varphi)$ in (4.33) can be written as

$$c(D, \varphi) = \frac{c_{\parallel}(D)}{D - 2} + c_{\text{edge}}(D)\varphi + \mathcal{O}(\varphi^2). \tag{4.48}$$

The coefficient $c(D, \varphi)$ and the expansion (4.48) are shown for small φ and $D = 4$ in Fig. 4.9 together with the Graham et al. solution [136].
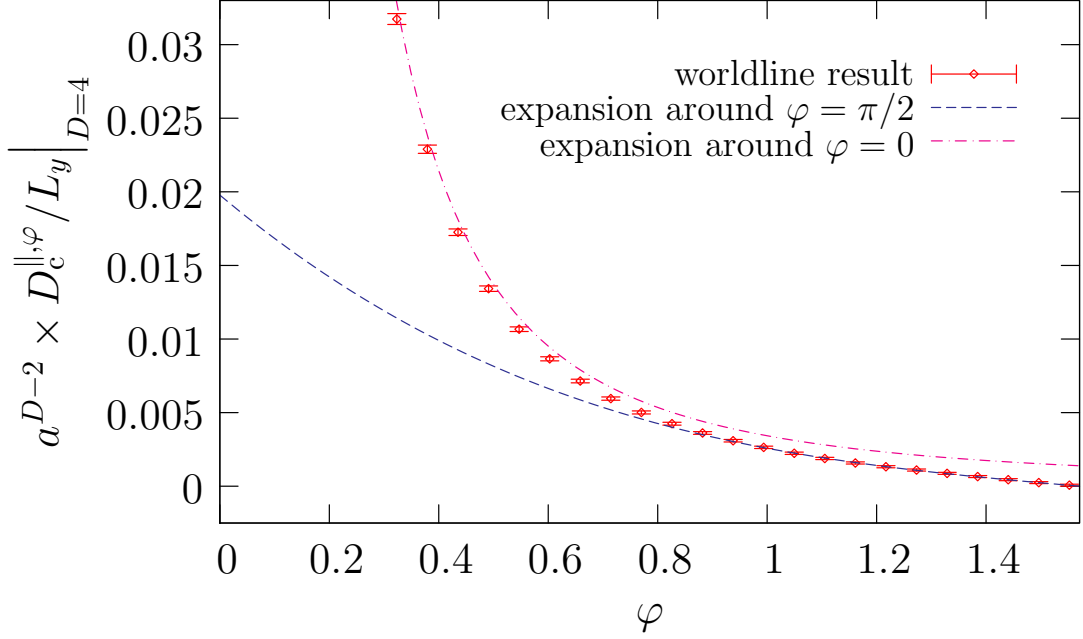
Figure 4.10: Normalized Casimir torque per edge length $\frac{D_c^{\text{i.p.},\varphi}}{L_y} \times a^{D-2}$ of the inclined-plates configuration in $D = 4$ and its expansion around $\varphi = \pi/2$ (Eq. (4.50)) and $\varphi = 0$ (Eq. (4.51)), respectively, versus the angle of inclination φ. We have used 10000 worldlines with 10^6 ppl each.

4.8 Casimir torque of inclined plates

The Casimir torque $D_c^{\text{i.p.},\varphi}$, referring to rotations of one of the plates about the edge axis, can easily be obtained by taking the derivative of the Casimir energy (4.32), (or Eq. (4.43) for small φ), with respect to the angle of inclination:

$$D_c^{\text{i.p.},\varphi} = \frac{\mathrm{d}E_c^{\text{i.p.},\varphi}}{\mathrm{d}\varphi}. \tag{4.49}$$

For φ near $\pi/2$, we can even set $\mathrm{d}\boldsymbol{\gamma}_{x_{\min}}(\varphi)/\mathrm{d}\varphi = 0$ before taking the average with respect to the loop ensemble, simplifying the calculations. This is, because the derivative $\mathrm{d}\boldsymbol{\gamma}_{x_{\min}}(\varphi)/\mathrm{d}\varphi$ changes its sign for perpendicular plates $\varphi = \pi/2$ if the worldline is rotated by an angle π about the normal axis of the lower plate, see Fig. 4.6. Therefore, the sign correlates with the position of the minimum on the x axis of the lower plate. But the position x of the minimum $\boldsymbol{\gamma}_{x_{\min}}(\varphi)$ does not correlate with the value of the integral in Eq. (4.32) leading to a mutual cancellation of terms involving $\mathrm{d}\boldsymbol{\gamma}_{x_{\min}}(\varphi)/\mathrm{d}\varphi$.

For $\varphi < \pi/2$, we have to rotate the worldline about the normal axis of the inclined lower plate. Then, the correlation between the position of the minimum

and the involved integrals does not vanish any more since the original and rotated worldline contribute differently to the integral.

In general, expressions containing derivatives of $\boldsymbol{\gamma}_{x_{\min}}(\varphi)$ cannot be neglected even at $\varphi = \pi/2$. Since the worldlines are not smooth, the convergence of averages of such expressions will be very slow. This is the case when calculating the coefficients of an expansion of Eq. (4.49) near $\varphi = \pi/2$. Since the second derivative already appears in the first expansion coefficient, more confident values are obtained by a numerical fit to Eq. (4.49). There, only the first derivative is present.

For $D = 4$, we obtain (see Fig. 4.10)

$$\frac{D_{\mathrm{c}}^{\mathrm{i.p.},\varphi\to\pi/2}a^2}{L_y} \approx 0.00329(5)\left(\frac{\pi}{2} - \varphi\right) + 0.0038(5)\left(\frac{\pi}{2} - \varphi\right)^3. \tag{4.50}$$

This should be compared to the worldline average based on the expansion of Eq. (4.49) around $\pi/2$: the linear coefficient in Eq. (4.50) then yields 0.003 ± 0.0002. If we neglect all derivatives of $\boldsymbol{\gamma}_{x_{\min}}(\varphi)$ the worldline result reads 0.00285 ± 0.00003. In all three cases 10000 worldlines with 10^6 ppl were used.

For $\varphi \to 0$, the Casimir torque diverges. The expansion about $\varphi = 0$ can easily be obtained analytically from (4.43)

$$D_{\mathrm{c}}^{\mathrm{i.p.},\varphi\to 0} \cong \frac{L_y\Gamma(D/2)\zeta(D)}{(4\pi)^{D/2}(D-2)a^{D-2}\varphi^2}, \tag{4.51}$$

where we have used Eq. (4.18). For $D = 4$, Eq. (4.51) yields

$$\frac{\pi^2 L_y}{2880\,a^2\varphi^2} \approx 0.00343\frac{L_y}{a^2\varphi^2},$$

being excellent approximation to Eq. (4.49) for φ not too close to $\pi/2$.

The divergent Casimir torque per length can be converted into finite torque per unit area by means of Eq. (4.43). Note that Eq. (4.43) leads to the classical result for the torque,

$$D_{\mathrm{c}}^{\|,\varphi\to 0} = \frac{AL_z\Gamma(D/2)\zeta(D)(D-1)}{2(4\pi)^{D/2}a^D}, \tag{4.52}$$

where A and L_z denote the semi-infinite plate's area and extent in z direction, respectively.

For $D = 4$, Eq. (4.52) becomes

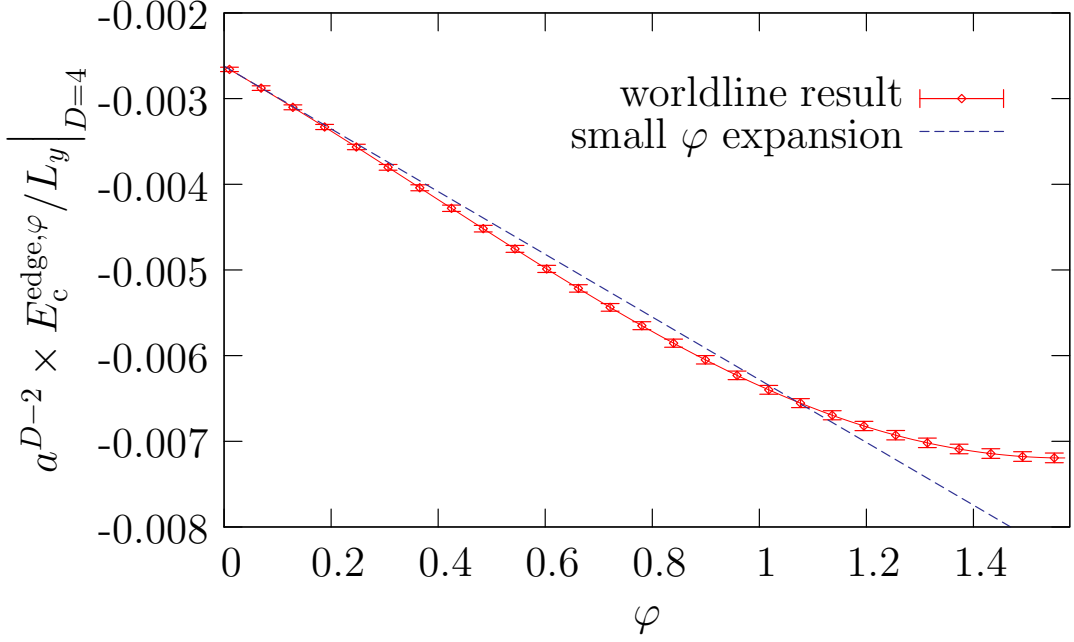$$\frac{AL_z\pi^2}{960\,a^4} \approx 0.0103\frac{AL_z}{a^4}.$$

Figure 4.11: Normalized edge energy per edge length $\frac{E_c^{\mathrm{edge},\varphi}}{L_y} \times a^{D-2}$ of the inclined-plates configuration in $D = 4$ and its expansion around $\varphi = 0$ versus the angle of inclination φ. We have used 10000 worldlines with 10^6 ppl each.

A new characteristic contribution emerges from the edge effect Eq. (4.40). Unlike the total inclined-plate Casimir energy

$$E_{\mathrm{c}}^{\mathrm{i.p.},\varphi} = E_{\mathrm{c}}^{\parallel,\varphi} + E_{\mathrm{c}}^{\mathrm{edge},\varphi},$$

the edge energy (4.40) decreases with the angle of inclination φ, see Fig. 4.11. This leads to a contribution which works against the standard torque (4.52).

For $D = 4$, the correction to Eq. (4.52) emerging from the edge effect reads

$$D_{\mathrm{c}}^{\mathrm{edge},\varphi \to 0} = -3.66(4) \cdot 10^{-3} \, \frac{L_y}{a^2}, \tag{4.53}$$

where we have used 10000 worldlines with 10^6 ppl each. The coefficient in Eq. (4.53) was calculated by expanding Eq. (4.40) around $\varphi = 0$. Equation (4.53) is shown in Fig. 4.11. We will see a similar subleading repulsive torque effect in the next section, where we investigate finite-temperature contributions.

4.9 Conclusions and summary of results in $D = 4$

In this chapter, we have presented a systematic treatment of the Casimir effect for the inclined plates geometry in D dimensions and at zero temperature. We have developed efficient worldline numerical algorithms that allow a fast calculation of all relevant physical quantities. We have also related the Casimir effect to simple geometric properties of worldlines.

Our worldline results nicely agree with a recent solution using scattering theory [136]. Also the special case of perpendicular plates and of semi-parallel plates confirms previous worldline studies [54, 56]. On the other hand, the widely used proximity force approximation is found to be valid to leading order in φ only. The other approximate scheme, the optical approximation, is very much similar to the PFA at small φ and becomes invalid for larger inclinations.

We will study the Casimir effect at finite temperature for the inclined plates configuration in the next chapter.

Let us summarize our most important results, specializing to $3 + 1$ dimensional spacetime and concentrating on the Casimir interaction energy; the corresponding force can straightforwardly be derived by differentiation. At zero temperature, the classical Casimir energy of two parallel Dirichlet plates at a distance a reads

$$\frac{E_c^{\parallel}}{A} = -\frac{c_{\parallel}\hbar c}{a^3}, \quad c_{\parallel} = \frac{\pi^2}{1440} \approx 0.00685, \tag{4.54}$$

where A is the area of the plates. We use natural units, setting $\hbar = c = 1$. The Casimir energy of inclined plates (i.p.) can be parameterized as

$$\frac{E_c^{\text{i.p.},\varphi}}{L_y} = -\frac{c(D = 4, \varphi)}{\sin(\varphi) \, a^2}, \tag{4.55}$$

where the coefficient $c(4, \varphi)$ is shown in Fig. 4.8 as a function of φ. The extent of the inclined plate in y direction along the edge is L_y.

For small φ, the coefficient $c(4, \varphi)$ can be written as

$$c(4, \varphi) = \frac{c_{\parallel}(4)}{2} + c_{\text{edge}} \, \varphi + \mathcal{O}(\varphi^2). \tag{4.56}$$

For all φ the coefficient $c(D = 4, \varphi)$ nicely agrees with the the Graham et al. solution [136].

At $\varphi = 0$, the energy per edge length (4.55) diverges and has to be replaced by

$$E_c^{\text{1si}} = E_c^{\text{1si},\parallel} + E_c^{\text{1si,edge}} = -\frac{A^{\text{1si}}c_{\parallel}}{a^3} - \frac{L_y c_{\text{edge}}}{a^2}, \tag{4.57}$$

where $E_c^{1si,\parallel}$ is the Casimir Energy (4.54) with A^{1si} being the semi-infinite plate's area and $E_c^{1si,edge}$ the so-called edge energy. The numerical value of c_{edge} is 0.00263(1) in agreement with [54, 56, 136].

The Casimir torque is obtained from Eq. (4.55) by

$$D_c^{i.p.,\varphi} = \frac{dE_c^{i.p.,\varphi}}{d\varphi}. \tag{4.58}$$

For $D = 4$, the torque $D_c^{i.p.,\varphi}$ as a function of φ is shown in Fig. 4.10. At $\varphi = 0$, the Casimir torque per unit length diverges as well but can be converted into finite torque per unit area. Remarkably, for $\varphi = 0$ the standard torque obtained from the Casimir energy of parallel plates (4.54)

$$D_c^{\parallel} = \frac{AL_z\pi^2}{960a^4} \approx 0.0103 \frac{AL_z}{a^4} \tag{4.59}$$

is reduced by a repulsive contribution $\approx -0.003660 L_y/a^2$ arising from the edge effect.

5 Inclined plates at finite temperature

In this chapter, we continue our analysis of the Casimir effect for the inclined plates induced by a fluctuating real scalar field obeying Dirichlet boundary conditions ("Dirichlet scalar") by extending the formalism to finite temperatures. Whereas the high-temperature behavior is always found to be linear in T in accordance with dimensional-reduction arguments, different power-law behaviors at small temperatures emerge due to the geometry-temperature interplay. We refer to this interplay as geothermal phenomena. Unlike the case of infinite parallel plates, which shows the well-known T^D behavior of the force, we find a T^{D-1} behavior for inclined plates. In the limit where the plates become parallel, the behavior of the edge effect is found to be in between T^{D-1} and T^D. The strongest temperature dependence $\sim T^{D-2}$ occurs for the Casimir torque of inclined plates. Numerical as well as analytical worldline results are presented. The results of this chapter were published in [57, 58].

5.1 Introduction

A distinctive feature of Casimir forces between test bodies is the dependence on the geometry, i.e., the shape and orientation of these bodies. For a comparison between theory and a real Casimir experiment, a number of properties such as finite conductivity, surface roughness and finite temperature have to be taken into account in addition. Generically, these latter corrections do not factorize but influence each other.

For instance, the interplay between dielectric material properties and finite temperature [139] is still a subject of intense theoretical investigations and has created a long-standing controversy [140–143]. Also the role of electrostatic patch potentials has been suggested as a potentially problematic issue [144, 145], which has become a matter of severe debate [146, 147].

Here, we do not mean to resolve these controversies. On the contrary, this work intends to draw attention to another highly nontrivial interplay which on the one hand needs to be accounted for when comparing theory and a real experiment and on the other hand is another characteristic feature of the Casimir effect: the interplay between geometry and temperature.

As first conjectured by Jaffe and Scardicchio [36], the temperature dependence of the Casimir effect can be qualitatively different for different geometries, as both the pure Casimir effect as well as its thermal corrections arise from the underlying spectral properties of the fluctuations. First analytical as well as numerical evidence of this "geothermal" interplay in a perpendicular-plates configuration has been found in [55] using the worldline formalism.

The physical reason for this interplay can be understood in simple terms (also see Sec. 1.2): for the classical parallel-plate case, the nontrivial part of the fluctuation spectrum is given by the modes orthogonal to the plates. This relevant part of the spectrum has a gap of wave number $k_{\mathrm{gap}} = \pi/a$, where a is the plate separation. For small temperatures $T \ll k_{\mathrm{gap}}$, the higher-lying relevant modes can hardly be excited, such that their thermal contribution to the Casimir force remains suppressed: the resulting force law for the parallel-plates case scales like $(aT)^4$. This argument for a suppression of thermal contributions applies to all geometries with a gap in the relevant part of the spectrum (e.g. concentric cylinders or spheres, Casimir pistons, etc.). These geometries are called *closed*.[1]

This reason for a suppression of thermal contributions is clearly absent for *open* geometries with a relevant gapless part of the spectrum. For these geometries, relevant modes of the spectrum can always be excited at any small temperature value. Therefore, a stronger thermal contribution $\sim (aT)^\alpha$ with $\alpha < 4$ can be expected.[2] Since experimentally important configurations such as the sphere-plate or the cylinder-plate geometry belong to this class of open geometries, a potentially significant geometry-temperature interplay may exist in the relevant parameter range $aT \sim 0.01\ldots0.1$.

An illustrative example for open geometries is also the inclined plates configuration, which was studied in detail at zero temperature in the previous chapter.

---

[1]Of course, parallel plates as well as concentric cylinders are not closed in the sense of compactness. Also, they have a gapless part of the spectrum along the symmetry axes. However, this part of the spectrum does not give rise to the Casimir force and hence is not a relevant part.

[2]Since the thermal correction has to disappear for $T \to 0$, the exponent α must be positive, $\alpha > 0$. A better lower bound for α can be found using our general argument presented in Sec. 7.3, where we show that the thermal correction remains finite at finite temperatures. From this, we find $\alpha \geq D - 1$ for inclined plates using dimensional analysis.

This configuration turns out to be an ideal scenario for the investigation of the nontrivial geothermal interplay since the transition from open to closed geometries and the role of long-range fluctuations become particularly transparent.

A reliable study of "geothermal" Casimir phenomena requires a method that is capable of dealing with very general Casimir geometries. The worldline approach to the Casimir effect [37] is splendidly suitable for such investigations.

In order to overcome standard approximative tools based, e.g., on the proximity-force theorem [83], a variety of new field-theoretical methods for Casimir phenomena have been developed in recent years, ranging from improved approximation methods [36, 131, 138, 148, 149] to exact methods mainly based on scattering theory [65–82] or a functional integral approach [62–64]. It will certainly be worthwhile to generalize these methods to finite temperature for a study of the geometry-temperature interplay.

In this chapter, we extend our investigation of the Casimir effect for the inclined plates to finite temperatures. We work in $D = d + 1$ dimensional spacetime, yielding many analytical as well as numerical results for the Casimir force and energy as well as for the torque. We demonstrate that the worldline approach can also be used to obtain novel analytical results (see also [61] for an analytical worldline approximation technique).

5.2 Worldline numerics for finite temperatures

Let us briefly review the worldline approach [37] to the Casimir effect as it is needed for the present line of argument; for details of the formalism, see chapter 3. We consider a fluctuating massless scalar field satisfying Dirichlet boundary conditions on the Casimir surfaces. For a configuration Σ consisting of two static surfaces Σ_1 and Σ_2, the worldline representation of the Casimir interaction energy reads

$$E_c = -\frac{1}{2(4\pi)^{D/2}} \int_0^\infty \frac{\mathrm{d}\mathcal{T}}{\mathcal{T}^{1+D/2}} \int \mathrm{d}^d x_{\mathrm{CM}} \left\langle \Theta_\Sigma[\mathbf{x}(\tau)] \right\rangle, \qquad (5.1)$$

where $D = d + 1$ denotes the spacetime dimensions. The worldline functional obeys $\Theta_\Sigma[\mathbf{x}] = 1$ if a worldline $\mathbf{x}(\tau)$ intersects both surfaces $\Sigma = \Sigma_1 \cup \Sigma_2$, and is zero otherwise.

The expectation value in Eq. (5.1) is taken with respect to an ensemble of d-dimensional closed Gaußian worldlines with center of mass $\mathbf{x}_{\mathrm{CM}}$. In Eq. (5.1), the Θ functional removes from the ensemble of allowed fluctuations all worldlines intersecting both surfaces. These fluctuations do not satisfy Dirichlet boundary

conditions on both surfaces and thus contribute to the negative Casimir interaction energy.

The worldlines in Eq. (5.1) are already rescaled such that the velocity distribution is independent of $\mathcal{T}$. We then have

$$\mathbf{x}(\tau) = \mathbf{x}_{\mathrm{CM}} + \sqrt{\mathcal{T}}\,\boldsymbol{\gamma}(\tau).$$

The auxiliary propertime parameter $\mathcal{T}$ scales the extent of a worldline by a factor of $\sqrt{\mathcal{T}}$. Large $\mathcal{T}$ correspond to long-range, small $\mathcal{T}$ to short-range fluctuations.

Finite temperature

$$T = \frac{1}{\beta}$$

in the Matsubara formalism is equivalent to a compactified Euclidean time on the interval $[0, \beta]$. The worldlines now live on $S^1 \times \mathbb{R}^d$ and can carry a winding number. Summing over all winding numbers, the Casimir free energy (5.1) becomes

$$E_{\mathrm{c}} = -\frac{1}{2(4\pi)^{D/2}} \int_0^\infty \frac{\mathrm{d}\mathcal{T}}{\mathcal{T}^{1+D/2}} \left(1 + 2\sum_{n=1}^\infty e^{-\frac{n^2\beta^2}{4\mathcal{T}}}\right) \int \mathrm{d}^d x_{\mathrm{CM}} \left\langle \Theta_\Sigma[\mathbf{x}(\tau)] \right\rangle. \quad (5.2)$$

Dealing with finite temperature, therefore, leads to an additional winding-number prefactor in front of the worldline expectation value for static configurations.

Decomposing the Casimir energy at finite temperature $T = 1/\beta$ into its zero-temperature part $E_{\mathrm{c}}(0)$ and finite-temperature correction $\Delta E_{\mathrm{c}}(T)$,

$$E_{\mathrm{c}}(T) = E_{\mathrm{c}}(0) + \Delta E_{\mathrm{c}}(T), \quad (5.3)$$

is straightforward in the worldline picture by using the relation (5.2). The finite-temperature correction is purely driven by the worldlines with nonzero winding number.

As the winding-number sum does not take direct influence on the worldline averaging, the complicated geometry-dependent part of the calculation remains the same for zero or finite temperature. This disentangles the technical complications arising from geometry on the one hand and temperature on the other hand in a convenient fashion. The same statement holds for the Casimir force

$$F_{\mathrm{c}}(T) = F_{\mathrm{c}}(0) + \Delta F_{\mathrm{c}}(T).$$

For convenience, we show the inclined-plates (i.p.) configuration again in Fig. 5.1. We recall that it consists of a perfectly thin semi-infinite plate above an infinite plate at an angle φ. The infinite plate has a $(d-1)$ dimensional area A and the
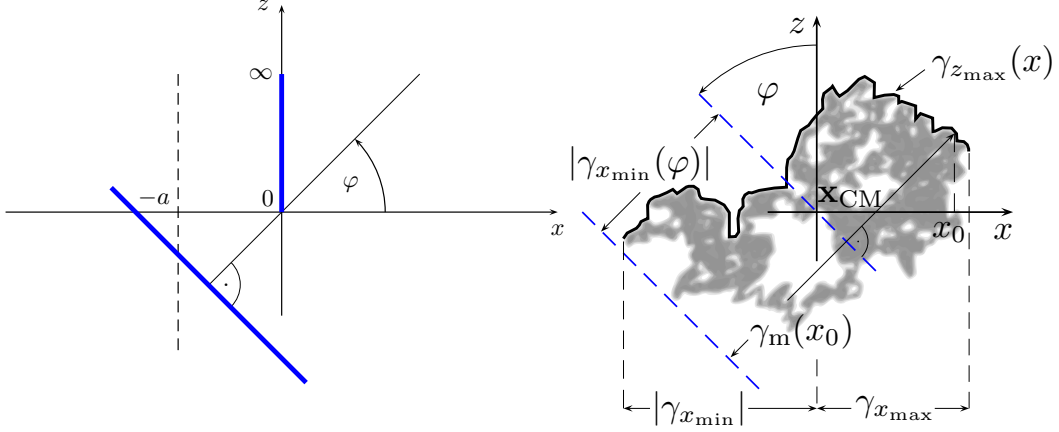
Figure 5.1: Left panel: sketch of the inclined-plates configuration. The infinite plate (dashed line) is rotated in the x, z plane by an angle φ. As special cases, $\varphi = 0$ corresponds to the configuration of one semi-infinite plate parallel to an infinite plate (1si configuration), whereas $\varphi = \pi/2$ yields the perpendicular-plates configuration. Right panel: all relevant information for the evaluation of the Casimir energy (4.32) of inclined plates is encoded in the function $\gamma_m(x)$, which has to be integrated from $\gamma_{x_{\min}}$ to $\gamma_{x_{\max}}$.

semi-infinite plate a $(d-2)$ dimensional edge with a length L_y. The minimal separation between the plates is a.

As we have found in the last chapter, the Casimir effect for this configuration can be understood in terms of simple geometric properties of the worldlines. All relevant information of a worldline needed for the evaluation of the Casimir energy is also shown in Fig. 5.1.

5.3 Parallel plates

In order to demonstrate the simplicity of the worldline method, let us calculate the well-known thermal contribution to the Casimir effect for parallel plates. In the following, we use the dimensionless parameter

$$\xi \equiv aT, \tag{5.4}$$

which distinguishes between the high-temperature $\xi \gg 1$ and low-temperature $\xi \ll 1$ parameter region.

Evaluating the general worldline formula for the Casimir energy Eq. (5.2) using the parallel-plates Θ functional of Eq. (4.9) results in

$$\frac{\Delta E_c^{\parallel}(T)}{A} = -\frac{1}{(4\pi)^{D/2} a^{D-1}} \sum_{n=1}^{\infty} \left\langle \lambda^D \int_1^{\infty} d\mathcal{T} \frac{\sqrt{\mathcal{T}} - 1}{\mathcal{T}^{1+D/2}} \exp\left(\frac{-n^2 \lambda^2}{4\xi^2 \mathcal{T}}\right) \right\rangle, \tag{5.5}$$

where and λ again denotes the maximum extent of the worldline in the direction orthogonal to the plates. Doing the propertime integral, we obtain

$$\int_1^\infty \mathrm{d}\mathcal{T} \, \frac{\sqrt{\mathcal{T}}-1}{\mathcal{T}^{1+D/2}} \exp\left(-\frac{n^2\lambda^2}{4\xi^2\mathcal{T}}\right) = \left(\frac{2\xi}{\lambda n}\right)^{D-1} \Gamma\left(\frac{D-1}{2}\right) - \left(\frac{2\xi}{\lambda n}\right)^D \Gamma\left(\frac{D}{2}\right)$$

$$+ E_{1-\frac{D}{2}}\left(\frac{\lambda^2 n^2}{4\xi^2}\right) - E_{\frac{3}{2}-\frac{D}{2}}\left(\frac{\lambda^2 n^2}{4\xi^2}\right), \quad (5.6)$$

where the exponential integral function $E_n(z)$ is given by

$$E_n(z) \equiv \int_1^\infty \frac{e^{-zt}}{t^n} \, \mathrm{d}t. \tag{5.7}$$

For $D > 2$ the sums over n converge. Normalizing the thermal correction to the zero temperature result yields

$$\frac{\Delta E_{\mathrm{c}}^{\parallel}(\xi)}{E_{\mathrm{c}}^{\parallel}(0)} = \frac{\Gamma\left(\frac{D-1}{2}\right)\sqrt{\pi}\zeta(D-1)(2\xi)^{D-1}}{\Gamma(D/2)\zeta(D)} - (2\xi)^D$$

$$+ \left\langle \sum_{n=1}^\infty \frac{\lambda^D}{\Gamma(D/2)\zeta(D)}\left[E_{1-\frac{D}{2}}\left(\frac{\lambda^2 n^2}{4\xi^2}\right) - E_{\frac{3}{2}-\frac{D}{2}}\left(\frac{\lambda^2 n^2}{4\xi^2}\right)\right]\right\rangle. \tag{5.8}$$

In the low-temperature limit,

$$2\xi \ll \sqrt{\langle\lambda^2\rangle} = \pi/\sqrt{3} \approx 1.8, \tag{5.9}$$

the exponential integral functions vanish exponentially and can be neglected.[3] We then obtain the small-temperature correction to $E_{\mathrm{c}}^{\parallel}(T=0)$ in D dimensions fully analytically:

$$\frac{\Delta E_{\mathrm{c}}^{\parallel}(\xi \to 0)}{E_{\mathrm{c}}^{\parallel}(0)} = \frac{\Gamma\left(\frac{D-1}{2}\right)\sqrt{\pi}\zeta(D-1)(2\xi)^{D-1}}{\Gamma(D/2)\zeta(D)} - (2\xi)^D. \tag{5.10}$$

The term $(2\xi)^D$ agrees with the standard textbook result [6]. It dominates the thermal correction to the Casimir force, yielding a comparatively suppressed power law dependence on the temperature for small T

$$\Delta F_{\mathrm{c}}^{\parallel}(T) \sim T^D.$$

This is an immediate consequence of the gap in the relevant part of the fluctuation spectrum in this closed geometry. This term can also be understood as an
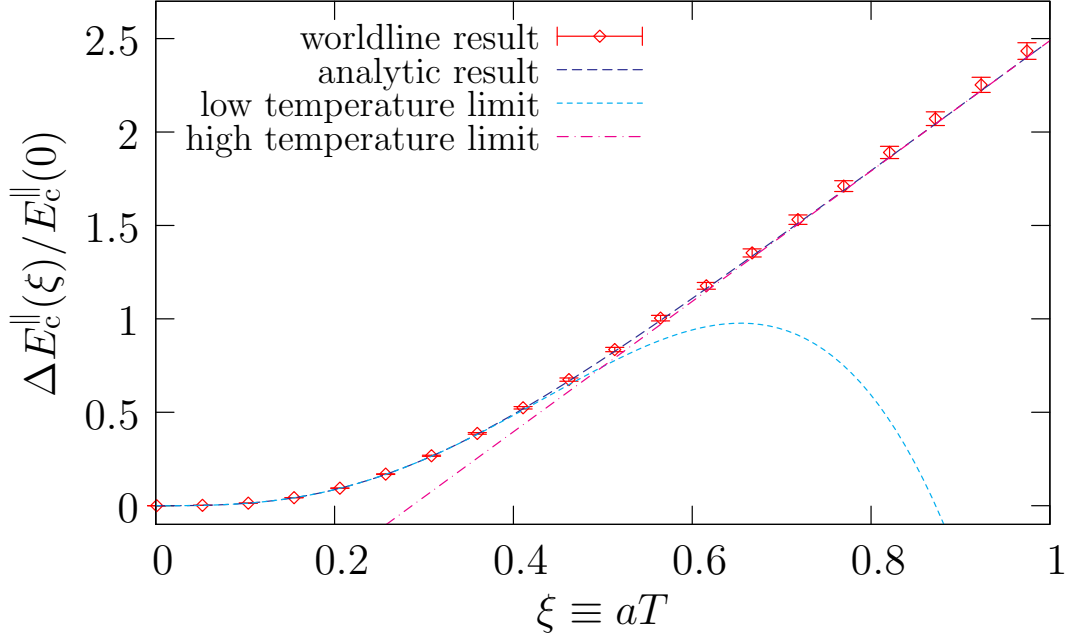
Figure 5.2: Parallel plates: temperature dependence of the thermal contribution to the Casimir energy $\Delta E_c^{\parallel}(\xi)/E_c^{\parallel}(0)$ normalized to the zero-temperature result in $D = 4$-dimensional space-time versus the dimensionless temperature variable $\xi = aT$. The worldline result for 1000 worldlines with 2×10^6 points each is plotted together with the analytic expressions (5.10)-(5.12).

excluded-volume effect: the volume in between the plates cannot be thermally populated by photons at low temperature due to the spectral gap.

Incidentally, the leading contribution to the energy $\sim \xi^{D-1}$ is much less known. It does not contribute to the Casimir force, since it is independent of a when multiplied by the normalization prefactor $E_c^{\parallel}(0)$. As we will see in section 5.4, a-independent terms in the energy should not be viewed as mere calculational artefacts but can also contribute to observables such as the Casimir torque. To the best of our knowledge, Eq. (5.10) represents the first exact analytic formula for this leading small temperature correction to the free energy.

The high-temperature limit of (5.8) can be obtained by a Poisson resummation of the winding-number sum (which is identical to returning to Matsubara

---

[3]Actually, the low temperature limit is already obtained for $\xi \lesssim 0.5$, see Fig. 5.8. Above $\xi \approx 0.5$, the behavior is given by the high temperature limit.

frequency space). Our result agrees with [6] and reads:

$$\frac{\Delta E_c^\parallel(\xi \to \infty)}{E_c^\parallel(0)} = -1 + \frac{2\Gamma\left(\frac{D-1}{2}\right)\zeta(D-1)\sqrt{\pi}}{\Gamma(D/2)\zeta(D)}\xi. \tag{5.11}$$

For arbitrary ξ and $D > 2$, Eq. (5.8) can be evaluated numerically. Figure 5.2 shows the worldline result together with the analytic asymptotics (5.10), (5.11) and the known exact analytic formula for $D = 4$, see e.g. [150]:

$$\frac{\Delta E_c^\parallel(\xi)}{E_c^\parallel(0)} = -1 + \frac{90\xi}{\pi^3}\sum_{n=1}^{\infty}\frac{\coth(2n\pi\xi) + 2n\pi\xi\,\operatorname{csch}^2(2n\pi\xi)}{n^3}. \tag{5.12}$$

Note that the result obtained in [150] for the electromagnetic field is twice as large as the result for the scalar field (5.12).

Of course, taking the derivative of (5.8), (5.10) or (5.11) with respect to a also gives immediate access to the thermal corrections $\Delta F_c^\parallel(T)$ to the Casimir force

$$\frac{\Delta F_c^\parallel(\xi)}{A} = -\frac{\zeta(D)\Gamma(D/2)}{\pi^{D/2}}T^D + \frac{1}{(4\pi)^{D/2}a^D}\left\langle \lambda^D\sum_{n=1}^{\infty}E_{1-D/2}\left(\frac{\lambda^2 n^2}{4\xi^2}\right)\right\rangle, \tag{5.13}$$

such that for instance the low-temperature limit results in

$$\Delta F_c(aT \ll 1) = -\frac{\Gamma(D/2)\zeta(D)A}{\pi^{D/2}}T^D, \tag{5.14}$$

again revealing the power-law suppressed temperature dependence which is characteristic for a closed geometry. Both magnitude and sign of the thermal force correction can be understood as an excluded-volume effect: as the temperature is small compared to the spectral gap, thermal modes in-between the plates cannot be excited. Hence, the thermal Stefan-Boltzmann energy density outside the plates is not balanced by a thermal contribution inside. Thermal effects therefore enhance the attractive force between the plates.

Let us finally remark that the comparison between the small-temperature limit of (5.12) (calculated with the help of the Poisson summation) and our analytic formula (5.10) closes a gap in the literature. With this comparison, we can find the exact value of the integral occurring in the prefactor of the leading low-temperature term in the energy,

$$\int_0^\infty \mathrm{d}x\frac{1}{2x^4}\left[-2 + x(\coth x + x\,\operatorname{csch}^2 x)\right] = \frac{\zeta(3)}{2\pi^2}, \tag{5.15}$$

numerically corresponding to ≈ 0.060897. This result has been observed numerically in the sum over odd reflection contributions to the parallel-plates Casimir energy in the optical approach to the Casimir effect [36].

5.4 Inclined plates

5.4.1 Casimir energy and force

Whereas the inclined-plate geometry is much more difficult to deal with than the parallel-plate case when using standard methods, there is comparatively little difference in the worldline language. Inserting the inclined-plates Θ functional (4.26) with

$$\boldsymbol{\gamma}_{\mathrm{m}}(x) \equiv x \cos(\varphi) + \sin(\varphi) \boldsymbol{\gamma}_{z_{\max}}(x) - \boldsymbol{\gamma}_{x_{\min}}(\varphi)$$

as in Eq. (4.31) into the general worldline formula (5.2) yields

$$E_{\mathrm{c}}^{\mathrm{i.p.},\varphi}(\xi) = E_{\mathrm{c}}^{\mathrm{i.p.},\varphi} + \Delta E_{\mathrm{c}}^{\mathrm{i.p.},\varphi}(\xi), \tag{5.16}$$

where $\Delta E_{\mathrm{c}}^{\mathrm{i.p.},\varphi}(\xi)$ is the thermal contribution to the energy. In order to calculate $\Delta E_{\mathrm{c}}^{\mathrm{i.p.},\varphi}(\xi)$, we proceed as in the last section. Doing the z integral as in (4.30) results in

$$\frac{\Delta E_{\mathrm{c}}^{\mathrm{i.p.},\varphi}}{L_y} = -\frac{\csc(\varphi)}{(4\pi)^{D/2} a^{D-2}} \left\langle \int_{\gamma_{x_{\min}}}^{\gamma_{x_{\max}}} \mathrm{d}x\, \boldsymbol{\gamma}_{\mathrm{m}}^{D-1}(x) \right.$$

$$\left. \times \sum_{n=1}^{\infty} \int_1^{\infty} \frac{\mathrm{d}\mathcal{T}(\sqrt{\mathcal{T}}-1)}{\mathcal{T}^{(1+D)/2}} \exp\left(-\frac{n^2 \boldsymbol{\gamma}_{\mathrm{m}}^2(x)}{4\xi^2 \mathcal{T}}\right) \right\rangle. \tag{5.17}$$

The propertime integral can be done analytically,

$$\int_1^{\infty} \frac{\mathrm{d}\mathcal{T}(\sqrt{\mathcal{T}}-1)}{\mathcal{T}^{(1+D)/2}} \exp\left(-\frac{n^2 \boldsymbol{\gamma}_{\mathrm{m}}^2(x)}{4\xi^2 \mathcal{T}}\right) =$$

$$\left(\frac{2\xi}{\boldsymbol{\gamma}_{\mathrm{m}}(x) n}\right)^{D-2} \Gamma\left(\frac{D-2}{2}\right) - \left(\frac{2\xi}{\boldsymbol{\gamma}_{\mathrm{m}}(x) n}\right)^{D-1} \Gamma\left(\frac{D-1}{2}\right)$$

$$+ E_{\frac{3}{2}-\frac{D}{2}}\left(\frac{\boldsymbol{\gamma}_{\mathrm{m}}^2(x) n^2}{4\xi^2}\right) - E_{2-\frac{D}{2}}\left(\frac{\boldsymbol{\gamma}_{\mathrm{m}}^2(x) n^2}{4\xi^2}\right), \tag{5.18}$$

such that the thermal contribution to the energy, $\Delta E_{\mathrm{c}}^{\mathrm{i.p.},\varphi}(\xi)$, can be written as

$$\Delta E_{\mathrm{c}}^{\mathrm{i.p.},\varphi}(\xi) = -\frac{L_y \csc(\varphi)}{(4\pi)^{D/2} a^{D-2}} \Bigg\{ \tag{5.19}$$

$$(2\xi)^{D-2} \zeta(D-2)\Gamma\left(\frac{D-2}{2}\right) \left\langle \int_{\gamma_{x\mathrm{min}}}^{\gamma_{x\mathrm{max}}} \mathrm{d}x \; \boldsymbol{\gamma}_{\mathrm{m}}(x) \right\rangle$$

$$- \zeta(D-1)\,(2\xi)^{D-1}\,\Gamma\left(\frac{D-1}{2}\right)\sqrt{\pi}$$

$$+ \left\langle \sum_{n=1}^{\infty} \int_{\gamma_{x\mathrm{min}}}^{\gamma_{x\mathrm{max}}} \mathrm{d}x \; \boldsymbol{\gamma}_{\mathrm{m}}^{D-1}(x) \left[E_{\frac{3}{2}-\frac{D}{2}}\left(\frac{\boldsymbol{\gamma}_{\mathrm{m}}^2(x)n^2}{4\xi^2}\right) - E_{2-\frac{D}{2}}\left(\frac{\boldsymbol{\gamma}_{\mathrm{m}}^2(x)n^2}{4\xi^2}\right) \right] \right\rangle \Bigg\}.$$

Here and in the following, we confine ourselves to spacetime dimensions $D > 3$, where all expressions exhibit well-controlled convergence.

In the low-temperature limit, the exponential integral functions can be neglected as long as $\boldsymbol{\gamma}_{\mathrm{m}}(x) \neq 0$ for all x. This is certainly the case for $\varphi \neq 0$, but not necessarily for $\varphi = 0$. The latter case is again identical to the semi-infinite plate parallel to an infinite one, and is being considered separately in the next sections.

For $\varphi \neq 0$, the low-temperature limit is then given by the first two terms (second and third line) of Eq. (5.19). Note that the first ξ^{D-2} term does not contribute to the Casimir force, since it is an a-independent contribution to E_{c} if read together with the normalization prefactor. This term is shown in Fig. 5.3. From the second term, we obtain the low-temperature thermal correction to the Casimir force upon differentiation with respect to a,

$$\Delta F^{\mathrm{i.p.},\varphi \neq 0} = -L_y \csc(\varphi) \frac{\Gamma\left(\frac{D-1}{2}\right)\zeta(D-1)}{2\pi^{(D-1)/2}} T^{D-1}. \tag{5.20}$$

The temperature dependence differs from the parallel-plates case by one power of T, implying a significantly stronger temperature dependence at small temperatures. This is a direct consequence of the fact that we are dealing with an open geometry. We emphasize that the result has been obtained fully analytically. In $D = 4$ and $\varphi = \pi/2$, our result agrees with the perpendicular-plates study of [55] where this nontrivial interplay between temperature and geometry has been demonstrated for the first time. As shown therein, the thermal correction for this open geometry at experimentally-relevant large separations can be an order of magnitude larger than for a closed geometry.

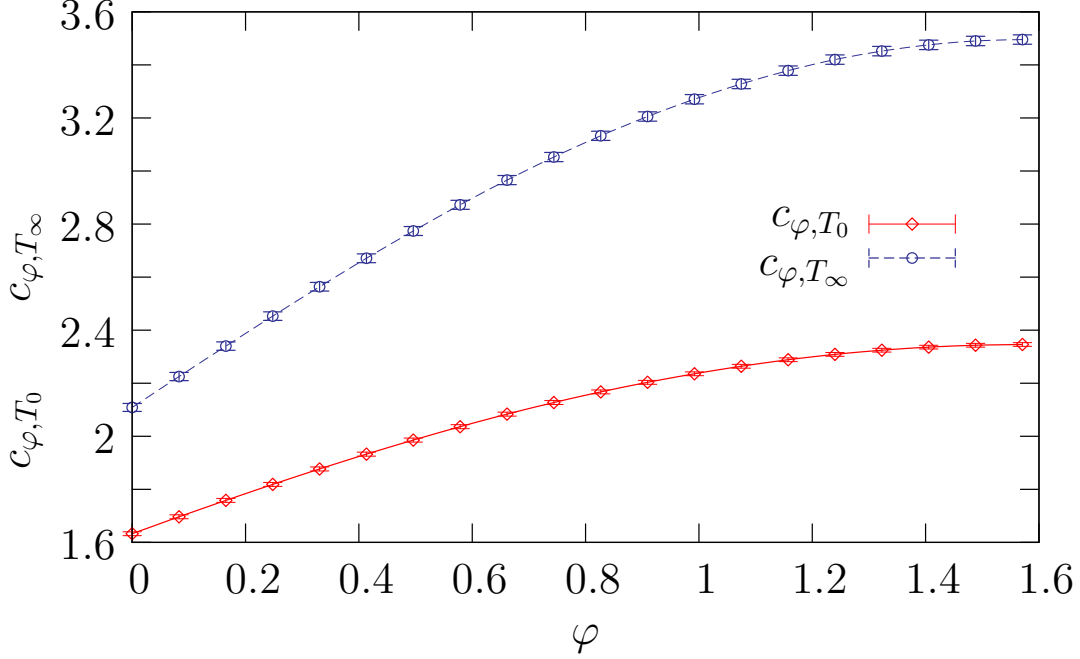For the sake of completeness we also give the full expression for the thermal

Figure 5.3: Integrals appearing in Eqs. (5.19) and (5.22) for $D = 4$. We have defined $c_{\varphi,T_0} \equiv \left\langle \int_{\gamma_{x_{\min}}}^{\gamma_{x_{\max}}} \mathrm{d}x \; \gamma_{\mathrm{m}}(x) \right\rangle$ and $c_{\varphi,T_\infty} \equiv \left\langle \int_{\gamma_{x_{\min}}}^{\gamma_{x_{\max}}} \mathrm{d}x \; \gamma_{\mathrm{m}}^2(x) \right\rangle$; see also Eqs. (5.70), (5.71) and (5.75). Employing Eq. (4.18), we can evaluate $c_{\varphi=0,T_0} = \zeta(2) \approx 1.645$ and $c_{\varphi=0,T_\infty} = \sqrt{\pi}\zeta(3) \approx 2.131$ analytically. We have used 10^4 worldlines with 10^6 ppl each.

correction to the Casimir force:

$$\Delta F^{\mathrm{i.p.},\varphi\neq0}(T) = - L_y \csc(\varphi) \frac{\Gamma\left(\frac{D-1}{2}\right)\zeta(D-1)}{2\pi^{(D-1)/2}} T^{D-1}$$

$$+ \frac{L_y \csc(\varphi)}{(4\pi)^{D/2}a^{D-1}} \sum_{n=1}^{\infty} \left\langle \int_{\gamma_{x_{\min}}}^{\gamma_{\mathrm{xmax}}} \mathrm{d}x \; \gamma_{\mathrm{m}}^{D-1}(x) E_{\frac{3}{2}-\frac{D}{2}}\left(\frac{\gamma_{\mathrm{m}}^2(x)n^2}{4\xi^2}\right) \right\rangle. \quad (5.21)$$

The high-temperature limit of Eq. (5.19) can again be obtained by Poisson summation. The result is:

$$\Delta E_{\mathrm{c}}^{\mathrm{i.p.},\varphi}(\xi \to \infty) = -E_{\mathrm{c}}^{\mathrm{i.p.},\varphi}(0) - \frac{L_y 2\sqrt{\pi} \left\langle \int_{\gamma_{x_{\min}}}^{\gamma_{\mathrm{xmax}}} \gamma_{\mathrm{m}}^{D-2}(x)\mathrm{d}x \right\rangle}{(4\pi)^{D/2}a^{D-2}(D-3)(D-2)\,\sin(\varphi)}\xi. \quad (5.22)$$

The remaining worldline average in this expression yields some positive finite number. Irrespective of its precise value for a given angle φ and spacetime dimension D (the precise value of the integral for a specific φ can be read off, for instance, from Fig. 5.3 for either $D = 3$ or $D = 4$ and Fig. 4.8 for $D = 5$), we stress that

we observe the same linear dependence on temperature $\xi = aT$ as in the parallel plate case. This is nothing but the familiar phenomenon of the dominance of the zeroth Matsubara mode at high temperatures, implying dimensional reduction, as discussed above. This mechanism is obviously geometry independent. Also the Casimir force remains attractive for high temperatures.

5.4.2 Casimir torque

Whereas the a-independent first term of Eq. (5.19) does not contribute to the force, both terms in the first line of Eq. (5.19) contribute to the low-temperature limit of the Casimir torque. The thermal contribution to the torque is

$$\Delta D_{\mathrm{c}}^{\mathrm{i.p.},\varphi}(\xi) = \frac{\mathrm{d}\Delta E_{\mathrm{c}}^{\mathrm{i.p.},\varphi}(\xi)}{\mathrm{d}\varphi}, \tag{5.23}$$

which at low temperature reads

$$\Delta D_{\mathrm{c}}^{\mathrm{i.p.},\varphi}(\xi \to 0) = -\frac{L_y \cos(\varphi)}{(4\pi)^{D/2} \sin^2(\varphi)} \left((2T)^{D-2} \zeta(D-2)\Gamma\left(\frac{D-2}{2}\right) \right.$$

$$\times \left(\langle \boldsymbol{\gamma}_{x_{\min}}(\varphi)\lambda_x \rangle - \tan(\varphi)\langle \boldsymbol{\gamma}'_{x_{\min}}(\varphi)\lambda_x \rangle \right)$$

$$\left. + a\zeta(D-1)(2T)^{D-1}\Gamma\left(\frac{D-1}{2}\right)\sqrt{\pi} \right), \tag{5.24}$$

where

$$\left\langle \int_{\boldsymbol{\gamma}_{x_{\min}}}^{\boldsymbol{\gamma}_{x_{\max}}} x\,\mathrm{d}x \right\rangle = 0 \tag{5.25}$$

has been used, and we have introduced

$$\lambda_x = \boldsymbol{\gamma}_{x_{\max}} - \boldsymbol{\gamma}_{x_{\min}}. \tag{5.26}$$

The expression (5.24) depends on only one nontrivial worldline average. In limiting cases, this average can be given analytically, as it reduces to the case described by Eq. (4.18): we find

$$-\langle \boldsymbol{\gamma}_{x_{\min}}(\varphi \to 0)\lambda_x \rangle = \frac{\langle \lambda_x^2 \rangle}{2} = \frac{\pi^2}{6} \tag{5.27}$$

and

$$-\langle \boldsymbol{\gamma}_{x_{\min}}(\varphi \to \pi/2)\lambda_x \rangle = \frac{\langle \lambda_x \rangle^2}{2} = \frac{\pi}{2}. \tag{5.28}$$

For arbitrary φ, this average can be well approximated by

$$\langle \boldsymbol{\gamma}_{x_{\min}}(\varphi)\lambda_x \rangle \approx -\frac{\pi}{2}\sin^2(\varphi) - \frac{\pi^2}{6}\cos^2(\varphi), \qquad (5.29)$$

as we will explain in the following. With Eq. (4.27), we can write

$$\boldsymbol{\gamma}_{x_{\min}}(\varphi) \equiv \boldsymbol{\gamma}_x(\hat{t})\cos(\varphi) + \boldsymbol{\gamma}_z(\hat{t})\sin(\varphi), \qquad (5.30)$$

where $\hat{t}$ denotes the value of t that satisfies the minimum condition in Eq. (4.27). Together with

$$\boldsymbol{\gamma}_{z_{\min}}(\varphi) \equiv -\boldsymbol{\gamma}_x(\hat{t})\sin(\varphi) + \boldsymbol{\gamma}_z(\hat{t})\cos(\varphi), \qquad (5.31)$$

we can interpret $(\boldsymbol{\gamma}_{x_{\min}}(\varphi), \boldsymbol{\gamma}_{z_{\min}}(\varphi))$ as the coordinates of the point $(\boldsymbol{\gamma}_x(\hat{t}), \boldsymbol{\gamma}_z(\hat{t}))$ in the φ-rotated system.

Since the $\boldsymbol{\gamma}_x$ and $\boldsymbol{\gamma}_z$ coordinates of each loop are generated independently of each other, $\boldsymbol{\gamma}_z(\hat{t})$ and λ_x are not correlated. We therefore obtain

$$\langle \lambda_x \boldsymbol{\gamma}_{x_{\min}}(\varphi) \rangle = \langle \lambda_x \boldsymbol{\gamma}_x(\hat{t}) \rangle \cos(\varphi) + \langle \lambda_x \rangle \langle \boldsymbol{\gamma}_z(\hat{t}) \rangle \sin(\varphi). \qquad (5.32)$$

By symmetry, the average $\langle \boldsymbol{\gamma}_{z_{\min}}(\varphi) \rangle$ vanishes, and we get from Eq. (5.31)

$$\langle \boldsymbol{\gamma}_x(\hat{t}) \rangle \sin(\varphi) = \langle \boldsymbol{\gamma}_z(\hat{t}) \rangle \cos(\varphi). \qquad (5.33)$$

On the other hand,

$$\langle \boldsymbol{\gamma}_{x_{\min}}(\varphi) \rangle = -\frac{\langle \lambda_x \rangle}{2}. \qquad (5.34)$$

Substituting Eq. (5.33) into the average of Eq. (5.30) leads to

$$\langle \boldsymbol{\gamma}_z(\hat{t}) \rangle = -\frac{\sin(\varphi)\langle \lambda_x \rangle}{2} \quad \text{and} \quad \langle \boldsymbol{\gamma}_x(\hat{t}) \rangle = -\frac{\cos(\varphi)\langle \lambda_x \rangle}{2}, \qquad (5.35)$$

such that the desired Eq. (5.29) can be motivated by Eq. (5.32). We would like to stress that only the second term in Eq. (5.29) has been estimated with the constraint imposed by the exactly known result for $\varphi \to 0$, see above. The first term is exact and dictates the behavior of the perpendicular-plates limit. This result is compared to the numerically obtained data in Fig. 5.4.

For the v-loop algorithm [53] used here to generate the loops, the expectation value of the maximal extent λ_x is systematically smaller. This error is about the average spacing

$$\langle |\boldsymbol{\gamma}_x(t_{i+1}) - \boldsymbol{\gamma}_x(t_i)| \rangle \approx \frac{1}{\sqrt{N}}, \qquad (5.36)$$
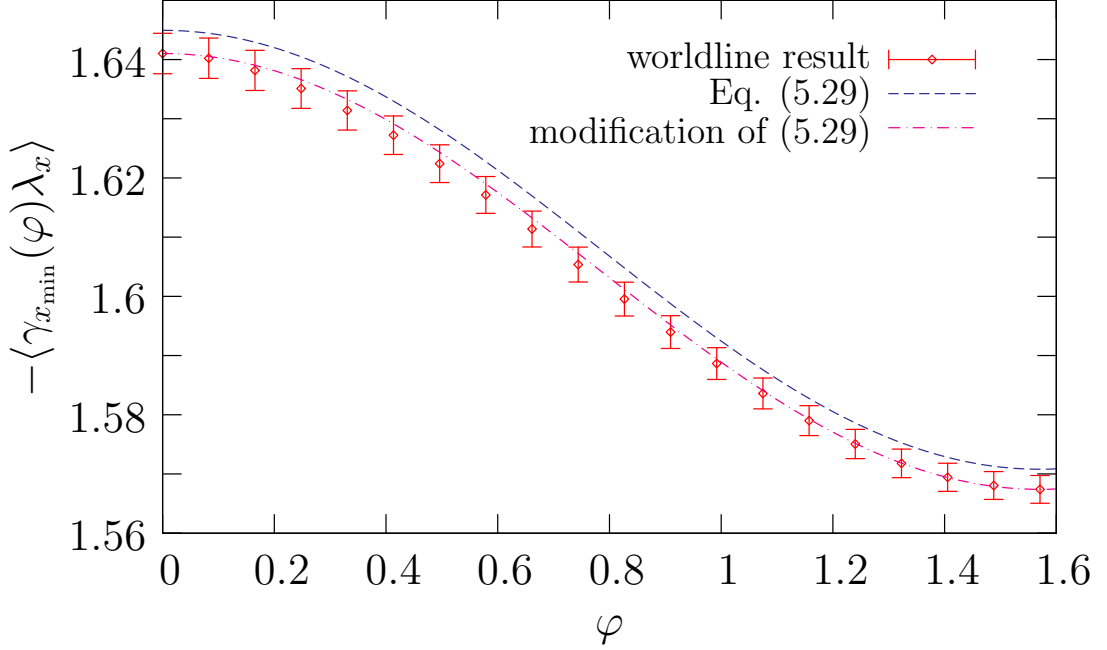
Figure 5.4: Angle dependence of the worldline average occurring in the Casimir torque (5.24): $\langle\gamma_{x_{\min}}(\varphi)\lambda_x\rangle$. The numerical result is compared to the estimate (5.29) (dashed line). The worldline result shows a small systematic error due to the finite discretization. We can include the systematic error into (5.29) by taking worldline estimates for the boundary values at $\varphi = 0$ and $\varphi = \pi/2$ (i.e. $1.567\sin^2(\varphi) + 1.641\cos^2(\varphi)$), respectively, which are smaller than $\pi/2$ and $\pi^2/6$. This yields the dot-dashed curve. The worldline result has been obtained from 5×10^4 loops with 10^6 ppl each.

see Eq. (3.44) and Sec. 3.6. As a consequence, the systematic error of $\langle\lambda_x^2\rangle/2$ and $\langle\lambda_x\rangle^2/2$ is about

$$\frac{\langle\lambda_x\rangle}{\sqrt{N}} \approx 1.84 \cdot 10^{-3} \tag{5.37}$$

at $N = 10^6$. We observe a good agreement of the data with Eq.(5.29) at $\varphi = 0$ and $\varphi = \pi/2$ if the systematic error is taken into account. However, the agreement is actually perfect for all φ when using worldline estimates for the prefactors in Eq. (5.29) instead of $\pi/2$ and $\pi^2/6$, see the modified curve in Fig. 5.4. This shows that Eq. (5.29) will well fit the data in the continuum limit $N \to \infty$.

Let us return to the calculation of the Casimir torque. In the vicinity of the perpendicular-plates configuration, $\varphi = \pi/2 - \delta\varphi$, we can now obtain an expression to first order in $\delta\varphi$:

$$\Delta D_{\text{c}}^{\text{i.p.},\varphi=\pi/2-\delta\varphi}(\xi \to 0) = -\frac{L_y \delta\varphi}{(4\pi)^{D/2}} (2T)^{D-2}$$

$$\times \left(-\zeta(D-2)\Gamma\left(\frac{D-2}{2}\right) \left[\frac{\pi}{2} - \left\langle \gamma_{x_{\min}}''\left(\frac{\pi}{2}\right)\lambda_x \right\rangle \right] \right.$$

$$\left. + 2\,aT\,\zeta(D-1)\Gamma\left(\frac{D-1}{2}\right)\sqrt{\pi} \right). \tag{5.38}$$

Here, we have used

$$\langle \gamma_{x_{\min}}'(\pi/2)\lambda_x \rangle = 0.$$

Apart from $\langle \gamma_{x_{\min}}''(\pi/2)\lambda_x \rangle$, Eq. (5.38) is an analytical expression. Using (5.29), we obtain

$$-\left\langle \gamma_{x_{\min}}''\left(\frac{\pi}{2}\right)\lambda_x \right\rangle \approx \frac{\pi^2}{3} - \pi \approx 0.148, \tag{5.39}$$

which is about ten percent of the dominating analytical term in square brackets $\sim \pi/2$. We observe that the first term, which dominates in the limit $aT \to 0$, gives a contribution to the torque which drives the system away from the perpendicular-plates case $\varphi = \pi/2$. Zero- and finite-temperature contributions thus have the same sign. The fact that $\varphi = \pi/2$ is a repulsive fixed point is also in agreement with naive expectations.

For $D = 4$, Eq. (5.38) reads

$$\frac{\Delta D_{\text{c}}^{\text{i.p.},\varphi=\pi/2-\delta\varphi}(\xi \to 0)}{L_y} = T^2 \left(0.0716 - 0.0957\xi\right)\delta\varphi, \tag{5.40}$$

which should be compared with the first-order term arising from the $T = 0$ contribution Eq. (4.50), which reads

$$\frac{D_{\text{c}}^{\text{i.p.},\varphi=\pi/2-\delta\varphi}}{L_y} \approx 0.00329\frac{\delta\varphi}{a^2}. \tag{5.41}$$

Thus, for $D = 4$ we obtain to first order in $\delta\varphi$

$$\frac{\Delta D_{\text{c}}^{\text{i.p.},\varphi=\pi/2-\delta\varphi}(\xi \to 0)}{D_{\text{c}}^{\text{i.p.},\varphi=\pi/2-\delta\varphi}(0)} \approx \xi^2 \left(21.8 - 29.1\xi\right). \tag{5.42}$$

In the validity regime of the low-temperature expansion, $\xi = aT \ll 1$, the positive first term is always dominant, hence the perpendicular-plates case remains a repulsive fixed point. Most importantly, we would like to stress that the quadratic dependence of the torque on the temperature $\sim T^2$ ($\sim T^{D-2}$ in the general case) for the inclined-plates configuration represents the strongest temperature dependence of all observables discussed in this thesis.

5.5 Semi-infinite plate parallel to an infinite plate

A particularly interesting example for the geometry-temperature interplay is given by the semi-infinite plate parallel to the infinite plate (1si configuration). In this case, the angle of inclination φ in Fig. 4.6 is zero. Analogously to Eq. (4.36), the finite-temperature Casimir energy can be decomposed as

$$E_{\mathrm{c}}^{\mathrm{1si}}(\xi) = E_{\mathrm{c}}^{\mathrm{1si,edge}}(\xi) + E_{\mathrm{c}}^{\mathrm{1si},\|}(\xi), \tag{5.43}$$

where

$$E_{\mathrm{c}}^{\mathrm{1si},\|}(T) = E_{\mathrm{c}}^{\mathrm{1si},\|}(0) + \Delta E_{\mathrm{c}}^{\mathrm{1si},\|}(T)$$

corresponds to the standard parallel-plate formula as given in Eqs. (4.17) and (5.8), with A now being the surface of the semi-infinite plate. Approaching the 1si limit of $\Delta E_{\mathrm{c}}^{\mathrm{1si},\|}(T)$ from the inclined-plates configuration in the limit $\varphi \to 0$ is again a delicate issue, as the proper order of limits $\varphi \to 0$ and $L_z \to \infty$ has to be accounted for, see Sect. 4.7. Since the analysis is technically involved, we defer it to Sec. 5.6. Let us here concentrate on the temperature-dependent edge contribution

$$\Delta E_{\mathrm{c}}^{\mathrm{1si,edge}}(T) = E_{\mathrm{c}}^{\mathrm{1si,edge}}(T) - E_{\mathrm{c}}^{\mathrm{1si,edge}}(0).$$

We set $\varphi = 0$ in Eq. (4.26) and evaluate Eq. (5.2). The result is (here and in the following, we confine ourselves to $D > 3$):

$$\Delta E_{\mathrm{c}}^{\mathrm{1si,edge}}(\xi) = -\frac{L_y}{(4\pi)^{D/2} a^{D-2}} \Bigg\{ \tag{5.44}$$

$$(2\xi)^{D-2} \zeta(D-2) \Gamma\left(\frac{D-2}{2}\right) \left\langle \int_{\boldsymbol{\gamma}_{x_{\min}}}^{\boldsymbol{\gamma}_{x_{\max}}} \mathrm{d}x\, \boldsymbol{\gamma}_{z_{\max}}(x) \right\rangle$$

$$-\sum_{n=1}^{\infty} \left\langle \int_{\boldsymbol{\gamma}_{x_{\min}}}^{\boldsymbol{\gamma}_{x_{\max}}} \mathrm{d}x\, (x - \boldsymbol{\gamma}_{x_{\min}})^{D-2} \boldsymbol{\gamma}_{z_{\max}}(x) E_{2-\frac{D}{2}}\left(\frac{(x - \boldsymbol{\gamma}_{x_{\min}})^2 n^2}{4\xi^2}\right) \right\rangle \Bigg\}.$$

Note that the first term (second line), being the main contribution to the Casimir energy at small T, does not contribute to the Casimir force since it is a independent. Contrary to the case with $\varphi \neq 0$, the exponential integral functions cannot be neglected in the low-temperature limit, since the argument of $E_n(z)$ becomes zero at the lower bound of the integral for any $\xi > 0$. This results in a correction $\sim \xi^{D-1+\alpha}$, with $\alpha > 0$, to the low-temperature limit of the first term.

Here, however, we concentrate on the last term, as it gives rise to the thermal
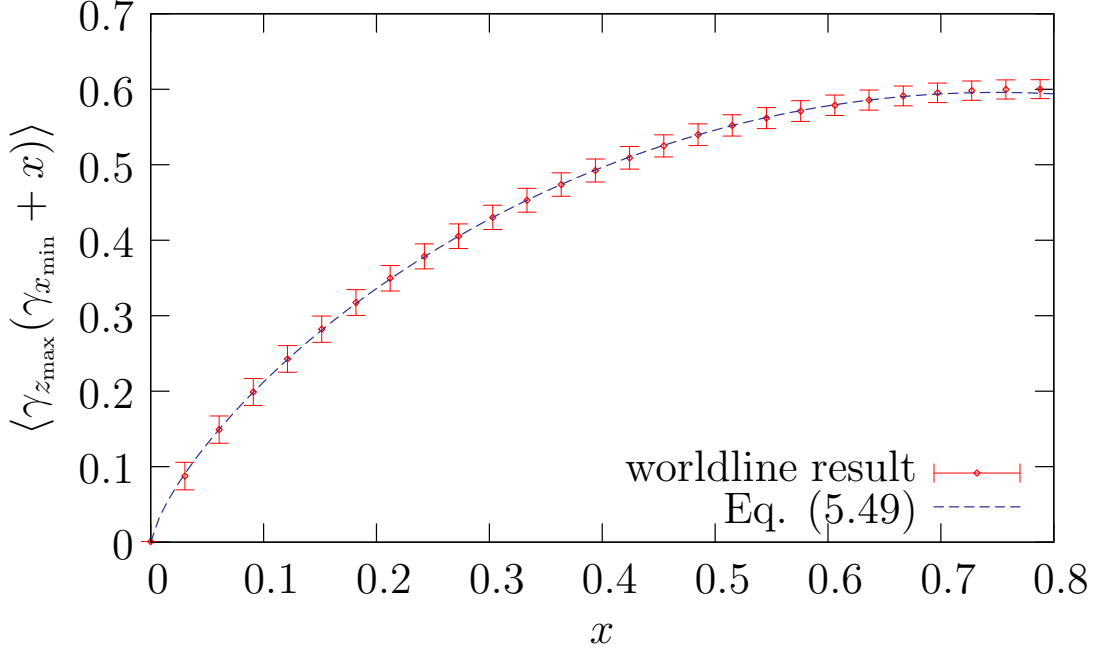
Figure 5.5: Numerical result of the worldline average $\langle \boldsymbol{\gamma}_{z_{\max}}(\boldsymbol{\gamma}_{x_{\min}} + x)\rangle$ obtained by 5×10^4 worldlines with 10^6 points each compared to the fit function of Eq. (5.49) obtained on the interval $x = [0, 0.7]$. The error bars have been plotted ten times larger. The observed small-x power law x^{α_1} with $\alpha_1 \simeq 0.74$ directly translates into a non-integer small-temperature behavior of the thermal edge contribution to the force, $\Delta F_{\mathrm{c}}^{\mathrm{1si,edge}} \sim T^{D-1+\alpha_1}$.

correction of the Casimir force. In the low-temperature limit, we find

$$\Delta F_{\mathrm{c}}^{\mathrm{1si,edge}}(\xi) = -\frac{2L_y}{(4\pi)^{D/2}a^{D-1}} \tag{5.45}$$

$$\times \sum_{n=1}^{\infty} \left\langle \int_0^{\lambda_x} \mathrm{d}x \; x^{D-2} \boldsymbol{\gamma}_{z_{\max}}(\boldsymbol{\gamma}_{x_{\min}} + x) \exp\left(-\frac{x^2 n^2}{4\xi^2}\right)\right\rangle.$$

For small ξ, the main contribution to the integral comes from its lower bound as the exponential function rapidly decreases for large arguments. At the lower bound, we can take the worldline average $\langle \boldsymbol{\gamma}_{z_{\max}}(\boldsymbol{\gamma}_{x_{\min}} + x)\rangle$ first, yielding a smooth function. We assume that we can expand the latter in a power series,

$$\langle \boldsymbol{\gamma}_{z_{\max}}(\boldsymbol{\gamma}_{x_{\min}} + x)\rangle = \sum_{n=0}^{\infty} c_n x^{\alpha_n}, \tag{5.46}$$

where the exponents α_n do not necessarily have to be integers. Inserting (5.46)

into (5.45) leads to

$$\Delta F_{\mathrm{c}}^{\mathrm{1si,edge}}(\xi \to 0) = - \frac{L_y}{(4\pi)^{D/2}a^{D-1}} \tag{5.47}$$

$$\times \sum_{n=0}^{\infty} c_n \, (2\xi)^{D+\alpha_n-1} \, \Gamma\left(\frac{D+\alpha_n-1}{2}\right) \zeta(D+\alpha_n-1),$$

where we have neglected exponentially suppressed contributions. For the lowest-order term, we obtain

$$\langle \boldsymbol{\gamma}_{z_{\max}}(\boldsymbol{\gamma}_{x_{\min}}) \rangle \equiv c_0 = 0, \tag{5.48}$$

since for a given worldline $(\boldsymbol{\gamma}_x(t), \boldsymbol{\gamma}_z(t))$ there exists a corresponding worldline in the ensemble with $(\boldsymbol{\gamma}_x(t), -\boldsymbol{\gamma}_z(t))$. This allows the conclusion that the coefficient of the T^{D-1} term vanishes.

We determine the higher coefficients c_n from computing $\langle \boldsymbol{\gamma}_{z_{\max}}(\boldsymbol{\gamma}_{x_{\min}} + x) \rangle$ in the vicinity of $x = 0$ by worldline numerics. Figure 5.5 depicts the form of $\langle \boldsymbol{\gamma}_{z_{\max}}(\boldsymbol{\gamma}_{x_{\min}} + x) \rangle$ near the lower bound $x = 0$. A global fit to this function including two coefficients c_1, c_2 is given by

$$\langle \boldsymbol{\gamma}_{z_{\max}}(\boldsymbol{\gamma}_{x_{\min}} + x) \rangle \approx 0.9132 \, (x(1.500 - x))^{0.7423}$$

$$\approx 1.234 x^{0.7423} - 0.6106 x^{1.7423}, \tag{5.49}$$

where we have kept $\alpha_2 - \alpha_1 = 1$ fixed. The resulting thermal correction to the force is shown in Fig. (5.6) for $D = 4$, where we compare the full numerical solution with different orders of the expansion (5.49) and the high-temperature asymptotics, see below.

As the low-temperature asymptotics is directly related to the lowest nonvanishing coefficient α_1, we have also performed local fits to the function $\langle \boldsymbol{\gamma}_{z_{\max}}(\boldsymbol{\gamma}_{x_{\min}} + x) \rangle$ in the vicinity of $x = 0$. Depending on the fit window, the leading exponent can grow up to $\alpha_1 \approx 0.8$. (Of course, the fit window must be large enough to avoid that the worldline discretization becomes visible; otherwise, the exponent trivially but artificially approaches $\alpha_1 \to 1$ as the discretized worldline is a polygon on a microscopic scale).

In any case, we conclude that if we assume the expansion (5.46), the low-temperature regime of the 1si edge effect is well described by a non-integer power law,

$$\Delta F_{\mathrm{c}}^{\mathrm{1si,edge}} \sim T^{D-1+\alpha_1} \simeq T^{D-0.3}, \tag{5.50}$$
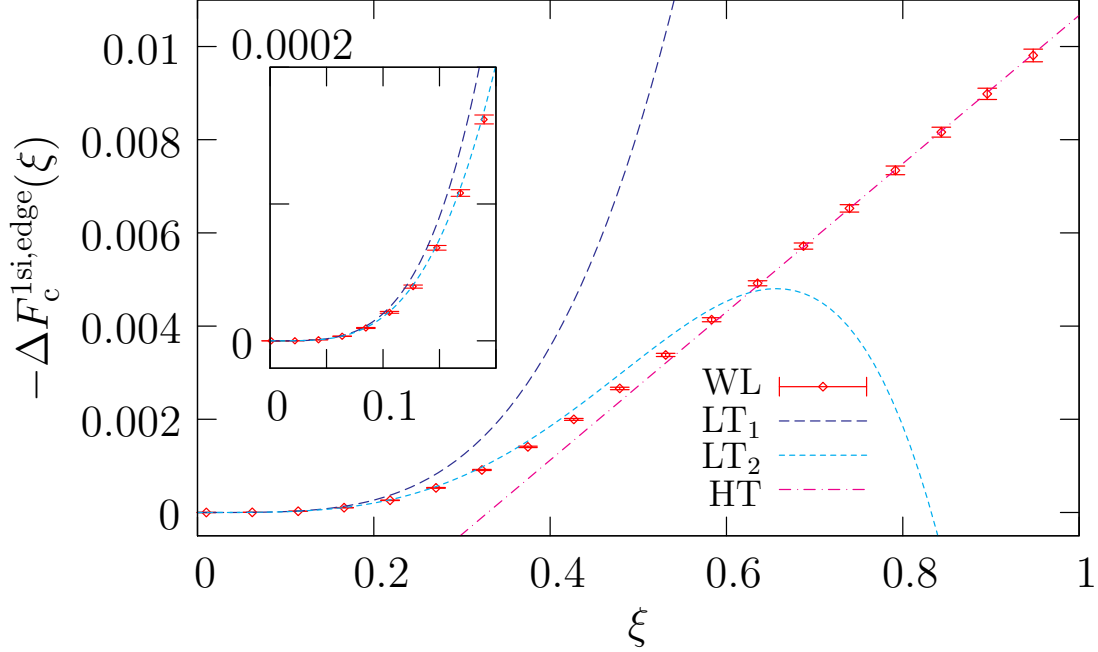
Figure 5.6: Thermal contribution to the Casimir edge force in the 1si configuration, $-\Delta F_c^{\text{1si,edge}}(\xi)$, plotted for $a = 1$ and $D = 4$. WL: worldline result Eq. (5.45) obtained using 1000 loops with 10^6 ppl each. LT_1, LT_2: leading and next-to-leading low-temperature corrections $0.1098\xi^{3.7423}$ and $0.1098\xi^{3.7423} - 0.131881\xi^{4.7423}$, respectively, obtained from Eqs. (5.47) and (5.49), using 5×10^4 loops 10^6 ppl each. HT: high temperature limit obtained from Eq. (5.58), using 5×10^4 loops 10^6 ppl each; a fit to the HT curve is provided by $-5.24062(\pm 0.0222)10^{-3} + 1.591(\pm 0.004138)10^{-2}\xi$. The inlay displays a magnified interval $\xi = [0, 0.2]$.

where the fractional exponent arises from the geometry-temperature interplay in this open geometry. Of course, our numerical analysis cannot guarantee to yield the true asymptotic behavior in the limit $\xi \to 0$, but our data in the low-temperature domain $0.01 \lesssim \xi \lesssim 0.4$ is well described by the non-integer scaling at next-to-leading order.

Our analysis so far has been based on the expansion (5.46) for $\langle \boldsymbol{\gamma}_{z_{\max}}(\boldsymbol{\gamma}_{x_{\min}} + x)\rangle$. However, for small x, the form of $\langle \boldsymbol{\gamma}_{z_{\max}}(\boldsymbol{\gamma}_{x_{\min}} + x)\rangle$ could also be for instance

$$\langle \boldsymbol{\gamma}_{z_{\max}}(\boldsymbol{\gamma}_{x_{\min}} + x)\rangle \sim x \ln(x). \tag{5.51}$$

Eq. (5.51) can not be expanded in a power series at $x = 0$. Nevertheless, like our approximation (5.49), the form (5.51) also leads to $\langle \boldsymbol{\gamma}_{z_{\max}}(\boldsymbol{\gamma}_{x_{\min}})\rangle = 0$ and

$$\frac{\langle \boldsymbol{\gamma}_{z_{\max}}(\boldsymbol{\gamma}_{x_{\min}} + x)\rangle}{x} \to \infty, \tag{5.52}$$

for $x \to 0$.

Assuming

$$\langle \boldsymbol{\gamma}_{z_{\max}} (\boldsymbol{\gamma}_{x_{\min}} + x) \rangle \approx \widetilde{c}_1 \, x \, \ln \left(\widetilde{c}_2 \, x \right), \tag{5.53}$$

and inserting Eq. (5.53) into Eq. (5.45) leads to

$$\Delta F_{\mathrm{c}}^{\mathrm{1si,edge}}(\xi \to 0) = - \frac{L_y \widetilde{c}_1 a \, T^D}{\pi^{D/2}} \left\{ \Gamma \left(\frac{D}{2} \right) \ln(\widetilde{c}_2) \zeta(D) \right. \tag{5.54}$$

$$\left. + \frac{1}{2} \Gamma \left(\frac{D}{2} \right) \left(\left(\ln \left(4\xi^2 \right) + \psi \left(\frac{D}{2} \right) \right) \zeta(D) + 2\zeta'(D) \right) \right\},$$

where ψ is the digamma function. We again have neglected exponentially suppressed contributions. The leading correction to $\Delta F_{\mathrm{c}}^{\mathrm{1si,edge}}$ is then given by

$$\Delta F_{\mathrm{c}}^{\mathrm{1si,edge}}(a \, T \to 0) \simeq - \frac{L_y \widetilde{c}_1 a \, T^D}{\pi^{D/2}} \Gamma \left(\frac{D}{2} \right) \zeta(D) \ln \left(a \, T \right). \tag{5.55}$$

For the constants $\widetilde{c}_1$, $\widetilde{c}_2$, we find

$$\widetilde{c}_1 = -0.62(1), \tag{5.56}$$

$$\widetilde{c}_2 = 0.32(5). \tag{5.57}$$

Let us finally turn to the high-temperature limit of Eq. (5.44) which can again be obtained by Poisson summation. The result for the edge energy reads

$$\Delta E_{\mathrm{c}}^{\mathrm{1si,edge}}(\xi \to \infty) = - E_{\mathrm{c}}^{\mathrm{1si,edge}}(0) \tag{5.58}$$

$$- \frac{2\sqrt{\pi} L_y \left\langle \int_0^{\lambda_x} \mathrm{d}x \, x^{D-3} \boldsymbol{\gamma}_{z_{\max}} (x + \boldsymbol{\gamma}_{x_{\min}}) \right\rangle}{(4\pi)^{D/2} a^{D-2}(D-3)} \xi,$$

where the worldline average is subject to numerical evaluation. The resulting high-temperature limit of the Casimir force is shown in Fig. (5.6) for $D = 4$. The high-temperature limit is again linear in T in accordance with general dimensional-reduction arguments.

5.6 The $\varphi \to 0$ limit for inclined plates

We have analyzed the $\varphi \to 0$ behavior of inclined plates at zero temperature in Sect. 4.7. Here, we consider the same limit for the thermal correction to the energy. The decomposition of the 1si Casimir energy into bulk and edge contributions can also be performed for the thermal corrections,

$$\Delta E_{\mathrm{c}}^{\mathrm{1si},\varphi}(\xi) = \Delta E_{\mathrm{c}}^{\mathrm{edge},\varphi}(\xi) + \Delta E_{\mathrm{c}}^{\parallel,\varphi}(\xi),$$

where

$$\Delta E_{\mathrm{c}}^{\parallel,\varphi}(\xi) = -\frac{L_y \csc(\varphi)}{(4\pi)^{D/2} a^{D-2}} \left\langle \left[-\Gamma\left(\frac{D-2}{2}\right) \zeta(D-2)(2\xi)^{D-2} \lambda_x \boldsymbol{\gamma}_{x_{\min}}(\varphi) \right.\right.$$

$$-\zeta(D-1)\Gamma\left(\frac{D-1}{2}\right)(2\xi)^{D-1}\sqrt{\pi}$$

$$-\sum_{n=1}^{\infty} \int_{\boldsymbol{\gamma}_{x_{\min}}}^{\boldsymbol{\gamma}_{x_{\max}}} \mathrm{d}x \left\{ \boldsymbol{\gamma}_{\mathrm{m}}^{D-2}(x) E_{2-\frac{D}{2}}\left(\frac{n^2 \boldsymbol{\gamma}_{\mathrm{m}}^2(x)}{4\xi^2}\right) (x\cos(\varphi) - \boldsymbol{\gamma}_{x_{\min}}(\varphi)) \right.$$

$$\left.\left.\left. -\boldsymbol{\gamma}_{\mathrm{m}}^{D-1}(x) E_{\frac{3-D}{2}}\left(\frac{n^2 \boldsymbol{\gamma}_{\mathrm{m}}^2(x)}{4\xi^2}\right) \right\} \right] \right\rangle, \tag{5.59}$$

with

$$\boldsymbol{\gamma}_{\mathrm{m}}(x) = x\cos(\varphi) + \sin(\varphi)\boldsymbol{\gamma}_{z_{\max}}(x) - \boldsymbol{\gamma}_{x_{\min}}(\varphi)$$

and

$$\Delta E_{\mathrm{c}}^{\mathrm{edge},\varphi}(\xi) = -\frac{L_y}{(4\pi)^{D/2} a^{D-2}} \left[\Gamma\left(\frac{D-2}{2}\right) \zeta(D-2)(2\xi)^{D-2} \left\langle \int_{\boldsymbol{\gamma}_{x_{\min}}}^{\boldsymbol{\gamma}_{x_{\max}}} \mathrm{d}x\, \boldsymbol{\gamma}_{z_{\max}}(x) \right\rangle \right.$$

$$\left. -\sum_{n=1}^{\infty} \left\langle \int_{\boldsymbol{\gamma}_{x_{\min}}}^{\boldsymbol{\gamma}_{x_{\max}}} \mathrm{d}x\, \boldsymbol{\gamma}_{\mathrm{m}}^{D-2}(x) E_{2-\frac{D}{2}}\left(\frac{n^2 \boldsymbol{\gamma}_{\mathrm{m}}^2(x)}{4\xi^2}\right) \boldsymbol{\gamma}_{z_{\max}}(x) \right\rangle \right]. \tag{5.60}$$

Whereas $\Delta E_{\mathrm{c}}^{\mathrm{edge},\varphi}(\xi)$ remains finite, $\Delta E_{\mathrm{c}}^{\parallel,\varphi}(\xi)$ shows a divergent behavior as $\varphi \to 0$. Let us therefore concentrate on $\Delta E_{\mathrm{c}}^{\parallel,\varphi}(\xi)$, in order to isolate the source of the apparent divergence which is related to the order of limits of $L_z \to \infty$ and $\varphi \to 0$. In the case of inclined plates, $(L_z\varphi)$ is infinite for all $\varphi \neq 0$, resulting in a $1/\varphi$ divergent energy density (energy per length) for $\varphi \to 0$. Parallel plates, on the other hand have a finite energy density (energy per area) and $(L_z\varphi) = 0$.

In the following, we show how to obtain an analytic transition from $(L_z\varphi) \to \infty$ to $(L_z\varphi) \to 0$ for small φ by working with large but finite L_z, and taking $L_z \to \infty$

at the end of the calculation. The first limit results in a divergent energy density per unit edge length of the inclined plates as $\varphi \to 0$,

$$
\Delta E_{\mathrm{c}}^{\parallel,\varphi\to 0}(\xi) = -\frac{L_y}{2a^{D-2}\varphi(4\pi)^{D/2}}\Big[\langle\lambda^2\rangle\Gamma\left(\frac{D-2}{2}\right)\zeta(D-2)(2\xi)^{D-2}
$$

$$
- 2(2\xi)^{D-1}\zeta(D-1)\Gamma\left(\frac{D-1}{2}\right)\sqrt{\pi} + \Gamma\left(\frac{D}{2}\right)\zeta(D)(2\xi)^D
$$

$$
- \left\langle\lambda^D\sum_{n=1}^{\infty}\left(E_{1-\frac{D}{2}}\left(\frac{\lambda^2 n^2}{4\xi^2}\right) + E_{2-\frac{D}{2}}\left(\frac{\lambda^2 n^2}{4\xi^2}\right) - 2E_{\frac{3}{2}-\frac{D}{2}}\left(\frac{\lambda^2 n^2}{4\xi^2}\right)\right)\right\rangle\Big]
$$

$$
+ \mathcal{O}\left(1\right). \tag{5.61}
$$

The second limit corresponds to the finite energy density of exact parallel plates (5.8).

In Eqs. (5.59-5.61), the z integration was performed first. Let us now do the proper time integration first. The θ function (4.42), valid for small φ, provides the lower bound of the proper time integral:

$$
\Delta E_{\mathrm{c}}^{\parallel,\varphi\to 0}(a,\beta) = -\frac{L_y}{(4\pi)^{D/2}}\left\langle\sum_{n=1}^{\infty}\int_1^{\infty}\frac{\exp\left(-\frac{\beta^2 x^2 n^2}{4\mathcal{T}(a+z\varphi)^2}\right)\mathrm{d}\mathcal{T}}{\mathcal{T}^{\frac{D+1}{2}}}\right.
$$

$$
\left.\times\int_0^{L_z/2}\frac{\mathrm{d}z}{(a+z\varphi)^{D-1}}\int_0^{\lambda_x}x^{D-1}\mathrm{d}x\right\rangle. \tag{5.62}
$$

For $\mathrm{Re}[D] > 1$, the proper time integration yields

$$
\int_1^{\infty}\frac{\exp\left(-\frac{\beta^2 x^2 n^2}{4\mathcal{T}(a+z\varphi)^2}\right)\mathrm{d}\mathcal{T}}{\mathcal{T}^{\frac{D+1}{2}}} =
$$

$$
\left(\frac{2(a+z\varphi)}{xn\beta}\right)^{D-1}\Gamma\left(\frac{D-1}{2}\right) - E_{\frac{3-D}{2}}\left(\frac{x^2\beta^2 n^2}{4(a+z\varphi)^2}\right). \tag{5.63}
$$

Inserting Eq. (5.63) into Eq. (5.62) leads to

$$\frac{\pi^{\frac{D}{2}} \Delta E_{\mathrm{c}}^{\|,\varphi \to 0}(a,\beta)}{A} = \sum_{n=1}^{\infty} \left\langle \frac{a^2 \left(\Gamma\left(\frac{D}{2}, \frac{\lambda_x^2 n^2 \beta^2}{4a^2}\right) - \Gamma\left(\frac{D}{2}, \frac{\lambda_x^2 n^2 \beta^2}{(2a+\phi)^2}\right) \right)}{\phi(n\beta)^D} \right.$$

$$+ \frac{\lambda_x^2 \left(\Gamma\left(\frac{D-2}{2}, \frac{\lambda_x^2 n^2 \beta^2}{4a^2}\right) - \Gamma\left(\frac{D-2}{2}, \frac{\lambda_x^2 n^2 \beta^2}{(2a+\phi)^2}\right) \right)}{4\phi(n\beta)^{D-2}}$$

$$- \frac{a\lambda_x \left(\Gamma\left(\frac{D-1}{2}, \frac{\lambda_x^2 n^2 \beta^2}{4a^2}\right) - \Gamma\left(\frac{D-1}{2}, \frac{\lambda_x^2 n^2 \beta^2}{(2a+\phi)^2}\right) \right)}{\phi(n\beta)^{D-1}}$$

$$+ \frac{\phi \left(\Gamma\left(\frac{D}{2}\right) - \Gamma\left(\frac{D}{2}, \frac{\lambda_x^2 n^2 \beta^2}{(2a+\phi)^2}\right) \right)}{4(n\beta)^D}$$

$$\left. + \frac{\lambda_x \Gamma\left(\frac{D-1}{2}, \frac{\lambda_x^2 n^2 \beta^2}{(2a+\phi)^2}\right)}{2(n\beta)^{D-1}} - \frac{a\Gamma\left(\frac{D}{2}, \frac{\lambda_x^2 n^2 \beta^2}{(2a+\phi)^2}\right)}{(n\beta)^D} \right\rangle$$

$$- \frac{\sqrt{\pi} \Gamma\left(\frac{D-1}{2}\right) \zeta(D-1)}{2\beta^{D-1}} + \frac{a\Gamma\left(\frac{D}{2}\right) \zeta(D)}{\beta^D}, \qquad (5.64)$$

where

$$\phi \equiv L_z \varphi \quad \text{and} \quad A = \frac{L_y L_z}{2}.$$

One can show that the first three terms of Eq. (5.64) are of order $\mathcal{O}(\phi^2)$. The forth term is clearly $\mathcal{O}(\phi)$. The last four terms can be converted into the parallel-plates energy density (5.8) by neglecting ϕ with respect to a and using the identity

$$z^\alpha E_{1-\alpha}(z) = \Gamma(\alpha, z);$$

the error is of order $\mathcal{O}(\phi^2)$. The first-order correction to the parallel-plates case is therefore encoded in the fourth term. The second-order correction is in the first three terms since the ϕ^2 terms cancel each other in the remainder. In this limit ($|\phi| \ll 1$), all sums converge for $\mathrm{Re}[D] > 2$.

Let us rearrange (5.64) so as to investigate the $\phi \to \infty$ case with φ being small but finite:

$$\frac{\pi^{\frac{D}{2}}\Delta E_{\mathrm{c}}^{\parallel,\varphi}(a,\beta)}{A} = \sum_{n=1}^{\infty}\left\langle \frac{(4a+\phi)\left(\Gamma\left(\frac{D}{2}\right) - \Gamma\left(\frac{D}{2},\frac{\lambda_x^2 n^2\beta^2}{(2a+\phi)^2}\right)\right)}{4(n\beta)^D}\right.$$

$$+\frac{\lambda_x\left(\Gamma\left(\frac{D-1}{2},\frac{\lambda_x^2 n^2\beta^2}{(2a+\phi)^2}\right) - \Gamma\left(\frac{D-1}{2}\right)\right)}{2(n\beta)^{D-1}}$$

$$-\frac{\lambda_x^2\Gamma\left(\frac{D-2}{2},\frac{\lambda_x^2 n^2\beta^2}{(2a+\phi)^2}\right)}{4\phi(n\beta)^{D-2}} + \frac{a\lambda_x\Gamma\left(\frac{D-1}{2},\frac{\lambda_x^2 n^2\beta^2}{(2a+\phi)^2}\right)}{\phi(n\beta)^{D-1}}$$

$$-\frac{a^2\Gamma\left(\frac{D}{2},\frac{\lambda_x^2 n^2\beta^2}{(2a+\phi)^2}\right)}{\phi(n\beta)^{D}} + \frac{\lambda_x^2\Gamma\left(\frac{D-2}{2},\frac{\lambda_x^2 n^2\beta^2}{4a^2}\right)}{4\phi(n\beta)^{D-2}}$$

$$\left.-\frac{a\lambda_x\Gamma\left(\frac{D-1}{2},\frac{\lambda_x^2 n^2\beta^2}{4a^2}\right)}{\phi(n\beta)^{D-1}} + \frac{a^2\Gamma\left(\frac{D}{2},\frac{\lambda_x^2 n^2\beta^2}{4a^2}\right)}{\phi(n\beta)^{D}}\right\rangle. \qquad (5.65)$$

A sketch of this formula for $D = 4$ and $a = \beta = \lambda_x = 1$ ignoring the worldline average is shown in Fig. 5.7. The large-ϕ behavior of the first two terms can be obtained through Poisson summation[4] and reads

$$\frac{(4a+\phi)(c_1 + c_2(2a+\phi))}{(2a+\phi)^D} + \frac{(c_3 + c_4(2a+\phi))}{(2a+\phi)^{D-1}}, \qquad (5.66)$$

where $c_1,\ldots,c_4$ are constants, the values of which are of no importance. We see that (5.66) vanishes for $D > 2$. For $D > 3$ the terms vanish even if multiplied by the infinite length L_z. Remember that the inclined-plates formulae at finite temperature are valid for $D > 3$ as well.

In order to keep the remaining terms of Eq. (5.65) finite, we multiply both sides with the infinite length L_z converting the vanishing Casimir energy per area into the finite energy per length. The Poisson summation of the second line of

---

[4]The large-x limit of $\sum_{n=1}^{\infty} f(n/x)$ yields $(-f(0) + \sqrt{2\pi}\hat{f}(0)\,x)/2$ where $\hat{f}$ is the Fouriertransform of f.
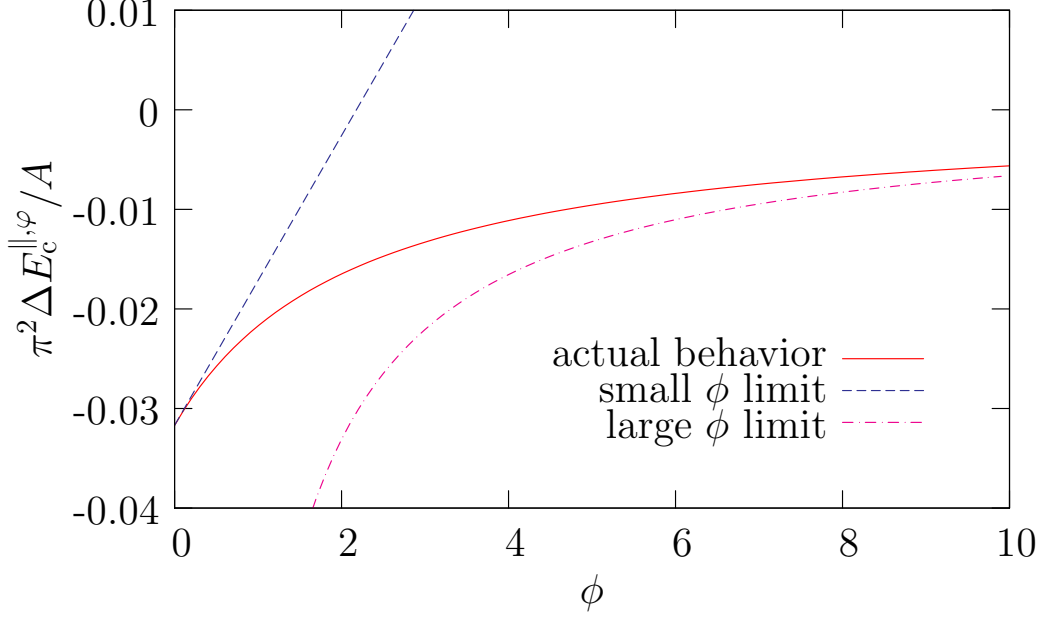
Figure 5.7: Qualitative behavior of the thermal Casimir contribution of the bulk in the inclined-plates case Eq. (5.65) (red line) and its small-ϕ (dashed blue line) and large-ϕ (dot-dashed magenta line) limit, respectively. Note the divergent $1/\phi$ behavior of the large-ϕ limit which corresponds to the divergent (as $\varphi \to 0$) energy per edge length in the inclined-plates formulae. For this illustration, we have chosen $D = 4$, $a = \beta = \lambda_x = 1$, ignoring the worldline average in Eq. (5.65) for simplicity.

Eq. (5.65) results in

$$\lim_{\phi \to \infty} \sum_{n=1}^{\infty} \left(-\frac{\lambda_x^2 \Gamma\left(\frac{D-2}{2}, \frac{\lambda_x^2 n^2 \beta^2}{(2a+\phi)^2}\right)}{4\varphi(n\beta)^{D-2}} + \frac{a\lambda_x \Gamma\left(\frac{D-1}{2}, \frac{\lambda_x^2 n^2 \beta^2}{(2a+\phi)^2}\right)}{\varphi(n\beta)^{D-1}} - \frac{a^2 \Gamma\left(\frac{D}{2}, \frac{\lambda_x^2 n^2 \beta^2}{(2a+\phi)^2}\right)}{\varphi(n\beta)^D} \right) =$$

$$- \frac{\lambda_x^2 \Gamma\left(\frac{D-2}{2}\right)\zeta(D-2)}{4\varphi\beta^{D-2}} + \frac{a\lambda_x \Gamma\left(\frac{D-1}{2}\right)\zeta(D-1)}{\varphi\beta^{D-1}} - \frac{a^2 \Gamma\left(\frac{D}{2}\right)\zeta(D)}{\varphi\beta^D}$$

$$+ \frac{d_1 + d_2(2a+\phi)}{\varphi(2a+\phi)^{D-2}} + \frac{d_3 + d_4(2a+\phi)}{\varphi(2a+\phi)^{D-1}} + \frac{d_5 + d_6(2a+\phi)}{\varphi(2a+\phi)^D}, \tag{5.67}$$

where $d_1, \ldots, d_6$ are constants. These terms containing d_i's vanish for $D > 3$ and $\phi \to \infty$. Applying the identity

$$z^a E_{1-a}(z) = \Gamma(a, z)$$

to the last three terms in Eq. (5.65), we rediscover the inclined-plates formula (5.61) from Eqs. (5.65), (5.67) valid for small angles φ. From Eqs. (5.66) and (5.67), one can infer that the first correction to Eq. (5.61) is of order $\mathcal{O}(1/\phi^{D-3})$.

5.7 Summary of results in $D = 4$

Let us summarize our most important results. We confine ourselves to $3 + 1$ dimensional spacetime. We give the results for the Casimir interaction energy – the corresponding force can be easily obtained by differentiation. As we have seen, thermal fluctuations modify the Casimir energy, yielding the free energy

$$E_c(T) = E_c(0) + \Delta E_c(T), \tag{5.68}$$

where $\Delta E_c(T)$ is the temperature correction. For $(aT) \to 0$, the correction $\Delta E_c^{\parallel}(aT \to 0)$ to the well-known parallel-plates energy reads

$$\frac{\Delta E_c^{\parallel}(aT \to 0)}{A} = -\frac{\zeta(3)T^3}{4\pi} + \frac{\pi^2 aT^4}{90}, \tag{5.69}$$

which is $\approx -0.0957\, T^3 + 0.110\, aT^4$. Note that only the T^4 term contributes to the force as the first term vanishes upon differentiation.

For $(aT) \to 0$, our result for the thermal correction $\Delta E_c^{\text{i.p.},\varphi}(T)$ to the inclined-plates energy reads

$$\frac{\Delta E_c^{\text{i.p.},\varphi}(aT \to 0)}{L_y} = -\frac{c_{\varphi,T_0}T^2}{24\sin(\varphi)} + \frac{\zeta(3)aT^3}{4\pi\sin(\varphi)}, \tag{5.70}$$

where c_{φ,T_0} is shown in Fig. 5.3 as a function of φ. The second term which is a purely analytical result is the generalization of a result for perpendicular plates, $\varphi = \pi/2$, found in [55]; numerically, this term evaluates to $\approx 0.0957aT^3/\sin(\varphi)$.

Again, Eq. (5.70) denotes an energy per edge length and diverges as $\varphi \to 0$. It has to be replaced by the formula for the energy of a semi-infinite plate above a parallel one,

$$E_c^{\text{1si}}(T) = E_c^{\text{1si,edge}}(T) + E_c^{\text{1si},\parallel}(T).$$

The thermal part of $E_c^{\text{1si},\parallel}(T)$ is as in (5.69), where A is the area of the semi-infinite plate. The leading thermal correction to the edge effect's *energy* $\Delta E_c^{\text{1si,edge}}(T)$ is

$$\frac{\Delta E_c^{\text{1si,edge}}(T)}{L_y} = -\frac{c_{\varphi,T_0}T^2}{24}. \tag{5.71}$$

However, this leading correction is independent of a and therefore does not contribute to the force. The leading correction to the force arising from the edge effect is numerically consistent with both

$$\frac{\Delta F_c^{\text{1si,edge}}(T)}{L_y} = -0.11a^{0.74}T^{3.74} \tag{5.72}$$

and

$$\frac{\Delta F_{\mathrm{c}}^{\mathrm{1si,edge}}(T)}{L_y} = 0.068aT^4 \ln(a\,T). \tag{5.73}$$

We prefer the second solution since it is more stable for $(aT) \to 0$.

For $(aT) \to \infty$, all thermal Casimir energies increase linearly in T due to dimensional reduction. For instance, the Casimir energy $E_{\mathrm{c}}^{\parallel}(T)$ for parallel plates becomes

$$E_{\mathrm{c}}^{\parallel}(aT \to \infty) = -\frac{A\zeta(3)T}{8\pi a^2}, \tag{5.74}$$

which is $\approx -0.0478AT/a^2$. Note that $E_{\mathrm{c}}^{\parallel}(aT \to \infty)$ is independent of $\hbar c$ as the dimensional analysis easily shows. The energy at large (aT) can therefore be interpreted as a classical effect.

The same holds for the large (aT) behavior of the inclined-plates case as well as for semi-infinite plates. For inclined plates, we get

$$E_{\mathrm{c}}^{\mathrm{i.p.},\varphi}(aT \to \infty) = -\frac{L_y\sqrt{\pi}c_{\varphi,T_\infty}T}{(4\pi)^2 a\,\sin(\varphi)}, \tag{5.75}$$

where c_{φ,T_∞} is shown in Fig. 5.3 as a function of φ.

The edge effect at large (aT) reads

$$E_{\mathrm{c}}^{\mathrm{1si,edge}}(aT \to \infty) = -\frac{0.016 L_y T}{a}. \tag{5.76}$$

The long-range nature of Casimir phenomena also becomes visible at the thermal correction to the torque. This is immediately transparent from Eq. (5.70). Whereas the a-independent first term of Eq. (5.70) does not contribute to the force, both terms in Eq. (5.70) contribute to the low-temperature limit of the Casimir torque, the thermal contribution being $\mathrm{d}\Delta E_{\mathrm{c}}^{\mathrm{i.p.},\varphi}(T)/\mathrm{d}\varphi$. Concentrating on the limit $aT \to 0$ for small deviations from the perpendicular-plates case, $\varphi = \pi/2 - \delta\varphi$, an expansion to first order in $\delta\varphi$ yields:

$$\frac{\Delta D_{\mathrm{c}}^{\mathrm{i.p.},\varphi=\pi/2-\delta\varphi}(aT \to 0)}{L_y} = (0.0716 - 0.0957aT)\,T^2\delta\varphi. \tag{5.77}$$

In the validity regime of the low-temperature expansion, $aT \ll 1$, the positive first term is always dominant, hence the perpendicular-plates case remains a repulsive fixed point. Most importantly, we would like to stress that the quadratic dependence of the torque on the temperature $\sim T^2$ ($\sim T^{D-2}$ in the general case) for the inclined-plates configuration represents the strongest temperature dependence of all observables discussed here.

5.8 Conclusions

In this chapter, we have provided further numerical as well as analytical evidence for the nontrivial interplay between geometry and temperature in the Casimir effect. Whereas closed geometries such as the parallel-plates case exhibit a comparatively strong suppression of thermal corrections at low temperatures, open geometries such as the general inclined-plates geometry reveal a more pronounced temperature dependence in this regime. The terminology *open* and *closed* corresponds to the absence or presence of a gap in the relevant part of the spectrum of fluctuations which gives rise to the Casimir effect. In closed geometries, the spectral gap inhibits sizable fluctuations at temperatures below the scale set by the gap. By contrast, open geometries allow for sizable thermal fluctuations at any value of the temperature.

Concentrating on the inclined-plates geometry in D dimensions, the temperature dependence of the Casimir force can become stronger by one power in the temperature parameter (implying thermal corrections which can be an order of magnitude larger than for a closed geometry). The inclined-plates geometry is particularly interesting as the limit of a semi-infinite plate parallel to an infinite plate (1si configuration) is somewhat in-between open and closed geometries: the open part of the spectrum only arises due to the edge of the semi-infinite plate. Interestingly, the resulting thermal correction numerically shows a low temperature behavior which lies in-between T^{D-1} and T^D as well.

The strongest temperature dependence $\sim T^{D-2}$ in the low-temperature limit occurs for the Casimir torque of the inclined-plates configuration. This is, because it arises from the leading thermal correction of the interaction energy which contributes to the torque but not to the Casimir force.

Our results have been derived for the case of a fluctuating scalar field obeying Dirichlet boundary conditions on the surfaces. Whereas this model system should not be considered as a quantitatively appropriate model for the real electromagnetic Casimir effect, our general conclusions about the geometry-temperature interplay are not restricted to the Dirichlet scalar case. On the contrary, all our arguments based on the presence or absence of a spectral gap will also be valid for the electromagnetic case. Whether or not the case of Neumann or electromagnetic boundary conditions leads to different power-law exponents for the temperature dependence of the "geothermal" phenomena remains an interesting question for future research.

In view of the fact that most (strictly speaking all) experiments are performed in open geometries, e.g., the sphere-plate geometry, at room temperature, an

analysis of the geometry-temperature interplay of these experimentally relevant configurations is most pressing.

We will therefore adress the sphere-plate and cylinder-plate geometries in the next two chapters.

6 Sphere-plate and cylinder-plate at zero temperature

In this chapter, we compute Casimir forces at zero temperature for the idealized sphere-plate and cylinder-plate configuration induced by scalar-field fluctuations obeying Dirichlet boundary conditions. We make contact with earlier results for the Casimir effect of a cylinder and sphere above a plate [39, 52, 53, 56, 65, 67, 68]. The main purpose of this chapter is to develop powerful algorithms to directly compute the Casimir force instead of the interaction energy. This leads to significant simplifications compared to previous energy calculations and allows us to calculate the Casimir force with high precision for a wide parameter range. Our procedure for the direct calculation of the Casimir force will be generalized to finite temperature in the next section. The content of this chapter was published in [59, 60].

6.1 Introduction

Although the configuration of two parallel plates is more accessible theoretically, high-precision measurements of the Casimir force rather prefer the configuration of a curved surface, such as a lens, sphere or cylinder, in front of the plate. For an extensive reference list, see [3–5].

As we have seen in chapter 4, the power law for the Casimir force of inclined plates is different from the corresponding law of two parallel plates. Precise measurements of the Casimir force between two parallel plates are very difficult since it is an enormous challenge to maintain the plates perfectly parallel on the nanometer scale.

Clearly, the use of curved surfaces elegantly avoids this problem. It spares investigators the difficult task to preserve parallelity and allows close approach of the surfaces. At the same time, however, this setup suffers from insufficient theoretical understanding. In order to compare theory and experiment, powerful theoretical methods are required which are capable of dealing with general geometries.

In recent years, a better understanding of the dependence of the Casimir force on the separation for the idealized sphere-plate and cylinder-plate configurations was achieved for the case of zero temperature [39, 52, 53, 56, 65, 67, 68, 72–74, 151]. We note that the limit of small separations between a sphere and a plate is the most important from the experimental point of view.

Our results agree excellently with the recently obtained analytic solutions for different limiting cases [65, 67, 68], from which Casimir force for the whole parameter range can be reconstructed at zero temperature. We also compare our results with the proximity force approximation, which is still widely used for comparison between theory and experiment.

6.2 Worldline numerics

We start with a short reminder of the worldline approach to the Casimir effect for a massless Dirichlet scalar, confining ourselves to 4 dimensions; for details, see chapter 3. For a configuration Σ consisting of two rigid objects with surfaces Σ_1 and Σ_2, the worldline representation of the Casimir interaction energy in $D = 4$ dimensional spacetime reads

$$E_{\mathrm{c}} = -\frac{1}{32\pi^2}\int_0^\infty \frac{\mathrm{d}\mathcal{T}}{\mathcal{T}^3}\int \mathrm{d}^3 x_{\mathrm{CM}}\,\langle\Theta_\Sigma[\mathbf{x}(t)]\rangle\,. \tag{6.1}$$

The worldline functional $\Theta_\Sigma[\mathbf{x}(\tau)]$ reads more explicitly

$$\Theta[\mathbf{x}(t)] \equiv \Theta[\mathbf{x}_{\mathrm{CM}} + \sqrt{\mathcal{T}}\,\boldsymbol{\gamma}(t)]. \tag{6.2}$$

It is 1 if the worldline $\mathbf{x}(\tau)$ intersects both objects $\Sigma = \Sigma_1 \cup \Sigma_2$, and is zero otherwise. The expectation value in Eq. (6.1) is taken with respect to an ensemble of 3-dimensional closed worldlines with a common center of mass $\mathbf{x}_{\mathrm{CM}}$ and obeying a Gaußian velocity distribution. During the $\mathcal{T}$ integration, the extent of a worldline is scaled by $\sqrt{\mathcal{T}}$. Large propertimes $\mathcal{T}$ correspond to IR fluctuations, small $\mathcal{T}$ to UV fluctuations.
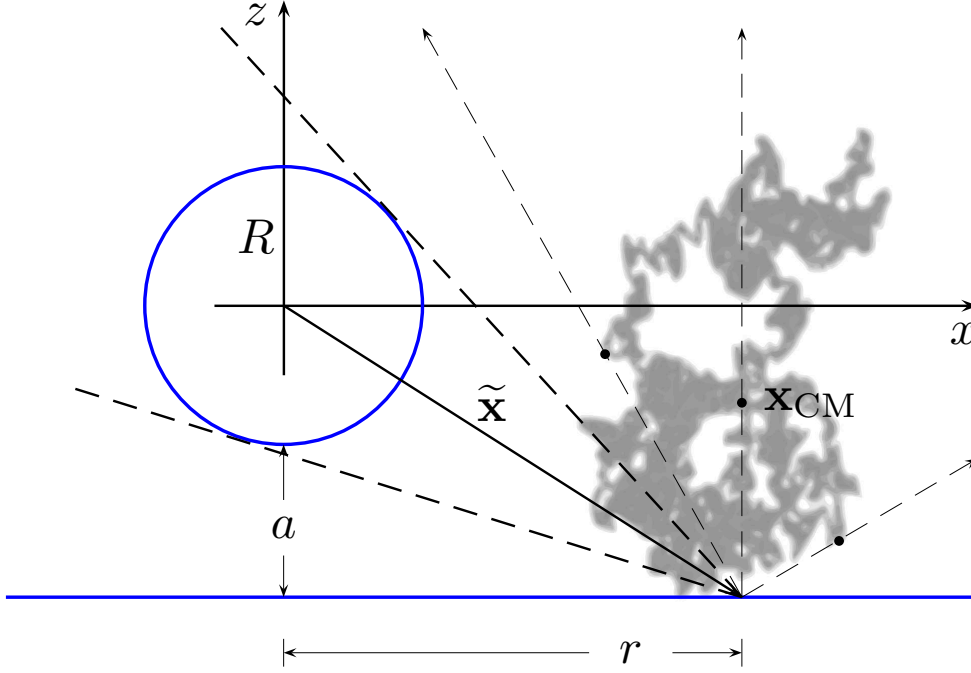
Figure 6.1: Sketch of the sphere-plate configuration. The infinite plate (blue line) is in the $z = -(R + a)$ plane. The sphere of radius R is in the origin. The center of mass $\mathbf{x}_{\mathrm{CM}}$ of the worldline is in $(r, 0, -a - R - \sqrt{\mathcal{T}}\boldsymbol{\gamma}_{z_{\mathrm{min}}})$. During the propertime integration the worldline always touches the plate, while all its points move on rays passing through $(r, 0, -a - R)$. Only points lying inside the cone will pass through the sphere.

6.3 Sphere above a plate

We begin with the configuration of a sphere above a plate. The sphere of radius R is centered around the origin $\mathbf{x} = 0$. The infinitely extended plate lies in the $z = -(a + R)$ plane, where a is the minimal distance between both objects, see Fig. 6.1.

Since the configuration has a rotational symmetry with respect to the z axis, the three-dimensional $\mathbf{x}_{\mathrm{CM}}$ integration reduces to a two-dimensional one. The Casimir energy (6.1) reads

$$E_{\mathrm{c}} = -\frac{1}{16\pi} \int_0^\infty \frac{\mathrm{d}\mathcal{T}}{\mathcal{T}^3} \int \mathrm{d}r \, \mathrm{d}z_{\mathrm{CM}} \, r \, \langle \Theta_\Sigma[\mathbf{x}(t)] \rangle \,, \tag{6.3}$$

where we have switched to cylindrical coordinates (r, z_{CM}) with

$$r^2 = x_{\mathrm{CM}}^2 + y_{\mathrm{CM}}^2.$$

The $\Theta_\Sigma[\mathbf{x}(t)]$ functional factorizes,

$$\Theta_\Sigma[\mathbf{x}(t)] = \Theta_{\mathrm{S}}[\mathbf{x}_{\mathrm{CM}} + \sqrt{\mathcal{T}}\boldsymbol{\gamma}]\,\Theta_{\mathrm{P}}[\mathbf{x}_{\mathrm{CM}} + \sqrt{\mathcal{T}}\boldsymbol{\gamma}]. \tag{6.4}$$

Here Θ_{S} and Θ_{P} account for the intersection of a worldline $\mathbf{x}_{\mathrm{CM}} + \sqrt{\mathcal{T}}\boldsymbol{\gamma}$ with the sphere and the plate, respectively. Notice that Θ_{S} is independent of a, whereas Θ_{P} reads

$$\Theta_{\mathrm{P}} = \theta(-(a + R + z_{\mathrm{CM}} + \sqrt{\mathcal{T}}\boldsymbol{\gamma}_{z_{\mathrm{min}}})), \tag{6.5}$$

where $\boldsymbol{\gamma}_{z_{\mathrm{min}}}$ denotes the worldline's extremal extent into the negative z direction.

As we are interested in calculating the Casimir force,

$$F_{\mathrm{c}} = -\frac{\mathrm{d}E_{\mathrm{c}}}{\mathrm{d}a},$$

the derivative acting only on Θ_{P} produces a δ function which eliminates the z_{CM} integral. The Casimir force thus simplifies to

$$F_{\mathrm{c}} = -\frac{1}{16\pi}\left\langle \int_0^\infty \frac{\mathrm{d}\mathcal{T}}{\mathcal{T}^3} \int_0^\infty \mathrm{d}r\, r\, \Theta_{\mathrm{S}}[\widetilde{\mathbf{x}} + \sqrt{\mathcal{T}}\,\widetilde{\boldsymbol{\gamma}}]\right\rangle. \tag{6.6}$$

Here, we have introduced

$$\widetilde{\mathbf{x}} = \begin{pmatrix} r \\ 0 \\ -a - R \end{pmatrix} \tag{6.7}$$

and

$$\widetilde{\boldsymbol{\gamma}} = \begin{pmatrix} \gamma_x \\ \gamma_y \\ \gamma_z - \gamma_{z_{\mathrm{min}}} \end{pmatrix}. \tag{6.8}$$

The transition from worldline calculations of the force does not only lead to technical simplifications. The classification of relevant worldlines also changes slightly: for the Casimir energy in Eq. (6.1) the worldlines are scaled by the propertime $\sqrt{\mathcal{T}}$ with respect to their center of mass which is finally integrated over. For a given center of mass, all points on a worldline $\mathbf{x}_{\mathrm{CM}} + \sqrt{\mathcal{T}}\boldsymbol{\gamma}(t_i)$ lie on rays originating from the center of mass. These rays are traced out by the $\mathcal{T}$ integral running from $\mathcal{T} = 0$ to $\mathcal{T} = \infty$.

By contrast, the Casimir force in Eq. (6.6) results from worldlines which are attached to the point $\widetilde{\mathbf{x}}$ on the plate. For a given point $\widetilde{\mathbf{x}}$, all points on a worldline

$\widetilde{\mathbf{x}} + \sqrt{\mathcal{T}}\,\widetilde{\boldsymbol{\gamma}}(t_i)$ lie on rays which now originate from $\widetilde{\mathbf{x}}$. Again, these rays are traced out by the $\mathcal{T}$ integral.

Now, the plate is always touched by construction for all values of $\mathcal{T}$, the remaining problem being the detection of intersection events with the sphere. Adapting methods from [53], it is clear that only those points of a worldline lying on the rays intersecting the sphere eventually pass through the sphere for some values of $\mathcal{T}$. Let $\{\widetilde{\boldsymbol{\gamma}}(t_k)\}$ denote the set of points on such rays intersecting the sphere, with k labeling these rays for a discretized worldline. Those values of propertime $\mathcal{T}$ for which this point lies exactly on the sphere can be obtained from the equation

$$(\widetilde{\mathbf{x}} + \sqrt{\mathcal{T}}\,\widetilde{\boldsymbol{\gamma}}(t_k))^2 = R^2. \tag{6.9}$$

Equation (6.9) has two solutions,

$$\mathcal{T}_k^{\pm} = \left(\frac{\widetilde{\mathbf{x}} \cdot \widetilde{\boldsymbol{\gamma}}(t_k)}{|\widetilde{\boldsymbol{\gamma}}(t_k)|^2} \mp \sqrt{\left(\frac{\widetilde{\mathbf{x}} \cdot \widetilde{\boldsymbol{\gamma}}(t_k)}{|\widetilde{\boldsymbol{\gamma}}(t_k)|^2} \right)^2 - \frac{|\widetilde{\mathbf{x}}|^2 - R^2}{|\widetilde{\boldsymbol{\gamma}}(t_k)|^2}} \right)^2. \tag{6.10}$$

For $\mathcal{T} \in (\mathcal{T}_k^-, \mathcal{T}_k^+)$ the point $\widetilde{\mathbf{x}} + \sqrt{\mathcal{T}}\,\widetilde{\boldsymbol{\gamma}}(t_k)$ lies inside the sphere. The point $\widetilde{\mathbf{x}}$ can be viewed as a tip of a cone that wraps around the sphere with the opening angle 2α, with $\sin(\alpha) = R/|\widetilde{\mathbf{x}}|$. The value of the square root in Eq. (6.10) varies between zero and R. The square root is zero if the ray merely touches the sphere, and R if the ray lies on the cone's axis, i.e., if it coincides with the direction spanned by $\widetilde{\mathbf{x}}$, see Fig. 6.1.

For a given r, the worldline intersects the sphere if the propertime $\mathcal{T}$ is in one of the intervals bounded by Eq. (6.10) for all possible values of k. Let us denote these intervals by

$$\overline{\mathcal{T}}_k := [\mathcal{T}_k^-, \mathcal{T}_k^+]. \tag{6.11}$$

The total support of the propertime integral then is

$$\mathcal{S}(r) = \bigcup_k \overline{\mathcal{T}}_k. \tag{6.12}$$

The r dependence of this support arises from the fact that the set of k rays lying inside the cone depends on the position r where the worldline is attached to the plate. The Casimir force (6.4) now reads

$$F_{\mathrm{c}} = -\frac{1}{16\pi} \left\langle \int_0^\infty \mathrm{d}r\, r \int_{\mathcal{S}(r)} \frac{\mathrm{d}\mathcal{T}}{\mathcal{T}^3} \right\rangle. \tag{6.13}$$
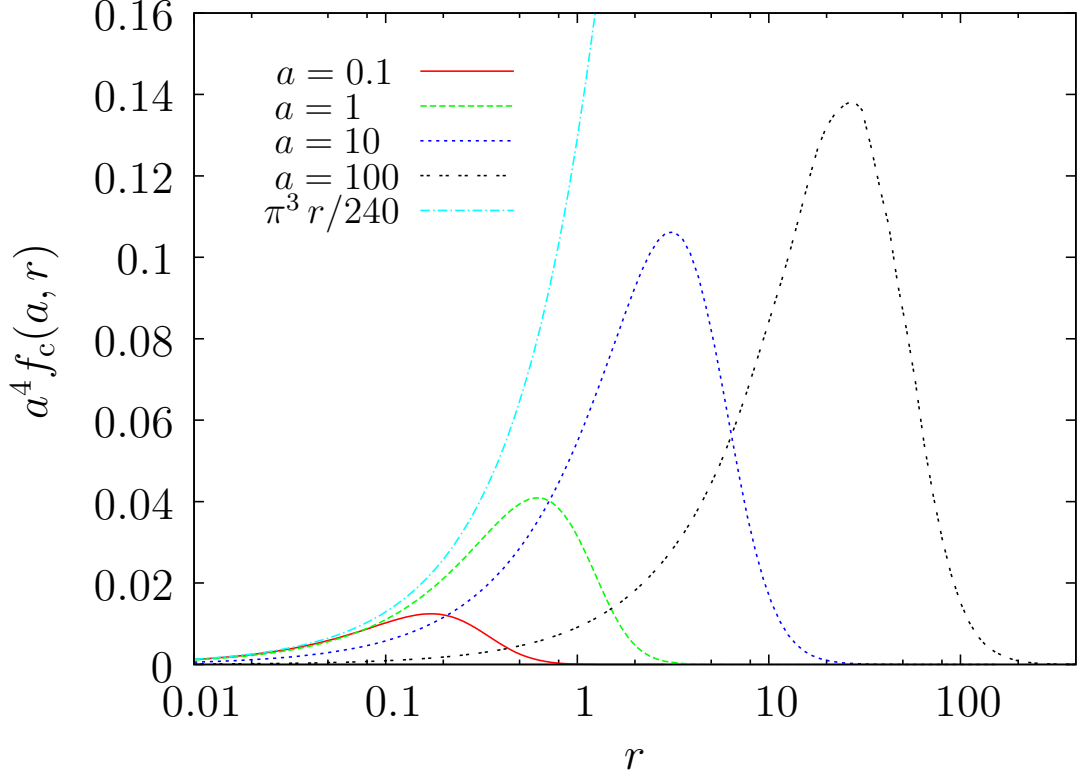
Figure 6.2: The (negative) radial force density $f_c(a, r)$ for a sphere above a plate for various separations a in units of $R = 1$, see Eq.(6.14). For small a and r the radial force density is well approximated by by $2\pi \times \pi^2 r / 480\, a^4 \approx 0.13/a^4$ (dotted-dashed cyan line). The slope corresponds to the parallel plates' force density times 2π. The statistical error is below one percent.

The (negative) radial force density $f_c(a, r)$,

$$f_c(a, r) = \frac{1}{16\pi} r \left\langle \int_{\mathcal{S}(r)}^\infty \frac{\mathrm{d}\mathcal{T}}{\mathcal{T}^3} \right\rangle, \tag{6.14}$$

is shown in Fig. 6.2. We observe that for small a and r, the slope of $f_c(a, r)$ corresponds to the parallel plates' force density times 2π. For small a, the force density is very sharp and the peak position is underneath the sphere. With increasing a, the peak moves outward, such that the force density spreads out over large regions.

The most time-consuming part of the algorithm is the process of determining $S(r)$. To reduce the computational time, it is advisable to reduce the N points per worldline to the subset of $k < N$ points on the above mentioned rays intersecting the sphere. For a given r, all points on rays outside the cone can immediately be

dropped. Furthermore in the process of taking the r integral from zero to infinity, the opening angle of the cone shrinks. All points on rays which leave the cone through its upper half can then be dropped completely from the calculation, as they will never enter the cone again. Only rays below the cone, i.e., between the cone and the plate, can enter the cone for larger values of r.

With these optimizations and with one integral less, the computational time for Casimir force calculations is significantly reduced compared with those of the Casimir energies studied in previous worldline investigations. These simplification facilitate to extend the previously studied parameter range to even larger a/R ratios with higher statistics.

6.4 Cylinder above a plate

In many respects, the cylinder-plate configuration is "in between" the sphere-plate configuration and the classic parallel-plates case. This also holds for the experimental realization: the effort of keeping the cylinder parallel to the plate is less than it is the case for two parallel plates [152]; for the sphere-plate case, this issue is simply absent. As a clear benefit, the force can, in principle, be made arbitrarily large, since it is proportional to the length of the cylinder.

The geometry of the cylinder-plate configuration can be parameterized analogously to the preceding sphere-plate case: we consider the symmetry axis of a cylinder of an (infinite) length L_y and radius R to coincide with the y axis. The infinite plate lies in the $z = -(R + a)$ plane, with a being the distance between the cylinder and the plate.

The Casimir force can be obtained directly from Eq. (6.1), where we use the fact that the Θ_Σ functional factorizes (cf. Eq. (6.4))

$$\Theta_\Sigma[\mathbf{x}(t)] = \Theta_{\mathrm{Cyl}}[\mathbf{x}_{\mathrm{CM}} + \sqrt{\mathcal{T}}\boldsymbol{\gamma}]\,\Theta_{\mathrm{P}}[\mathbf{x}_{\mathrm{CM}} + \sqrt{\mathcal{T}}\boldsymbol{\gamma}]. \tag{6.15}$$

Here Θ_{Cyl} and Θ_{P} account for the intersection of a worldline $\mathbf{x}_{\mathrm{CM}} + \sqrt{\mathcal{T}}\boldsymbol{\gamma}$ with the cylinder and the plate, respectively. Again, only Θ_{P} depends on a and is given in Eq. (6.5).

The y integral in the Casimir energy (6.1) is now trivial due to translational symmetry. The Casimir force can then be obtained directly from Eq. (6.6) and reads

$$F_{\mathrm{c}} = \frac{L_y}{16\pi^2} \left\langle \int_0^\infty \frac{\mathrm{d}\mathcal{T}}{\mathcal{T}^3} \int_0^\infty \mathrm{d}r \, \Theta_{\mathrm{Cyl}}\left[\widetilde{\mathbf{x}} + \sqrt{\mathcal{T}}\,\widetilde{\boldsymbol{\gamma}}\right] \right\rangle, \tag{6.16}$$
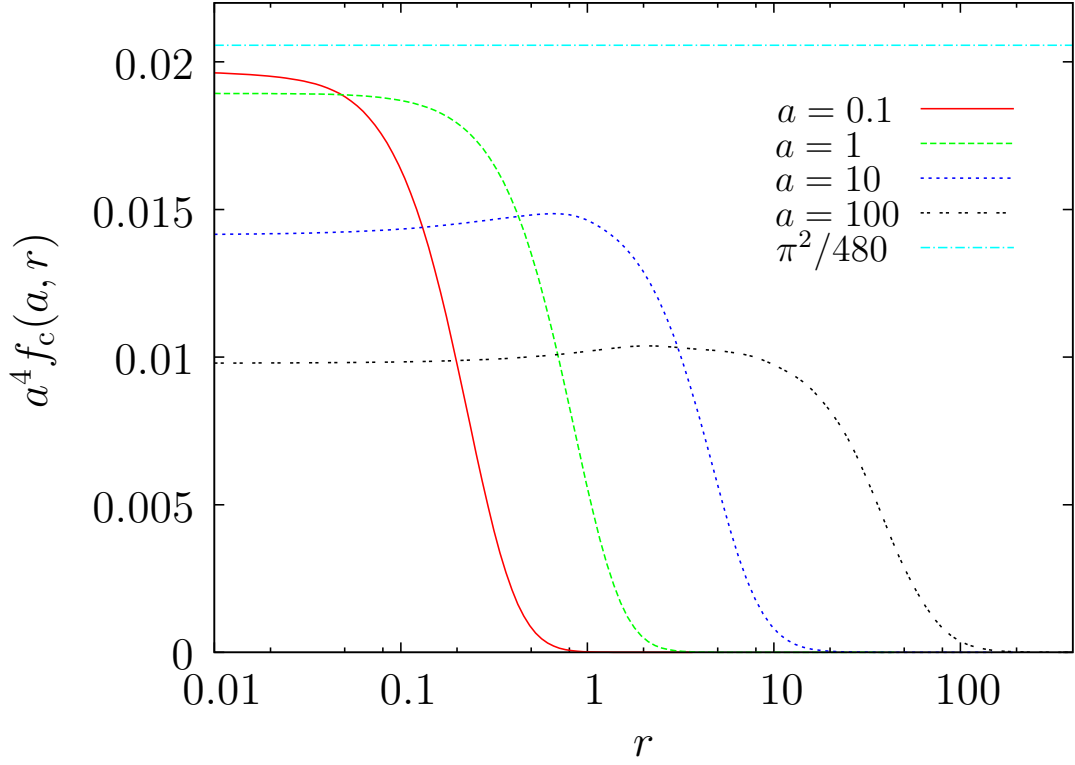
Figure 6.3: Force density $f_c(a, r)$ for a cylinder above a plate for various separations a in units of $R = 1$, see Eq. (6.14). In the limit $a \to 0$, the force density becomes $\pi^2/480 \, a^4 \approx 0.021/a^4$ (dotted-dashed cyan line) around $r = 0$. This value corresponds to the parallel plates' force density. Note that for larger separation a, the force density first stays nearly constant, and surprisingly, increases slightly with r, such that for $r = 0$ a local minimum is formed. The statistical error is below one percent.

where $r = |x_{\text{CM}}|$ and

$$\widetilde{\mathbf{x}} = \begin{pmatrix} r \\ -a - R \end{pmatrix}, \qquad \widetilde{\boldsymbol{\gamma}} = \begin{pmatrix} \gamma_x \\ \gamma_z - \gamma_{z_{\text{zmin}}} \end{pmatrix}. \tag{6.17}$$

As in the case of the sphere, the worldlines $\widetilde{\mathbf{x}} + \sqrt{\mathcal{T}} \, \widetilde{\boldsymbol{\gamma}}$ are attached to the plate at the point $\widetilde{\mathbf{x}}$. The only difference is that the worldlines are now 2-dimensional – a fact which reduces the computational cost. Only those points of a worldline lying on the rays intersecting the cylinder pass through the latter for some values of $\mathcal{T}$. The construction of the support of the $\mathcal{T}$ integral is identical to that for the sphere-plate case, such that the total Casimir force on the cylinder can be

written as in Eq. (6.13)

$$F_{\rm c} = -\frac{L_y}{16\pi^2} \int_0^\infty {\rm d}r \left\langle \int_{\mathcal{S}(r)} \frac{{\rm d}\mathcal{T}}{\mathcal{T}^3} \right\rangle . \qquad (6.18)$$

The (negative) force density $f_{\rm c}(a, r)$ per unit L_y then reads

$$f_{\rm c}(a, r) = \frac{1}{16\pi^2} \left\langle \int_{\mathcal{S}(r)} \frac{{\rm d}\mathcal{T}}{\mathcal{T}^3} \right\rangle . \qquad (6.19)$$

The force density is shown in Fig. 6.3 for various a as a function of r. Notice that for small a, the force density has a sharp peak at $r = 0$. In the limit $a \to 0$, the maximum becomes $\pi^2/480 \, a^4 \approx 0.021/a^4$, which corresponds to the force density of two parallel plates. Surprisingly, for larger a, the force density develops a local minimum at $r = 0$. We therefore conclude that on average, the cylinder is intersected by worldlines earlier at some $r \neq 0$ rather than at $r = 0$. The force density becomes broader with increasing a, and remains nearly constant to eventually disappear for large r.

6.5 Proximity force approximation

It is instructive to compare our results not only with analytic estimates, but also with the much simpler proximity force approximation (PFA). The latter is used by default for the data analysis of geometry corrections in most experiments. It derives from a classical reasoning for generalizing the parallel-plate case; thus, deviations of the exact result from the PFA estimate also parameterize genuine geometry-induced quantum behavior.

Roughly speaking, the PFA subdivides the surfaces into small surface elements. It then applies the parallel-plate force or energy law to pairs of surface elements and integrates the resulting force density. The PFA is inherently ambiguous as the measure for this final integration is not unique: possible alternatives are the surface measures of one of the involved surfaces or any intermediate auxiliary surface. Later on, we will refer to the "sphere-based" or "plate-based" PFA as two generic options for the integration measure. The PFA for the present configuration is discussed in detail in Sec. 8.1.

The concept of the PFA can also be translated into the worldline picture: as an approximation to the ensemble of complicated multi-dimensional worldlines, we may reduce the worldlines to one-dimensional straight lines. The length of a line then corresponds to the average extent of a worldline into a certain relevant direction in a given geometry.

This picture also explains the occurrence of deviations from the PFA as well as the sign of these deviations in the Dirichlet case. Indeed, due to their spatial extent, the worldlines generically intersect both boundaries for smaller values of $\mathcal{T}$ than simple straight lines would. As small propertimes yield quantitatively larger contributions, this then results in a greater force.

More precisely, the size squared of a worldline is proportional to the propertime parameter which is in the denominator of the worldline formula, see Eq. (6.1). This explains why worldline results are typically underestimated by the PFA for small separations of the objects. For very small separations, the upper bound of the propertime integration can effectively be set to infinity, whereas the lower bound is a measure for the first (proper-)time, when a worldline intersects both objects.

For large separations, the PFA breaks down dramatically. Using for example the "plate-based" PFA, we have to stop the integration at the end of the sphere or cylinder. However, the real force density is spread out over regions which can exceed $r \sim R$ by many times, as is shown in Fig. 6.2 and 6.3. The "plate-based" PFA will therefore predict the Casimir force to be much smaller for larger separations, compared with worldline numerics. A systematic study of the PFA, also from the worldline point of view, is given in chapter 8. Let us now move on to the worldline results for the Casimir force.

6.6 Zero-temperature results for the Casimir force

The Casimir force for the sphere and cylinder is compared to the PFA estimates in Fig. 6.4 and 6.5 respectively. For similar comparisons for the Casimir energy, see [53]. We have normalized the force to the leading-order PFA, which is exact in the limit of vanishing separation a.

We observe that the normalized force obtained with worldline numerics does not lie inside the range spanned by the ambiguity of the PFA estimates. Most prominently, the sign of the deviations from the $a \to 0$ limit is different in the Dirichlet scalar case, as can be understood in the worldline picture described above. These observations have been frequently made in the literature before [37, 52, 65, 67, 138].

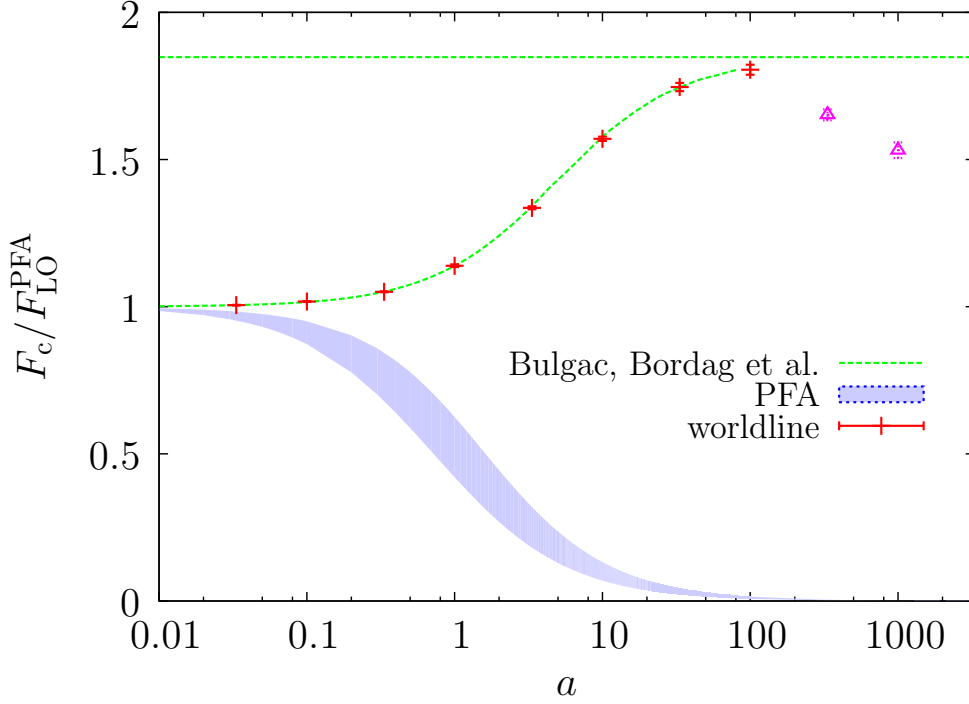In the remainder of this section, we discuss both configurations separately.

Figure 6.4: Casimir Force of a sphere of radius $R = 1$ above an infinite plate vs. the distance a. The force is normalized to the leading-order PFA formula. We observe an excellent agreement with the exact asymptotic solutions for small a [68] and for large a [65] up to $a = 100$. For larger a, the number of N points per loop has to be increased far beyond $N = 2 \cdot 10^7$ used for this plot; otherwise, the sphere falls through the rough mesh provided by the insufficiently discretized worldline, leading to a systematically underestimated force as is visible here for $a > 100$ (pink triangles).

6.6.1 Sphere above a plate

Figure 6.4 shows the Casimir force for a wide range of the distance parameter a. The force is normalized to the leading order of the PFA prediction

$$F_{\text{LO}}^{\text{PFA}}(a) = -\frac{\pi^3 R}{720 \, a^3}. \tag{6.20}$$

At small separations, the leading order PFA and the worldline result show reasonable agreement. The same can be said for the full sphere- and plate-based PFA estimates, which bound the blue area. However, this agreement holds for the leading order only: with increasing a, the full normalized PFA result decreases, whereas the corresponding worldline result increases. Using the analytical result for the next-to-leading order [68], the Casimir force at small separation can then

be written as

$$F_{\mathrm{c}}(a \to 0) = -\frac{\pi^3 R}{720\, a^3} \left(1 + \frac{a}{6\, R} + \ldots \right). \tag{6.21}$$

The corresponding results for the full "plate-based" and "sphere-based" PFA estimates on the other hand read

$$F_{\mathrm{PB}}^{\mathrm{PFA}}(a \to 0) = -\frac{\pi^3 R}{720\, a^3} \left(1 - \frac{1}{2}\frac{a}{R} + \ldots \right) \tag{6.22}$$

and

$$F_{\mathrm{SB}}^{\mathrm{PFA}}(a \to 0) = -\frac{\pi^3 R}{720\, a^3} \left(1 - \frac{3}{2}\frac{a}{R} + \ldots \right). \tag{6.23}$$

We see a more drastic difference in the large distance limit. The Casimir force behaves as $\sim R/a^3$, whereas the full PFA predicts a different power law decay, namely $\sim R^2/a^4$. The large a limit can be calculated analytically [66] and reads

$$F_{\mathrm{c}}(a \to \infty) = -\frac{180}{\pi^4} \frac{\pi^3 R}{720\, a^3} \tag{6.24}$$

$$\approx 1.85\, F_{\mathrm{LO}}^{\mathrm{PFA}}(a \to \infty). \tag{6.25}$$

We observe an excellent agreement with the exact asymptotic solution for small a [68] and for larger a [65] up to $a = 100$.

In order to obtain Fig. 6.4 we have used ensembles with up to $n_{\mathrm{L}} = 1.6 \cdot 10^6$ and $N = 2 \cdot 10^7$. At very small distances a the number of points per loop is not very important, since part of the systematic error is reduced by normalizing to the leading order result; thus, even $N = 5000$ is sufficient for example for $a = 0.0333$ at a precision level of 0.1%. On the other hand at $a = 100$ the number of points per loop used was $1.5 \cdot 10^7$. For larger distances the number of points per loop has to be increased far beyond $2 \cdot 10^7$, otherwise the systematic error from the discretized worldlines becomes large, leading to smaller results for the force, see Fig. 6.4 for $a > 100$ (pink triangles). It turns out that even such high resolution is not sufficient to resolve the small sphere for larger distances.

Already anticipating our results for finite temperature, this observation gives us a rough estimate for the validity limits at small temperatures. In the next chapter, we observe that for $a/R \ll 1$, the maximum of the thermal contribution to the force density at low temperatures $T < 1/R$ lies outside the sphere, and that the position of the maximum increases with decreasing temperature. From the fact that ensembles with $N = 1.5 \cdot 10^7$ are reliable for those cases where the dominant contribution to the force density lies within $r \lesssim 100$, we conclude that
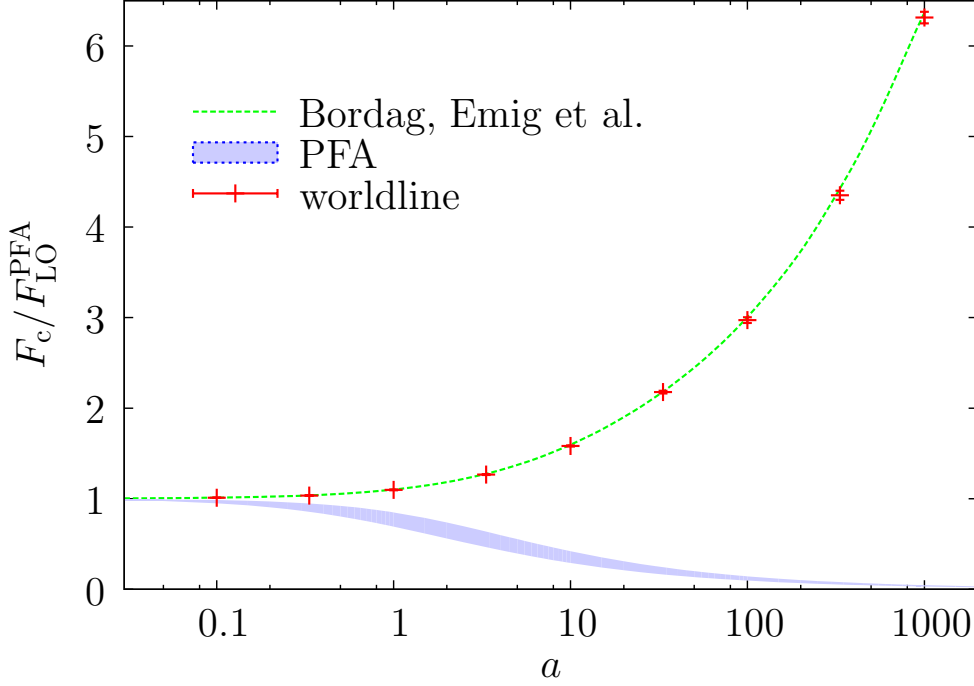
Figure 6.5: Casimir Force of a cylinder of radius $R = 1$ above an infinite plate vs. the distance a. The force is normalized to the leading-order PFA formula. We observe an excellent agreement with the exact asymptotic solutions for small a [68] and for large a [67] up to $a = 1000$.

temperatures above $T_{\min} \approx 0.01/R$ are accessible also in the limit $a \to 0$. For smaller values of N, the corresponding value of $T_{\min}$ is larger.

6.6.2 Cylinder above a plate

From an algorithmic point of view, the sphere-plate and cylinder-plate configurations differ with respect to computational efficiency also beyond the trivial dimensional factors: for a sphere at large separations, a large fraction of points of a worldline can be dropped right from the beginning, as they never "see" the sphere, i.e, they never lie on a ray inside the cone. The situation is different for a cylinder. Dealing with a two-dimensional problem, we use two-dimensional worldlines and the number of points per worldline, which now have to lie in a wedge, is higher than those lying in a cone for the sphere-plate case.

Using comparable worldlines with a large number of points per loop, we thus expect the worldline numerics to break down at far larger distances a than in the case of a sphere. This is indeed the case as is visible in Fig. 6.5.

Figure 6.5 also compares the Casimir force for a cylinder above a plate with the

PFA estimates. As for the case of a sphere, it is convenient to normalize the result to the leading order PFA estimate, which for the present configuration reads (see chapter 8)

$$\frac{F_{\mathrm{LO}}^{\mathrm{PFA}}(a)}{L_y} = -\frac{\pi^3 \sqrt{a\,R}}{768\sqrt{2}\,a^4}. \tag{6.26}$$

Comparing Eq. (6.26) with the full PFA formulae, we again observe that they all agree to the leading order only. There also exists an analytic result for the next-to-leading order [68], such that for small a we have

$$\frac{F_{\mathrm{c}}(a \to 0)}{L_y} = -\frac{\pi^3 \sqrt{a\,R}}{768\sqrt{2}\,a^4} \left(1 + \frac{7}{60}\frac{a}{R} + \dots\right). \tag{6.27}$$

The corresponding results for the full "plate-based" and "cylinder-based" PFA estimates on the other hand read

$$\frac{F_{\mathrm{PB}}^{\mathrm{PFA}}(a \to 0)}{L_y} = -\frac{\pi^3 \sqrt{a\,R}}{768\sqrt{2}\,a^4} \left(1 - \frac{3}{20}\frac{a}{R} + \dots\right) \tag{6.28}$$

and

$$\frac{F_{\mathrm{CB}}^{\mathrm{PFA}}(a \to 0)}{L_y} = -\frac{\pi^3 \sqrt{a\,R}}{768\sqrt{2}\,a^4} \left(1 - \frac{11}{20}\frac{a}{R} + \dots\right). \tag{6.29}$$

Again, the full PFA estimates predict the wrong sign of the next-to-leading order correction. Comparing these results with the corresponding ones for the sphere, we notice that the next-to-leading order correction is much smaller for the cylinder than for the sphere, meaning that the cylinder configuration is better approximated by the PFA than the one for a sphere.

This can be explained by recalling that the cylinder-plate geometry is effectively a two-dimensional problem since the y integration is trivial. Thus, two-dimensional worldlines were used for the calculation of the Casimir force. The sphere above a plate, on the other hand, despite the rotational symmetry, remains a three-dimensional problem and also requires three-dimensional wordlines. To obtain the PFA result we can use worldline numerics with one-dimensional straight lines. Therefore, the configuration for the cylinder is approximated better by the PFA in the small a limit, where the force density is concentrated underneath the compact object.

The force law in the large a limit differs qualitatively from the one of the sphere-plate configuration. For the cylinder, the behavior of the force changes

from $\sim \sqrt{Ra}/a^4$ at small a to $\sim 1/a^3 \ln(a/R)$ at large a. The exact asymptotic form can be calculated analytically [67] and reads

$$\frac{F_c(a \rightarrow \infty)}{L_y} = -\frac{1}{8\pi(a+R)^3 \ln\left(\frac{a+R}{R}\right)}, \tag{6.30}$$

whereas the full PFA predicts

$$\frac{F_c}{L_y} \sim \frac{R}{a^4}.$$

Comparing our worldline results with known exact asymptotic solutions, we observe an excellent agreement for small a [68] and for larger a [67] up to $a = 1000$, see Fig. 6.5.

For the Fig. 6.5 we have also used ensembles with up to $n_L = 1.1 \cdot 10^6$ and $N = 2 \cdot 10^7$. At $a = 100$, the number of points per loop used was $3 \cdot 10^6$, and increased to $N = 1 \cdot 10^7$ for $a = 333$ and up to $N = 2 \cdot 10^7$ for $a = 1000$. As expected, the required number of points per loop for a certain a is less here than in the case of a sphere. Even at such large separations as $a = 1000$, our results agree nicely with [67].

The corresponding estimate for the validity limits at small temperatures for $N = 2 \cdot 10^7$ then is $T > 0.001/R$.

7 Sphere-plate and cylinder-plate at finite temperature

In this chapter, we investigate the nontrivial interplay between geometry and temperature in the Casimir effect for the sphere-plate and cylinder-plate configurations. At low temperature, thermal fluctuations on scales of the thermal wavelength lead to a delocalization of the thermal force density, implying that standard approximation techniques such as the PFA are inapplicable even in the limit of small surface separation. As a consequence, the temperature dependence strongly differs from naive expectations. We perform a comprehensive study of the geothermal phenomena for sphere-plate and cylinder-plate configurations using analytical and numerical worldline techniques for Dirichlet scalar fluctuations. The results of this chapter were published in [58–60].

7.1 Introduction

Investigating finite temperature effects for inclined plates, we observed that the free energy contains temperature dependent terms which, however, do not depend on the separation of the plates and thus do not lead to a force. Moreover, at low temperature, these distance independent terms form a *leading* contribution to the thermal part of the free energy. Fortunately, the configuration of the inclined plates allows us to identify these terms analytically, without the need of performing this task numerically, such that distance dependent and distance independent contributions can be evaluated independently.

For the configurations studied in the present chapter, this separation is analytically not possible within worldline numerics. The dependence of the force on temperature is then to be found by numerical differentiation of the thermal free energy with respect to the distance parameter. Given that the distance dependent contribution may be only subleading, this procedure leads to a loss of precision for the numerical results for the thermal force.

Fortunately, we found a method of direct calculation of the Casimir force in the previous chapter. In the following sections, we generalize this method to finite temperature and then perform investigations for the Casimir *force* rather than for the free energy.

The use of the worldline approach to the Casimir effect on the one hand provides for a highly intuitive picture of the fluctuations, and on the other hand facilitates analytical as well as numerical computations from first principles [37–47].

For instance, the failure of local or additive approximation techniques can directly be inferred from the temperature dependence of the force density: the latter tends to delocalize for decreasing temperatures on scales of the thermal wavelength [58–60]. Local approximation techniques may only be useful at finite temperature if the strict weak-coupling limit is taken [164], or in the high-temperature limit.

We analyze the thermal force density distributions, compute thermal forces for a wide nonperturbative range of parameters, and determine asymptotic limits. This facilitates a careful comparison with local approximation techniques, and, most importantly, yields new and unexpected results for the geometry dependence of thermal forces. For instance, the pure thermal force, i.e., the thermal contribution to the Casimir force, reveals a non-monotonic behavior below a critical temperature for the sphere-plate and cylinder-plate case [59]: the attractive thermal force can increase for increasing distances. This anomalous feature is triggered by a reweighting of relevant fluctuations on the scale of the thermal wavelength – a phenomenon which becomes transparent within the worldline picture of the Casimir effect. Whereas these non-monotonic features already occur for a simple Dirichlet scalar model, non-monotonicities can also arise from a competition between TE and TM modes of electromagnetic fluctuations in configurations with side walls [153, 154].

While there are a number of impressive verifications of the zero-temperature Casimir force [27, 28, 155–157], a comparison between theory and thermal force measurements suffers from the interplay between dielectric material properties and finite temperature [139], still being a subject of intense theoretical investigations [140–143, 158, 159]. In view of the geothermal interplay, we expect that the full resolution of this issue requires the comprehensive treatment of geometry, temperature and material properties, possibly also including edge effects [54, 57, 136, 160, 161]. First results on the sphere-plate configuration using scattering theory and specific dielectric models demonstrate this nontrivial interplay [82, 162, 163].

7.2 Worldline approach to the Casimir effect

Let us shortly review our approach to the direct calculation of the Casimir *force* as presented in the previous chapter and generalize the approach to finite temperatures.

Introducing finite temperature $T = 1/\beta$ by the Matsubara formalism is equivalent to compactifying Euclidean time on the interval $[0, \beta]$. At finite temperature and four-dimensional spacetime, the Casimir free energy induced by a fluctuating Dirichlet scalar reads for any configuration

$$E_{\rm c} = -\frac{1}{32\pi^2} \int_0^\infty \frac{{\rm d}\mathcal{T}}{\mathcal{T}^3} \sum_{n=-\infty}^\infty \exp\left(-\frac{n^2\beta^2}{4\mathcal{T}}\right) \int {\rm d}^3 x_{\rm CM} \, \langle \Theta_\Sigma[\mathbf{x}(t)] \rangle. \tag{7.1}$$

Here, $\langle \dots \rangle$ denotes an average over an ensemble of worldlines $\boldsymbol{\gamma}$ with Gaußian velocity distribution and with a common center of mass $\mathbf{x}_{\rm CM}$. The auxiliary proper-time parameter $\mathcal{T}$ acts as a spatial scaling factor and governs the size of the worldlines. The sum over winding number n counting the round trips of a worldline around the finite-temperature torus takes care of thermal fluctuations, with the $n = 0$ term corresponding to the zero-temperature $T = 1/\beta \to 0$ result. The Θ functional obeys $\Theta_\Sigma = 1$ if a given worldline intersects two or more interacting surfaces, and $\Theta_\Sigma = 0$ otherwise.

In the following, we are exclusively interested in the thermal contribution $n \neq 0$, serving as the interaction potential for the thermal force,

$$\Delta F_{\rm c}(T) = -\frac{{\rm d}}{{\rm d}a} E_{\rm c} \Big|_{n \neq 0}. \tag{7.2}$$

Here, a is a distance parameter between disjoint bodies. For instance, for a sphere above a plate, a configuration that allows to cancel the zero-temperature forces is sketched in Fig. 7.1 [165]. Alternatively, the zero-temperature force could be balanced by applying suitable electrostatic potentials to a single-sphere setup. We stress that the thermal-force phenomena discussed in the following are dominated by the corresponding zero-temperature forces in the standard setups where $a \ll R$. After removing the zero-T contribution, the thermal force for the sphere-plate configuration reads

$$\Delta F_{\rm c} = -\frac{1}{8\pi} \sum_{n=1}^\infty \int_0^\infty {\rm d}\mathcal{T} \, \frac{\exp\left(-\frac{n^2\beta^2}{4\mathcal{T}}\right)}{\mathcal{T}^3} \int_0^\infty {\rm d}r \, r \, \langle \Theta_{\rm S} \rangle, \tag{7.3}$$

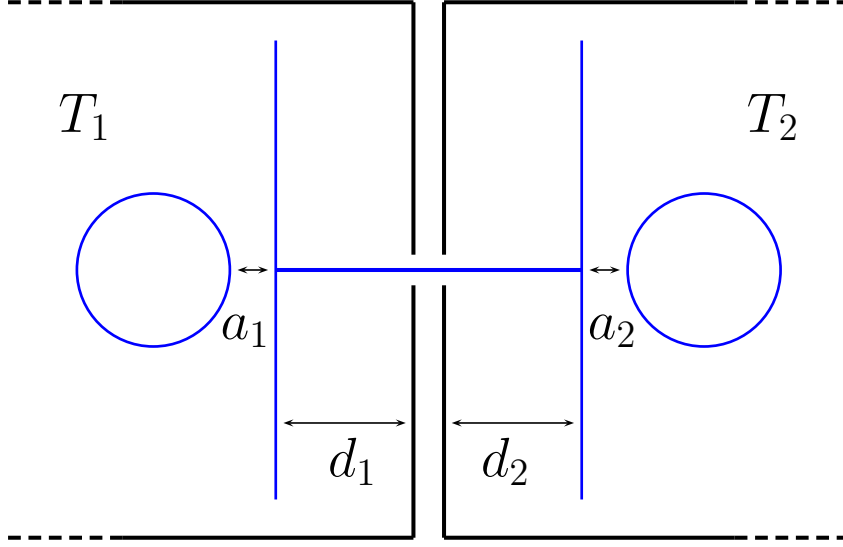where r is the polar center-of-mass coordinate on the plate.

Figure 7.1: Setup for a measurement of the thermal force for the sphere-plane configuration: by tuning the sphere positions to identical distances $a_1 = a_2$, the zero-temperature force on the tightly connected pair of plates cancels. Placing the two sphere-plate subsystems into two heat baths at different temperatures T_1 and T_2, the different thermal forces induce a net force on the pair of plates. We assume that all distances between the (blue) Casimir surfaces and the (black) heat-bath boundaries are large, e.g., $d_{1,2} \gg a_{1,2}$, such that corresponding Casimir interactions can be neglected.

As we have found in the previous chapter, for the calculation of the Casimir *force*, Θ_S measures whether a worldline *which is attached to the plate* also intersects with the sphere for certain scaling sizes $\sim \mathcal{T}$, see Fig. 7.2. Therefore, the classification of relevant worldlines has changed now. They are scaled not with respect to the center of mass (as it was the case in Eq. (7.1)), but with respect to the tip of the cone, which lies on the plate, see Fig. 7.2. Also, the spatial integration does not run over all space. For example, worldlines whose lowest point is underneath the infinite plate are not taken into account at all. The details can be found in the previous chapter.

For the cylinder-plate case, the factor of r has to be replaced by the (infinite) length L_y of the cylinder divided by π, leading to

$$\Delta F_c = -\frac{L_y}{8\pi^2} \sum_{n=1}^{\infty} \int_0^{\infty} d\mathcal{T} \, \frac{\exp\left(-\frac{n^2 \beta^2}{4\mathcal{T}}\right)}{\mathcal{T}^3} \int_0^{\infty} dr \, \langle \Theta_C \rangle . \tag{7.4}$$
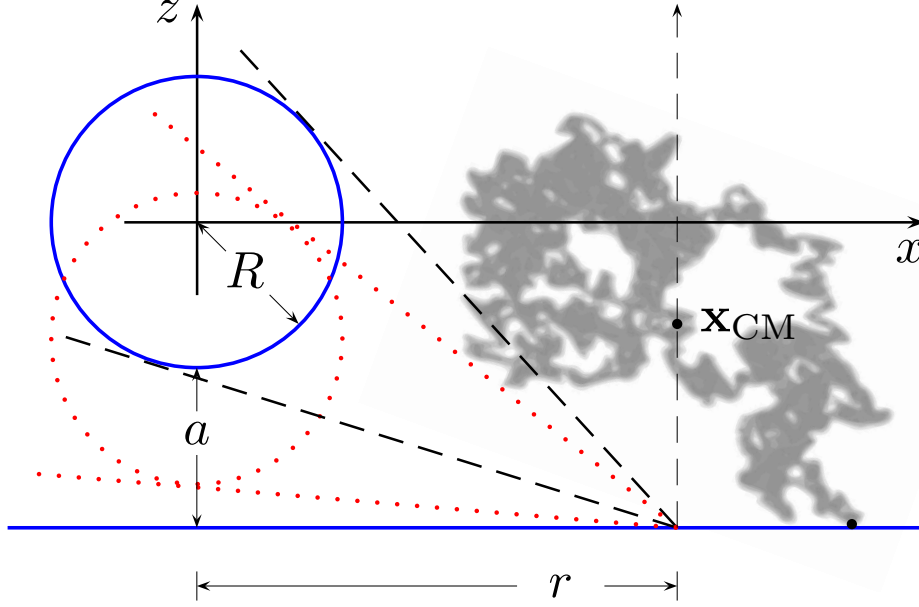
Figure 7.2: Sketch of the sphere-plate configuration. During the propertime integration, the worldline is always attached to the plate, while all its points move on rays originating from the projection of its center of mass $\mathbf{x}_{CM}$ on the plate at polar coordinate r. Only points lying inside a cone wrapping around the sphere with the tip of the cone at r (thick dashed lines) pass through the sphere for increasing $\mathcal{T}$ and thus contribute to the Casimir force. In general, for every $r \gg R$ there exists a maximal separation a, such that the sphere can be intersected by the worldline. If the sphere separation is reduced (dotted red circle), it can become invisible for a given worldline, such that the worldline stops contributing to the Casimir force. This induces the phenomenon that the thermal force can increase for increasing separation.

For the sphere, the expectation value in Eq. (7.3) is taken with respect to an ensemble of 3-dimensional closed worldlines. For the cylinder, it is sufficient to use 2-dimensional worldlines, due to the trivial y coordinate.

Here, we use the same set up as in the previous chapter: the infinite plate lies in the $z = -(R + a)$ plane, the minimal distance between the objects is a. The sphere of radius R is placed in the origin, see Fig. 7.2. The cylinder-plate configuration is analogous: the symmetry axis of a cylinder of an infinite length L_y and radius R coincides with the y axis.

7.3 General considerations

7.3.1 The $a \to 0$ limit

At finite temperature $T = 1/\beta$, the Casimir free energy can be decomposed into its zero-temperature part $E_c(0)$ and finite-temperature correction $\Delta E_c(T)$,

$$E_c(T) = E_c(0) + \Delta E_c(T). \tag{7.5}$$

The same relation holds for the Casimir force

$$F_c(T) = F_c(0) + \Delta F_c(T).$$

Within the worldline representation of the free energy (7.1), the finite-temperature correction is purely driven by the worldlines with nonzero winding number n. Most importantly, the complicated geometry-dependent part of the calculation remains the same for zero or finite temperature.

Let us first perform a general analysis of the thermal correction for a generic Casimir configuration following our argument given in [58]. We start from the assumption that the Casimir free energy can be expanded in terms of the dimensionless product aT,

$$\frac{E_c(T)}{E_c(0)} = 1 + c_1 aT + c_2 (aT)^2 + c_3 (aT)^3 + \dots \tag{7.6}$$

No negative exponents should be present in Eq. (7.6), since the thermal part of the energy disappears as $T \to 0$.

Generically, the $T = 0$ Casimir energy $E_c(0)$ diverges for surfaces approaching contact $a \to 0$. From Eq. (7.6), we would naively expect the same for the thermal correction. If, however, sufficiently many of the first c_i's in Eq. (7.6) vanish, then the thermal part of the Casimir energy is well behaved and without any divergence for $a \to 0$.

This indeed turns out to be the case for two parallel plates, where

$$c_1 = c_2 = 0 \quad \text{and} \quad E_c(0) \sim \frac{1}{a^3}, \tag{7.7}$$

and for inclined plates, where

$$c_1 = 0 \quad \text{and} \quad E_c(0) \sim \frac{1}{a^2}, \tag{7.8}$$

as we have seen in chapter 4.

Consequently, an extreme simplification arises: the low-temperature limit of the thermal correction can be obtained by first taking the formal limit $a = 0$. This was first observed in [58] and then successfully applied in [167].

In the following, we argue that there is no divergence in the local thermal force density in the limit $a \to 0$ for general geometries. For a generic geometry, the a-divergent part can only arise from the regions of contact as $a \to 0$. The divergence for these regions at $T = 0$ is due to the diverging propertime integral over $1/\mathcal{T}^{1+D/2}$ which is bounded from below by $\sim a^2$. This is because for worldlines smaller than a the worldline functional is always zero. At finite temperature the divergence in the thermal correction for $a \to 0$ is removed since one now integrates over $\exp(-n^2\beta^2/4\mathcal{T})/\mathcal{T}^{1+D/2}$, which is zero for every $n > 0$ in the limit $\mathcal{T} \to 0$. The only nonanalyticity could arise from the infinite sum. That this is not the case can directly be verified: instead of integrating over the support $\mathcal{S}$, we integrate over $\mathcal{T}$ from zero to infinity, yielding

$$\sum_{n=1}^{\infty} \int_0^{\infty} \frac{\exp\left(\frac{-n^2\beta^2}{4\mathcal{T}}\right)}{\mathcal{T}^{1+D/2}} \, \mathrm{d}\mathcal{T} = (2T)^D \, \Gamma(D/2) \, \zeta(D). \tag{7.9}$$

For finite temperature $T > 0$, Eq. (7.9) is a finite upper bound for the original local thermal force density.

This procedure corresponds to substituting the critical regions of contact by broader (and infinitely extended) parallel plates, see [58]. The thermal contribution is estimated from above by flattening the surfaces in the contact region. The local thermal contribution to the Casimir force of the original configuration is clearly smaller than the finite thermal contribution of parallel plates. As the latter does not lead to divergences for $a \to 0$, there can also be no divergence for the general curved case arising from the contact regions.

Of course, infinite geometries may still experience an infinite thermal force, as it is the case for two infinitely extended parallel plates, but the local thermal contribution to the force density will be finite. From a practical viewpoint, taking the limit $a \to 0$ first simplifies the calculations considerably.

7.3.2 Delocalization of the thermal force density

Another important feature of low-temperature contributions to the Casimir effect is the spread of the thermal force density over regions of size $\sim 1/T$ even for very small separations a. This phenomenon has first been demonstrated for the configuration of two perpendicular plates at a distance a [58].[1]

The thermal force density

$$\Delta f_{\mathrm{c}}(r, T) = f_{\mathrm{c}}(r, T) - f_{\mathrm{c}}(r, 0)$$

for this case as a function of the coordinate r on the infinite surface measuring the distance from the edge (i.e., the contact point at $a = 0$) can indeed be obtained analytically on the worldline from the thermal force,

$$\Delta F_{\mathrm{c}}(\beta) = -\frac{L_y}{16\pi^2} \sum_{n=1}^{\infty} \left\langle \int \mathrm{d}r \int_{r^2/\lambda_1^2}^{\infty} \frac{\exp\left(-\frac{n^2\beta^2}{4\mathcal{T}}\right)}{\mathcal{T}^3} \, \mathrm{d}\mathcal{T} \right\rangle. \qquad (7.10)$$

Here, λ_1 is a worldline parameter measuring the extent of half a unit worldline, i.e., the distance measured in x direction from the left end to the center of mass. It is clear from Fig. 7.2 that the lower bound in the $\mathcal{T}$ integral in Eq. (7.10) is given by r^2/λ_1^2: this is the minimal scaling value for which the worldline intersects the semi-infinite vertical plate. From Eq. (7.10), we read off the following force density:

$$\frac{\Delta f_{\mathrm{c}}(r, T)}{L_y} = -\frac{\pi^2 T^4}{90} + \frac{1}{\pi^2} \sum_{n=1}^{\infty} \left\langle \exp\left(-\frac{n^2\lambda_1^2}{4r^2T^2}\right) \left(\frac{T^4}{n^4} + \frac{T^2\lambda_1^2}{4n^2r^2}\right) \right\rangle. \qquad (7.11)$$

Analytic results for the thermal force can be obtained by rescaling the radial coordinate

$$r \to \lambda_1 \, r$$

per worldline and using

$$\langle \lambda_1 \rangle = \frac{\sqrt{\pi}}{2}.$$

The force density in Eq. (7.11) then becomes[2]

$$\frac{\Delta \tilde{f}_{\mathrm{c}}(r, T)}{L_y} = -\frac{\pi^{5/2} T^4}{180} + \frac{1}{2\pi^{3/2}} \sum_{n=1}^{\infty} \left\langle \exp\left(-\frac{n^2}{4r^2T^2}\right) \left(\frac{T^4}{n^4} + \frac{T^2}{4n^2r^2}\right) \right\rangle. \qquad (7.12)$$

---

[1] In this configuration, the sphere in Fig. 7.2 is replaced by a vertical semi-infinite plate extending along the positive z axis and an edge at $z = 0$.

[2] Equations (7.11) and (7.12) possibly differ by a total derivative, but both provide for a reasonable thermal force density.

The thermal force between the perpendicular plates in the limit $a \to 0$ upon integration then yields

$$\Delta F_{\mathrm{c}}(T) = -\frac{\zeta(3)\, L_y T^3}{4\pi}$$

in agreement with [55].

The thermal force density of two perpendicular plates at $a = 0$ can also be calculated for arbitrary spacetime dimension D. All we have to do is to replace the prefactor in Eq. (7.10) by $1/(4\pi)^{D/2}$ and the propertime exponent in the denominator by $1 + D/2$. This gives

$$\frac{\Delta f_{\mathrm{c}}(r,T,D)}{L_y} = -\,\zeta(D)\Gamma\left(\frac{D}{2}\right)\pi^{-D/2}\,T^D + \pi^{-D/2}\,T^D\left\langle\sum_{n=1}^{\infty}\frac{\Gamma\left(\frac{D}{2},\frac{\lambda_1^2 n^2}{4r^2 T^2}\right)}{n^D}\right\rangle.$$

$$(7.13)$$

This force density can also be made independent of λ_1 by rescaling $r \to \lambda_1 r$. Integrating Eq. (7.13) and using $\langle\lambda_1\rangle = \sqrt{\pi}/2$ we obtain

$$\frac{\Delta F_{\mathrm{c}}}{L_y} = -\frac{1}{2}\,\pi^{(1-D)/2}\,\zeta(D-1)\,\Gamma\left(\frac{D-1}{2}\right)\,T^{D-1}, \qquad (7.14)$$

in agreement with our result for perpendiculat plates in D dimensions, see Eq. (5.20).

The perpendicular-plates configuration is special as it features a scale invariance in the $a \to 0$ limit: Eq. (7.11) remains invariant under

$$T \to T\alpha, \quad r \to r/\alpha, \quad \Delta f_{\mathrm{c}} \to \Delta f_{\mathrm{c}}/\alpha^4 \qquad (7.15)$$

for arbitrary α. As a consequence, knowing (7.11) for a single temperature value, say $T = 1$, is sufficient to infer its form for all other T. Equation (7.11) is shown for $T = 1/R$, $R = 1$ in Fig. 7.3. For $r < 1/T$, the force density stays nearly constant, corresponding to the first term in (7.11). It rapidly approaches zero for $r > 1/T$. From this, we draw the important conclusion that the region of constant force density in r direction can be made arbitrarily large by choosing sufficiently low T.

Similar consequences arise for temperature effects in other geometries. We plot the thermal force densities for the sphere-plate and cylinder-plate configuration in Fig. 7.3. The thermal force density for a cylinder above a plate at $a = 0$ has a shape similar to the one of two perpendicular plates, whereas the radial force density of a sphere above a plate exhibits a maximum due to the cylindric measure factor r, see Fig. 7.3.

Although these force densities are not scale invariant due to the additional dimensionful scale R (sphere radius), its maximum nevertheless moves away from
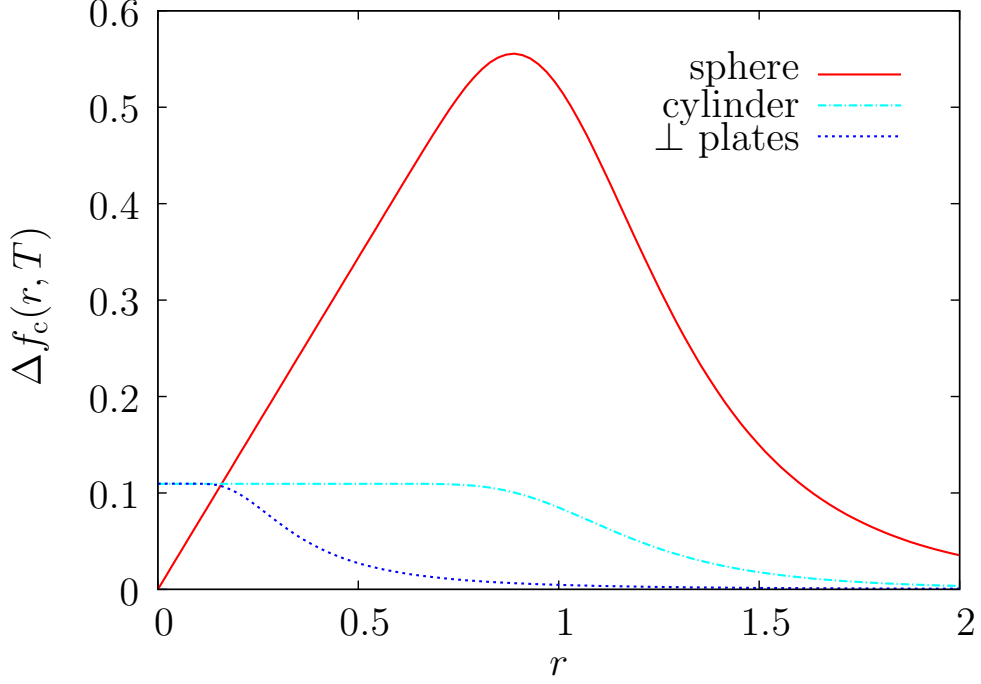
Figure 7.3: The (negative) thermal force density Eq. (7.11) for perpendicular plates (dashed blue line), cylinder above plate (dotted dashed line) and sphere above plate (solid red line) both of radius $R = 1$ in the zero-distance limit $a \to 0$ for $T = 1$. The sphere-plate curve represents the radial density including the radial measure factor $\sim 2\pi r$. The thermal force densities of cylinder and perpendicular plates at $r = 0$ are equal to the force density of two parallel plates, $\pi^2/90 \approx 0.1097$. The thermal force density in the sphere-plate case has a maximum of $\approx 2\pi \times \pi^2/90$, where the factor 2π arises from the cylindrical measure. Note that a considerable fraction of the force density lies outside the sphere which only extends to $r = 1$. As the temperature drops, the maximum moves monotonously to the right.

the sphere as the temperature drops. We conclude that no local approximate tools such as the PFA will be able to predict the correct thermal force in particular at low temperatures. The fact that the force densities for sphere and cylinder are not scale invariant leads to different temperature behaviors for $T < 1/R$ and $T > 1/R$, even in the limit $a \to 0$.

The spread of thermal force density can be easily understood in the worldline picture: at zero temperature, the Casimir force is generically dominated by small propertimes, i.e., small worldlines with a minimal extent such that the worldlines can intersect with both surfaces. As a consequence, the energy density is typically peaked in the region near minimal separation. By contrast, the peak of the finite-temperature propertime factor $\sim e^{-n^2\beta^2/(4\mathcal{T})}/\mathcal{T}^3$ moves to larger $\mathcal{T}$ values for decreasing temperature. Therefore, as larger worldlines can contribute, the free-
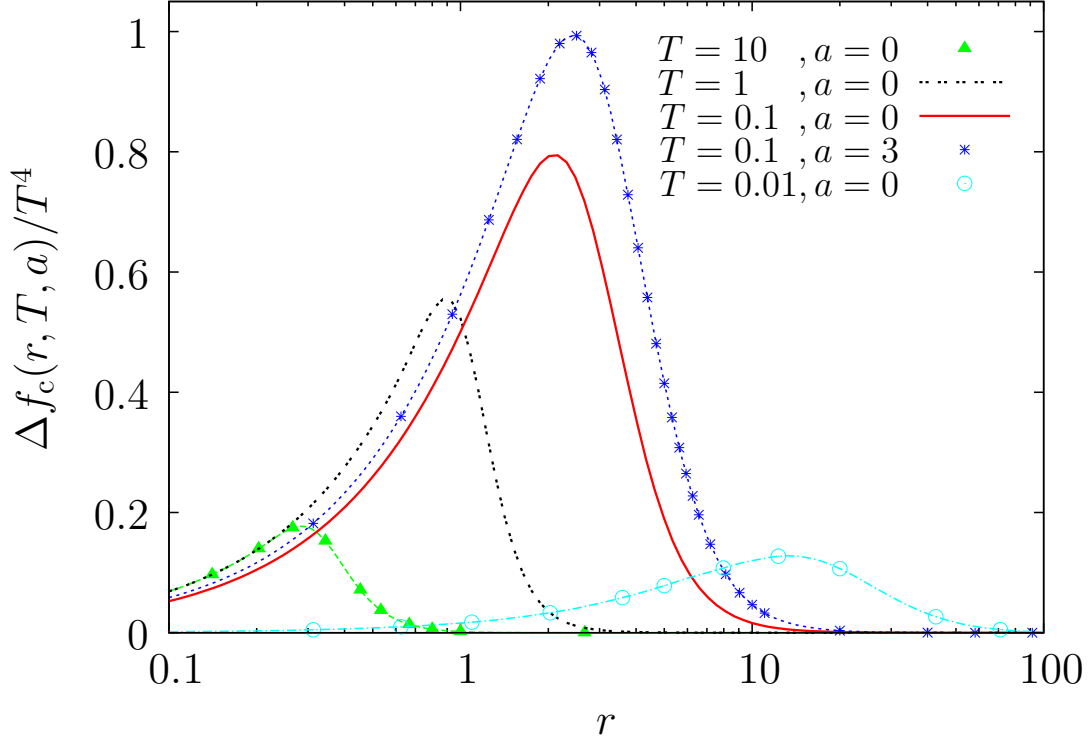
Figure 7.4: Radial (negative) thermal force density $\Delta f_c(r, T, a)$ for a sphere above a plate for different temperatures T in units of $R = 1$. The peak position as a function of r increases with decreasing temperature. Notice also that the thermal force density corresponding to $T = 0.1$ and $a = 3$ lies clearly above the one corresponding to $T = 0.1$ and $a = 0$ for sufficiently large r, resulting in a stronger thermal force for $a = 3$. The statistical error is below one percent.

energy density is potentially distributed over a larger region of space. Whether or not this broadening occurs depends on the details of the geometry, as worldlines at larger distances still have to intersect the Casimir surfaces.

In Fig. 7.4, we plot the radial distribution of the thermal force density of a sphere above a plate for various temperature values. Its peak position increases with decreasing temperature. This corresponds to the fact that low temperatures can still excite long-wavelength modes if the spectrum is not gapped. Figure 7.4 also demonstrates that any local approximation of the Casimir force such as the proximity force approximation (PFA) is generically bound to fail for a proper description of the geometry-temperature interplay; see, however, [164] for semitransparent surfaces. For experiments at low temperature, our results indicate that the idealized sphere-plate configuration requires the plate to be much larger than the sphere. Otherwise thermal edge effects have to be accounted for, being more severe than edge effects at $T = 0$.

7.3.3 Non-monotonic thermal forces

For standard materials, the Casimir force is generally attractive [70] and decreases monotonically with distance. The latter seems intuitively clear from spectral properties of the fluctuations: in this picture, the Casimir effect arises from the difference between the fluctuation spectrum in the presence of the surfaces and that of the trivial vacuum (at infinite surface separation). For increasing separation, the spectrum is expected to monotonically approach the vacuum spectrum, implying a monotonic force depletion.

A first non-monotonic behavior has been observed in a more involved piston-like geometry of two squares moving between metal walls [153]; similar observations hold for two cylinders near a sidewall [154]. Here, the non-monotonic behavior arises from a competition between the TE and TM modes of the electromagnetic fluctuations. Its strength is governed by the dependence of the force on a lateral geometry parameter. The example demonstrates that an unexpected behavior of the Casimir force may occur in the presence of competing scales (in this case: normal and lateral distances).

Here, we show that a non-monotonic behavior already exists for a single fluctuating scalar obeying Dirichlet boundary conditions on the surfaces (similar to a TM mode in a cavity-like configuration). This anomalous phenomenon requires a nonzero temperature and occurs for the thermal contribution to the Casimir force. This phenomenon is a prime example of the geothermal interplay.

Typical configurations used in experiments involve spheres or cylinders above a plate, which are open geometries without a spectral gap. Investigating the geothermal interplay for these geometries therefore is an urgent problem. For the fluctuating electromagnetic field, first results for the thermal Casimir force in the sphere-plate configuration have recently been obtained [82, 167] using scattering techniques.

In the limit of temperature being smaller than both the inverse sphere radius, $T \ll 1/R$, and the inverse sphere-plate distance, $T \ll 1/a$, the thermal force in [167] is always attractive for any value of a/R and monotonically decreasing with increasing separation a. By contrast, the thermal force derived in [82] using a truncated multipole summation shows a repulsive behavior for smaller distances and becomes attractive at larger distances. From their data, a non-monotonic behavior of the thermal force at larger distances $a/R \gg 1$ and low temperatures $TR \lesssim 1$ can be anticipated. Whereas both studies nicely agree in the limit of low temperature and small spheres, the seeming disagreement beyond the strictly asymptotic validity regimes of the two different expansions requires clarification.

In this chapter, we demonstrate that non-monotonic thermal forces indeed occur unambiguously for the sphere-plate and cylinder-plate configuration in the low-temperature region. Dealing with Dirichlet scalar fluctuations, we avoid additional complications from competing polarization modes. Most importantly, the occurrence of this anomalous behavior can be understood as a temperature-induced reweighting of different relevant fluctuations in a given geometry. This is at the heart of the geothermal interplay.

In the worldline picture, formalized by Eq. (7.3) and (7.4), the Casimir force arises from all worldlines that are attached to the plate and intersect the sphere (cylinder). Consider a worldline with center of mass polar coordinate r in the sphere-plate geometry at separation a, see Fig. 7.2. Upon integrating over propertime $\mathcal{T}$, the size of the worldlines is scaled but the center of mass projection onto the sphere stays fixed at r. Therefore, the worldline points that eventually intersect the sphere have to lie inside a cone with its tip attached to the plate at r, wrapping around the sphere, see Fig. 7.2.

Let us now reduce the sphere-plate separation a for a given worldline. As this moves the corresponding cone towards the plate (red dotted lines in Fig. 7.2), all points of a given worldline may drop out of the cone such that this worldline no longer contributes to the Casimir force. This is the mechanism that potentially *reduces* the Casimir force for smaller separations. The same arguments apply to the cylinder-plate configuration.

While this geometric argument is independent of any temperature, this loss mechanism of relevant fluctuations is negligible at zero temperature: the effect is outweighed by small worldlines intersecting sphere and plate near the point of closest separation, which dominate the zero-temperature Casimir force. By contrast, the finite-temperature propertime factor $\sim e^{-n^2\beta^2/(4\mathcal{T})}/\mathcal{T}^3$ favors the contribution of larger worldlines at low temperature and thus emphasizes the relevance of the loss mechanism at larger separations. Compare, for example, the force density for $a = 0$ and $T = 0.1$ with those for $a = 3$ and same temperature $T = 0.1$ in Fig. 7.4.

Whether or not a non-monotonic thermal force law arises then is a competition between small worldlines in the region of close separation and large worldlines on the scale of the thermal wavelength. If the contribution of the latter to the thermal force is dominant, the thermal force can increase for increasing distance as more and more worldlines can contribute, i.e., become relevant fluctuations.

With this general considerations in mind, let us now turn to a detailed analysis of the Casimir effect at finite temperature for the sphere-plate and cylinder-plate configurations.

7.4 Sphere above a plate

7.4.1 Expansion of the thermal force for $a \ll R$ and $T \ll 1/R$

We start with the expansion of the thermal force for $a \ll R$ and for small temperature $T \ll 1/R$. Following our general argument given above, no singularities in a appear in the limit $a \to 0$. Also, we expect that the thermal force decreases with decreasing R. This motivates an expansion of the thermal force with only positive exponents for a and R. Assuming integer exponents, dimensional analysis permits

$$\Delta F_{\mathrm{c}}(T) = c_0 R T^3 + c_1 a T^3$$

$$+ c_2 R^2 T^4 + c_3 a R T^4 + \mathcal{O}\left((a/R)^2, (TR)^5\right). \tag{7.16}$$

From our numerical results in the limit $a \to 0$, we observe a T^4 behavior of the thermal force, see Fig. 7.5. We conclude that $c_0 \approx 0$ is negligible with respect to c_2 in the regime $T > 0.01$, where numerical data is available.

In fact, we conjecture that c_0 vanishes identically, $c_0 = 0$; if so, also c_1 vanishes, since the configuration would otherwise be more sensitive to temperatures at small a than at $a = 0$. Our conjecture is supported by the following argument based on scaling properties: the dimensionless ratio of the thermal correction and the zero-temperature force has to be invariant under the rescaling

$$a \to a/\alpha, \quad R \to R/\alpha, \quad T \to \alpha T. \tag{7.17}$$

The same holds for the ratio of $\Delta F_c(a, T)$ at $a = 0$ and the zero-temperature force at $a \neq 0$. For $a \ll R$, we can use the PFA for the zero-temperature force, which to leading order yields $\sim R/a^3$. If $c_0 \neq 0$, this leading ratio would be $\sim c_0(aT)^3$ which is invariant under the rescaling (7.17); in addition, this ratio would be invariant under (7.17) with R fixed. If $c_0 = 0$, then this ratio is $\sim c_2 R a^3 T^4$ which is invariant only under the full transformation (7.17).

The result that for $c_0 \neq 0$ the thermal correction would exhibit the same R dependence as the zero-temperature force for small distances $a \ll R$ is counter-intuitive: whereas the radial force density in the small-distance limit at $T = 0$ is peaked right under the sphere near $r \simeq 0$, the thermal correction arises from contributions at much larger r, cf. Fig. 7.4.

As a simple estimate, we expect that the thermal correction is proportional to an effective area of the sphere,
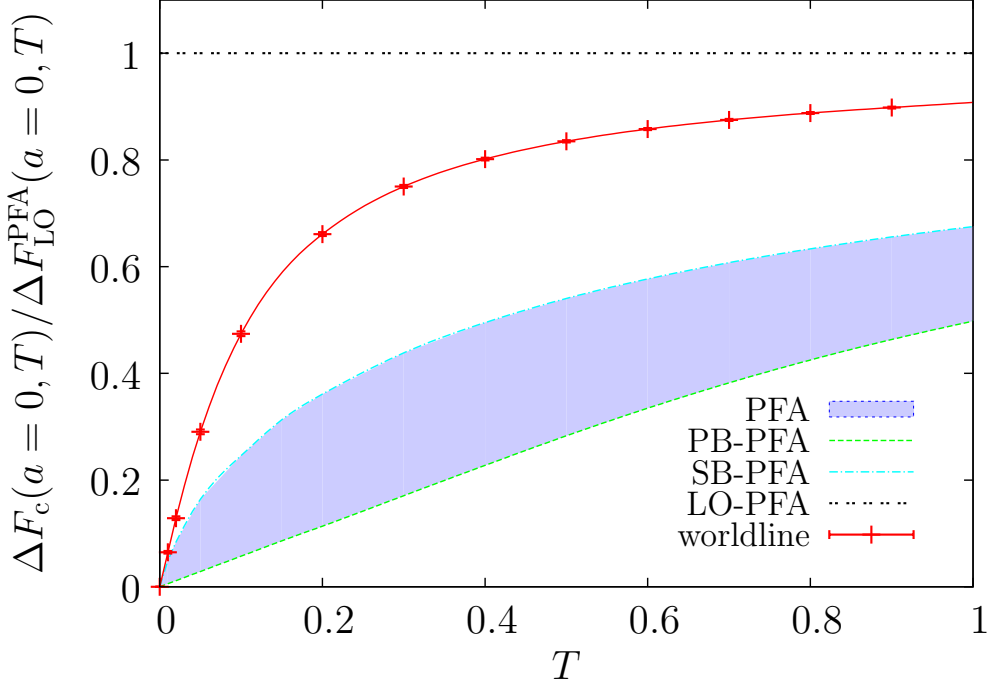
$$A_{\mathrm{eff}} \approx (a + R)2R + \frac{\pi R^2}{2},$$

Figure 7.5: Thermal Casimir force of a sphere above a plate in the limit $a \to 0$ and for $R = 1$. The worldline result and the PFA predictions are normalized to the leading-order PFA, cf. Eq. (7.20). The leading-order PFA predicts a T^3 behavior of the thermal force for all T. On the other hand, for small T the plate-based PFA and the worldline result see a T^4 behavior, whereas the sphere-based PFA sees a $T^4 \ln(T)$ one. For large $T \gg 1/R$ the behavior is T^3 for all curves. All predictions agree in the large T limit. For very small T, the worldline result runs into the blue area which spans the PFA predictions.

as seen by the worldlines. This estimate then is compatible with

$$c_0 = c_1 = 0$$

and

$$\frac{c_2}{c_3} \approx 1.8.$$

The question arises why the leading-order PFA approximation yields a T^3 behavior despite the additional scale R. The reason is that R appears only in the combination r^2/R in the force density, such that

$$T \to \alpha T, \quad r \to r/\alpha^2$$

leaves the force density invariant up to a multiplicative constant.
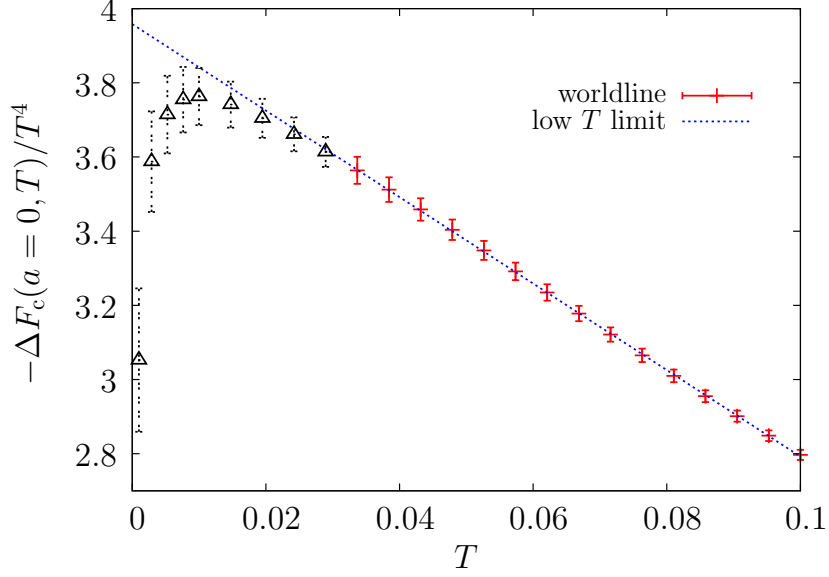
Figure 7.6: Low-temperature behavior of $-\Delta F_\mathrm{c}(T)/T^4$ for the sphere-plate configuration in the limit $a \to 0$ for $R = 1$. For $0.03 < T < 0.1$, we observe a linear behavior which can be fitted to $\Delta F_\mathrm{c}(a = 0, T) \approx -3.96\, R^2 T^4 + 11.66\, R^3 T^5$. We have used $40\,000$ loops with $2 \cdot 10^6$ ppl each. For $T < 0.03$, the number of points per loop used is not sufficient to resolve the sphere properly, inducing systematic errors (black triangles).
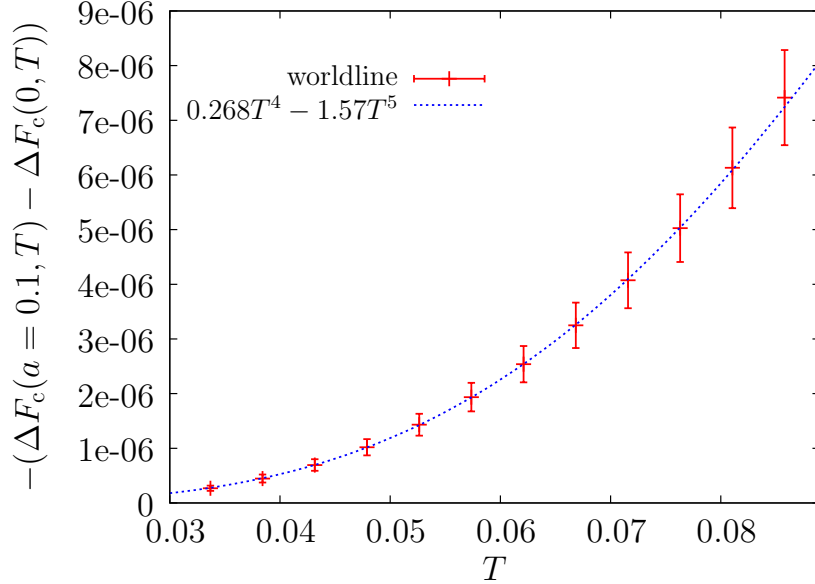

Figure 7.7: Plot of the a-dependent part of the (negative) thermal Casimir force for a sphere at $a = 0.1$ and $R = 1$ in the low-temperature regime. In the range $0.03 < T < 0.08$, the worldline data for $-(\Delta F_\mathrm{c}(0.1, T) - \Delta F_\mathrm{c}(0, T))$ is well approximated by $0.268\, T^4 - 1.57\, T^5$ (dashed blue curve), corresponding to a c_3 coefficient in Eq. (7.16) $c_3 \approx -2.7$. Note that the absolute value of the Casimir force has increased with a. We have used $40\,000$ loops with $2 \cdot 10^6$ ppl each.

Let us return to Eq. (7.16). For c_2 and c_3, we obtain numerically (see Fig. 7.6 and Fig. 7.7)

$$c_2 \approx -3.96(5), \quad c_3 \approx -2.7(2). \tag{7.18}$$

These numbers can be confirmed by the exact T-matrix representation [166].

Note that both coefficients have the same sign, implying that the absolute value of the thermal correction to the Casimir force *increases* with increasing a for sufficiently small a and T. This apparently anomalous behavior can be understood in geometric terms within the worldline picture [59], see also Sec. 7.3.3.

7.4.2 Critical temperature

The sphere-plate configuration has a critical temperature

$$T_{\mathrm{cr}} \simeq \frac{0.34(1)}{R}. \tag{7.19}$$

For $T > T_{\mathrm{cr}}$, the thermal force decreases monotonically for increasing sphere-plate separation a in accordance with standard expectations. For smaller temperatures $T < T_{\mathrm{cr}}$, the thermal force first increases for increasing separation, develops a maximum and then approaches zero as $a \to \infty$. The peak position is shifted to larger a values for increasing thermal wavelength, i.e., decreasing temperature. In all cases, the force remains attractive, see Fig. 7.8.

As an example, room temperature $T = 300$K corresponds to the critical temperature for spheres of radius $R \simeq 2.6\mu$m. For larger spheres, room temperature is above the critical temperature such that the thermal force is monotonic. For smaller spheres, the thermal force is non-monotonic at room temperature. If, for instance, $T = 70$K and $R = 1.6\mu$m, the thermal force increases up to $a \simeq 9\mu$m.

7.4.3 Comparison with the PFA

The high-temperature limit $T \gg 1/R$ agrees with the PFA prediction for $a \to 0$ and reads

$$\Delta F_{\mathrm{c}}(T \to \infty) = -\frac{\zeta(3)R}{2}T^3. \tag{7.20}$$

In the limit $a \to 0$, the leading-order PFA yields Eq. (7.20) for *all* T. This is because geometrically the leading-order PFA corresponds to approximating the sphere by a paraboloid, which is a scale-invariant configuration at $a = 0$. At
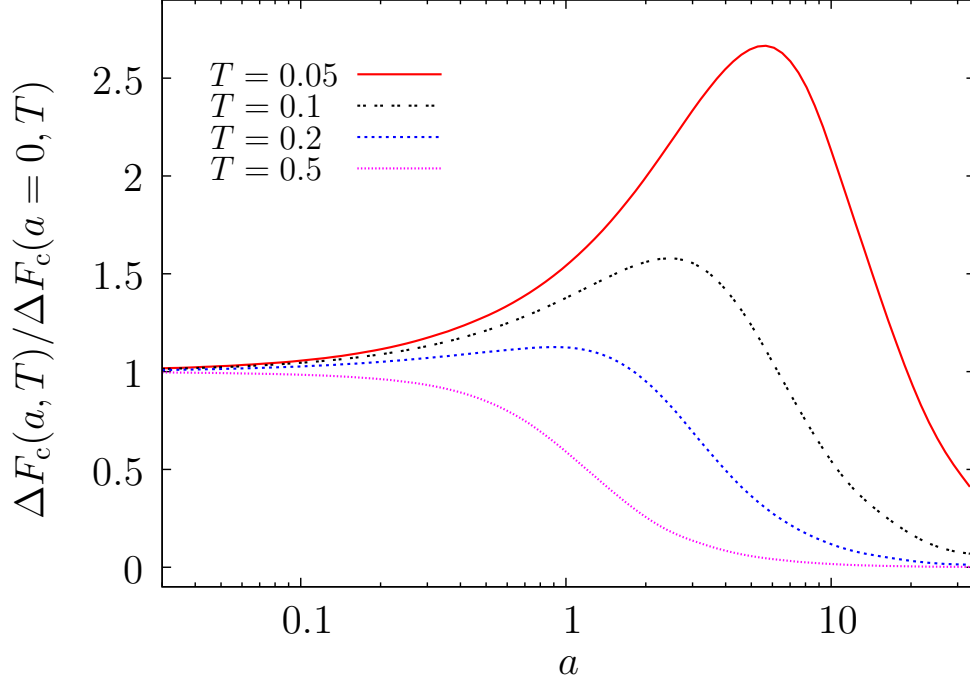
Figure 7.8: Thermal correction to the Casimir force of a sphere for various temperatures T and $R = 1$, normalized to the thermal force at $a = 0$. For sufficiently small temperatures, the absolute value of the thermal force correction $\Delta F(T)$ first *increases* with increasing a. For $T \leq 0.05$ the small a behavior is well described by $1 + a(2.68RT^4 - R^2 15.7\,T^5)/\Delta F(a = 0, T)$. This verifies the fit used in Fig. 7.7 with coefficient linear in $\sim a$ in front of T^5. From this prediction, we would expect the curves to be monotonically decreasing for $T > 2.7/15.7R \approx 0.17/R$ in the leading order. Due to higher-order terms, the $T = 0.2$ curve still increases slightly first. The statistical errors of the worldline calculation are of the order of the thickness of the curves.

finite a, the scale invariance is broken and a term $\sim +R\,\pi^3 a T^4/45$ appears on the right-hand side of Eq. (7.20) at low temperature in the leading-order PFA.

By contrast, we observe that the true $a \to 0$ limit is characterized by a T^4 behavior for small T and T^3 behavior for large T. Also, the sign of the correction at finite a is different: the full worldline result predicts an increase whereas the PFA correction reduces the absolute value of the force, see Fig. 7.7.

It is interesting to compare our results to another PFA scheme beyond the leading-order PFA: the plate-based PFA. This scheme is not scale invariant at $a = 0$, as the low-temperature limit for $a \ll R$ is also quartic and given by

$$\Delta F_{\mathrm{PB}}^{\mathrm{PFA}}(a \ll R, T \to 0) = -\frac{\pi^2 T^4}{90}\,\pi R^2. \tag{7.21}$$

Equation (7.21), in fact, corresponds to the thermal force density of two parallel plates integrated over the area of the region below the sphere, πR^2. Numerically,

the corresponding worldline coefficient is more than ten times larger than the PFA prefactor $\pi^3/90 \approx 0.345$.

In Eq. (7.21), the low-T behavior at finite a is exponentially suppressed, implying that the plate-based PFA prediction for c_3 is zero – which is again in contradiction with our worldline analysis.

In the other PFA scheme, the sphere-based PFA, the coefficient in front of T^4 is T dependent itself,

$$\Delta F_{\text{SB}}^{\text{PFA}}(a \ll R, T \to 0) = \frac{R^2(2\zeta'(4) + \zeta(4)(3 + 2\ln\left(\frac{RT}{\pi}\right)))}{\pi} T^4. \qquad (7.22)$$

For very small temperatures, this becomes $\sim T^4 \ln(T)$, such that the absolute value of the thermal force is larger than the worldline result as $T \to 0$.

The formulae (7.20)-(7.22) are derived in the next chapter. The thermal force at $a = 0$ is shown together with the PFA predictions in Fig. 7.5.

7.4.4 High temperature limit

We now turn to the high-temperature limit, in a strict sense corresponding to

$$T \gg \frac{1}{a} \quad \text{and} \quad T \gg \frac{1}{R}. \qquad (7.23)$$

The second requirement is automatically fulfilled in the small-distance limit $a \ll R$. Quantitatively, for large a, it turns out that the high-temperature regime is already approached for

$$T \gg \frac{1}{a} \quad \text{and} \quad T \ll \frac{1}{R}. \qquad (7.24)$$

A special case arises for $a \to 0$, where the high-temperature limit agrees with the PFA prediction Eq. (7.20) in the leading order. For $a > 0$, the high-temperature limit is linear in T and the total force becomes classical, i.e., independent of $\hbar c$. This behavior is rather universal being a simple consequence of *dimensional reduction* in high-temperature field theories, or equivalently, of the linear high-temperature asymptotics of bosonic thermal fluctuations [57, 131–134, 150]. In order to find the high-temperature limit, we perform the Poisson summation of the winding sum. The Poisson summation for an appropriate function f reads

$$\sum_{n=-\infty}^{\infty} f(n/T) = \sqrt{2\pi} T \sum_{k=-\infty}^{\infty} \hat{f}(2\pi kT), \qquad (7.25)$$

where $\hat{f}$ is the Fourier transform (including a $1/\sqrt{2\pi}$ prefactor) of f, see appendix A. Applying Eq. (7.25) to the winding sum, we obtain

$$2 \sum_{n=1}^{\infty} \exp\left(-\frac{n^2 \beta^2}{4\mathcal{T}}\right) = -1 + 2T\sqrt{\mathcal{T}\pi}$$

$$+ 4T\sqrt{\mathcal{T}\pi} \sum_{k=1}^{\infty} \exp\left(-\mathcal{T}(2\pi k T)^2\right). \tag{7.26}$$

For finite a, the propertime integral is bounded from below and the last term is exponentially vanishing as $\mathcal{T} \to \infty$. Evaluating the worldline integrals for the first two terms, we obtain

$$\Delta F_{\mathrm{c}}(a, T) = -F_{\mathrm{c}}(a) + T\widetilde{F}_{\mathrm{c}}(a). \tag{7.27}$$

The evaluation of $\widetilde{F}(a)$ is analogous to Eq. (6.12),

$$\widetilde{F}_{\mathrm{c}}(a) = -\frac{1}{8\sqrt{\pi}} \left\langle \int_0^\infty \mathrm{d}r\, r \int_{\mathcal{S}(r)}^\infty \frac{\mathrm{d}\mathcal{T}}{\mathcal{T}^{5/2}} \right\rangle, \tag{7.28}$$

where the support $\mathcal{S}(r)$ is the same as in the $T = 0$ case, see Eqs. (6.10) and (6.12).

The Casimir force remains attractive also for high temperatures. The function $\widetilde{F}_{\mathrm{c}}(a)$, normalized to the leading-order PFA prediction

$$\widetilde{F}_{\mathrm{LO}}^{\mathrm{PFA}}(a) = -\frac{R\zeta(3)}{8a^2}, \tag{7.29}$$

is shown in Fig. 7.9. The function $a^2\widetilde{F}_{\mathrm{c}}(a)$ is monotonically increasing on $0 < a < 100$ (similar to $a^3 F_{\mathrm{c}}(a)$). At small a, we obtain

$$\frac{\widetilde{F}_{\mathrm{c}}(a)}{\widetilde{F}_{\mathrm{LO}}^{\mathrm{PFA}}(a)} = 1 + (0.14 \pm 0.015)a. \tag{7.30}$$

In analogy to the zero-temperature force, we conjecture that also $a^2\widetilde{F}_{\mathrm{c}}(a)$ remains monotonically increasing and finally approaches a constant for $a \to \infty$. A consequence of this conjecture is that the high-temperature limit then has a simple form, $T \gg 1/a$, without any relation to R. Indeed, demanding

$$\Delta F_{\mathrm{c}}(a, T) = -F_{\mathrm{c}}(a) + T\widetilde{F}_{\mathrm{c}}(a, T) < 0 \tag{7.31}$$

for a fixed T, the limit $a \to \infty$ corresponds immediately to $T \gg 1/a$, since $a^3 F_{\mathrm{c}}(a)$ itself approaches a constant. Our numerical data shown in Fig. 7.9 is indeed compatible with this conjecture. However, the large-a limit is difficult to assess due to the onset of systematic errors for $a > 100$.
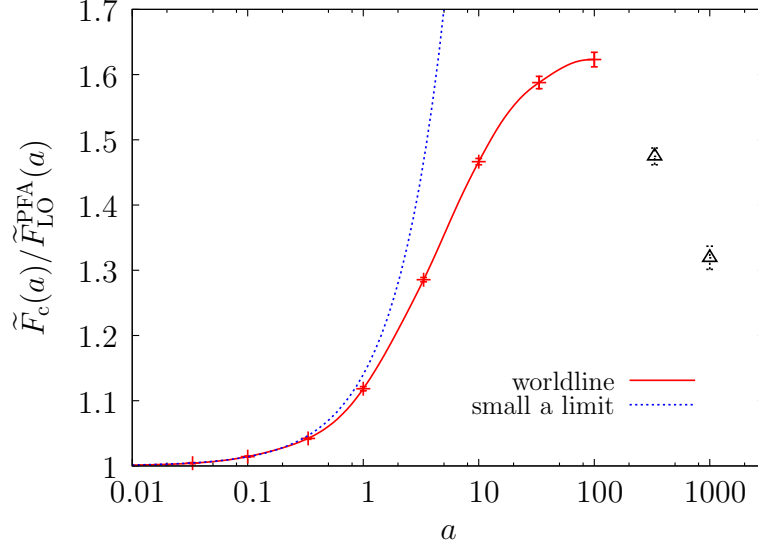
Figure 7.9: High-temperature coefficient $\widetilde{F}_c(a)$ for the sphere-plate configuration normalized to the corresponding PFA coefficient. At large a, the normalized coefficient is conjectured to approach a constant. For small a, the behavior is well described by $1 + (0.14 \pm 0.015)\, a$. For $a > 100$, systematic errors similar to those of Fig. 6.4 set in (black triangles); at finite temperature, these errors are even more pronounced due to a softer propertime exponent $5/2$.

7.4.5 Normalizing thermal force to zero temperature force

Comparing Fig. 6.4 and 7.9, we notice that the zero-temperature force $F_c(a)$ and the high temperature coefficient $\widetilde{F}_c(a)$ behave similarly. This is not surprising since $\widetilde{F}_c(a)$ in $D = 4$ Minkowski space corresponds to $F_c(a)$ in $D = 3$ Euclidean space due to dimensional reduction in the high-temperature limit.

For finite a, the high-temperature limit is already well reached for $T \gtrsim 1/2a$. In the PFA approximation, the weaker thermal force at not too small temperatures is normalized by the weaker zero-temperature force, leading to an accidental cancellation, such that for $T \gtrsim 1/2a$

$$\frac{\Delta \widetilde{F}_c(a)}{F_c(a)}\, T \approx \frac{90\, \zeta(3)}{\pi^3}\, aT \approx 3.49\, aT, \tag{7.32}$$

independently of R. A comparison between the full worldline result and the leading-order PFA for the normalized force is shown in Fig. 7.10 for various a and T. Since for small separations $a < R$, the leading-order PFA is a reasonable approximation already at medium temperature

$$1/2a > T > 1/2R,$$

see Fig. 7.5, we observe that the ratio between the thermal Casimir force and the zero-temperature result is surprisingly well described by the PFA for quite a wide parameter range. We stress that the PFA is inapplicable for each quantity alone.
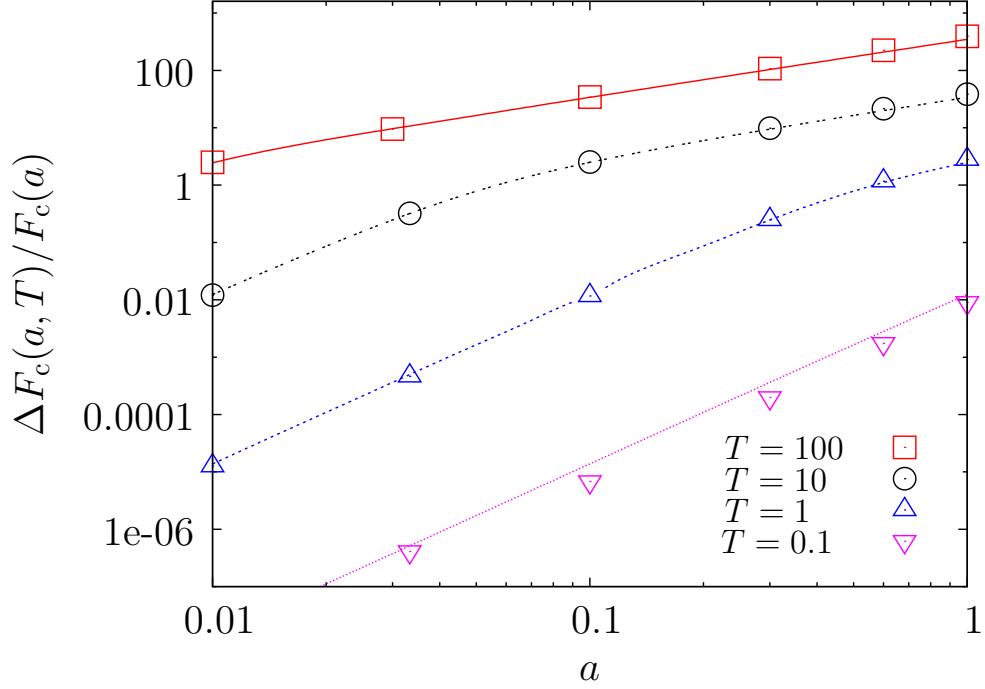
Figure 7.10: Thermal correction to the Casimir force for a sphere with $R = 1$ normalized to the zero temperature force for various temperatures and $a < R$. The worldline results (symbols) should be compared with the leading-order PFA estimate (lines). We observe that this ratio of thermal to zero-temperature force is surprisingly well described by the PFA for a wide parameter range, especially in the high-temperature regime. This happens because both $\widetilde{F}_c(a)$ and $F_c(a)$ increase with respect to the PFA with roughly the same rate, see Fig. 6.4 and Fig. 7.9.

7.5 Cylinder above a plate

The case of a cylinder above a plate is different from the sphere-plate case in two respects: first, the missing polar measure factor r reduces the weight of distant worldlines. Second, the probability for a given worldline to intersect the infinitely long cylinder is larger than for a sphere. We observe that these two effects seem to balance each other, leading again to a T^4 behavior at low T.

7.5.1 Expansion of the thermal force for $a \ll R$ and $T \ll 1/R$

In analogy to the sphere-plate case, we start with the expansion of the thermal force at low temperature T and for $a \ll R$ as in Eq. (7.17). Again, we allow only for positive exponents for a and R. Even though $\sqrt{R}$ terms appear in an $a/R \ll 1$ expansion at zero temperature, our numerical results at small finite temperatures,
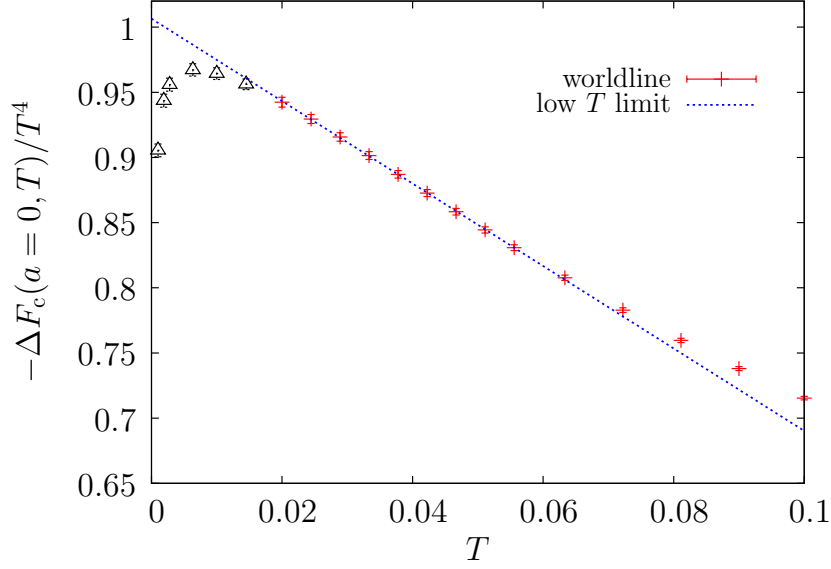
Figure 7.11: Low-temperature behavior of $-\Delta F_{\rm c}(T)/T^4$ for a cylinder above a plate for $R = 1$ in the limit $a \to 0$. For $0.02 < T < 0.06$, we observe a linear behavior. In the range $0.03 < T < 0.05$, our data can be fitted to the form $\Delta F_{\rm c}(a = 0, T)/L_y \approx -1.0065\,RT^4 + 3.163\,R^2T^5$. For $T < 0.02$, systematic errors due to worldline discretization artifacts lead to a fast decrease of the data (black triangles). We have used $44\,000$ loops with $2 \cdot 10^6$ ppl each.
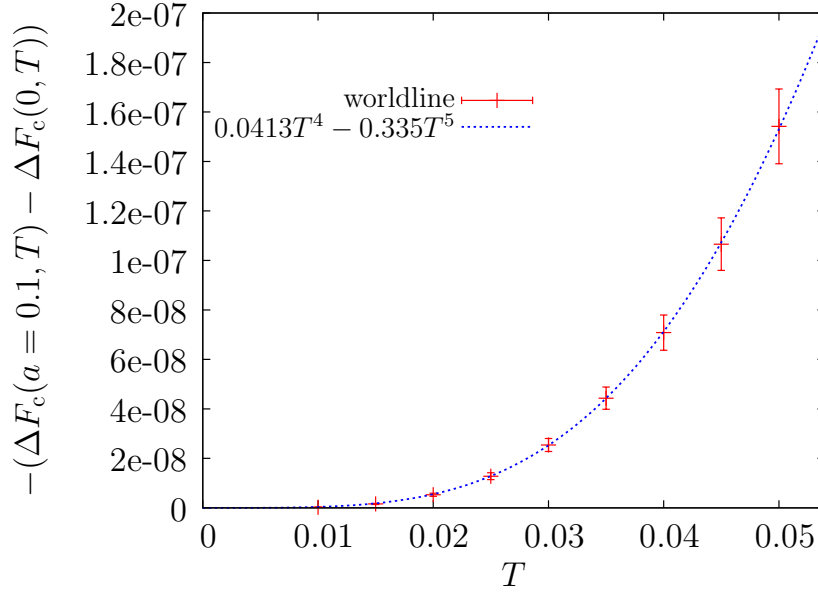
Figure 7.12: Plot of the a-dependent part of the (negative) thermal contribution to the Casimir force for the cylinder-plate configuration at $a = 0.1$ and $R = 1$ in the low-temperature regime. In the range $0.025 < T < 0.05$, the worldline data for $-(\Delta F_{\rm c}(0.1, T) - \Delta F_{\rm c}(0, T))$ is well approximated by $0.04125\,T^4 - 0.335187\,T^5$. We thus conclude that the c_3 coefficient in Eq. (7.33) is ≈ -0.4125. Note that the absolute value of the Casimir force has increased with a. We have used $44\,000$ loops with $2 \cdot 10^6$ ppl each.

somewhat surprisingly, are consistent with an expansion of the type

$$\frac{\Delta F_{\mathrm{c}}(T)}{L_y} = c_2 R T^4 + c_3 a T^4 + \mathcal{O}\left(T^{9/2}\right). \tag{7.33}$$

The potential leading-order terms $c_0\sqrt{R}T^{7/2}$ and $c_1\sqrt{a}T^{7/2}$ are expected to be zero similar to the sphere-plate case, see above, since the configuration of a cylinder above a plate is not invariant unter

$$a \to a/\alpha \quad \text{and} \quad T \to \alpha T.$$

We have no evidence for a term $\sim \sqrt{aR}T^4$, which would lead to a nonanalytic increase of the force. Thus at small temperatures, the powers of T are found to be integers in leading order. Similar to the sphere-plate case, we expect the low-temperature contributions to the thermal force to be proportional to the effective area

$$A_{\mathrm{eff}} \approx L_y(2R + a)$$

seen by the distant worldlines. This results in the rough estimate

$$\frac{c_2}{c_3} \approx 2,$$

which also implies that both coefficients have the same sign.

In the limit $a \to 0$, our data in the regime $T > 0.01$ is compatible with a T^4 behavior of the thermal force. For c_2 and c_3, we obtain (see Figs. 7.11 and 7.12)

$$c_2 \approx -1.007(7), \quad c_3 \approx -0.41(4). \tag{7.34}$$

As in the case of the sphere, both coefficients have the same sign, i.e., the absolute value of the thermal Casimir force increases with increasing a for sufficiently small a and $T < T_{\mathrm{cr}}$.

For the critical temperature, we obtain

$$T_{\mathrm{cr}} \approx \frac{0.31(1)}{R}. \tag{7.35}$$

As in the case of a sphere, the thermal force decreases monotonically with increasing a for $T > T_{\mathrm{cr}}$; below the critical temperature, the thermal force first increases up to a maximum and then decreases again approaching zero for $a \to \infty$. The position of the maximum depends on T and increases with inverse temperature, see Fig. 7.13. In both cases, however, the thermal force remains attractive.
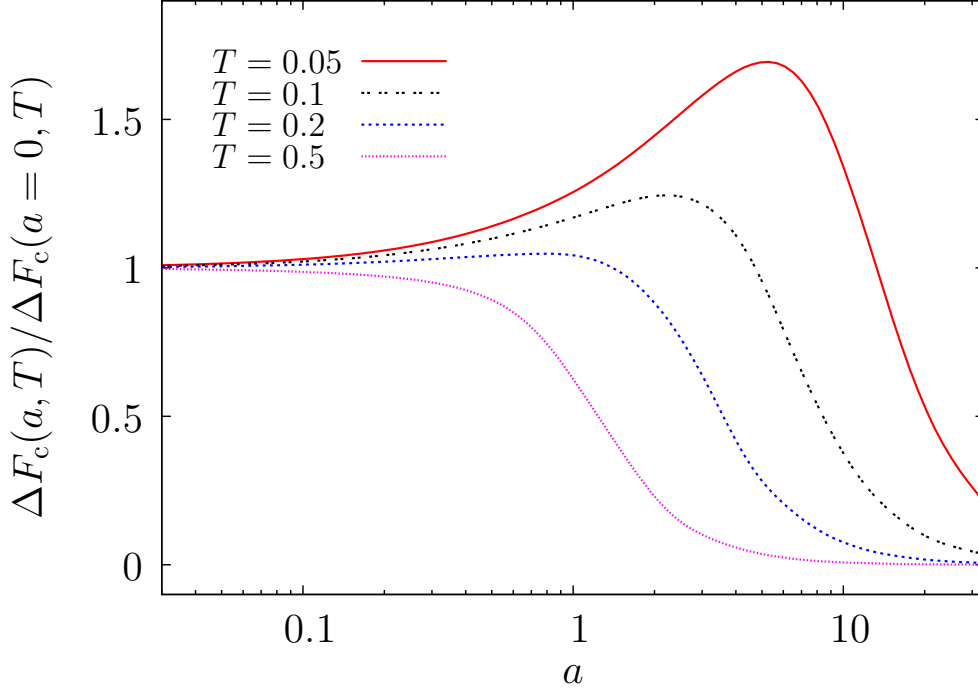
Figure 7.13: Thermal correction to the Casimir force of a cylinder above a plate for various temperatures T and $R = 1$ normalized to the thermal correction at $a = 0$. For sufficiently small temperatures, the absolute value of the thermal force $\Delta F(T)$ first *increases* with increasing a. For $T \leq 0.05$, the small-a behavior is well described by $a(0.4125T^4 - 3.35187 \, RT^5)/\Delta F(a = 0, T)$. This verifies the fit found for Fig. 7.12 with a coefficient linear in a in front of T^5. From this form, we would expect the curves to be monotonically decreasing for $T > 0.41/3.35R \approx 0.12/R$ to leading order. Due to higher-order terms the $T = 0.2$ curve still increases slightly at the beginning.

7.5.2 Comparison with the PFA

The high-temperature limit $T \gg 1/R$ agrees with the PFA prediction in the limit $a \to 0$ as expected,

$$\frac{\Delta F_{\mathrm{c}}(T \to \infty)}{L_y} = \frac{3 \, \zeta(1/2)\zeta(7/2)\sqrt{R}}{4\sqrt{2}\pi} T^{\frac{7}{2}} \tag{7.36}$$

$$\approx -0.278\sqrt{R} T^{\frac{7}{2}}.$$

As for the sphere, the leading-order PFA predicts the same force law (7.36) in the limit $a \to 0$ for *all* T. At finite a, the scale invariance is broken and a term $\sim +0.185a\sqrt{R}T^{9/2}$ appears on the right-hand side of Eq. (7.36) in leading-order PFA at low temperature.

By contrast, we observe different power laws for different temperatures in the limit $a \to 0$: a T^4 behavior for small T and $T^{7/2}$ behavior for large T. Also, the
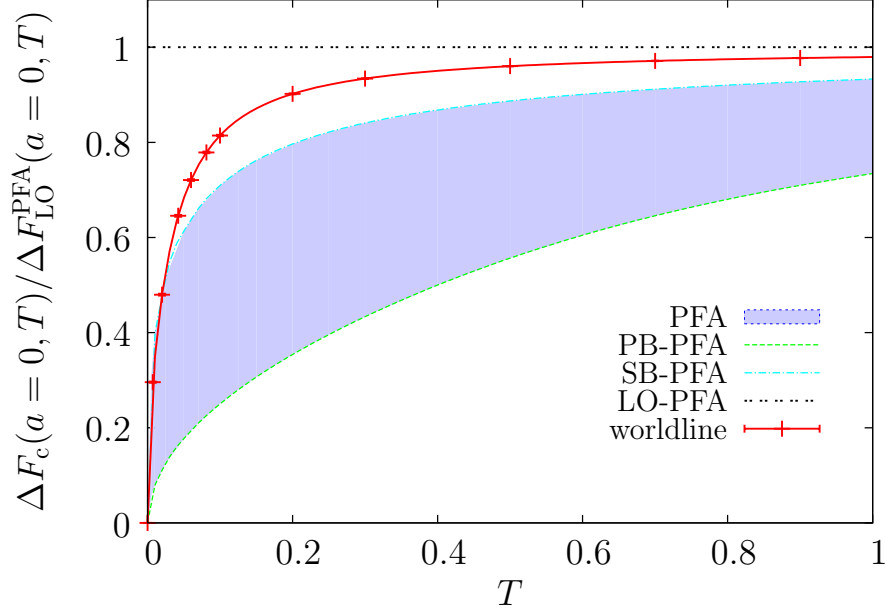
Figure 7.14: Normalized thermal contribution to the Casimir force of a cylinder above a plate for $R = 1$ in the limit $a \to 0$. The worldline result and the PFA predictions are normalized to the leading-order PFA Eq. (7.36). The leading-order PFA predicts a $T^{7/2}$ behavior of the thermal force for all T. On the other hand, worldline numerical data is compatible with a T^4 behavior for small $T \ll 1/R$ and a T^3 behavior for large $T > 1/R$. This is also observed in the plate-based PFA, whereas the cylinder based PFA goes as $T^4 \ln(T)$ for small T. All predictions agree in the high-temperature limit. The worldline result enters the blue area for small T into, which is the region spanned by the different PFA approximations.

sign of the finite-a correction of the full result is opposite to that of the PFA, see Fig. 7.12, all of which is reminiscent to the sphere-plate case.

Incidentally, the beyond-leading-order PFA schemes reflect the correct behavior much better. We observe that the cylinder-based PFA turns out to be the better approximation (as for the sphere-based PFA in the preceding section). This is different from the zero-temperature case.

For the plate-based and cylinder-based PFA, we obtain

$$\frac{\Delta F_{\mathrm{PB}}^{\mathrm{PFA}}(0, T \to 0)}{L_y} = -\frac{\pi^2 T^4}{90} 2R \tag{7.37}$$

$$\approx -0.219 \, RT^4,$$

$$\frac{\Delta F_{\mathrm{CB}}^{\mathrm{PFA}}(0, T \to 0)}{L_y} = \frac{RT^4 \left(3\pi^4 + 2\pi^4 \ln\left(\frac{RT}{2\pi}\right) + 180\zeta'(4)\right)}{90\pi^2} \qquad (7.38)$$

$$\approx (0.22 \ln(RT/2\pi) + 0.32)RT^4.$$

The plate-based result is equal to the thermal force of two parallel plates integrated over an area $2RL_y$. The plate-based coefficient is more than four times smaller than the worldline coefficient, whereas the leading coefficient of the cylinder-based formula becomes arbitrarily large as $T \to 0$. The formulae (7.37) and (7.38) are derived in the next chapter. The thermal contribution to the force in the limit $a \to 0$ is shown together with the PFA predictions in Fig. 7.14.

7.5.3 High temperature limit

Let us now investigate the high-temperature limit, which can be obtained by Poisson summation of the winding-number sum as in Eq. (7.26). A special case arises in the limit $a \to 0$, where the high-temperature limit corresponds to the PFA prediction Eq. (7.36) in leading order. For $a > 0$, the high-temperature limit is again linear in T and the total force "classical", i.e., independent of $(\hbar c)$,

$$\Delta F_{\mathrm{c}}(a, T) = -F_{\mathrm{c}}(a) + T\widetilde{F}_{\mathrm{c}}(a), \qquad (7.39)$$

as in Eq. (7.27). For $\widetilde{F}_{\mathrm{c}}(a)$, we obtain

$$\widetilde{F}_{\mathrm{c}}(a) = -\frac{L_y}{8\pi^{3/2}} \left\langle \int_0^\infty \mathrm{d}r \int_{\mathcal{S}(r)}^\infty \frac{\mathrm{d}\mathcal{T}}{\mathcal{T}^{5/2}} \right\rangle, \qquad (7.40)$$

where the support $\mathcal{S}(r)$ is the same as in the $T = 0$ case, see Eq. (6.18).

The Casimir force remains attractive also for high temperatures. The function $\widetilde{F}_{\mathrm{c}}(a)$, normalized to the leading-order PFA prediction

$$\widetilde{F}_{\mathrm{LO}}^{\mathrm{PFA}}(a) = -\frac{3\sqrt{R}\,\zeta(3)}{32\sqrt{2}\,a^{5/2}}, \qquad (7.41)$$

is shown in Fig. 7.15. The function $a^{5/2}\widetilde{F}_{\mathrm{c}}(a)$ is monotonically increasing for $0 < a < 1000$ and is reminiscent to $a^{7/2}F_{\mathrm{c}}(a)$. At small a, we obtain

$$\frac{\widetilde{F}_{\mathrm{c}}(a)}{\widetilde{F}_{\mathrm{LO}}^{\mathrm{PFA}}(a)} = 1 + (0.125 \pm 0.017)a. \qquad (7.42)$$

At large a, we find using Eq. (7.31) and the analytical zero-temperature law [67],

$$\frac{\widetilde{F}_{\mathrm{c}}(a)}{\widetilde{F}_{\mathrm{LO}}^{\mathrm{PFA}}(a)} \simeq 1.46(2)\frac{a^{5/2}}{(a+R)^2 \ln(a+R)}. \qquad (7.43)$$
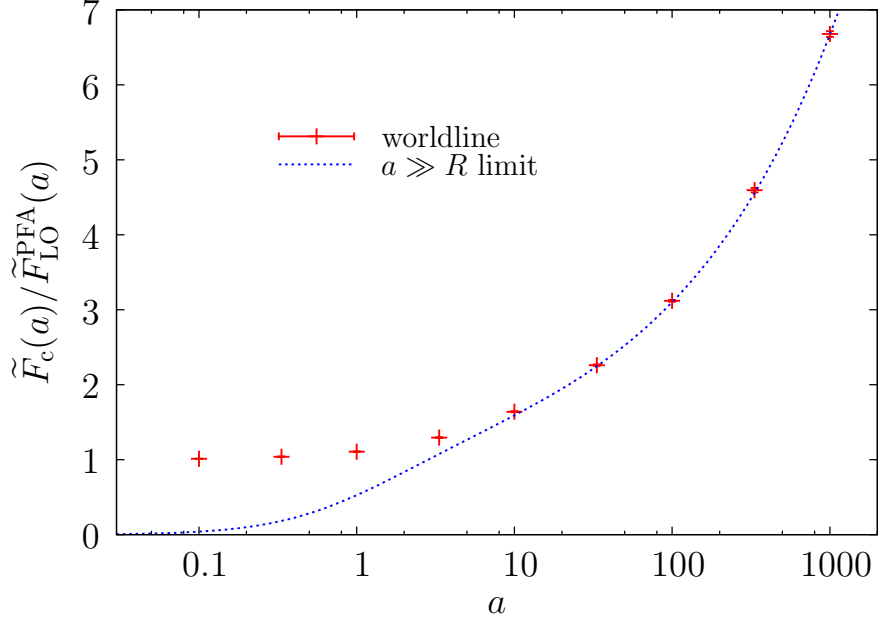
Figure 7.15: High-temperature coefficient $\widetilde{F}_c(a)$ normalized to the corresponding leading-order PFA coefficient for a cylinder above a plate. The large-a behavior is well described by Eq. (7.43). At small a, we find a behavior $\sim 1 + (0.125 \pm 0.017)a$.

7.5.4 Normalizing thermal force to $T = 0$ force

Let us finally remark that also in the case of a cylinder the thermal Casimir force normalized to the zero temperature result is well described by the PFA for $T \gtrsim 1/2a$. Analogously to Eq. (7.32), we conclude from the dimensional-reduction argument, that the ratio of thermal to zero-temperature force in the high-temperature limit $T \gtrsim 1/2a$ is approximately

$$\frac{\Delta \widetilde{F}_c(a)}{F_c(a)}\, T \approx \frac{72\,\zeta(3)}{\pi^3}\, aT \approx 2.79\, aT. \tag{7.44}$$

Also at medium temperatures this ratio is surprisingly well-described by the PFA, even better than in the case of a sphere, see Fig. 7.10. The normalized thermal force is shown in Fig. 7.16 for various a and T.
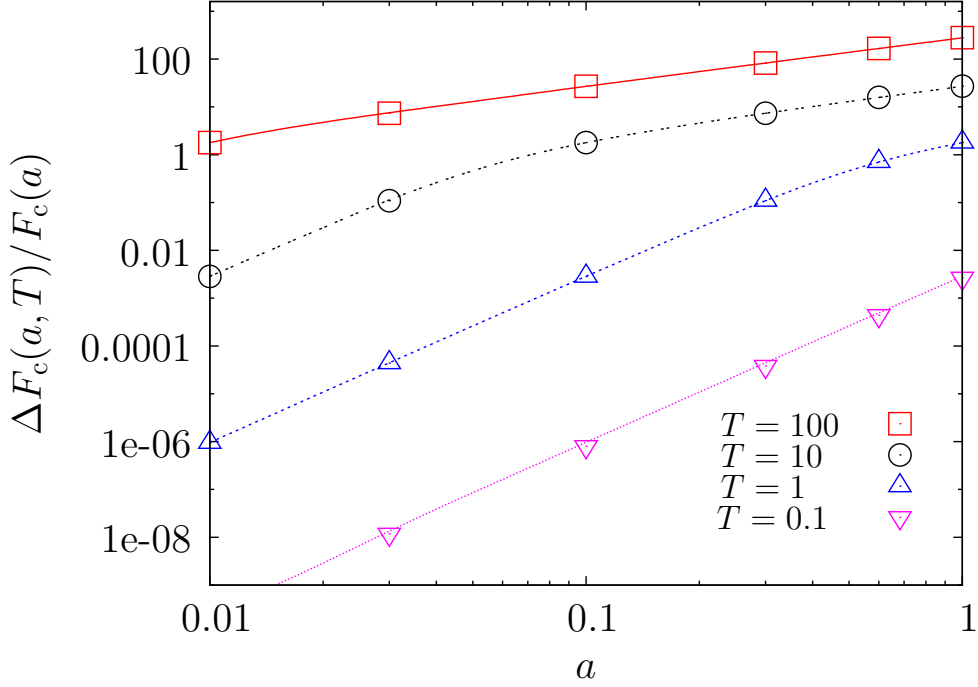
Figure 7.16: Thermal correction to the Casimir force for a cylinder with $R = 1$ normalized to the zero-temperature force for various temperatures and $a < R$. The worldline results (symbols) are in a better agreement with the leading-order PFA estimates (lines) than in the case of a sphere, see Fig. 7.10. The normalized PFA results agree with the worldline results for not too low T because again both $\widetilde{F}_c(a)$ and $F_c(a)$ increase with respect to the PFA with roughly the same rate, see Fig. 6.5 and Fig. 7.15.

7.5.5 Comparison with the result of Emig et al.

We can compare our results with those of an analytical result [67] in the limit

$$R \ll H = R + a. \tag{7.45}$$

The leading-order thermal contribution to the Casimir force in this computation based on scattering theory reads

$$\Delta F_c(a, T) = L_y T \int_0^\infty \frac{q e^{-2q(R+a)} \, \mathrm{st}(q)}{\ln(qR)} \, \mathrm{d}q, \tag{7.46}$$

where the integrand has been approximated to leading order in $\ln^{-1}(qR)$. Here, $\mathrm{st}(q)$ is a $2\pi T$ periodic sawtooth function which in the range from 0 to $2\pi T$ is given by

$$\mathrm{st}(q) = -\frac{q}{2\pi T} + \frac{1}{2}. \tag{7.47}$$

7 Sphere-plate and cylinder-plate at finite temperature

The authors of [67] have given a simple estimate of the integral for the limit $R \ll 1/2\pi T$ by replacing $\ln(qR)$ by $\ln(2\pi RT)$ and carrying out the resulting integral. We compare our worldline results with Eq. (7.46) as well as with the simple estimate in Fig. 7.17 and 7.18.

Here, we propose another estimate which is valid for arbitrary $T > 1/(R+a)$. In this case, the sawtooth function is approximately constant for $q < 1/(R+a)$. We approximate the logarithm by inserting the value q_0 for which $q \exp(-2q(R+a))$ is maximal:

$$q_0 = \frac{1}{2(R+a)}, \quad \text{for} \quad T > \frac{1}{R+a}. \tag{7.48}$$

In turn for $T < 1/(R+a)$, the logarithm can be approximated by insertion of the value q_0 where $q \exp(-2q(R+a))\mathrm{st}(q)$ has its first maximum:

$$q_0 = \frac{\pi T}{2}, \quad \text{for} \quad T < \frac{1}{R+a}. \tag{7.49}$$

We choose the first maximum, as the integrand is oscillating for $q > q_0$, such that cancellation can be expected to occur. However, choosing $q_0 \sim T$ always leads to a regular $T^4/\ln(T)$ behavior for small T, whereas Eq. (7.46) changes sign at very small T, see Figs. 7.17 and 7.18. We thus conclude that Eq. (7.46) is valid for not too small T.

The thermal contribution to the Casimir force then reads

$$\Delta F_{\mathrm{c}}(a, T) \approx \frac{-TL_y}{\ln(q_0 R)} \frac{\mathrm{d}}{\mathrm{d}a} \frac{\coth(2\pi(R+a)T) - \frac{1}{2\pi(R+a)T}}{8(R+a)}, \tag{7.50}$$

where

$$q_0 = 2\pi T \tag{7.51}$$

in the Emig et al. approximation [67], whereas

$$q_0 = \frac{1}{2(a+R)}, \quad \text{for} \quad T > 1/(R+a) \tag{7.52}$$

and

$$q_0 = \frac{\pi T}{2}, \quad \text{for} \quad T < 1/(R+a) \tag{7.53}$$

in the approximation proposed here. See Figs. 7.17 and 7.18 for the results at $a = 10R$ and $a = 100R$ respectively.
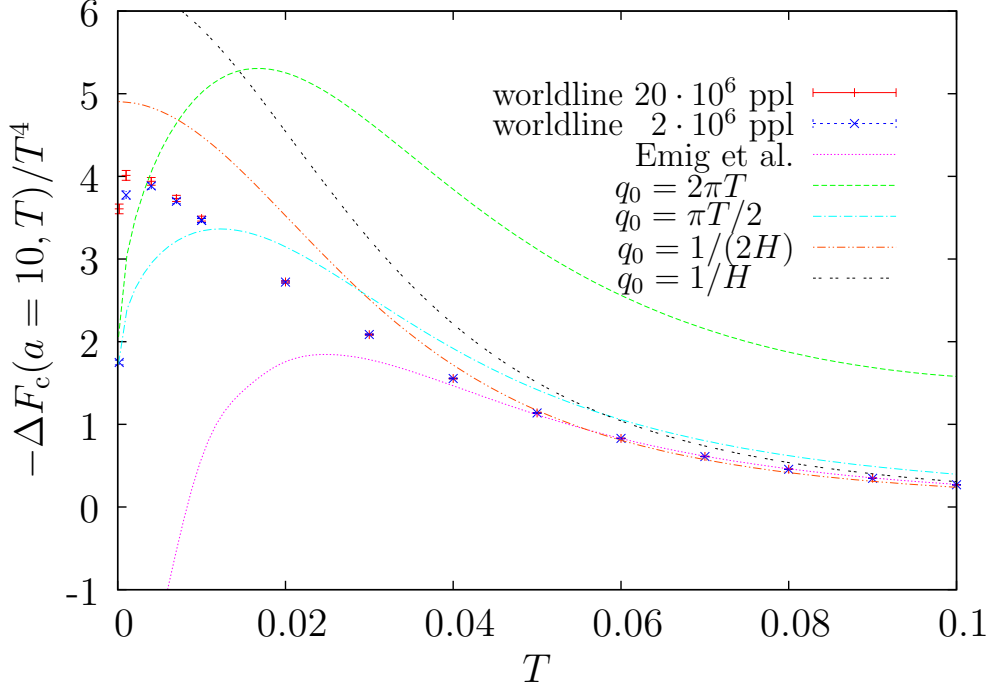
In the small T limit, Eq. (7.50) reads

Figure 7.17: Thermal contribution to the Casimir force for a cylinder above a plate for $a = 10$ and $R = 1$ compared with the analytic result (7.46) ("Emig et al." [67]) and various approximations as discussed in the text. Here, we use the abbreviation $H = R + a$. Remarkably, our proposed estimates using $q_0 = \pi R T/2$ and $q_0 = 1/2H$, cf. Eq. (7.50), describe the actual behavior far better than the analytic result (7.46), which changes sign as $T \to 0$. Also the $T > 1/(R+a)$ approximation using $q_0 = 1/2H$ remains a reasonable estimate even for $T < 1/(R+a)$. For the worldline data, we have used 5000 loops with $2 \cdot 10^7$ ppl and 7000 loops with $2 \cdot 10^6$ ppl.

$$\Delta F_c(a, T) = L_y \frac{2\pi^3(a + R)T^4}{45\ln(q_0 R)}. \tag{7.54}$$

Writing this as

$$\frac{\Delta F_c(a, T)}{L_y} = c(T, a, R)\, T^4, \tag{7.55}$$

the T^4 coefficient $c(T, a, R)$ always disappears for $q_0 \sim T$ as $T \to 0$. In our numerical worldline analysis, the systematic discretization errors lead to a vanishing of the corresponding coefficient as well, since the number of points per worldline becomes insufficient for resolution of the cylinder at very small T. For an increasing number of points per worldline, however, our data actually appears to point to a non-vanishing coefficient, see Figs. 7.17 and 7.18. In any case, we expect the leading-order multipole expansion which is behind the asymptotic result (7.46) to break down at low temperatures due to the geothermal interplay.
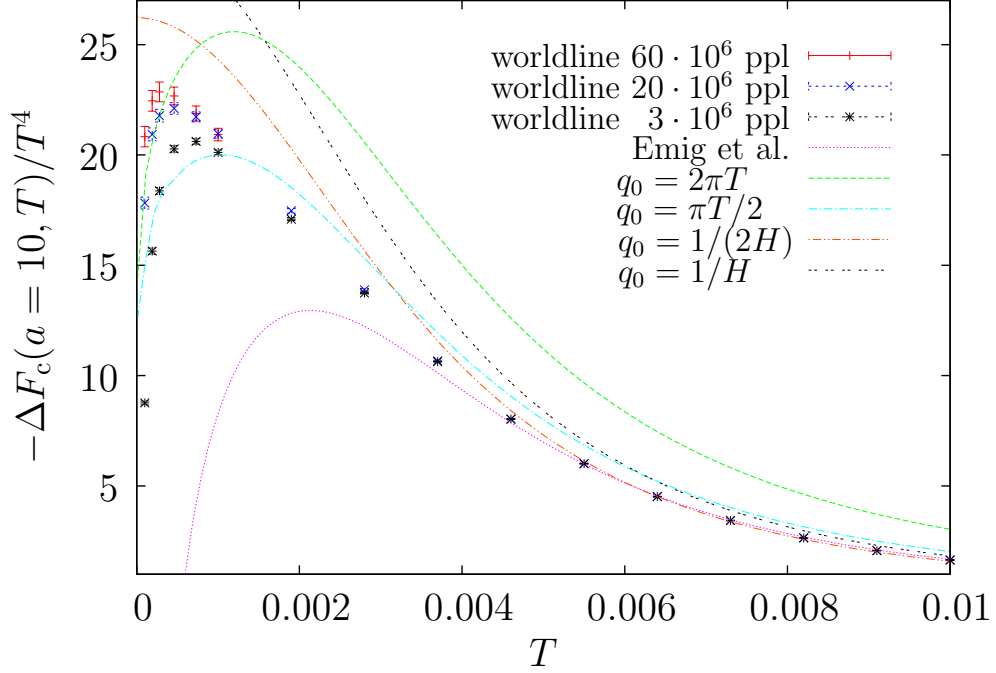
Figure 7.18: Thermal contribution to the Casimir force for a cylinder above a plate for $a = 100$ and $R = 1$ compared with the analytic result (7.46) ("Emig et al." [67]) and various approximations as discussed in the text. Even at such large separations, we observe that the analytic result (7.46) becomes invalid and even changes sign as the temperature approaches zero. Incidentally our simple $T > 1/(R + a)$ approximation using $q_0 = 1/2H$ describes the actual behavior rather well also for smaller temperatures. For the worldline data, we have used 2500 loops with $6 \cdot 10^7$, 5000 loops with $3 \cdot 10^7$ ppl and 14000 loops with $3 \cdot 10^6$ ppl.

For large T on the other hand, Eq. (7.50) becomes

$$\Delta F_c(a, T) = -\frac{L_y \left(1 - T\pi(a + R)\right)}{8\pi \ln(q_0 R)(R + a)^3}. \tag{7.56}$$

We observe that the negative of the T-independent part approaches the zero-temperature limit of the Casimir force for large a/R faster if we choose

$$q_0 = \frac{1}{R + a} \tag{7.57}$$

rather than $q_0 = 1/2(R + a)$. This choice of $q_0 = 1/(R + a)$ then constitutes our second estimate for $T > 1/(R + a)$.

For not too small T, the analytic result and the various q_0 approximations nicely agree with our worldline data, see Figs. 7.17 and 7.18. For higher temperature, the behavior becomes $\sim T$ and the different results acquire different slopes which partly disagree for $T \to \infty$.

For $a = 10$ and high T, the analytic result (7.46) becomes

$$\Delta F_{\mathrm{c}}(a, T) \sim 0.000424 L_y T, \tag{7.58}$$

the $q_0 = 1/(R + a)$ approximation yields

$$\Delta F_{\mathrm{c}}(a, T) \sim 0.000431 L_y T, \tag{7.59}$$

and the $q_0 = 1/2(R + a)$ approximation

$$\Delta F_{\mathrm{c}}(a, T) \sim 0.000334 L_y T. \tag{7.60}$$

The numerical worldline result is

$$\Delta F_{\mathrm{c}}(a, T) \sim 0.00041(3) L_y T. \tag{7.61}$$

At $a = 100$ and high T, the analytic result is

$$\Delta F_{\mathrm{c}}(a, T) \sim 2.57 \cdot 10^{-6} L_y T, \tag{7.62}$$

the $q_0 = 1/(R + a)$ approximation yields

$$\Delta F_{\mathrm{c}}(a, T) \sim 2.66 \cdot 10^{-6} L_y T, \tag{7.63}$$

and the $q_0 = 1/2(R + a)$ approximation

$$\Delta F_{\mathrm{c}}(a, T) \sim 2.31 \cdot 10^{-6} L_y T, \tag{7.64}$$

The worldline result is

$$\Delta F_{\mathrm{c}}(a, T) \sim 2.4(9) \cdot 10^{-6} L_y T. \tag{7.65}$$

For large $a + R$, the temperature coefficient becomes $0.125/(R + a)^2 \ln(R + a)$ for both $q_0 = 1/(R + a)$ and $1/2(R + a)$. For the analytic result the corresponding prefactor is greater than 0.123 and may become 0.125 for $H \rightarrow \infty$. The corresponding worldline prefactor is 0.116(2), see Eq. (7.43).

7.6 Conclusions

In this chapter, we have analyzed the geometry-temperature interplay in the Casimir effect for the case of a sphere or a cylinder above a plate. Since finite-temperature contributions to the Casimir effect are induced by a thermal population of the fluctuation modes, the geometry has a decisive influence on the thermal corrections as the mode spectrum follows directly from the geometry. A strong geometry-temperature interplay can generically be expected whenever the length scale set by the thermal wavelength is comparable to typical geometry scales.

Within our comprehensive study of the Casimir effect induced by Dirichlet scalar fluctuations for the sphere-plate and cylinder-plate geometry, we observe several signatures of this geometry-temperature interplay: the thermal force density is delocalized at low temperatures. This is natural as only low-lying long-wavelength modes in the spectrum can be thermally excited at low T. As a consequence, the force density is spread over length scales set not only by the geometry scales but also by the thermal wavelength. This implies that local approximation techniques such as the PFA are generically inapplicable at low temperatures. Quantitatively, the low-temperature force follows a T^4 power law whereas the leading-order PFA correction predicts a T^3 behavior. Only for ratios of thermal to zero-temperature forces, we observe a potentially accidental agreement with the PFA prediction for larger temperatures. Here, the errors introduced by the PFA for the aspect of geometry appear to cancel, whereas the thermal aspects might be included sufficiently accurately.

In the past, the analysis of experimental data has conventionally been based on the T^3 behavior as predicted by the leading-order PFA. As typical experiments operate in a parameter range of $a/R = \mathcal{O}(0.01 \ldots 0.001)$ and $TR = \mathcal{O}(10 \ldots 100)$, our results suggest that the error on the thermal correction from PFA-estimates is only on the percent level. Once, TR approaches $TR \simeq 1$, the difference between PFA estimates in various forms and the full result of the thermal correction can exceed the 10% level. In such a case, our results suggest that the influence of the geometry can be estimated by using the PFA only for the ratio between the thermal correction and the zero-temperature force, cf. Figs. 7.10 and 7.16.

Another signature of this geometry-temperature interplay is the occurrence of a non-monotonic behavior of the thermal contribution to the Casimir force. Below a critical temperature, this thermal force first grows for increasing distance and then approaches zero only for larger distances. This phenomenon is not related to a competition of polarization modes as in [153, 154], but exists already for the

Dirichlet scalar case. The phenomenon can be understood within the worldline picture of the Casimir effect [59, 60] being triggered by a reweighting of relevant fluctuations on the scale of the thermal wavelength. From this picture, it is clear that the phenomenon is not restricted to spheres or cylinders above a plate; we expect it to occur for general compact or semi-compact objects in front of surfaces, as long as the lateral surface extension is significantly larger than the thermal wavelength. In fact, another consequence of the delocalized force density is that edge effects due to finite plates or surfaces will be larger for the thermal part than for the zero-temperature force.

Furthermore, we have presented a general argument that low-temperature corrections to Casimir forces become much more easily accessible by taking the (formal) contact limit $a \to 0$ (only for the thermal contributions), as thermal corrections remain well behaved in this limit. Whereas the existence of this limit is well known for parallel plates, we have argued that the same result holds for general geometries. The existence of this limit is also a reason why thermal corrections, for instance in the perpendicular-plate case, can be determined analytically. We expect that this observation will be useful for many other geometries as well. This should lead to practical simplifications also in other field theory approaches, such as functional-integral approaches [62, 63], scattering theory [67, 70, 72, 75, 79], and mode summation [77].

Our results have been derived for the case of a fluctuating scalar field obeying Dirichlet boundary conditions on the surfaces. For different fields or boundary conditions, the temperature dependence can significantly differ from the quantitative results found in this work. This is only natural as different boundary conditions can strongly modify the fluctuation spectrum. For instance, the thermal part of the free energy in the sphere-plate case exhibits different power laws for Dirichlet or Neumann boundary conditions in the low-temperature and small-distance limit [167]. For future realistic studies of thermal corrections, all aspects of geometry, temperature, material properties, boundary conditions and edge effects will have to be taken into account simultaneously, as their mutual interplay inhibits a naive factorization of these phenomena.

8 PFA from the worldline approach

For reasons of comparison, we work out in detail the proximity-force approximation (PFA) for the sphere-plate and cylinder-plate case in a self-consistent way. In addition to explicit formulae, we relate the PFA to an approximate treatment of the worldline path integral. This helps to understand the differences between the exact and approximate treatments.

8.1 The proximity-force approximation (PFA)

The proximity force approximation is a scheme for estimating Casimir energies between two objects. In this approach, the surfaces of the bodies are treated as a superposition of infinitesimal parallel plates, and the Casimir energy is approximated by

$$E^{\mathrm{PFA}}(a) = \int_{\Sigma} \varepsilon^{\mathrm{PP}}(h) \, \mathrm{d}\sigma. \tag{8.1}$$

Here, one integrates over an auxiliary surface Σ, which should be chosen appropriately. The quantity $\varepsilon^{\mathrm{PP}}(h)$ denotes the energy per unit area of two parallel plates at a distance h, which at zero temperature reads

$$\varepsilon^{\mathrm{PP}}(h) = -\frac{c_{\mathrm{PP}}}{h^3}, \tag{8.2}$$

where $c_{\mathrm{PP}} = \pi^2/1440$ for the Dirichlet scalar case.

As the PFA does not make any reference to boundary conditions, all the formulas in this chapter are analogously valid for the electromagnetic case; all force formulae then have to be multiplied by a factor of two for the two polarization modes.

At finite temperature, the corresponding expression is

$$\frac{\Delta \varepsilon^{\mathrm{PP}}(h)}{c_{\mathrm{PP}}} = \frac{1}{h^3} - \frac{90T}{h^2} \sum_{n=1}^{\infty} \frac{\coth(2n\pi hT) + 2n\pi hT \operatorname{csch}^2(2n\pi hT)}{\pi^3 n^3}. \tag{8.3}$$

The distance has to be measured along the normal to Σ. The two extreme cases in which Σ coincides with one of the two surfaces provides us with a region spanning the inherently ambiguous estimates of the PFA.

For a sphere at a distance a above a plate, we thus integrate either over the plate ("plate-based" PFA), or over the sphere ("sphere-based" PFA), see Fig. 8.1. The Casimir force is then obtained by taking the derivative of (8.1) with respect to a. However, for the "sphere-based" PFA, $\mathrm{d}h/\mathrm{d}a \neq 1$ (see below). This implies that deriving the force estimate from the PFA of the energy in general is not the same as setting up the PFA directly for the force. The latter would correspond to a surface integral over the parallel-plates force per unit area. In this work, we use the derivation via the energy (8.1).

The dependence of the PFA prediction on the choice of Σ disappears in the limit $a \to 0$ at zero temperature to leading order. This result shall be called "leading-order" PFA. It can also be obtained by expanding the surface of the sphere/cylinder to second order from the point of minimal distance to the plate and then using the "plate-based" PFA for this expansion.

The corresponding expressions for h read

$$h_{\mathrm{PB}} = a + R - \sqrt{R^2 - r^2}, \tag{8.4}$$

$$h_{\mathrm{SB}} = h_{\mathrm{CB}} = \frac{a + R}{\cos(\theta)} - R, \tag{8.5}$$

$$h_{\mathrm{LO}} = a + \frac{r^2}{2R}. \tag{8.6}$$

For h_{PB}, we integrate over $[-R, R]$, for h_{LO} over all r and for h_{SB}, h_{CB} over $[-\pi/2, \pi/2]$ with an appropriate measure. Note that right underneath the sphere (cylinder) all h are equal to a. Demanding $\mathrm{d}\theta = \mathrm{d}r$ for $\theta \to 0$ we can transform the integration over θ into an integration over r in a simple way by the substituting $\sin(\theta) \to r/R$. The integral then goes from $-R$ to R, and the corresponding h reads

$$h_{\mathrm{SB}} = h_{\mathrm{CB}} = -R + R\frac{a + R}{\sqrt{R^2 - r^2}}. \tag{8.7}$$

Also a measure factor resulting from $R\mathrm{d}\theta = R/\sqrt{R^2 - r^2}$ and $\mathrm{d}h/\mathrm{d}a$ have to be taken into account. At zero temperature, we can absorb these factors into the new effective height

$$h_{\mathrm{SB-eff}} = h_{\mathrm{CB-eff}} = \frac{\sqrt{R}\left(a + R - \sqrt{R^2 - r^2}\right)}{(R^2 - r^2)^{1/4}}. \tag{8.8}$$
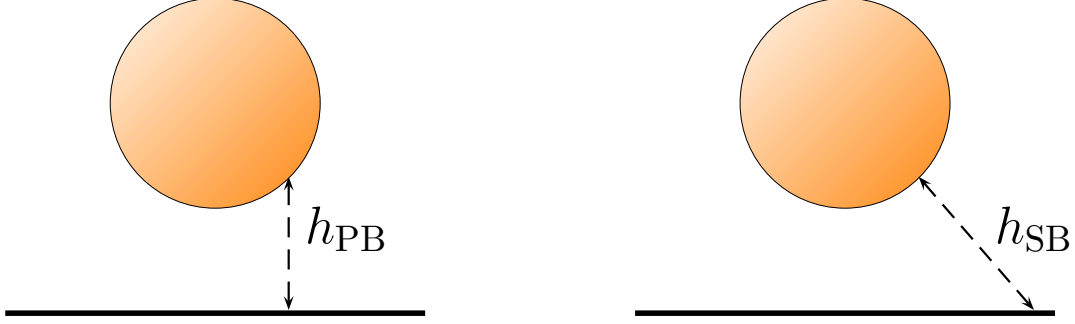
Figure 8.1: The proximity force approximation (PFA) for a sphere above a plate. The distance to be put into the parallel plates formula is conventionally measured along the normal to an auxiliary surface. The two extreme choices for this surface are either the plate or the sphere. Taking the lower plate as a "basis" (left panel) leads to the distance function h_{PB} ("plate-based" PFA). Taking the sphere as a basis (right panel) leads to a different distance function h_{SB} ("sphere-based" PFA). These two choices are not equivalent and result in different force laws.

With or without the prefactors, $h_{\mathrm{SB/CB}}$ is always greater than h_{PB} and h_{LO} and diverges for $r \to R$. Since the factor approaches 1 for small r, all functions h coincide in this limit.

The PFA can also be developed within worldline formalism. Calculating the Casimir force density for two parallel plates, we have to determine that value of propertimes $\mathcal{T}$ for which one-dimensional worldlines, attached to one of the plates, touch the other plate for the first time. This event is encoded in the lower bound of the proper time integral, whereas the upper bound is set to infinity. Thus, we obtain

$$f_{\mathrm{c}}^{\mathrm{PP}}(h,\beta) = -\frac{1}{32\pi^2}\left\langle \int_{(h/\lambda)^2}^{\infty} \sum_{n=-\infty}^{\infty} \frac{e^{-\frac{n^2\beta^2}{4\mathcal{T}}}}{\mathcal{T}^3}\mathrm{d}\mathcal{T} \right\rangle. \tag{8.9}$$

The representation (8.9) is suitable for zero and low temperatures, whereas for high temperatures one should use in (8.9) the Poisson resummed winding sum (7.26). We encounter cumulants of worldline extents λ in low and high temperature limits which can be determined via the analytic expression [53], also see Eq. (4.18),

$$\left\langle \lambda^D \right\rangle = D(D-1)\Gamma(D/2)\zeta(D). \tag{8.10}$$

Let us now point out the difference between the PFA and the worldline approach. In the PFA, we always use one-dimensional worldlines to determine the distance, whereas the worldline dimension in the full formalism corresponds to the dimension of the geometry. To obtain the Casimir force for configurations containing
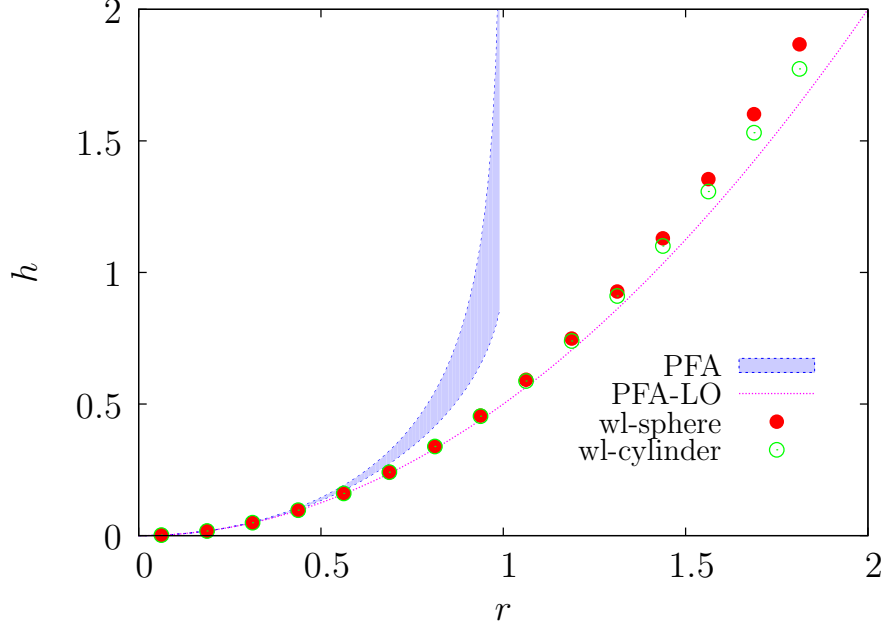
Figure 8.2: The effective heights predicted by the PFA for $a = 0$, $R = 1$ and $T = 0$ compared with those of worldline numerics for a sphere and a cylinder, respectively, obtained from the $T = 0$ force density. The PFA predictions lie in the blue area which is bounded by Eq. (8.4) from below and by Eq. (8.8) from above. The effective heights seen by worldlines are well approximated by the leading order PFA for r not too large. We conclude that for small a/R the force is described best by the leading order order PFA, since for small a/R the force density is concentrated around $r = 0$.

one infinite plate in the worldline formalism, we integrate over this infinite plate as in the plate-based approach. However, the integration does not stop at the end of the second body, which in the present case is a sphere or cylinder. At arbitrarily large distances, there are still worldlines which see the sphere/cylinder, i.e., we have to integrate to infinity. We therefore expect the leading-order PFA to reflect best the exact force laws. However, the propertime support is not the same, and thus worldlines see an effective height different from the one of the leading-order PFA, see Fig. 8.2 and 8.3.

The shape of the effective worldline height is roughly the same for zero and high temperatures. But at low temperature, the worldlines are reweighted. Only worldlines for large propertimes contribute considerably and thus worldlines at larger distances from the sphere become increasingly more important. Also their inner structure comes into play. Using the "plate-based" PFA, we ignore these effects and take into account only the region below the sphere/cylinder with the same function h_{PB}; hence, the result is expected to be too small.
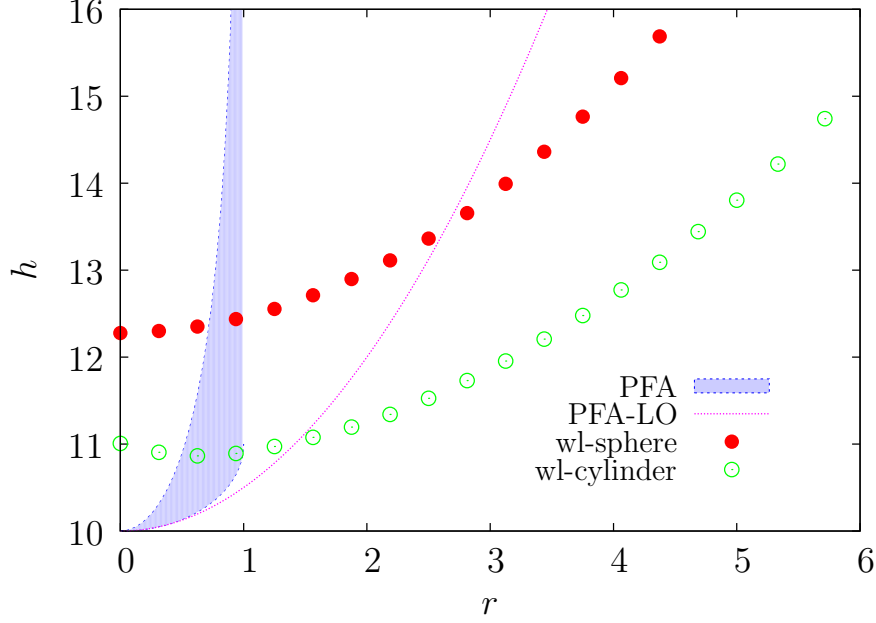
Figure 8.3: The effective heights predicted by the PFA for $a = 10$, $R = 1$ and $T = 0$ compared with those of worldline numerics for a sphere and a cylinder, respectively, obtained from the $T = 0$ force density. Note that the effective height for the cylinder is in a local maximum at $r = 0$. At greater separations the heights seen by worldlines are on average lower than the PFA predictions resulting in greater Casimir force. Also at larger separations the leading order PFA reflects best the actual situation, while the "sphere/cylinder based" PFA turns out to be the worst.

Incidentally, using instead of one-dimensional straight lines two-dimensional circles improves the PFA predictions: the next-to-leading order correction to the Casimir force at zero temperature obtains a correct sign, and also non monotonic thermal Casimir force arises. The corresponding height is then given by the diameter of the circle intersecting both surfaces. The predictions are improved due to the fact that the two-dimensional circles reflect the spatial extent of the worldlines, and d-dimensional worldlines are d-dimensional spheres on average. However, whereas in general the full PFA underestimates the Casimir force at zero temperature, the "circle-PFA" overestimates the worldline results for sphere- and cylinder-plate configurations in the small distance limit. The "circle-PFA" is illustrated in Fig. 8.4. We will not pursue the "circle-PFA" in the remainder of this chapter.

In the following, we apply Eq. (8.9) (multiplied by dh/da if necessary) to find the PFA expressions for the sphere and cylinder above an infinite plate, respectively.
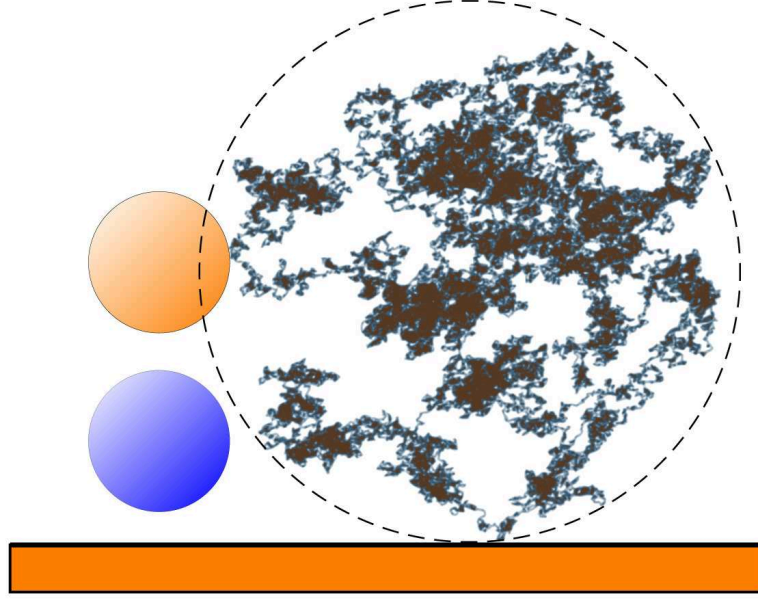
Figure 8.4: Sketch of the "circle-PFA" approximation for the sphere-plate configuration. The worldlines are approximated by circles (dashed line). Only those worldlines intersecting both boundaries contribute to the Casimir force. If the sphere-plate separation is reduced (blue sphere), the sphere can become invisible for a given worldline. This is the underlying mechanism for the non-monotonic thermal force, see Sec. 7.3.3. This mechanism remains valid if instead of worldlines one uses circles.

8.2 Sphere above a plate

8.2.1 Leading-order PFA

For the sphere, the evaluation of the leading-order PFA results in an especially simple expression,

$$-\frac{\mathrm{d}}{\mathrm{d}a}E_{\mathrm{LO}}^{\mathrm{PFA}} = 2\pi\,c_{\mathrm{PP}}\frac{\mathrm{d}}{\mathrm{d}a}\int_0^\infty \frac{r\,\mathrm{d}r}{(a+r^2/2R)^3} \qquad (8.11)$$

$$= 2\pi R\,c_{\mathrm{PP}}\frac{\mathrm{d}}{\mathrm{d}a}\int_a^\infty \frac{\mathrm{d}h_{\mathrm{LO}}}{h_{\mathrm{LO}}^3}$$

$$= 2\pi R\,\varepsilon^{\mathrm{PP}}(a).$$

Obviously, the relation

$$F_{\mathrm{LO}}^{\mathrm{PFA}} = 2\pi R\,\varepsilon^{\mathrm{PP}}(a)$$

remains valid also at finite temperature. We thus obtain

$$F_{\text{LO}}^{\text{PFA}}(a, T = 0) = -\frac{2\pi R\, c_{\text{PP}}}{a^3} = -\frac{\pi^3 R}{720 a^3}. \tag{8.12}$$

At finite T and small aT ($aT \lessgtr 1/2$), Eq. (8.9) yields

$$\Delta F_{\text{LO}}^{\text{PFA}}(a, T) = -\frac{R\,\zeta(3)}{2} T^3 + \frac{aR\,\pi^3}{45} T^4. \tag{8.13}$$

For large aT ($aT \gtrless 1/2$), the expression (8.3) leads directly to

$$\Delta F_{\text{LO}}^{\text{PFA}}(a, T) = \frac{\pi^3 R}{720 a^3} - \frac{R\,\zeta(3)}{8 a^2} T \tag{8.14}$$

$$= -F_{\text{LO}}^{\text{PFA}}(a, 0) + T \widetilde{F}_{\text{LO}}^{\text{PFA}}(a). \tag{8.15}$$

Note that at $a = 0$ the leading-order PFA predicts a T^3 behavior of the thermal force for all T. At finite a, the validity of the low-temperature limit is independent of R. With increasing a, the absolute value of the PFA thermal force is always reduced, irrespective of T, quite the contrary to the full worldline results as discussed in the main text.

8.2.2 Plate-based PFA

Using Eq. (8.9), we obtain

$$-\Delta F_{\text{PB}}^{\text{PFA}}(a, T) = \frac{1}{8\pi} \int_0^R r\, \mathrm{d}r \left\langle \sum_{n=1}^{\infty} \int_{h_{\text{PB}}^2/\lambda^2}^{\infty} \frac{e^{-\frac{\beta^2 n^2}{4\mathcal{T}}}}{\mathcal{T}^3} \, \mathrm{d}\mathcal{T} \right\rangle$$

$$= \frac{\zeta(4) R^2}{\pi \beta^4} + \frac{1}{\pi} \sum_{n=1}^{\infty} \left\langle \frac{a e^{-\frac{n^2 \beta^2 \lambda^2}{4 a^2}} (a + 2R)}{n^4 \beta^4} - \frac{e^{-\frac{n^2 \beta^2 \lambda^2}{4(a+R)^2}} (a + R)^2}{n^4 \beta^4} \right.$$

$$\left. - \frac{\sqrt{\pi}(a + R)\lambda \mathrm{Erfc}\left(\frac{n\beta\lambda}{2a}\right)}{2 n^3 \beta^3} + \frac{\sqrt{\pi}(a + R)\lambda \mathrm{Erfc}\left(\frac{n\beta\lambda}{2(a+R)}\right)}{2 n^3 \beta^3} \right\rangle . \tag{8.16}$$

Let us first analyze Eq. (8.16) for $a = 0$,

$$\Delta F_{\text{PB}}^{\text{PFA}}(a = 0, T) = -\frac{\zeta(4) R^2}{\pi} T^4$$

$$+ \frac{1}{\pi} \sum_{n=1}^{\infty} \left\langle \frac{e^{-\frac{n^2 \lambda^2}{4 T^2 R^2}} R^2}{n^4} T^4 - \frac{\sqrt{\pi} R\lambda \mathrm{Erfc}\left(\frac{n\lambda}{2 T R}\right)}{2 n^3} T^3 \right\rangle . \tag{8.17}$$

Equation (8.17) distinguishes low- $(T \ll 1/R)$ and high-temperature $(T \gg 1/R)$ regimes. The low-temperature regime is already well approached for $T \lesssim 1/2R$. For higher T, the thermal force is in the high-temperature regime, $T \gtrsim 1/2R$.

At low temperatures, we have a T^4 behavior which is given by the first term in Eq. (8.17). For higher T, this T^4 term is canceled by the T^4 term with the exponential function, such that the leading behavior is given by the T^3 term. Then, expanding Eq. (8.17), we get a T^2 contribution:

$$\Delta F_{\mathrm{PB}}^{\mathrm{PFA}}(a = 0, T) = -\frac{\zeta(3)R}{2}T^3 + \frac{\zeta(2)}{4\pi}\left\langle \lambda^2 \right\rangle T^2$$

$$= -\frac{\zeta(3)R}{2}T^3 + \frac{\zeta(2)\zeta(2)}{2\pi}T^2. \tag{8.18}$$

Subtracting Eq. (8.18) from Eq. (8.17) and performing the Poisson resummation, we obtain the full $T \gtrsim 1/2R$ behavior at $a = 0$

$$\Delta F_{\mathrm{PB}}^{\mathrm{PFA}}(0, T) = -\frac{\zeta(3)RT^3}{2} + \frac{\pi^3 T^2}{72} - \frac{\zeta(3)T}{8R} + \frac{\pi^3}{1440R^2}. \tag{8.19}$$

Thus, the leading large-T behavior at $a = 0$ is $\sim T^3$.

Let us now consider the case $a \neq 0$. For $a \ll R$ and low temperature

$$T \lesssim \frac{1}{2(R + a)} \approx \frac{1}{2R},$$

we have a T^4 behavior given by the first term in Eq. (8.16). The dependence on a is exponentially suppressed. This corresponds to the case of two parallel plates with an area of πR^2, where the dependence on a is suppressed exponentially as well.

At medium temperature,

$$2(R + a) \approx 2R \gtrsim \frac{1}{T} \gtrsim 2a,$$

only the second and fourth term in Eq. (8.16) are exponentially suppressed and can be neglected. The leading order can be found by expanding the remainder and considering only the converging sums.

To find the subleading terms, we again perform the Poisson resummation. For medium temperature $2R \gtrsim 1/T \gtrsim 2a$ and $a \ll R$, we then obtain

$$\Delta F_{\mathrm{PB}}^{\mathrm{PFA}}(a, T) = \frac{a(a + 2R)\pi^3 T^4}{90} - \frac{(a + R)\zeta(3)T^3}{2} \tag{8.20}$$

$$+ \frac{\pi^3 T^2}{72} - \frac{\zeta(3)}{8(a + R)}T + \frac{\pi^3}{1440(a + R)^2}.$$

The high-temperature limit,

$$\frac{1}{T} \lesssim 2a,$$

can be performed irrespective of the actual value a/R by summing up the whole Eq. (8.16). The result reads

$$\Delta F_{\mathrm{PB}}^{\mathrm{PFA}}(a,T) = \frac{\pi^3 R^2(3a+2R)}{1440a^3(a+R)^2} - \frac{R^2\,\zeta(3)}{8a^2(a+R)}T \tag{8.21}$$

$$= -F_{\mathrm{PB}}^{\mathrm{PFA}}(a,0) + T\widetilde{F}_{\mathrm{PB}}^{\mathrm{PFA}}(a). \tag{8.22}$$

Note that Eq. (8.21) reduces to Eq. (8.14) for $a \to 0$ as it should.

For a larger than $a \approx R$, the following temperature behavior occurs. At low temperature $1/T \gtrsim 2(R+a)$, a T^4 behavior arises from the first term in Eq. (8.16). At higher temperatures, the behavior becomes rapidly linear as given by Eq. (8.20), being valid for $1/T \lesssim 2a$.

The plate-based force can be obtained in closed form from Eq. (8.3) also without using the worldline language:

$$\Delta F_{\mathrm{PB}}^{\mathrm{PFA}}(a,T) = \frac{\pi^3 R^2(3a+2R)}{1440a^3(a+R)^2} - \frac{T}{8}\sum_{n=1}^{\infty}\left[\frac{\coth(2n\pi(a+R)T)}{(a+R)n^3}\right.$$

$$\left. + \frac{\mathrm{csch}^2(2an\pi T)\left[2an\pi RT + (R - (a+R)/2)\sinh(4an\pi T)\right]}{a^2 n^3}\right]. \tag{8.23}$$

8.2.3 Sphere-based PFA

For the sphere-based PFA, the thermal Casimir force is given by

$$\Delta F_{\mathrm{SB}}^{\mathrm{PFA}}(a,T) = -\left\langle \frac{R^2}{8\pi}\int_0^{\pi/2}\sin(\theta)h'_{\mathrm{SB}}(a)\mathrm{d}\theta\int_{h_{\mathrm{SB}}^2/\lambda^2}^{\infty}\sum_{n=1}^{\infty}\frac{e^{-\frac{n^2\beta^2}{4\mathcal{T}}}}{\mathcal{T}^3}\,\mathrm{d}\mathcal{T}\right\rangle, \tag{8.24}$$

where $h_{\mathrm{SB}}(a)$ is given by (8.5). For $a=0$, we obtain the PFA approximation using the worldline language

$$\Delta F_{\mathrm{SB}}^{\mathrm{PFA}}(a=0,T) = \left\langle \frac{2R^2\ln\left(\frac{2RT}{n\lambda}\right)}{n^4\pi}T^4 - \frac{\gamma R^2\zeta(4)}{\pi}T^4 + \frac{R\zeta(3)}{2}T^3\right.$$

$$\left. - \sum_{n=1}^{\infty}\frac{R^2 T^4}{4n^4\pi}\left(4 + \frac{n^2\lambda^2}{R^2 T^2}\right)\exp\left(-\frac{n^2\lambda^2}{4T^2 R^2}\right)\left(\pi\mathrm{Erfi}\left(\frac{n\lambda}{2RT}\right) - \mathrm{Ei}\left(\frac{n^2\lambda^2}{4R^2 T^2}\right)\right)\right\rangle, \tag{8.25}$$

where γ is Euler's constant. The expansion in T does not terminate after a few terms, so we concentrate on the two leading coefficients. The coefficient in front of T^4 contains the worldline average $\langle \ln \lambda \rangle$. For an analytical expression, we note that

$$\ln \lambda = m \ln \lambda^{1/m}.$$

For large m, we get $\lambda^{1/m} \to 1$, such that we can expand the logarithm,

$$\langle \ln \lambda \rangle = \langle \lim_{m \to \infty} m(\lambda^{1/m} - 1) \rangle = -1 - \gamma/2 + \ln(2\pi), \tag{8.26}$$

where we have used Eq. (8.10).

Thus, the small-T limit of Eq. (8.25) reads

$$\Delta F_{\mathrm{SB}}^{\mathrm{PFA}}(0,T) = \frac{R^2(2\zeta'(4) + \zeta(4)(3 + 2\ln(\frac{RT}{\pi})))}{\pi} T^4 - R^3 \zeta(5) T^5. \tag{8.27}$$

At $a = 0$, the PFA estimate $|\Delta F_{\mathrm{SB}}^{\mathrm{PFA}}(a = 0, T)|$ lies above $|\Delta F_{\mathrm{PB}}^{\mathrm{PFA}}(a = 0, T)|$, see Fig. 7.5. For not too small T, the worldline result lies above both these PFA predictions, but due to the logarithm in the T^4 coefficient, the sphere-based PFA becomes larger at smaller T, such that the worldline force enters the area spanned by the PFA prediction, see Fig. 7.5.

The high-temperature limit can be obtained by expanding Eq. (8.25) about $T = \infty$. The converging terms give the leading-order behavior. For the subleading orders, one has to perform the Poisson summation. However, the integral involved is rather complicated and may still be inflicted with artificial convergence problems. The leading-order behavior for $a = 0$ and large T reads

$$\Delta F_{\mathrm{SB}}^{\mathrm{PFA}}(0,T) = -\frac{R\zeta(3)}{2} T^3 + \frac{\pi^3}{72} T^2 + \mathcal{O}(T), \tag{8.28}$$

and corresponds to the leading behavior of the plate-based limit (8.19).

Let us turn to the case of finite a. Expanding Eq. (8.24), we obtain the a dependent part of the thermal force,

$$\Delta F_{\mathrm{SB}}^{\mathrm{PFA}}(a,T) - \Delta F_{\mathrm{SP}}^{\mathrm{PFA}}(0,T) = \frac{2aR\zeta(4)T^4}{\pi}$$

$$\times \left(1 - \frac{a}{2R} + \frac{a^2}{3R^2} - \frac{a^3}{4R^3} + \ldots \right). \tag{8.29}$$

The series in parentheses has a form of $(R/a)\ln(1 + a/R)$, which we verified explicitly to 10th order. Assuming that this form holds to all orders, we get

$$\Delta F_{\mathrm{SB}}^{\mathrm{PFA}}(a,T) - \Delta F_{\mathrm{SP}}^{\mathrm{PFA}}(0,T) = \frac{R^2 \pi^3 T^4}{45} \ln\left(1 + \frac{a}{R} \right). \tag{8.30}$$

Note that the first two terms in Eq. (8.29) agree with the T^4 coefficient of the plate-based formula (8.20); we also see that the absolute value of the thermal force decreases with increasing a. As Eq. (8.30) was obtained by interchanging summation and integration, we cannot expect Eq. (8.30) to describe the full a dependence for all a and T. Indeed at a fixed, the thermal correction $\Delta F_{\mathrm{SB}}^{\mathrm{PFA}}(a, T)$ becomes $\sim T$ as $T \to \infty$, which is clearly not the case for Eq. (8.30).

We can estimate the range of applicability of Eq. (8.30) as follows. At high temperature and $a \approx 0$, all PFA estimates agree. For large T, the leading behavior is $\sim T^3$, see e.g. Eq. (8.28). With increasing a the force is still attractive. Demanding $\Delta F_{\mathrm{SB}}^{\mathrm{PFA}}(a, T) < 0$, we see that that Eq. (8.30) leads to a positive thermal force for $a \gtrsim 1/T$. On the other hand, in the low-temperature regime, the $a = 0$ contribution is given by Eq. (8.27). Taking only the leading contribution into account and demanding $\Delta F_{\mathrm{SB}}^{\mathrm{PFA}}(a, T) < 0$, we again obtain that the force becomes positive at $a \gtrsim 1/T$. These rather rough estimates demonstrate that the validity range for a becomes narrower with increasing temperature. For very small a, however, the thermal correction is linear in a irrespectively of T, whereas the dependence on a in the plate-based PFA is exponentially suppressed for small $T \ll 1/(R + a)$.

At large temperatures $T > 1/a$, we have the familiar situation

$$\Delta F_{\mathrm{SB}}^{\mathrm{PFA}}(a, T) = -F_{\mathrm{SB}}^{\mathrm{PFA}}(a, 0) + T \widetilde{F}_{\mathrm{SB}}^{\mathrm{PFA}}(a), \tag{8.31}$$

where

$$F_{\mathrm{SB}}^{\mathrm{PFA}}(a, 0) = -\frac{\pi^3 \left(6a^2 - 3aR + 2R^2\right)}{1440 a^3 R} - \frac{\pi^3 \ln\left(\frac{a}{a+R}\right)}{240 R^2}, \tag{8.32}$$

and

$$\widetilde{F}_{\mathrm{SB}}^{\mathrm{PFA}}(a) = \frac{(R - 2a)\zeta(3)}{8a^2} - \frac{\ln\left(\frac{a}{a+R}\right)\zeta(3)}{4R}. \tag{8.33}$$

8.3 Cylinder above a plate

8.3.1 Leading-order PFA

Unfortunately, a simple relation similar to $F_{\mathrm{LO}}^{\mathrm{PFA}} = 2\pi R\, \varepsilon^{\mathrm{PP}}(a)$ does not hold any longer for the cylinder, such that the resulting formulae are not related to the known results of parallel plates and are rather complicated. For arbitrary a and T, we obtain

$$\frac{F_{\mathrm{LO}}^{\mathrm{PFA}}(a,T)}{L_y} = \sum_{n=1}^{\infty} \left\langle \frac{\lambda^2 \sqrt{aR}\, T^2}{4\sqrt{2}\, a^2 n^2 \pi} \left({}_2F_2\left(\frac{3}{4}, \frac{5}{4}; 1, \frac{3}{2}; -\frac{\lambda^2 n^2}{4a^2 T^2}\right) \right.\right.$$

$$\left.\left. - {}_2F_2\left(\frac{3}{4}, \frac{5}{4}; \frac{3}{2}, 2; -\frac{\lambda^2 n^2}{4a^2 T^2}\right) \right) \right\rangle, \quad (8.34)$$

where ${}_2F_2$ is the hypergeometric function in the standard notation. Eq. (8.34) does not distinguish between $a < R$ and $a > R$, since the relevant parameter for different temperature regions is aT. For small aT ($aT \lesssim 1/2$), we can expand Eq. (8.34), resulting in

$$\frac{F_{\mathrm{LO}}^{\mathrm{PFA}}(a,T)}{L_y} = \frac{3\sqrt{R}\,\zeta(7/2)\zeta(1/2)}{4\sqrt{2}\,\pi} T^{7/2}$$

$$- \frac{15 a\sqrt{R}\,\zeta(9/2)\zeta(-1/2)}{4\sqrt{2}\,\pi} T^{9/2} + \mathcal{O}(a^2). \quad (8.35)$$

For large aT, the Poisson resummation of Eq. (8.34) leads to

$$\Delta F_{\mathrm{LO}}^{\mathrm{PFA}}(a,T) = \frac{\pi^3 \sqrt{aR}}{768\sqrt{2}\,a^4} - \frac{3\sqrt{aR}\,\zeta(3)}{32\sqrt{2}\,a^3} T, \quad (8.36)$$

which is, of course, $-F_{\mathrm{LO}}^{\mathrm{PFA}}(a,0) + T\widetilde{F}_{\mathrm{LO}}^{\mathrm{PFA}}(a)$. Note that at $a = 0$ the leading-order PFA predicts a $T^{7/2}$ behavior of the thermal force for all T. At finite a, the validity of the low-temperature limit is independent of R. With increasing a, the absolute value of the thermal force is always reduced, irrespective of T, quite the contrary to the full worldline results.

8.3.2 Plate-based PFA

Here, we give only the analytic expressions for special limits, since no general expression could be found in a closed form. At $a = 0$ and $T \ll 1/R$, the thermal force can be found from the result of two parallel plates with an area of $A = 2RL_y$,

$$\Delta F_{\mathrm{PB}}^{\mathrm{PFA}}(a = 0, T) = -2RL_y \frac{\pi^2}{90} T^4. \tag{8.37}$$

As temperature rises, the T behavior changes from T^4 to $T^{7/2}$. For $T \gg 1/R$ and $a = 0$, the plate-based PFA agrees with the leading-order PFA, and the thermal force is given by the first term in Eq. (8.35). At low temperatures and $a \ll R$, the dependence on a is exponentially suppressed, just as in the case of the plate-based PFA for the sphere.

Finally, at finite a and $T \gg 1/a$, the force becomes classical

$$F_{\mathrm{PB}}^{\mathrm{PFA}} = -F_{\mathrm{PB}}^{\mathrm{PFA}}(a, 0) + T \widetilde{F}_{\mathrm{PB}}^{\mathrm{PFA}}(a),$$

with

$$\frac{F_{\mathrm{PB}}^{\mathrm{PFA}}(a, 0)}{L_y} = -\frac{(15 + 2a(2 + a)(11 + 3a(2 + a)))\pi^2}{1440 a^3 (1 + a)^2 (2 + a)^3}$$

$$-\frac{(5 + 4a(2 + a))\pi^3}{960 a^{7/2}(2 + a)^{7/2}} \tag{8.38}$$

$$-\frac{(5 + 4a(2 + a))\pi^2 \mathrm{ArcTan}\left[\frac{1}{\sqrt{a(2+a)}}\right]}{480 a^{7/2}(2 + a)^{7/2}},$$

and

$$\frac{\widetilde{F}_{\mathrm{PB}}^{\mathrm{PFA}}(a)}{L_y} = -\frac{3(1 + a)\zeta(3)}{16 a^{5/2}(2 + a)^{5/2}} - \frac{(3 + 4a + 2a^2)\zeta(3)}{8 a^2 (1 + a)(2 + a)^2 \pi}$$

$$-\frac{3(1 + a)\mathrm{ArcTan}\left[\frac{1}{\sqrt{a(2+a)}}\right]\zeta(3)}{8 a^{5/2}(2 + a)^{5/2}\pi}. \tag{8.39}$$

In Eqs. (8.38) and (8.39), we set $R = 1$; general expressions can be reconstructed by simple dimensional analysis.

8.3.3 Cylinder-based PFA

For the cylinder-based PFA, the thermal Casimir force is given by

$$\Delta F_{\mathrm{CB}}^{\mathrm{PFA}}(a, T) = -\frac{RL_y}{8\pi^2} \int_0^{\pi/2} h'_{\mathrm{SB}}(a)\mathrm{d}\theta \int_{h_{\mathrm{CB}}^2/\lambda^2}^{\infty} \sum_{n=1}^{\infty} \frac{e^{-\frac{n^2\beta^2}{4\mathcal{T}}}}{\mathcal{T}^3} \, \mathrm{d}\mathcal{T}, \qquad (8.40)$$

where $h_{\mathrm{CB}}(a)$ is given by Eq. (8.5). At $a = 0$, the thermal force can be found in closed form,

$$\frac{\Delta F_{\mathrm{CB}}^{\mathrm{PFA}}(a = 0, T)}{L_y} = \Big\langle \sum_{n=1}^{\infty} \frac{c}{1680} \sqrt{x} \Big[35 e^{-\frac{x^2}{8}} \pi x^{3/2} \left(I_{-1/4}\left(\frac{x^2}{8}\right) + 7 I_{3/4}\left(\frac{x^2}{8}\right) \right)$$

$$- 1260\sqrt{2}\Gamma\left(\frac{3}{4}\right) \, {}_1F_1\left(\frac{3}{4}; \frac{1}{2}; -\frac{x^2}{4}\right)$$

$$- 16x^{3/2} \left(-35 \, {}_2F_2\left(1, \frac{3}{2}; \frac{5}{4}, \frac{7}{4}; -\frac{x^2}{4}\right) + 16 \, {}_2F_2\left(1, \frac{3}{2}; \frac{9}{4}, \frac{11}{4}; -\frac{x^2}{4}\right) \right)$$

$$+ 16 \, {}_2F_2\left(\frac{3}{2}, 2; \frac{9}{4}, \frac{11}{4}; -\frac{x^2}{4}\right) + 3 \, {}_3F_3\left(1, 1, \frac{3}{2}; 2, \frac{9}{4}, \frac{11}{4}; -\frac{x^2}{4}\right) \Big)$$

$$- 504\sqrt{2}x^2\Gamma\left(\frac{3}{4}\right) \, {}_2F_2\left(\frac{5}{4}, \frac{7}{4}; \frac{3}{2}, \frac{9}{4}; -\frac{x^2}{4}\right)$$

$$+ 5\sqrt{2}x^3\Gamma\left(-\frac{3}{4}\right) \, {}_2F_2\left(\frac{5}{4}, \frac{7}{4}; \frac{5}{2}, \frac{11}{4}; -\frac{x^2}{4}\right) \Big] \Big\rangle, \qquad (8.41)$$

where I_n is the modified Bessel function of the first kind, ${}_pF_q$ the generalized hypergeometric function, $c = 2RT^4/n^4\pi^2$ and $x = n\lambda/2RT$. At small T, the expansion of Eq. (8.41) leads to

$$\frac{\Delta F_{\mathrm{CB}}^{\mathrm{PFA}}(0, T)}{L_y} = \frac{RT^4 \left(3\pi^4 + 2\pi^4 \ln\left(\frac{RT}{2\pi}\right) + 180\zeta'(4)\right)}{90\pi^2} - \frac{R^2T^5\zeta(5)}{\pi} + \mathcal{O}(T^6).$$
$$(8.42)$$

As temperature rises, the T behavior changes to $T^{7/2}$. For $T \gg 1/R$ and $a = 0$, the cylinder-based PFA agrees with the leading-order PFA and the thermal force is given by the first term in Eq. (8.35). For sufficiently small a, the difference to the $a = 0$ result reads

$$\frac{\Delta F_{\mathrm{CB}}^{\mathrm{PFA}}(a, T) - \Delta F_{\mathrm{CB}}^{\mathrm{PFA}}(0, T)}{L_y} = \frac{a\pi^2}{45}T^4 + \mathcal{O}(T^6). \qquad (8.43)$$

At finite a and $T \gg 1/a$, the force becomes classical, $-F_{\text{CB}}^{\text{PFA}}(a,0) + T\widetilde{F}_{\text{CB}}^{\text{PFA}}(a)$, with

$$\frac{F_{\text{CB}}^{\text{PFA}}(a,0)}{L_y} = -\frac{(15 + 8a + 4a^2)\pi^2}{1440a^3(2+a)^3} - \frac{\sqrt{a(2+a)}\,(5 + 6a + 3a^2)\,\pi^3}{960a^4(2+a)^4}$$

$$-\frac{(5 + 6a + 3a^2)\,\pi^2\text{ArcTan}\left[\frac{1}{\sqrt{a(2+a)}}\right]}{480a^{7/2}(2+a)^{7/2}}, \tag{8.44}$$

and

$$\frac{\widetilde{F}_{\text{PB}}^{\text{PFA}}(a)}{L_y} = -\frac{3\zeta(3)}{8a^2\pi(a+2)^2} - \frac{(a^2 + 2a + 3)\zeta(3)}{16(a(a+2))^{5/2}}$$

$$-\frac{(a^2 + 2a + 3)\,\text{ArcTan}\left[\frac{1}{\sqrt{a(a+2)}}\right]\zeta(3)}{8a^{5/2}\pi(a+2)^{5/2}}. \tag{8.45}$$

In Eqs. (8.44) and (8.45), we set $R = 1$, general expressions can be reconstructed by dimensional analysis.

9 Conclusions and outlook

In this thesis, we applied worldline numerics to obtain a general understanding of *geothermal* Casimir phenomena. Worldline numerics [37–40] is a unique tool for computing quantum energies. It originates in the string-inspired approach to quantum field theory [41–44] and is based on a mapping of field-theoretic fluctuation averages onto quantum-mechanical path integrals [45–50]. Worldline numerics is independent of the Casimir geometry and is readily applied to systems at a finite temperature. These are the main advantages over other approaches to the Casimir effect.

We started our analysis with the classic configuration of two parallel plates. Although this configuration is the most accessible theoretically, precise measurements of the Casimir force turn out to be an enormous challenge for experimentalists since the plates must be maintained in perfect alignment on a nanometer scale. The necessity to preserve parallelity of the plates is circumvented by using a curved surface in front of the plate. In this context, the sphere-plate configuration is most important for modern experiments measuring the Casimir force. Another promising geometry is the cylinder-plate configuration. We therefore performed a comprehensive analysis of both the sphere-plate and cylinder-plate configurations.

A distinctive feature of Casimir forces is, however, the strong dependence on the geometry – the shape and orientation – of the test bodies. For instance, investigating the Casimir effect for two inclined plates, we observed that even at zero temperature the dependence of the Casimir force on the separation exhibits a different power law to the case of parallel plates. General setups nevertheless suffer from insufficient theoretical understanding. For comparison between theory and experiment, powerful theoretical methods are required which can deal with arbitrary geometries. In addition to the worldline methods [37–40, 51–61] used in this work, many approaches have been developed in recent years. Two prominent examples are the functional integral approach [62–64] and scattering theory [65–82].

Moreover, for real materials, properties such as finite conductivity, surface roughness and finite temperature have to be taken into account. Generically, these corrections do not factorize but influence each other.

In this thesis, we drew attention to the highly nontrivial interplay between geometry and temperature, which is at the same time a characteristic feature of the Casimir effect. The geothermal interplay yields new and unexpected results for the geometry dependence of thermal forces. For instance, the pure thermal force reveals a non-monotonic behavior for the sphere-plate and cylinder-plate case, and can increase for increasing distances. This anomalous behavior is caused by a reweighting of relevant fluctuations, and has a transparent explanation within the worldline picture of the Casimir effect. This phenomenon is not restricted to spheres or cylinders above a plate and is expected to occur for general objects in front of surfaces, as long as the lateral surface extent is sufficiently larger than the thermal wavelength.

Another example is the delocalization of the thermal force density at low temperatures. The width of the force density is dictated not only by the geometry scales but also by the thermal wavelength. As a consequence, local approximation techniques such as the proximity force approximation (PFA) in general break down at low temperatures. The thermal force for a sphere-plate configuration, for example, follows a T^4 power law at low temperatures, whereas the leading-order PFA correction predicts a T^3 behavior. Another consequence of this delocalization is that edge effects emerging from surfaces will be larger for the thermal force than for the zero-temperature force.

Geothermal phenomena become most pronounced in geometries where the relevant part of the spectrum is gapless. In these so-called open geometries, any small value of the temperature can excite low-lying thermal modes, giving rise to thermal corrections. Open geometries, thus, support a stronger influence of long-range fluctuations on thermal Casimir phenomena. By contrast, a gap in the relevant part of the spectrum of closed geometries suppresses thermal excitations at low temperature.

The transition from open to closed geometries and the role of long-range fluctuations can be illustrated best by the inclined-plates configuration. Here, at low temperature T the thermal corrections to the Casimir force at finite inclinations become an order of magnitude larger, $\sim T^{D-1}$ in D spacetime dimensions. In a closed geometry of two parallel plates, the thermal behavior is $\sim T^D$.

The limit of zero inclination is particularly interesting since here the configuration is somewhat in-between open and closed geometries – the open part of the spectrum only arises due to the edge of the semi-infinite plate. Numerical eval-

uation of the thermal contribution resulting from the edge shows a temperature dependence which also lies between $\sim T^{D-1}$ and $\sim T^D$. The strongest temperature dependence, $\sim T^{D-2}$ in the low-temperature limit, was found for the Casimir torque of the inclined-plates configuration.

Incidentally, the Casimir effect for the inclined plates configuration can be understood in terms of simple geometric properties of the worldlines. All relevant information of a worldline needed for the evaluation of the Casimir energy is encoded in the boundary curves of worldlines. For the special case of two parallel plates, only the worldline extent is important. This connection between Casimir energies and worldline properties also relates Casimir energies to questions in polymer physics [53].

The observation that only the boundary of worldlines are relevant for the Casimir effect in the inclined-plates configuration helped us to develop powerful numerical algorithms for fast Casimir computations. Our investigation generalized earlier studies of edge-configurations [54, 56].

For the sphere-plate and cylinder-plate configurations, on the other hand, an efficient approach to direct force computation was found. This lead to strong simplifications compared to previous energy calculations [52] and allowed us to determine the Casimir force with high precision for a wide parameter range. At finite temperature, our procedure automatically removes distance-independent terms which build up the leading contribution to the thermal Casimir energy, eliminating the necessity of taking the derivative numerically. Thus, first unambiguous and consistent predictions for the thermal Casimir forces in the sphere/cylinder-plate configurations could be achieved.

Surprisingly, worldline numerics can also lead to novel analytical results. The main examples are the exact temperature and separation exponents, and the first exact low-temperature result of the thermal force for the inclined plates in arbitrary spacetime dimensions. For arbitrary dimensions, we also obtained the exact leading low-temperature correction to the thermal energy for parallel plates; to the best of our knowledge this is the first such exact analytic formula.

Furthermore, we argued that for general geometries, low-temperature corrections to Casimir forces are much more easily accessible in the (formal) contact limit $a \to 0$, since in this limit thermal corrections do not exhibit any divergences and remain well-behaved. The existence of this limit allows, for instance, the analytic calculation of the thermal correction for the inclined-plate case. It also helped us devise the low temperature behavior of the Casimir force for sphere/cylinder-plate configurations. This observation will be equally useful for many other geometries. We also expect the occurrence of similar strong simplifications in other

field theoretical approaches, such as functional-integral approaches [62, 63], scattering theory [67, 70, 72, 75, 79], and mode summation [77].

Our numerical and analytical results have been derived for the case of a fluctuating scalar field obeying Dirichlet boundary conditions on the surfaces. Although this model should not generally be considered as a quantitatively appropriate estimate for the real electromagnetic Casimir effect, our general conclusions about the geothermal phenomena are not restricted to the Dirichlet-scalar case. On the contrary, all our arguments, based on general considerations about the spectral gap, will also be qualitatively valid for the electromagnetic case. Of course, for a realistic description of the Casimir effect, all aspects of geometry, temperature, material properties, boundary conditions and edge effects will have to be taken into account simultaneously. Their mutual interplay inhibits a naive factorization of these phenomena and is a challenge for future research.

In the present work, we have developed a general picture underlying geothermal Casimir phenomena. However, the particular geothermal interplay which we have observed in the context of the Casimir effect is certainly not restricted to Casimir physics. The crucial ingredients are a gapless fluctuation spectrum in a spatially inhomogeneous background – though small gaps may not necessarily exert a strong quantitative influence. We expect that similar phenomena can occur for the thermal response of a system with an inhomogeneous condensate and an (almost) gapless fluctuation spectrum.

We conclude this thesis with the remark that the interplay between geometry and temperature is only one out of several highly nontrivial interferences between deviations from the ideal Casimir limit. For instance, the interplay between dielectric material properties and finite temperature [139] is still a subject of intense theoretical investigation and has created a long-standing controversy [140–143, 158]. Additionally, the interplay between dielectric properties and geometry has also shown to lead to significant deviations from ideal curvature effects [162]. Whereas we have concentrated on Casimir forces and interaction energies between disconnected surfaces, also Casimir free energies of single bodies can exhibit a sophisticated temperature dependence, as has recently been analyzed for wedges and cylindrical shells [168]. All of this exemplifies the beauty and richness of Casimir phenomena.

A The Poisson summation formula

The Poisson summation formula is a powerful method to speed up the convergence of certain slowly converging series.

Let $f : \mathbb{R} \to \mathbb{C}$ be a continuous function and $c_1, c_2, \varepsilon_1, \varepsilon_2 > 0$, such that

$$|f(x)| \leq \frac{c_1}{|x|^{1+\varepsilon_1}} \quad \text{and} \quad |\hat{f}(x)| \leq \frac{c_2}{|x|^{1+\varepsilon_2}} \tag{A.1}$$

for $x \neq 0$. Here, $\hat{f}$ is the Fourier transform of f,

$$\hat{f}(k) \equiv \frac{1}{\sqrt{2\pi}} \int_{-\infty}^{\infty} f(x) \, e^{-ixk} \, \mathrm{d}x, \tag{A.2}$$

which exists because of the condition on f. Then for $T > 0$ the Poisson summation formula is stated as

$$T \sum_{n \in \mathbb{Z}} f(nT) = \sqrt{2\pi} \sum_{k \in \mathbb{Z}} \hat{f}\left(\frac{2\pi k}{T}\right). \tag{A.3}$$

In order to prove this formula, we construct a 2π periodic function φ as follows,

$$\varphi(x) = \sum_{n \in \mathbb{Z}} f\left(\frac{T}{2\pi}(x + 2n\pi)\right), \tag{A.4}$$

and expand φ in a Fourier series. The corresponding Fourier coefficients then are

$$c_k = \frac{1}{2\pi} \sum_{n \in \mathbb{Z}} \int_0^{2\pi} f\left(\frac{T}{2\pi}(x + 2n\pi)\right) e^{-ikx} \, \mathrm{d}x. \tag{A.5}$$

A The Poisson summation formula

We substitute $x \to 2\pi\, t/T$ and Eq. (A.5) becomes

$$
\begin{aligned}
c_k &= \frac{1}{T} \sum_{n \in \mathbb{Z}} \int_0^T f(t + nT)\ e^{-ik\frac{2\pi}{T}t}\, \mathrm{d}t \\
&= \frac{1}{T} \sum_{n \in \mathbb{Z}} \int_{nT}^{(n+1)T} f(t)\ e^{-ik\frac{2\pi}{T}t}\, \mathrm{d}t \\
&= \frac{1}{T} \int_{-\infty}^{\infty} f(t)\ e^{-ik\frac{2\pi}{T}t}\, \mathrm{d}t \\
&= \frac{\sqrt{2\pi}}{T} \hat{f}\left(\frac{2\pi k}{T}\right).
\end{aligned}
\tag{A.6}
$$

We thus obtain for all x

$$
\varphi(x) = \sum_{n \in \mathbb{Z}} c_k e^{ikx} = \frac{\sqrt{2\pi}}{T} \sum_{k \in \mathbb{Z}} \hat{f}\left(\frac{2\pi k}{T}\right) e^{ikx}.
\tag{A.7}
$$

For $x = 0$, we find with (A.4) the Poisson summation formula (A.3). For mathematical details and justifications of the steps (A.3)-(A.7), see [169].

The functions f and $\hat{f}$ in (A.3) are vanishing as $|x| \to \infty$. For small T the right hand side of (A.3) converges very rapidly, for large T the left hand side does.

B Inclined plates in the optical approximation

The inclined plates geometry studied in chapter 4 can be obtained from the geometry of the so called "Casimir torsion pendulum", see Fig. B.1, if we substitute

$$h \rightarrow a + \frac{1}{2} w \sin(\varphi) \tag{B.1}$$

and then take the limit $w \rightarrow \infty$. The Casimir torsion pendulum was studied in [36, 138] using the optical approach. Here, we give the expressions from which the function representing the result of the optical approximation in Fig. 4.8 can be reconstructed. The following expressions can be found in [36]. However some of them, unfortunately, are misprinted. We give here their, in our opinion, correct version.

According to [36, 138], the Casimir force per unit length can be obtained from the following fast convergent series

$$\frac{F_c^{\text{opt}}}{L_y} = F_{1u+3u} + F_{2u+2d} + F_{3d+5d} + F_{4u+4d} + \cdots , \tag{B.2}$$

where F_{1u+3u} dominates for small φ. The contributions in B.2 (with the notation defined in Fig. B.1) should read

$$F_{1u+3u} = - \frac{\cos(\varphi)}{16\pi^2 \sin^4(\varphi)} \left(\frac{1}{(h/\sin(\varphi) - w/2)^3} - \frac{1}{(h/\sin(\varphi) + w/2)^3} \right), \tag{B.3}$$

$$F_{2u+2d} = - \frac{\cos^3(\varphi)}{48\pi^2 \sin^2(\varphi)} \left(\frac{1}{(h/\sin(\varphi) - w/2)^3} - \frac{1}{(h/\sin(\varphi) + w/2)^3} \right), \tag{B.4}$$

$$F_{3d+5d} = - \frac{1}{16\pi^2} \frac{\cos^5(2\varphi)}{\sin^4(2\varphi)} \left(\frac{1}{(h/\sin(\varphi) - w/2)^3} - \frac{1}{(h/\sin(\varphi) + w/2)^3} \right), \tag{B.5}$$

$$F_{4u+4d} = - \frac{\cos^3(2\varphi)}{48\pi^2 \sin^2(2\varphi)} \left(\frac{1}{(h/\sin(\varphi) - w/2)^3} - \frac{1}{(h/\sin(\varphi) + w/2)^3} \right). \tag{B.6}$$

Notice that the force per length diverges when the upper plate touches the lower plate, i.e. if

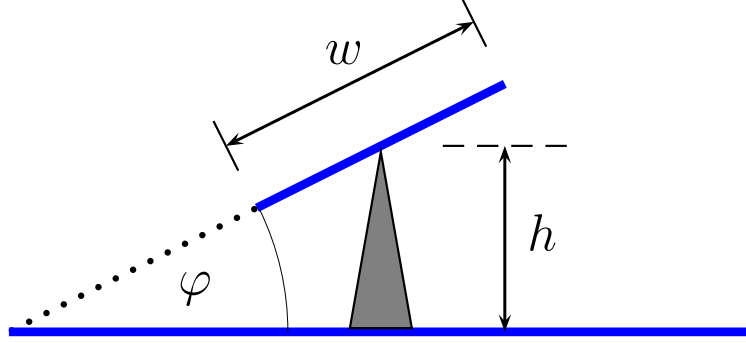$$w > 2h \quad \text{and} \quad h/\sin(\varphi) - w/2 = 0. \tag{B.7}$$

Figure B.1: The configuration for the Casimir pendulum. The lower plate is assumed to be infinite. The upper plate is inclined at an angle φ and is held at its midpoint at a distance h above the lower plate. The length of the upper plate is w. The plates' depth L_y (out of page) is taken to be infinite. This configuration becomes for $h \to a + \frac{1}{2} w \sin(\varphi)$ and then $w \to \infty$ the inclined plates configuration shown in Fig. 4.6 and studied in detail in chapter 4.

However, there is another source of divergence, independent of the upper plates length w. The contributions F_{3d+5d} and F_{4u+4d} diverge at $\varphi = \pi/2$.

The reference [36] also gives the Casimir energy $\mathcal{E}_{1u+3u}$ and torque $\mathcal{T}_{1u+3u}$, which are misprinted as well. In [138] the authors notice that the optical approximation predicts a non vanishing Casimir torque at $\varphi = 0$, which seems to be quite counterintuitive. Here we would like to mention that the torque does vanish at $\varphi = 0$ if calculated for the first four terms (Eq.(B.3)-(B.6)) of the expansion (B.2).

Let us now substitute

$$h \to a + \frac{1}{2} w \sin(\varphi),$$

and then take the limit $w \to \infty$ to obtain the expressions for the inclined plates geometry. Eq. (B.3)-(B.6) become

$$F_{1u+3u} = -\frac{\cot(\varphi)}{16\pi^2 a^3}, \tag{B.8}$$

$$F_{2u+2d} = -\frac{\cos^3(\varphi)\sin(\varphi)}{48\pi^2 a^3}, \tag{B.9}$$

$$F_{3d+5d} = -\frac{\cos^5(2\varphi)\csc(\varphi)\sec^4(\varphi)}{256\pi^2 a^3}, \tag{B.10}$$

$$F_{4u+4d} = -\frac{\cos^3(2\varphi)\sec(\varphi)\tan(\varphi)}{192\pi^2 a^3}. \tag{B.11}$$

At small φ, the Casimir force (B.2) per unit *length* diverges as it should, since for $\varphi \to 0$ the force becomes proportional to the *area* of the upper semi-infinite

plate. For vanishing φ, the force should diverge like the worldline- and the PFA result,

$$\frac{F_{\mathrm{c}}^{\mathrm{opt}}(\varphi \to 0)}{L_y} \simeq -\frac{\pi^2}{1440\, a^3\, \varphi}. \tag{B.12}$$

Indeed, expanding the force at small φ, we obtain

$$\frac{F_{\mathrm{c}}^{\mathrm{opt}}(\varphi \to 0)}{L_y} \simeq -\frac{1}{16\pi^2\, a^3\, \varphi} \left(1 + \frac{1}{16} + \dots \right), \tag{B.13}$$

where the series in round brackets becomes $\zeta(4) = \pi^4/90$.

Note that the leading force obtained from (B.8)-(B.11) also diverges (with a change of sign) for $\varphi = \pi/2$. This divergence is not due to the infinite length of the upper plate, as we have observed above.

The force calculated from (B.8)-(B.11) is shown in Fig. 4.8.

B Inclined plates in the optical approximation

Bibliography

[1] H.B.G. Casimir, "On The Attraction Between Two Perfectly Conducting Plates," Kon. Ned. Akad. Wetensch. Proc. **51**, 793 (1948).

[2] M. J. Sparnaay, Physica **24**, 751 (1958).

[3] M. Bordag, U. Mohideen and V. M. Mostepanenko, "New developments in the Casimir effect," Phys. Rept. **353**, 1 (2001) [arXiv:quant-ph/0106045].

[4] M. Bordag, G. L. Klimchitskaya, U. Mohideen and V. M. Mostepanenko, "Advances in the Casimir effect," Int. Ser. Monogr. Phys. **145**, 1 (2009).

[5] G. L. Klimchitskaya, U. Mohideen and V. M. Mostepanenko, "The Casimir force between real materials: experiment and theory," Rev. Mod. Phys. **81**, 1827 (2009) [arXiv:0902.4022 [cond-mat.other]].

[6] K. A. Milton, "The Casimir effect: Physical manifestations of zero-point energy," *River Edge, USA: World Scientific (2001).*

[7] G. Plunien, B. Muller and W. Greiner, "TEMPERATURE CORRECTIONS TO THE CASIMIR EFFECT," *In *Maratea 1986, Proceedings, Physics of strong fields* 899-906. (see Conference Index)*

[8] V. M. Mostepanenko and N. N. Trunov, "The Casimir effect and its applications," Sov. Phys. Usp. **31**, 965 (1988) [Usp. Fiz. Nauk **156**, 385 (1988)].

[9] V. M. Mostepanenko and N. N. Trunov, "The Casimir effect and its applications," *Oxford, UK: Clarendon (1997) 199 p*

[10] M. Krech, "The Casimir Effect in Critical Systems," *World Scientific, Singapore (1994)..*

[11] P. W. Milonni, "The Quantum vacuum: An Introduction to quantum electrodynamics," *Boston, USA: Academic (1994) 522 p*

[12] M. Kardar and R. Golestanian, "The 'Friction' of Vacuum, and other Fluctuation-Induced Forces," Rev. Mod. Phys. **71**, 1233 (1999) [arXiv:cond-mat/9711071].

Bibliography

[13] K. A. Milton, "The Casimir effect: Recent controversies and progress," J. Phys. A **37**, R209 (2004) [arXiv:hep-th/0406024].

[14] S. K. Lamoreaux, "The Casimir force: Background, experiments, and applications," Rept. Prog. Phys. **68**, 201 (2005).

[15] V. A. Parsegian, "Van der Waals Forces: A Handbook for Biologists, Chemists, Engineers, and Physicists," *Cambridge University Press, Cambridge (2005).*

[16] E. Buks, M.L. Roukes, Phys. Rev. B 63 (2001) 033402.

[17] E. Elizalde, S. D. Odintsov and A. A. Saharian, "Repulsive Casimir effect from extra dimensions and Robin boundary conditions: from branes to pistons," Phys. Rev. D **79**, 065023 (2009) [arXiv:0902.0717 [hep-th]].

[18] A. A. Saharian, "Bulk Casimir densities and vacuum interaction forces in higher dimensional brane models," Phys. Rev. D **73**, 064019 (2006) [arXiv:hep-th/0508185].

[19] E. Elizalde, S.D. Odintsov, A. Romeo, A.A. Bytsenko, S. Zerbini, "Zeta Regularization Techniques with Applications," *World Scientific, Singapore, (1994).*

[20] E. Elizalde, "Ten Physical Applications of Spectral Zeta Functions," *Springer, Berlin, Heidelberg, (1995).*

[21] M. Bordag, B. Geyer, G. L. Klimchitskaya and V. M. Mostepanenko, "Constraints for hypothetical interactions from a recent demonstration of the Casimir force and some possible improvements," Phys. Rev. D **58**, 075003 (1998) [arXiv:hep-ph/9804223].

[22] M. Bordag, B. Geyer, G. L. Klimchitskaya and V. M. Mostepanenko, "Stronger constraints for nanometer scale Yukawa-type hypothetical interactions from the new measurement of the Casimir force," Phys. Rev. D **60**, 055004 (1999) [arXiv:hep-ph/9902456].

[23] M. Bordag, B. Geyer, G. L. Klimchitskaya and V. M. Mostepanenko, "New constraints for non-Newtonian gravity in nanometer range from the improved precision measurement of the Casimir force," Phys. Rev. D **62**, 011701 (2000) [arXiv:hep-ph/0003011].

[24] J. C. Long, H. W. Chan and J. C. Price, "Experimental status of gravitational-strength forces in the sub-centimeter regime," Nucl. Phys. B **539**, 23 (1999) [arXiv:hep-ph/9805217].

[25] V. M. Mostepanenko and M. Novello, "Constraints on non-Newtonian gravity from the Casimir force measurements between two crossed cylinders," Phys. Rev. D **63**, 115003 (2001) [arXiv:hep-ph/0101306].

[26] K. A. Milton, R. Kantowski, C. Kao and Y. Wang, "Constraints on extra dimensions from cosmological and terrestrial measurements," Mod. Phys. Lett. A **16**, 2281 (2001) [arXiv:hep-ph/0105250].

[27] R.S. Decca, E. Fischbach, G.L. Klimchitskaya, D.E. Krause, D.L. Lopez and V.M. Mostepanenko, "Improved tests of extra-dimensional physics and thermal quantum field theory from new Casimir force measurements," Phys. Rev. D **68**, 116003 (2003) [arXiv:hep-ph/0310157].

[28] R.S. Decca, D. Lopez, H.B. Chan, E. Fischbach, D.E. Krause and C.R. Jamell, "Constraining new forces in the Casimir regime using the isoelectronic technique," Phys. Rev. Lett. **94**, 240401 (2005) [arXiv:hep-ph/0502025].

[29] R. Onofrio, "Casimir forces and non-Newtonian gravitation," New J. Phys. **8**, 237 (2006) [arXiv:hep-ph/0612234].

[30] R. S. Decca, D. Lopez, E. Fischbach, G. L. Klimchitskaya, D. E. Krause and V. M. Mostepanenko, "Novel constraints on light elementary particles and extra-dimensional physics from the Casimir effect," Eur. Phys. J. C **51**, 963 (2007) [arXiv:0706.3283 [hep-ph]].

[31] R. S. Decca, D. Lopez, E. Fischbach, G. L. Klimchitskaya, D. E. Krause and V. M. Mostepanenko, "Tests of new physics from precise measurements of the Casimir pressure between two gold-coated plates," Phys. Rev. D **75**, 077101 (2007) [arXiv:hep-ph/0703290].

[32] V. M. Mostepanenko, R. S. Decca, E. Fischbach, G. L. Klimchitskaya, D. E. Krause and D. Lopez, "Stronger constraints on non-Newtonian gravity from the Casimir effect," J. Phys. A **41**, 164054 (2008) [arXiv:0802.0866 [hep-th]].

[33] H. B. G. Casimir and D. Polder, Phys. Rev. **73**, 360 (1948).

Bibliography

[34] P. J. F. Harris, "Carbon Nanotubes and Related Structures," *Cambridge University Press, (2002).*

[35] Yu. S. Nechaev, "The nature, kinetics, and ultimate storage capacity of hydrogen sorption by carbon nanostructures," Usp. Fiz. Nauk,**176**, 581-610 (2006).

[36] A. Scardicchio and R. L. Jaffe, "Casimir Effects: an Optical Approach II. Local Observables and Thermal Corrections," Nucl. Phys. B **743** (2006) 249 [arXiv:quant-ph/0507042].

[37] H. Gies, K. Langfeld and L. Moyaerts, "Casimir effect on the worldline," JHEP **0306**, 018 (2003) [arXiv:hep-th/0303264].

[38] L. Moyaerts, K. Langfeld and H. Gies, "Worldline approach to the Casimir effect," arXiv:hep-th/0311168.

[39] H. Gies and K. Langfeld, "Quantum diffusion of magnetic fields in a numerical worldline approach," Nucl. Phys. B **613**, 353 (2001) [arXiv:hep-ph/0102185].

[40] H. Gies and K. Langfeld, "Loops and loop clouds: A numerical approach to the worldline formalism in QED," Int. J. Mod. Phys. A **17**, 966 (2002) [arXiv:hep-ph/0112198].

[41] M. G. Schmidt and I. O. Stamatescu, "Determinant calculations using random walk worldline loops," Nucl. Phys. Proc. Suppl. **119**, 1030 (2003) [arXiv:hep-lat/0209120].

[42] M. G. Schmidt and I. O. Stamatescu, "Determinant calculations with random walk worldline loops," arXiv:hep-lat/0201002.

[43] M. G. Schmidt and C. Schubert, "On the calculation of effective actions by string methods," Phys. Lett. B **318**, 438 (1993) [arXiv:hep-th/9309055].

[44] C. Schubert, "Perturbative quantum field theory in the string-inspired formalism," Phys. Rept. **355**, 73 (2001) [arXiv:hep-th/0101036].

[45] R.P. Feynman, Phys. Rev. **80**, 440 (1950); **84**, 108 (1951).

[46] M. B. Halpern and W. Siegel, "The Particle Limit Of Field Theory: A New Strong Coupling Expansion," Phys. Rev. D **16**, 2486 (1977).

[47] M. B. Halpern, A. Jevicki and P. Senjanovic, "Field Theories In Terms Of Particle - String Variables: Spin, Internal Symmetries And Arbitrary Dimension," Phys. Rev. D **16**, 2476 (1977).

[48] A. M. Polyakov, "Gauge Fields And Strings," Harwood, Chur (1987).

[49] Z. Bern and D.A. Kosower, Nucl. Phys. **B362**, 389 (1991); **B379**, 451 (1992).

[50] M.J. Strassler, Nucl. Phys. **B385**, 145 (1992).

[51] H. Gies and K. Klingmuller, "Quantum energies with worldline numerics," J. Phys. A **39** 6415 (2006) [arXiv:hep-th/0511092].

[52] H. Gies and K. Klingmuller, "Casimir effect for curved geometries: PFA validity limits," Phys. Rev. Lett. **96**, 220401 (2006) [arXiv:quant-ph/0601094].

[53] H. Gies and K. Klingmuller, "Worldline algorithms for Casimir configurations," Phys. Rev. D **74**, 045002 (2006) [arXiv:quant-ph/0605141].

[54] H. Gies and K. Klingmuller, "Casimir edge effects," Phys. Rev. Lett. **97**, 220405 (2006) [arXiv:quant-ph/0606235].

[55] H. Gies and K. Klingmuller, "Geothermal Casimir Phenomena," J. Phys. A **41**, 164042 (2008).

[56] K. Klingmuller, PhD Dissertation, Heidelberg U., URN: urn:nbn:de:bsz:16-opus-78464, URL: http://www.ub.uni-heidelberg.de/archiv/7846 ˜(2007).

[57] A. Weber and H. Gies, "Interplay between geometry and temperature for inclined Casimir plates," Phys. Rev. D **80**, 065033 (2009) [arXiv:0906.2313 [hep-th]].

[58] H. Gies and A. Weber, "Geometry-Temperature Interplay in the Casimir Effect," arXiv:0912.0125 [hep-th].

[59] A. Weber and H. Gies, "Non-monotonic thermal Casimir force from geometry-temperature interplay," arXiv:1003.0430 [hep-th].

[60] A. Weber and H. Gies, "Geothermal Casimir phenomena for the sphere-plate and cylinder-plate configurations," arXiv:1003.3420 [hep-th].

[61] M. Schaden, "Dependence of the Direction of the Casimir Force on the Shape of the Boundary," Phys. Rev. Lett. **102**, 060402 (2009).

Bibliography

[62] M. Bordag, D. Robaschik and E. Wieczorek, "Quantum Field Theoretic Treatment Of The Casimir Effect. Quantization Procedure And Perturbation Theory In Covariant Gauge," Annals Phys. **165**, 192 (1985).

[63] T. Emig, A. Hanke and M. Kardar, "Probing the Strong Boundary Shape Dependence of the Casimir Force," Phys. Rev. Lett. **87** (2001) 260402 [arXiv:cond-mat/0106028].

[64] T. Emig and R. Buscher, "Towards a theory of molecular forces between deformed media," Nucl. Phys. B **696**, 468 (2004) [arXiv:cond-mat/0308412].

[65] A. Bulgac, P. Magierski and A. Wirzba, "Scalar Casimir effect between Dirichlet spheres or a plate and a sphere," Phys. Rev. D **73**, 025007 (2006) [arXiv:hep-th/0511056].

[66] A. Wirzba, A. Bulgac and P. Magierski, "Casimir interaction between normal or superfluid grains in the Fermi sea," J. Phys. A **39** (2006) 6815 [arXiv:quant-ph/0511057].

[67] T. Emig, R. L. Jaffe, M. Kardar and A. Scardicchio, "Casimir interaction between a plate and a cylinder," Phys. Rev. Lett. **96** (2006) 080403 [arXiv:cond-mat/0601055].

[68] M. Bordag, "The Casimir effect for a sphere and a cylinder in front of plane and corrections to the proximity force theorem," Phys. Rev. D **73**, 125018 (2006) [arXiv:hep-th/0602295].

[69] M. Bordag, "Generalized Lifshitz formula for a cylindrical plasma sheet in front of a plane beyond proximity force approximation," Phys. Rev. D **75**, 065003 (2007) [arXiv:quant-ph/0611243].

[70] O. Kenneth and I. Klich, "Opposites Attract - A Theorem About The Casimir Force," Phys. Rev. Lett. **97**, 160401 (2006) [arXiv:quant-ph/0601011].

[71] O. Kenneth and I. Klich, "Casimir forces in a T operator approach," arXiv:0707.4017.

[72] T. Emig, N. Graham, R. L. Jaffe and M. Kardar, "Casimir forces between arbitrary compact objects," Phys. Rev. Lett. **99**, 170403 (2007) [arXiv:0707.1862 [cond-mat.stat-mech]].

[73] T. Emig, N. Graham, R. L. Jaffe and M. Kardar, "Casimir Forces between Compact Objects: I. The Scalar Case," Phys. Rev. D **77**, 025005 (2008) [arXiv:0710.3084 [cond-mat.stat-mech]].

[74] T. Emig and R. L. Jaffe, "Casimir forces between arbitrary compact objects: Scalar and electromagnetic field," J. Phys. A **41**, 164001 (2008) [arXiv:0710.5104 [quant-ph]].

[75] R. B. Rodrigues, P. A. Maia Neto, A. Lambrecht and S. Reynaud, "Lateral Casimir force beyond the Proximity Force Approximation," Phys. Rev. Lett. **96**, 100402 (2006) [arXiv:quant-ph/0603120].

[76] R. B. Rodrigues, P. A. Maia Neto, A. Lambrecht and S. Reynaud, "Lateral Casimir forces beyond the proximity force approximation: A Nontrivial interplay between geometry and quantum vacuum," Phys. Rev. A **75**, 062108 (2007).

[77] F. D. Mazzitelli, D. A. R. Dalvit and F. C. Lombardo, "Exact zero-point interaction energy between cylinders," New J. Phys. **8**, 240 (2006) [arXiv:quant-ph/0610181].

[78] D. A. R. Dalvit, F. C. Lombardo, F. D. Mazzitelli and R. Onofrio, "Exact Casimir interaction between eccentric cylinders," Phys. Rev. A **74**, 020101 (2006).

[79] K. A. Milton and J. Wagner, "Exact Casimir Interaction Between Semi-transparent Spheres and Cylinders," Phys. Rev. D **77**, 045005 (2008) [arXiv:0711.0774 [hep-th]].

[80] K. A. Milton and J. Wagner, "Multiple Scattering Methods in Casimir Calculations," J. Phys. A **41**, 155402 (2008) [arXiv:0712.3811 [hep-th]].

[81] K. A. Milton, P. Parashar and J. Wagner, "Exact results for Casimir interactions between dielectric bodies: The weak-coupling or van der Waals Limit," arXiv:0806.2880 [hep-th].

[82] A. Canaguier-Durand, P. A. M. Neto, A. Lambrecht and S. Reynaud, "Thermal Casimir Effect in the Plane-Sphere Geometry," Phys. Rev. Lett. **104**, 040403 (2010) [arXiv:0911.0913 [quant-ph]].

[83] B.V. Derjaguin, I.I. Abrikosova, E.M. Lifshitz, Q.Rev. **10**, 295 (1956).

[84] J. Blocki, J. Randrup, W.J. Swiatecki, C.F. Tsang, Ann. Phys. (N.Y.) **105**, 427 (1977).

Bibliography

[85] J. D. van der Waals: "Over de Continuiteit van den Gas- en Vloeistoftoestand", Leiden, (1873).

[86] F. London, Zs. Phys. **63**, 245 (1930).

[87] T. H. Boyer, "Quantum Electromagnetic Zero Point Energy Of A Conducting Spherical Shell And The Casimir Model For A Charged Particle," Phys. Rev. **174**, 1764 (1968).

[88] B. Davies, J. Math. Phys., **13** 1324-9 (1972).

[89] R. Balian and B. Duplantier, Ann. Phys. (N.Y.) **112**, 165-208 (1978).

[90] K. A. Milton, L. L. DeRaad, Jr., and J. Schwinger, Ann. Phys. (N.Y.) **115**, 388 (1978).

[91] L. L. . DeRaad and K. A. Milton, "Casimir Selfstress On A Perfectly Conducting Cylindrical Shell," Annals Phys. **136**, 229 (1981).

[92] P. Candelas and S. Weinberg, Nucl. Phys. B **237**, 397-441 (1984).

[93] A. Chodos, R. L. Jaffe, K. Johnson, C. B. Thorn and V. F. Weisskopf, "A New Extended Model Of Hadrons," Phys. Rev. D **9**, 3471 (1974).

[94] A. Chodos, R. L. Jaffe, K. Johnson and C. B. Thorn, "Baryon Structure In The Bag Theory," Phys. Rev. D **10**, 2599 (1974).

[95] A. Chodos and C. B. Thorn, Phys. Rev. D **12**, 2733 (1975).

[96] T. DeGrand, R. L. Jaffe, K. Johnson and J. Kiskis, Phys. Rev. D **12**, 2060 (1975).

[97] J. F. Donoghue, E. Golowich and B. R. Holstein, Phys. Rev. D **12**, 2875 (1975).

[98] R. E. Schrock and S. B. Treiman, Phys. Rev. D **19**, 2148 (1979).

[99] K. Johnson, Acta Phys. Pol. **B6**, 865 (1975).

[100] R. L. Jaffe, "The Casimir effect and the quantum vacuum," Phys. Rev. D **72**, 021301 (2005) [arXiv:hep-th/0503158].

[101] For a review of work connecting vacuum fluctuations to the cosmological constant see S. Weinberg, "The Cosmological Constant Problem," Rev. Mod. Phys. **61**, 1 (1989).

[102] S. M. Carroll, "The cosmological constant," Living Rev. Rel. **4**, 1 (2001) [arXiv:astro-ph/0004075].

[103] V. Sahni and A. A. Starobinsky, "The Case for a Positive Cosmological Lambda-term," Int. J. Mod. Phys. D **9**, 373 (2000) [arXiv:astro-ph/9904398].

[104] The Ref. [100] gives further examples: S. M. Carroll, W. H. Press, and E. L. Turner, Ann. Rev. Astron. Astrophys. **30** 499 (1992); J. D. Cohn, Astrophys. J. Suppl. **259**, 213 (1998) [arXiv:astro-ph/9807128]; J. L. Feng, J. March-Russell, S. Sethi and F. Wilczek, Nucl. Phys. B **602**, 307 (2001) [arXiv:hep-th/0005276]; P. J. E. Peebles and B. Ratra, Rev. Mod. Phys. **75**, 559 (2003) [arXiv:astro-ph/0207347].

[105] E. Elizalde, "Uses of zeta regularization in QFT with boundary conditions: a cosmo-topological Casimir effect," J. Phys. A **39**, 6299 (2006) [arXiv:hep-th/0607185].

[106] K. V. Shajesh, K. A. Milton, P. Parashar and J. A. Wagner, "How does Casimir energy fall? III. Inertial forces on vacuum energy," J. Phys. A **41**, 164058 (2008) [arXiv:0711.1206 [hep-th]].

[107] K. A. Milton, S. A. Fulling, P. Parashar, A. Romeo, K. V. Shajesh and J. A. Wagner, "Gravitational and Inertial Mass of Casimir Energy," J. Phys. A **41**, 164052 (2008) [arXiv:0710.3841 [hep-th]].

[108] H. Verschelde, L. Wille and P. Phariseau, "Casimir Effect In N Dimensions," Phys. Lett. B **149**, 396 (1984).

[109] N. F. Svaiter and B. F. Svaiter, "CASIMIR EFFECT IN A D-DIMENSIONAL FLAT SPACE-TIME AND THE CUTOFF METHOD," J. Math. Phys. **32** , 175 (1991).

[110] H. Jeffreys and B. S. Jeffreys, "Methods of Mathematical Physics," *Cambridge University Press (1950).*

[111] W. Dittrich, M. Reuter, *Classical and Quantum Dynamics*, Springer (1994).

[112] H. Kleinert, *Path Integrals*, World Scientific (2006).

[113] W. Greiner, J. Reinhardt *Field Quantization*, Springer (1996).

[114] D. Deutsch and P. Candelas, "Boundary Effects In Quantum Field Theory," Phys. Rev. D **20**, 3063 (1979).

Bibliography

[115] P. Candelas, "Vacuum Polarization In The Presence Of Dielectric And Conducting Surfaces," Annals Phys. **143**, 241 (1982).

[116] G. Barton, "Perturbative Casimir energies of dispersive spheres, cubes and cylinders," J. Phys. A **34**, 4083 (2001).

[117] N. Graham, R. L. Jaffe, V. Khemani, M. Quandt, O. Schroeder and H. Weigel, "The Dirichlet Casimir problem," Nucl. Phys. B **677**, 379 (2004) [arXiv:hep-th/0309130].

[118] H. Weigel, "Dirichlet spheres in continuum quantum field theory," arXiv:hep-th/0310301.

[119] K. A. Milton, "Recent Developments in the Casimir Effect," J. Phys. Conf. Ser. **161**, 012001 (2009) [arXiv:0809.2564 [hep-th]].

[120] I. Cavero-Pelaez, K. A. Milton and J. Wagner, "Local Casimir energies for an annulus," arXiv:hep-th/0508001.

[121] K. A. Milton, "Calculating Casimir energies in renormalizable quantum field theory," Phys. Rev. D **68**, 065020 (2003) [arXiv:hep-th/0210081].

[122] C. M. Bender and K. A. Milton, "Casimir effect for a D-dimensional sphere," Phys. Rev. D **50**, 6547 (1994) [arXiv:hep-th/9406048].

[123] K. A. Milton, "Casimir energies and pressures for delta-function potentials," J. Phys. A **37**, 6391 (2004) [arXiv:hep-th/0401090].

[124] M. Bordag, K. Kirsten and D. Vassilevich, "On the ground state energy for a penetrable sphere and for a dielectric ball," Phys. Rev. D **59**, 085011 (1999) [arXiv:hep-th/9811015].

[125] M. Bordag and D. V. Vassilevich, "Nonsmooth backgrounds in quantum field theory," Phys. Rev. D **70**, 045003 (2004) [arXiv:hep-th/0404069].

[126] M. Bordag, D. Hennig and D. Robaschik, "Vacuum energy in quantum field theory with external potentials concentrated on planes," J. Phys. A **25**, 4483 (1992).

[127] N. Graham, R. L. Jaffe, V. Khemani, M. Quandt, M. Scandurra and H. Weigel, "Calculating vacuum energies in renormalizable quantum field theories: A new approach to the Casimir problem," Nucl. Phys. B **645**, 49 (2002) [arXiv:hep-th/0207120].

[128] C. D. Fosco, F. C. Lombardo and F. D. Mazzitelli, "Derivative expansion for the boundary interaction terms in the Casimir effect: generalized δ-potentials," Phys. Rev. D **80**, 085004 (2009) [arXiv:0908.1796 [hep-th]].

[129] C. D. Fosco, F. C. Lombardo and F. D. Mazzitelli, "Singular boundary interactions: regularization and Casimir effect," arXiv:0912.0886 [hep-th].

[130] T. Matsubara, Prog. Theor. Phys., **14**, 351 (1955).

[131] R. Balian and B. Duplantier, "Electromagnetic Waves Near Perfect Conductors. 2. Casimir Effect," Annals Phys. **112**, 165 (1978).

[132] I. Klich, J. Feinberg, A. Mann and M. Revzen, "Casimir energy of a dilute dielectric ball with uniform velocity of light at finite temperature," Phys. Rev. D **62**, 045017 (2000) [arXiv:hep-th/0001019].

[133] V. V. Nesterenko, G. Lambiase and G. Scarpetta, "Casimir effect for a dilute dielectric ball at finite temperature," Phys. Rev. D **64**, 025013 (2001) [arXiv:hep-th/0006121].

[134] M. Bordag, V. V. Nesterenko and I. G. Pirozhenko, "On the high temperature asymptotics of the free energy of quantum fields in confined regions," arXiv:hep-th/0107024.

[135] H. Gies, J. Sanchez-Guillen and R. A. Vazquez, "Quantum effective actions from nonperturbative worldline dynamics," JHEP **0508**, 067 (2005) [arXiv:hep-th/0505275].

[136] N. Graham, A. Shpunt, T. Emig, S. J. Rahi, R. L. Jaffe and M. Kardar, "Casimir Force at a Knife's Edge," Phys. Rev. D **81**, 061701 (2010) [arXiv:0910.4649 [quant-ph]].

[137] E.M. Lifshitz, Sov. Phys. JETP **2**, 73 (1956).

[138] A. Scardicchio and R. L. Jaffe, "Casimir Effects: An Optical Approach I. Foundations and Examples," Nucl. Phys. B **704**, 552 (2005) [arXiv:quant-ph/0406041].

[139] M. Boström and Bo E. Sernelius, Phys. Rev. Lett. **84**, 4757 (2000).

[140] V. M. Mostepanenko *et al.*, "Present status of controversies regarding the thermal Casimir force," J. Phys. A **39**, 6589 (2006) [arXiv:quant-ph/0512134].

Bibliography

[141] I. Brevik, S. A. Ellingsen and K. A. Milton, "Thermal corrections to the Casimir effect," arXiv:quant-ph/0605005.

[142] G. Bimonte, "The Bohr-van Leeuwen theorem and the thermal Casimir effect for conductors," Phys. Rev. A **79**, 042107 (2009) [arXiv:0903.0951 [quant-ph]].

[143] G.-L. Ingold, A. Lambrecht, S. Reynaud, arXiv:0905.3608 [quant-ph] (2009).

[144] C.C. Speake and C. Trenkel, Phys. Rev. Lett. **90**, 160403 (2003).

[145] W.J. Kim, M. Brown-Hayes, D.A.R. Dalvit, J.H. Brownell, R. Onofrio, Phys. Rev. A **78**, 020101(R) (2008) [arXiv:0812.0028v1 [quant-ph]].

[146] R. S. Decca, E. Fischbach, G. L. Klimchitskaya, D. E. Krause, D. López, U. Mohideen, V. M. Mostepanenko, Phys. Rev. A **79**, 026101 (2009), [arXiv:0809.3576 [quant-ph]].

[147] W.J. Kim, M. Brown-Hayes, D.A.R. Dalvit, J.H. Brownell, R. Onofrio, Phys. Rev. A **79**, 026102 (2009) [arXiv:0903.1085 [quant-ph]].

[148] R. L. Jaffe and A. Scardicchio, "The Casimir Effect and Geometric Optics," Phys. Rev. Lett. **92**, 070402 (2004) [arXiv:quant-ph/0310194].

[149] M. Schaden and L. Spruch, Phys. Rev. A **58**, 935 (1998); Phys. Rev. Lett. **84** 459 (2000).

[150] J. Feinberg, A. Mann and M. Revzen, "Casimir effect: The classical limit," Annals Phys. **288** (2001) 103 [arXiv:hep-th/9908149].

[151] M. Bordag and V. Nikolaev, "First analytic correction beyond the proximity force approximation in the Casimir effect for the electromagnetic field in sphere-plane geometry," Phys. Rev. D **81**, 065011 (2010) [arXiv:0911.0146 [hep-th]].

[152] M. Brown-Hayes, D. A. R. Dalvit, F. D. Mazzitelli, W. J. Kim and R. Onofrio, "Towards a precision measurement of the Casimir force in a cylinder-plane geometry," Phys. Rev. A **72**, 052102 (2005) [arXiv:quant-ph/0511005].

[153] A. Rodriguez *et al.*, M. Ibanescu, D. Iannuzzi, F. Capasso, J.D. Joannopoulos, and S.G. Johnson, Phys. Rev. Lett. **99**, 080401 (2007); Phys. Rev. A **76**, 032106 (2007).

[154] S.J. Rahi, T. Emig, R.L. Jaffe, and M. Kardar, Phys. Rev. A 78, 012104 (2008).

[155] S. K. Lamoreaux, "Demonstration of the Casimir force in the 0.6 to 6 micrometers range," Phys. Rev. Lett. **78**, 5 (1997).

[156] U. Mohideen and A. Roy, "Precision measurement of the Casimir force from 0.1 to 0.9 μm," Phys. Rev. Lett. **81**, 4549 (1998) [arXiv:physics/9805038].

[157] H.B. Chan *et al.*, Science 291, 1941 (2001).

[158] F. Intravaia and C. Henkel, "Casimir interaction from magnetically coupled eddy currents," Phys. Rev. Lett. **103**, 130405 (2009) [arXiv:0903.4771 [quant-ph]].

[159] S.A. Ellingsen, S.Y. Buhmann, S. Scheel, arXiv:1003.1261v1 [quant-ph].

[160] D. Kabat, D. Karabali and V. P. Nair, "Edges and Diffractive Effects in Casimir Energies," arXiv:1002.3575.

[161] Q. Wei and R. Onofrio, private communication (2010).

[162] A. Canaguier-Durand, P. A. Maia Neto, I. Cavero-Pelaez, A. Lambrecht and S. Reynaud, "Casimir interaction between plane and spherical metallic surfaces," Phys. Rev. Lett. **102**, 230404 (2009) [arXiv:0901.2647 [quant-ph]].

[163] R. Zandi, T. Emig, and U. Mohideen, Quantum and thermal Casimir interaction between a sphere and a plate: Comparison of Drude and plasma models arXiv:1003.0068 [cond-mat.stat-mech]

[164] K. A. Milton, P. Parashar, J. Wagner and K. V. Shajesh, "Exact Casimir energies at nonzero temperature: Validity of proximity force approximation and interaction of semitransparent spheres," arXiv:0909.0977 [hep-th].

[165] T. Emig, private communication (2010).

[166] M. Bordag, private communication (2010).

[167] M. Bordag and I. Pirozhenko, "Vacuum energy between a sphere and a plane at finite temperature," [arXiv:0912.4047 [quant-ph]].

[168] I. Brevik, S. A. Ellingsen and K. A. Milton, "Electromagnetic Casimir Effect in Wedge Geometry and the Energy-Momentum Tensor in Media," arXiv:0911.2688 [hep-th].

[169] K. Königsberger, *Analysis 1*, Springer (2001).

Bibliography

178

Danksagung

Ich möchte mich ganz besonders bei Prof. Holger Gies für die hervorragende Betreuung und die ausgezeichnete Zusammenarbeit an einem sehr spannenden Thema bedanken. Ich habe von seiner Unterstützung sehr profitiert.

Prof. Michael G. Schmidt danke ich dafür, dass er kurzfristig bereit war, die vorliegende Arbeit zu begutachten. Außerdem bin ich sehr dankbar für seine guten Ratschläge zu Beginn meiner Doktorarbeit.

Ferner danke ich Prof. Thorsten Emig, Prof. Emilio Elizalde, Prof. Michael Bordag, Prof. Vladimir M. Mostepanenko, Prof. Franz Wegner und Prof. Yuri Pismak für fruchtbare Gespräche.

Dr. Eduard Thommes danke ich für seine stets unglaublich freundliche Unterstützung und die wunderbare Atmosphäre am Institut. Danke auch für die gute Stimmung im Westzimmer und Dr. Stefan Flörchinger, Dr. Lily Schrempp, Dr. Klaus Klingmüller, Dr. Jürgen Stiewe, Emal Alekozai, Christoph Deil und Josef Ludescher für ihre Tipps.

Vera Spillner danke ich für das kreative Zuhören, kritische Fragen, wichtige Hinweise und die Inspiration für die Gestaltung der Grafiken.

Die Arbeit wurde von Josef Ludescher, Dr. Iain Brown und Vera Spillner korrekturgelesen, wobei viele nützliche Verbesserungsvorschläge gemacht wurden, wofür ich mich besonders herzlich bedanke.

Außerdem danke ich meiner Familie für den Rückhalt.

Für die finanzielle Unterstützung bedanke ich mich bei der Landesgraduiertenförderung Baden-Württemberg, der Graduiertenschule für Fundamental Physics in Heidelberg, bei dem Casimir-Network und bei der Universität Jena für die Reisekosten.

Erklärung

Ich versichere, dass ich diese Arbeit selbstständig verfasst und keine anderen als die angegebenen Quellen und Hilfsmittel verwendet habe.

Heidelberg, den ⎯⎯⎯⎯⎯⎯⎯⎯⎯   ⎯⎯⎯⎯⎯⎯⎯⎯⎯

(Alexej Weber)